Determination of the Gluon Polarisation in the Nucleon using Hadron Pairs with High Transverse Momentum at COMPASS

Sonja Hedicke

Fakultät für Mathematik und Physik
Albert-Ludwigs-Universität Freiburg

Determination of the Gluon Polarisation in the Nucleon using Hadron Pairs with High Transverse Momentum at COMPASS

Dissertation

zur Erlangung des

Doktorgrades

der

Fakultät für Mathematik und Physik

der

Albert-Ludwigs-Universität

Freiburg im Breisgau

vorgelegt von

Sonja Hedicke

aus Wiesbaden

Freiburg, November 2005

Dekan:	Prof. Dr. Josef Honerkamp
Leiter der Arbeit:	Prof. Dr. Kay Königsmann
Referent:	Prof. Dr. Kay Königsmann
Koreferent:	Prof. Dr. Klaus Desch
Tag der Verkündigung des Prüfungsergebnisses:	22.12.2005

Contents

Chapter 1

Introduction

Over the last 100 years scattering experiments have been a valuable tool for the exploration of the structure of matter. In 1911 the famous Rutherford experiment, scattering α-particles off a gold foil, led to the hypothesis of the nuclear atom, a nucleus surrounded by an electron cloud. Half a century later, it became possible to investigate the structure of the nucleus with electron scattering experiments. In the 1950s Hofstadter et al. performed elastic electron scattering off hydrogen at Stanford. From these experiments an estimate of the size of the proton was given. The naturally following question about the substructure of the proton was first answered in deep inelastic scattering experiments carried out at SLAC[1] in the 1960s. The first look inside the proton revealed that it is made of pointlike constituents. These constituents are now known as quarks, spin-1/2 particles carrying fractions of the elementary electric charge e, and gluons, neutral spin-1 particles. The investigations of the substructure of the proton led to theoretical advances that allow us today to describe interactions of leptons and quarks by the electroweak theory and Quantum-Chromo Dynamics (QCD) in the Standard Model of particle physics.

Unpolarised lepton-nucleon scattering experiments carried out at many particle physics laboratories in the world like CERN[2], DESY[3], FNAL[4] and SLAC have established our understanding of the nucleon structure. It is well known today that the combination of three valence quarks leads to integer charges for the proton and the neutron and that only about half of the nucleon's momentum is carried by the quarks. As a logical consequence the next question was about the nucleon's spin and how much of it is carried by the quarks. The Ellis-Jaffe sum rule predicts about 60% of the nucleon spin to be carried by the quarks. The investigation of

[1] Stanford Linear Accelerator Center
[2] Conseil Europeen pour la Recherche Nucleaire
[3] Deutsches Elektronen-SYnchrotron
[4] Fermi National Accelerator Laboratory

the nucleon spin structure with polarised beams and polarised targets which became available in the 1970s were expected to result just in a confirmation of these theoretical predictions. But a first precise measurement by the European Muon Collaboration (EMC) at CERN in 1983 resulted in a contribution of the quarks to the nucleon spin that was compatible with zero. This led to the so-called spin crisis. In the meantime this is not a crisis anymore but still a puzzle.

It is known that the nucleon spin, $s_N = 1/2$ (using $\hbar = c = 1$), is composed of helicity contributions from quarks, $\Delta\Sigma = \sum(\Delta q + \Delta\bar{q})$, and gluons, ΔG, as well as orbital angular momentum contributions of quarks and gluons, L_q and L_G, respectively, and can be written as

$$s_N = \frac{1}{2} = \frac{1}{2}\Delta\Sigma + \Delta G + L_q + L_G. \tag{1.1}$$

The contribution from the quarks, $\Delta\Sigma$, has meanwhile been established to be $\sim 25\%$. However, the contributions from the gluons and the orbital angular momentum of quarks and gluons have not been disentangled yet. One of the experiments that will contribute to the solution of the spin puzzle is the COMPASS[5] experiment at CERN. Using deep inelastic muon-nucleon scattering the gluon polarisation $\Delta G/G$ will be determined and, with the knowledge of the unpolarised gluon distribution G, the extraction of the helicity contribution of the gluons ΔG to the nucleon spin becomes possible. COMPASS makes use of the photon-gluon fusion process, which directly probes the gluons inside the nucleon. This process has to be discriminated from the deep inelastic scattering off the quarks inside the nucleon. The requirement of hadron pairs with high transverse momenta enriches the photon-gluon fusion process in an event sample and allows the extraction of the gluon polarisation from these data.

This thesis is dedicated to the determination of the gluon polarisation $\Delta G/G$ using high-p_t hadron pairs. The structure of the thesis is as follows: In Chapter 2 an overview of the basic theoretical concepts for the investigation of the nucleon structure via deep inelastic scattering experiments is given. The experimental setup, the COMPASS spectrometer, used to carry out the measurements is presented in Chapter 3. In Chapter 4 a short introduction to the Monte Carlo simulation, that is part of the analysis will be given. In Chapter 5 the experimental results will be presented and, combined with the results from the Monte Carlo simulation, the gluon polarisation will be extracted in Chapter 6. The result on $\Delta G/G$ obtained in this thesis will be compared to the data already available as well as theoretical models in Chapter 7.

[5]COmmon Muon and Proton Apparatus for Structure and Spectroscopy

Chapter 2

Theoretical Motivation

2.1 The Gluon in the Nucleon and the Gluon Polarisation

The gluon contribution to the spin of the nucleon is still not fully explained. To understand the role of the gluon within the nucleon and related unsolved problems, the relevant theoretical background about the nucleon structure is briefly reviewed. Starting with the basic kinematic processes (Section 2.2), unpolarised and polarised lepton-nucleon cross sections (Section 2.3) and structure functions are introduced. Then the interpretation of the nucleon in the Quark Parton Model (QPM) (Section 2.4) is discussed. The QCD improved parton model as well as its implications together with some relevant measurements that support the theoretical models are explained in Section 2.5.

The QCD improved parton model connects the gluons as gauge bosons of the strong interaction with the quarks that make up the nucleon in the naive QPM. The gluons do not couple to the photon and thus cannot be accessed directly in the leading order deep inelastic scattering (DIS) process. But they contribute to the cross section in higher order QCD processes. The gluon distribution can then be obtained indirectly from the scaling violations of the quark distributions with evolution equations. Alternatively the higher order processes can be separated experimentally and the unpolarised gluon density can be determined directly. Compared to the unpolarised case, the data on polarised experiments cover a relatively small kinematic range. Therefore it is extremely difficult to obtain an accurate gluon helicity contribution via QCD evolution and a direct measurement of the gluon polarisation $\Delta G/G$ is needed. The direct measurement can either be done in deep inelastic scattering as performed by COMPASS and will be the topic of this thesis, or in polarised $p-p$ collisions, a method followed at the Relativistic Heavy Ion

Collider (RHIC) (Section 2.7). This chapter will give some basic information on the topics mentioned here. A more detailed treatment of the underlying polarised and unpolarised physics and experimental results can for example be found in the review articles [1]-[4].

2.2 Kinematic Variables in Deep Inelastic Scattering

The scattering of pointlike leptons l, i.e. particles without inner structure, off a nucleon N offers a clean probe to investigate the structure of protons and neutrons. In the process

$$l + N \rightarrow l + X$$

X either denotes the nucleon itself if the process is elastic or the final hadronic state in case the proton breaks up. The lepton with 4-momentum $k = (E, \vec{k})$ is scattered at an angle θ, that in case of elastic scattering is directly connected to the energy of the scattered lepton with 4-momentum $k' = (E', \vec{k'})$. Thus one variable is sufficient to describe the process. To describe inelastic scattering, when the lepton has enough energy to break up the proton, two independent variables are needed, e.g. θ and E'. In deep inelastic scattering the invariant mass W of the hadronic final state X is well above the resonance region and the 4-momentum transfer $q = k - k'$ of the exchanged boson is large enough to resolve the nucleon's constituents and to investigate their properties. For COMPASS kinematics the exchanged boson is usually a virtual photon. Z-exchange does not play a significant role. Fig. 2.1 shows the basic diagram for deep inelastic lepton-nucleon scattering. In inclusive DIS the final hadronic state is not measured and is denoted by X. In semi-inclusive DIS one or more hadrons are detected in the final state.

The relevant kinematic variables for the description of the DIS process are summarised in Table 2.1. Instead of using E' and the lepton scattering angle θ to characterise the process two dimensionless scaling variables can be used

$$y = \frac{P \cdot q}{P \cdot k} \overset{lab.}{=} \frac{\nu}{E} \tag{2.1}$$

and

$$x = \frac{Q^2}{2P \cdot q} \overset{lab.}{=} \frac{Q^2}{2M\nu}, \tag{2.2}$$

where P is the 4-momentum of the target proton, $\nu = E - E'$ the virtual photon energy, y the fractional energy, x the Bjorken scaling variable and $Q^2 = -q^2$. The

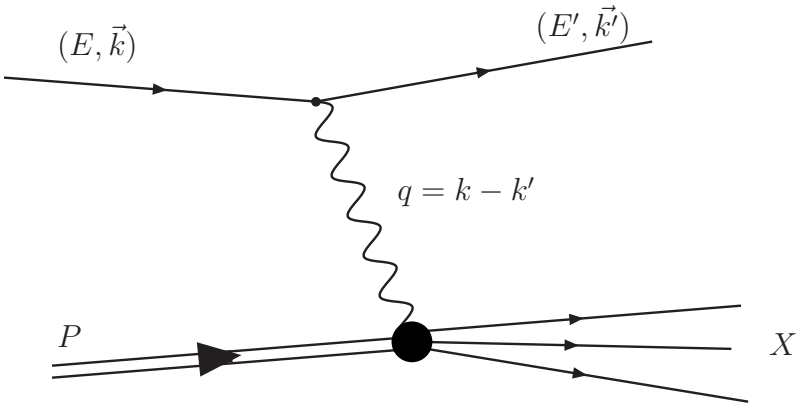

Figure 2.1: Schematic representation of the DIS process.

invariant mass of the photon nucleon system is

$$W^2 = (P + q)^2 = M^2 + 2P \cdot q + q^2. \tag{2.3}$$

Since W must be at least the mass of the target nucleon it follows that

$$W^2 \geq M^2 \Rightarrow M^2 + 2P \cdot q - Q^2 \geq M^2 \Rightarrow 2M\nu - Q^2 \geq 0 \tag{2.4}$$

and thus with a positive energy ν follows

$$0 \leq x \leq 1. \tag{2.5}$$

Table 2.1: Relevant variables in deep inelastic lepton-nucleon scattering. The laboratory frame is defined by the target proton at rest.

incoming lepton 4-momentum k	$(E, \vec{k}) \stackrel{lab}{=} (E, 0, 0, \lvert\vec{k}\rvert)$
outgoing lepton 4-momentum k'	$(E', \vec{k'})$
target proton 4-momentum P	$(M, \vec{P}) \stackrel{lab}{=} (M, 0, 0, 0)$
virtual photon 4-momentum q	$q = k - k'$
virtual photon energy ν	$\nu \stackrel{lab}{=} E - E'$
fractional energy loss of the lepton y	$y = \frac{P \cdot q}{P \cdot k} \stackrel{lab}{=} \frac{\nu}{E}$
scattering angle (lab) θ	θ
neg. virtual photon 4-mom. squared Q^2	$Q^2 = -q^2 \stackrel{lab}{\approx} 4EE' sin^2\theta/2$
Bjorken variable x	$x = \frac{Q^2}{2P \cdot q} \stackrel{lab}{=} \frac{Q^2}{2M\nu}$

The Bjorken variable x can be seen as a measure for the inelasticity of the process, $x = 1$ corresponds to elastic scattering where $W^2 = M^2$. Another interpretation of x in the quark-parton model (QPM) is the momentum fraction of the struck parton in the infinite momentum frame.

2.3 Lepton-Nucleon Scattering Cross Section

The differential cross section for lepton-nucleon scattering, where the scattered lepton has an energy between E' and $E' + dE'$ and is found in the solid angle $d\Omega$ can be written in a general form as [5, 6]

$$\frac{d^2\sigma}{d\Omega dE'} = \frac{\alpha^2}{2Mq^4}\frac{E'}{E}L_{\mu\nu}W^{\mu\nu}. \tag{2.6}$$

$L_{\mu\nu}$ is the lepton tensor, $W^{\mu\nu}$ the hadron tensor and α the strong coupling constant (for a detailed derivation of Eq. (2.6) see also e.g. [7, 8]). The lepton tensor $L_{\mu\nu}$ describes the emission of a virtual photon by a lepton of mass m with spin vector s and can be calculated in QED[1]. It is given by

$$L_{\mu\nu}(k, s; k') = 2\left[L^{(s)}_{\mu\nu}(k; k') + iL^{(a)}_{\mu\nu}(k, s; k')\right], \tag{2.7}$$

where

$$\begin{aligned} L^{(s)}_{\mu\nu}(k; k') &= k_\mu k'_\nu + k'_\mu k_\nu - g_{\mu\nu}(k \cdot k' - m^2) \\ L^{(a)}_{\mu\nu}(k, s; k') &= \epsilon_{\mu\nu\alpha\beta}s^\alpha(k - k')^\beta. \end{aligned}$$

$W^{\mu\nu}$ parametrises our lack of knowledge of the nucleon structure and is defined by

$$W^{\mu\nu}(q; P, S) = \frac{1}{2\pi}\int d^4x e^{iq\cdot x}\langle P, S|[J^\mu(x), J^\nu(0)]|P, S\rangle. \tag{2.8}$$

S is the spin vector of the nucleon with momentum P and $\langle P, S|[J^\mu(x), J^\nu(0)]|P, S\rangle$ the nucleon matrix elements of the commutator of electromagnetic currents $J^\mu(x)$ and $J^\nu(0)$. Using translation, parity and time reversal invariance, completion of states and current conservation, the most general form of the hadronic tensor for DIS reads

$$W_{\mu\nu}(q; P, S) = W^{(s)}_{\mu\nu}(q; P) + iW^{(a)}_{\mu\nu}(q; P, S) \tag{2.9}$$

with

$$\begin{aligned} W^{(s)}_{\mu\nu}(q; P) &= 2F_1\left(-g_{\mu\nu} + \frac{q_\mu q_\nu}{q^2}\right) + \frac{2F_2}{P\cdot q}\left(P_\mu - \frac{P\cdot q}{q^2}q_\mu\right)\left(P_\nu - \frac{P\cdot q}{q^2}q_\nu\right) \\ W^{(a)}_{\mu\nu}(q; P, S) &= \frac{2Mg_1}{P\cdot q}\epsilon_{\mu\nu\lambda\sigma}q^\lambda S^\sigma + \frac{2Mg_2}{(P\cdot q)^2}\epsilon_{\mu\nu\lambda\sigma}q^\lambda\left((P\cdot q)S^\sigma - (S\cdot q)P^\sigma\right). \end{aligned}$$

[1] Quantum Electrodynamics

The coefficients F_1,F_2, g_1 and g_2 are called structure functions, they depend on x and Q^2. Eq. (2.6) can be split in two parts

$$\frac{d\sigma}{d\Omega dE'} = \frac{\alpha^2}{Mq^4}\frac{E'}{E}\left[L^{(s)}_{\mu\nu}W^{\mu\nu(s)} - L^{(a)}_{\mu\nu}W^{\mu\nu(a)}\right], \tag{2.10}$$

where $L^{(s)}_{\mu\nu}W^{\mu\nu(s)}$ arises from the symmetric part, which does not depend on the spin of the particles and describes the unpolarised cross section, and $L^{(a)}_{\mu\nu}W^{\mu\nu(a)}$ arises from the antisymmetric part depending on the spin of lepton and nucleon and is needed to describe polarised lepton-nucleon scattering.

2.3.1 The Unpolarised Cross Section

The unpolarised cross section for lepton-nucleon scattering is

$$\frac{d\sigma^{unpol}}{d\Omega dE'} = \frac{\alpha^2}{Mq^4}\frac{E'}{E}L^{(s)}_{\mu\nu}W^{\mu\nu(s)} \tag{2.11}$$

$$= \frac{4\alpha^2 E'^2}{q^4}\left[\frac{2F_1(x,Q^2)}{M}\sin^2\frac{\theta}{2} + \frac{F_2(x,Q^2)}{\nu}\cos^2\frac{\theta}{2}\right], \tag{2.12}$$

where the structure functions F_1 and F_2 contain the information about the inner structure of the nucleon.

The first DIS experiments have been performed at the end of the 1960s at SLAC [9]-[13]. Electrons were scattered off a hydrogen target. It turned out that above the resonance region there was only a weak Q^2-dependence of the structure function F_2 (in the covered kinematic range). This is a consequence of the fact, that one scatters off a pointlike particle, i.e. that the nucleon has a substructure made out of pointlike constituents. The measured F_2 is the incoherent sum of the scattering off these pointlike constituents. The phenomenon, that the structure functions are approximately independent of the momentum transfer from the probe to the nucleon, is known as Bjorken scaling [14].

In the Bjorken limit ($Q^2, \nu \to \infty$, x fixed) the structure functions obey the Callan-Gross relation [15]:

$$\lim_{Q^2,\nu\to\infty} F_2(x) = 2xF_1(x). \tag{2.13}$$

This relation has been verified experimentally from early SLAC data [16, 17] and is an evidence that the nucleon's constituents are spin-$\frac{1}{2}$ particles.

2.3.2 Polarised Lepton-Nucleon Scattering

To gain information about the part of the cross section which contains the anti-symmetric parts of lepton- and hadron tensor (Eq. (2.10)), and thus about the structure functions g_1 and g_2, experiments with polarised beam and polarised target are required. To separate the polarised structure functions from the unpolarised F_1 and F_2, one measures differences of cross sections with different beam and target polarisations, as F_1 and F_2 cancel out in such differences.

We consider the case of longitudinally polarised leptons, i.e. the initial leptons with helicity along or opposite their direction of motion, and the nucleon at rest, polarised along an arbitrary direction $\mathbf{S}$ (Fig. 2.2). If α is the polar angle of the nucleon spin direction and ϑ the angle between the outgoing lepton direction and $\mathbf{S}$, then we obtain [1]

$$\frac{d^2\sigma(\alpha)}{d\Omega dE'} - \frac{d^2\sigma(\alpha+\pi)}{d\Omega dE'} = -\frac{4\alpha^2}{Q^2\nu M}\frac{E'}{E}\left\{[E\cos\alpha + E'\cos\vartheta]g_1 + \frac{2EE'}{\nu}[\cos\vartheta - \cos\alpha]g_2\right\}, \quad (2.14)$$

where $\cos\vartheta = \sin\theta\sin\alpha\cos\phi + \cos\theta\cos\alpha$. In case of a longitudinally polarised beam and target ($\alpha = 0, 180^\circ$ and $\theta = \vartheta$) Eq. (2.14) simplifies to

$$\frac{d^2\sigma^{\rightrightarrows}}{d\Omega dE'} - \frac{d^2\sigma^{\rightleftarrows}}{d\Omega dE'} = -\frac{4\alpha^2}{Q^2\nu M}\frac{E'}{E}\left[(E + E'\cos\theta)g_1 - 2xMg_2\right] \quad (2.15)$$

and for a transversely polarised target ($\alpha = 90^\circ, 270^\circ$) one obtains

$$\frac{d^2\sigma^{\rightarrow\Uparrow}}{d\Omega dE'} - \frac{d^2\sigma^{\rightarrow\Downarrow}}{d\Omega dE'} = -\frac{8\alpha^2(E')^2}{Q^2M\nu^2}\left(\frac{\nu}{2E}g_1 + g_2\right)\sin\vartheta\cos\phi. \quad (2.16)$$

From experimental side, it is more convenient to measure asymmetries than differences of cross sections (the notation until the end of this section follows [2], with fixed negative beam polarisation and variable target polarisation as in the COMPASS experiment):

$$A(\alpha) = \frac{\sigma(\alpha) - \sigma(\alpha+\pi)}{\sigma(\alpha) + \sigma(\alpha+\pi)}. \quad (2.17)$$

The longitudinal asymmetry with beam and target spin (anti)parallel ($\alpha = 0^\circ, 180^\circ$) is

$$A_{\mathrm{L}} = \frac{\sigma^{\rightrightarrows} - \sigma^{\rightleftarrows}}{\sigma^{\rightrightarrows} + \sigma^{\rightleftarrows}}, \quad (2.18)$$

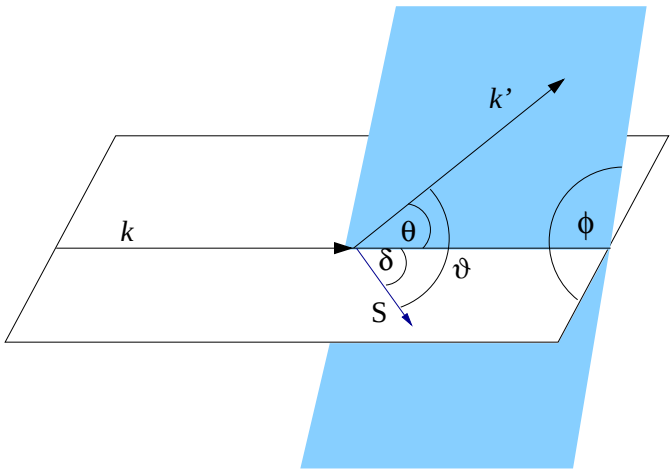

Figure 2.2: Polarised DIS: Definition of the angles: α, ϑ, θ, ϕ.

and the transverse asymmetry ($\alpha = 90°, 270°$) is

$$A_{\mathrm{T}} = \frac{\sigma^{\leftarrow\Downarrow} - \sigma^{\leftarrow\Uparrow}}{\sigma^{\leftarrow\Downarrow} + \sigma^{\leftarrow\Uparrow}}. \tag{2.19}$$

Data on A_{L} and A_{T} can be obtained by reversing the polarisation direction of a longitudinally or transversely polarised target. The interesting physics quantities are the virtual photon cross section asymmetries

$$A_1 = \frac{\sigma_{1/2} - \sigma_{3/2}}{\sigma_{1/2} + \sigma_{3/2}}, \tag{2.20}$$

$$A_2 = \frac{2\sigma_{\mathrm{T}L}}{\sigma_{1/2} + \sigma_{3/2}}, \tag{2.21}$$

where $\sigma_{1/2}$ and $\sigma_{3/2}$ are the virtual photon photo-absorption cross sections when the projection of the total angular momentum of the photon-nucleon system along the incident lepton direction is 1/2 and 3/2. $\sigma_{\mathrm{T}L}$ is an interference term between transverse and longitudinal amplitudes. The measured lepton asymmetries are related to the longitudinal and transverse asymmetries A_1 and A_2 by

$$A_{\mathrm{L}} = D(A_1 + \eta A_2), \tag{2.22}$$

$$A_{\mathrm{T}} = d(A_2 - \xi A_1). \tag{2.23}$$

Measurements of A_1 and A_2 allow a determination of the structure functions g_1 and g_2 using the relations

$$A_1 = (g_1 - \gamma^2 g_2)/F_1 \tag{2.24}$$

$$A_2 = \gamma(g_1 + g_2)/F_1 \tag{2.25}$$

with the kinematic factors

$$D = \frac{y(2-y)}{y^2+2(1-y)(1+R)} \tag{2.26}$$

$$\eta = 2\gamma(1-y)/(2-y) \tag{2.27}$$

$$d = D\sqrt{\frac{2\varepsilon}{1+\varepsilon}} \tag{2.28}$$

$$\xi = \eta(1+\varepsilon)/2\varepsilon \tag{2.29}$$

with $\gamma^2 = \frac{Q^2}{\nu^2} = \frac{4M^2x^2}{Q^2}$ and ε expressing the magnitude of the virtual photon transverse polarisation

$$\varepsilon \approx \frac{(1-y)}{(1-y+y^2/2)}. \tag{2.30}$$

The factors D and d can be regarded as depolarisation factors of the virtual photon, i.e. D is the fraction of the longitudinal lepton beam polarisation transfered to the virtual photon. The quantity $R = \sigma_L/\sigma_T$ is the ratio of the longitudinal to transverse virtual photon absorption cross section, which is related to the unpolarised structure functions F_1 and F_2 by

$$R = \frac{F_2}{2xF_1}\left(1+\gamma^2\right) - 1. \tag{2.31}$$

Since g_2 is suppressed by the kinematic factor γ in Eq. (2.24) one can derive g_1 from a measurement of the longitudinal lepton asymmetry A_{L} by

$$g_1(x) \approx \frac{F_1(x)}{1+\gamma^2}\frac{A_{\mathrm{L}}(x)}{D(y)}. \tag{2.32}$$

Fig. 2.3 shows results from different experiments on the structure function g_1 for proton, deuteron and neutron targets. The accuracy of $g_1^d(x)$ is clearly improved by a new measurement of the COMPASS collaboration [18], which in Fig. 2.4 is compared to the data of the Spin Muon Collaboration (SMC) that were up to now the only data points available in the kinematic region of low x.

2.4 Interpretation in the Frame of the Quark Parton Model

In the 1960s Gell-Mann [20] and Zweig [21] had arranged the hadrons known up to this time assuming they were made up of elementary constituents, the quarks.

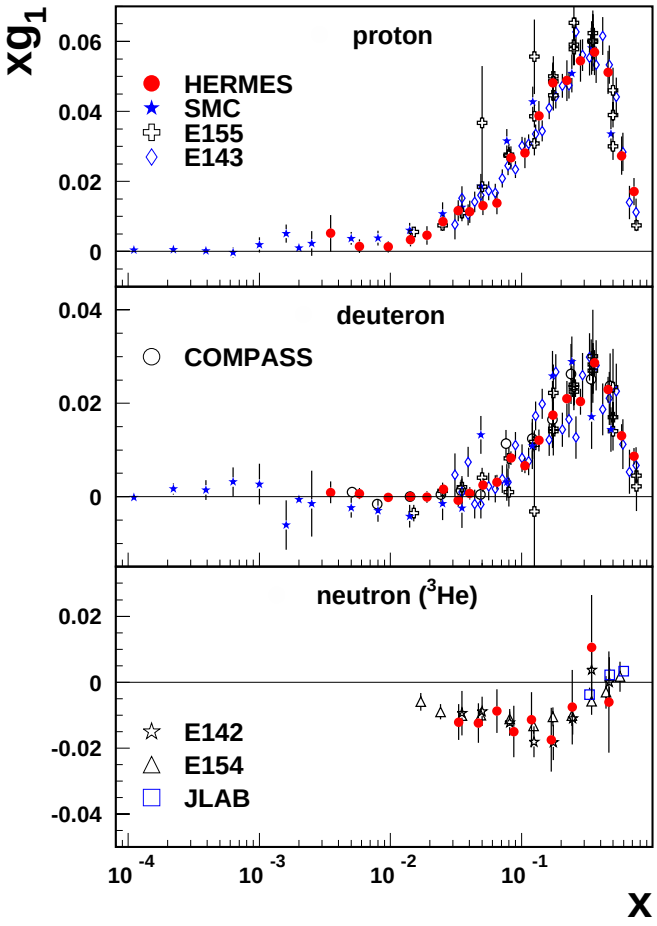

Figure 2.3: The spin dependent structure function $xg_1(x)$ of the proton, deuteron and neutron measured in deep inelastic scattering of electrons/positrons (E142, E143, E154, E155, HERMES, JLAB) and muons (SMC, COMPASS). Figure taken from [19].

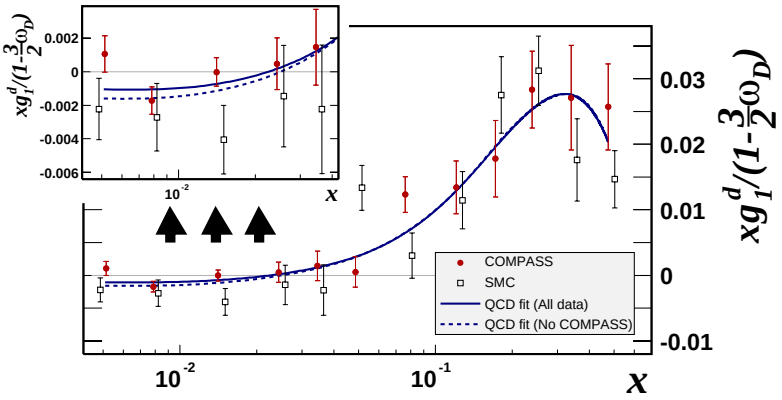

Figure 2.4: Values of $x\,g_1^d(x)$ measured by COMPASS (full circles) and SMC (open squares) for $Q^2 > 1\,(\mathrm{GeV/c})^2$. The curves represent the results of the fits at the Q^2 of the COMPASS points (solid line for all data, dashed line with COMPASS excluded). The data points are corrected for the deuterium D-wave state probability $\omega_D = 0.05$ (i.e. they correspond to the published values of g_1^d divided by 0.925).

With this knowledge Feynman developed the Quark Parton Model (QPM) to provide a simple physical picture of the observed scaling behaviour [22, 23]. In this model the nucleon is made up of pointlike constituents, known as partons, which are the scattering centres one observes in deep inelastic scattering. The charged partons carrying fractions of the elementary charge e and spin-$\frac{1}{2}$ were later identified as quarks and the electrically neutral spin-1 partons, which do not interact with the virtual photon, as gluons. The QPM is formulated in the infinite momentum frame where the target nucleon moves with $p_z \to \infty$, the rest masses and the transverse momenta of the partons can be neglected and Q^2 is large. During the time, in which the virtual photon interacts with the quark, it is essentially a free particle, not interacting with the other partons in the nucleon. In a good approximation the structure of the nucleon can then be described by the longitudinal momenta of its components. In the infinite momentum frame the interpretation of the Bjorken scaling variable x as momentum fraction of the nucleon carried by the struck parton becomes exact.

2.4.1 Parton Distributions

Having structureless constituents, the scattering process off a nucleon can be described as an incoherent sum of the interaction of the virtual photon with the partons. Here the single interaction can be seen as elastic scattering. The cross section of a lepton scattering off a pointlike quark of flavour f, that carries a momentum fraction x_f of the nucleon, can be calculated in QED. By comparing the cross section for inelastic scattering with the one for elastic scattering, the structure functions for a single pointlike parton become [24]

$$2F_1^{point}(\nu, Q^2) = e_f^2 \frac{Q^2}{2m}\, \delta\left(\nu_p - \frac{Q^2}{2m}\right) = e_f^2\, \delta\left(x_f - \frac{Q^2}{2M\nu}\right) \tag{2.33}$$

$$F_2^{point}(\nu, Q^2) = e_f^2 \nu\, \delta\left(\nu_p - \frac{Q^2}{2m}\right) = e_f^2 x_f\, \delta\left(x_f - \frac{Q^2}{2M\nu}\right). \tag{2.34}$$

Here m is the mass of the parton, e_f its charge, $\nu_p = (p_{parton} \cdot q)/m$ with $p_{parton} = x_f P$ being the parton momentum, which is the fraction x_f of the nucleon momentum P, and $\frac{Q^2}{2M\nu} = x$ is the Bjorken variable. Thus x has to be equal to x_f and the virtual photon can only be absorbed by the quark with the right momentum fraction. Summing over all quarks and antiquarks in the nucleon gives

$$F_2(x) = \sum_f \int dx_f\, e_f^2\, q_f(x_f)\, x_f\, \delta\left(x_f - x\right), \tag{2.35}$$

where the $q_f(x)$ are the parton distribution functions, i.e. $q_f(x)\, dx$ is the probability to find a quark of flavour f with a momentum fraction in the range $[x, x + dx]$,

and the weighted integral with the parton distributions has been performed. This leads to the following form of the structure functions:

$$F_2(x) = x \sum_f e_f^2 \left(q_f(x) + \bar{q}_f(x)\right) \tag{2.36}$$

and with Eq. (2.13)

$$F_1(x) = \frac{1}{2} \sum_f e_f^2 \left(q_f(x) + \bar{q}_f(x)\right). \tag{2.37}$$

The sum runs over all quarks inside the nucleon, i.e. the valence quarks carrying the quantum numbers of the nucleon and the sea quarks, virtual quark-antiquark pairs, that are produced by the gluons.

From the parton distributions one can obtain the number densities of the quarks inside the nucleon. For a proton e.g.

$$\int_0^1 [u(x) - \bar{u}(x)]dx = \int_0^1 u_v(x)dx = 2 \tag{2.38}$$

$$\int_0^1 [d(x) - \bar{d}(x)]dx = \int_0^1 d_v(x)dx = 1 \tag{2.39}$$

$$\int_0^1 [s(x) - \bar{s}(x)]dx = 0 \tag{2.40}$$

with $u_v(x)$ and $d_v(x)$ being the valence quark distributions and their integral corresponds to the number of quarks in the static picture of the nucleon, where the proton is composed of two up- and one down-quark. The distributions for the neutron can be obtained using isospin symmetry by exchanging u- and d-quarks:

$$u^p(x) \equiv d^n(x), \quad d^p(x) \equiv u^n(x), \quad s^p(x) \equiv s^n(x). \tag{2.41}$$

The integral $x\,q(x)$ gives the fraction of the total momentum of the nucleon that is carried by all quarks,

$$\int_0^1 dx\, x[u(x) + \bar{u}(x) + d(x) + \bar{d}(x) + s(x) + \bar{s}(x)] = 1 - \varepsilon_g, \tag{2.42}$$

where $\varepsilon_g = \frac{p_{gluon}}{p_{proton}}$ is the momentum fraction carried by the gluons, which are not directly probed by the photon. It turns out that about half of the proton's momentum is carried by the charged partons, the remaining constituents interact neither electromagnetically nor weak (as known from neutrino scattering experiments) and are identified with the gluons.

The analysis of inclusive and semi-inclusive DIS experiments using hadron identification with electron, muon and neutrino beams on proton and deuteron targets allows to further disentangle the contributions from the various types of quarks. Fig. 2.5 shows the parametrisation of valence-, sea-quark and gluon distributions using these data. At HERA the gluon distribution has also been measured directly using methods analogue to the determination of the polarised gluon density that will be presented later in Section 2.7. Fig. 2.6 shows one of the measurements done by H1 using multi-jet events from boson-gluon fusion in deep inelastic scattering. The gluon density increases with decreasing fractional momenta of the gluons.

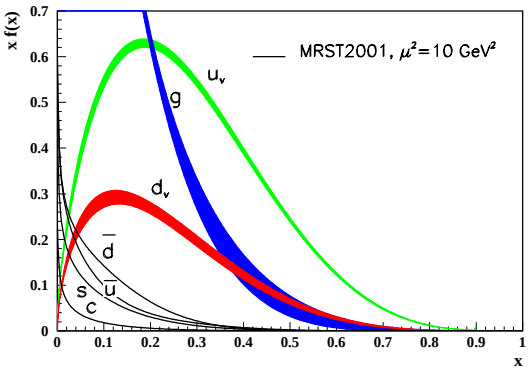

Figure 2.5: Distributions of x times the unpolarised parton distributions $f(x)$ (where $f = u_v, d_v, \bar{u}, \bar{d}, s, c, g$) using the MRST2001 parametrisation [25, 26] (with uncertainties for u_v, d_v and g) at a scale of $10\,\mathrm{GeV}^2$. Figure taken from [27].

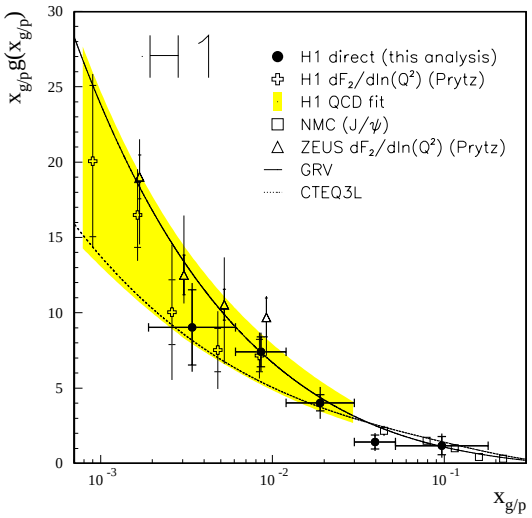

Figure 2.6: Direct determination of the gluon distribution at HERA. The measured gluon density at an average Q^2 of $30\,\mathrm{GeV}^2$ is compared with the indirect determinations by H1 [28] and ZEUS [29] at $Q^2 = 20\,\mathrm{GeV}^2$, and with a determination from J/Ψ production by NMC [30] evolved to $Q^2 = 30\,\mathrm{GeV}^2$. Figure taken from [31].

2.4.2 The First Moment of g_1 and the Spin of the Nucleon

In analogy to the unpolarised structure function F_1 (Eq. (2.37)), the polarised structure function g_1 can be written as

$$g_1(x) = \frac{1}{2}\sum_f e_f^2 \left(\Delta q_f(x) + \Delta\bar{q}_f(x)\right), \tag{2.43}$$

where

$$\Delta q_f(x) = q_f^+(x) - q_f^-(x) \tag{2.44}$$

and (q^-) q^+ are the number densities of quarks with momentum fraction x of the parent nucleon momentum P and spin (anti-)parallel to the parent nucleon spin. The unpolarised parton densities are then

$$q_f(x) = q_f^+(x) + q_f^-(x). \tag{2.45}$$

The structure function g_1 can be determined by a measurement of A_{L} via Eq. (2.32). A photon with a positive helicity can, due to angular momentum conservation, only be absorbed by a quark with negative helicity, since the final state, a quark, has spin $\frac{1}{2}$ and hence cannot have spin $\frac{3}{2}$ (Fig. 2.7). If the helicity of the parent nucleon is opposite to the photon helicity one probes the distribution $q^+(x)$, while the distribution $q^-(x)$ is probed when photon and nucleon have the same helicity. For g_2 there is no such simple interpretation in the quark parton model, but $g_2(x) \overset{QPM}{=} 0$.

Information about $g_1(x)$ for all x gives information about the quark helicity contribution to the nucleon spin. The first moment of g_1 is

$$\Gamma_1 = \int_0^1 g_1(x)dx = \frac{1}{2}\sum_f e_f^2 \int_0^1 [\Delta q_f(x) + \Delta\bar{q}_f(x)]dx \tag{2.46}$$

with $\Delta q_f = \int_0^1 [\Delta q_f(x) + \Delta\bar{q}_f(x)]dx$

$$\Gamma_1 = \frac{1}{2}\sum_f e_f^2 \Delta q_f. \tag{2.47}$$

For the proton (neglecting contributions from heavy quarks), this gives

$$\Gamma_1^p = \frac{1}{2}\left(\frac{4}{9}\Delta u + \frac{1}{9}\Delta d + \frac{1}{9}\Delta s\right) \tag{2.48}$$

$$= \frac{1}{12}\left(\Delta u - \Delta d\right) + \frac{1}{36}\left(\Delta u + \Delta d - 2\Delta s\right) + \frac{1}{9}\left(\Delta u + \Delta d + \Delta s\right) \tag{2.49}$$

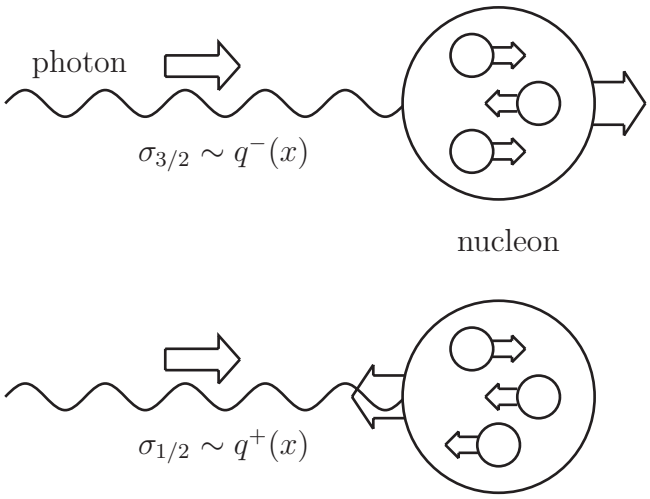

Figure 2.7: Simple explanation of the asymmetry in photon-nucleon scattering. The quark can only absorb a photon if its spin is antiparallel to the photon spin.

In the naive parton model the interpretation of

$$\Delta\Sigma = \Delta u + \Delta d + \Delta s \tag{2.50}$$

gives the helicity contribution of the quarks to the nucleon spin.

With the operator product expansion (OPE) there is an approach to connect the three terms in Eq. (2.49) to the expectation values a_i of the proton matrix elements of a SU(3) flavour octet of quark axial-vector currents [1]. The a_i can be calculated from

$$\langle P, S|J^j_{5\mu}|P, S\rangle = Ma_j S_\mu, \qquad j = 1 \ldots 8 \tag{2.51}$$

with

$$J^j_{5\mu} = \bar{\Psi}\gamma_\mu\gamma_5\frac{\lambda_j}{2}\Psi. \tag{2.52}$$

The λ_j are the Gell-Mann matrices and Ψ is a column vector in flavour space

$$\Psi = \begin{pmatrix} \Psi_u \\ \Psi_d \\ \Psi_s \end{pmatrix}, \tag{2.53}$$

a_0 is a measure for the flavour singlet operator

$$J^0_{5\mu} = \bar{\Psi}\gamma_\mu\gamma_5\Psi \tag{2.54}$$

and thus

$$\langle P,S|J^0_{5\mu}|P,S\rangle = Ma_0S_\mu. \tag{2.55}$$

The octet of currents are conserved, and therefore a_j, $j = 1\ldots8$ are independent of Q^2. The singlet current a_0 is not conserved, i.e. depends on Q^2. This is a consequence of the axial anomaly that is dealt with later in Section 2.5.3.

The two values a_3, a_8 are well known from the hyperon decays. This SU(3) octet of axial-vector currents controls the weak β-decay of the neutron and spin-$\frac{1}{2}$-hyperons (e.g. $\Lambda \to p$, $\Sigma \to n$, $\Xi \to \Lambda$). As a consequence, a_3 and a_8 can be expressed in terms of two parameters F and D which are measured in the hyperon β-decay [27, 3]:

$$a_3 = F + D \equiv \left|\frac{g_A}{g_V}\right| = 1.2695 \pm 0.0029 \tag{2.56}$$

$$a_8 = 3F - D = 0.579 \pm 0.025. \tag{2.57}$$

Eq. (2.49) can now be rewritten using

$$a_3 = \Delta u - \Delta d \tag{2.58}$$

$$a_8 = \Delta u + \Delta d - 2\Delta s \tag{2.59}$$

$$a_0 = \Delta u + \Delta d + \Delta s = \Delta\Sigma \tag{2.60}$$

and then reads

$$\Gamma_1^p = \frac{1}{12}a_3 + \frac{1}{36}a_8 + \frac{1}{9}a_0. \tag{2.61}$$

Thus a measurement of Γ_1 is, via Eq. (2.61) and the knowledge of a_3 and a_8, a measurement of a_0.

The QCD improved parton model, which will be explained in the next section, leads to corrections [32]-[34] modifying Eq. (2.61) to

$$\Gamma_1^p = \frac{1}{12}\left\{(a_3 + \frac{1}{3}a_8)E_{NS}(Q^2) + \frac{4}{3}a_0E_S(Q^2)\right\} \tag{2.62}$$

with

$$E_{NS}(Q^2) = 1 - \frac{\alpha_s}{\pi} - \binom{3.58}{3.25}\left(\frac{\alpha_s}{\pi}\right)^2 \ldots \tag{2.63}$$

$$E_S(Q^2) = 1 - \binom{0.333}{0.040}\frac{\alpha_s}{\pi} - \binom{1.10}{-0.07}\left(\frac{\alpha_s}{\pi}\right)^2 \ldots, \tag{2.64}$$

where the upper values correspond to the number of flavours $n_f = 3$ and the lower number to $n_f = 4$ (the result is renormalisation scheme dependent, the quoted numbers correspond to the $\overline{\text{MS}}$ scheme).

In a first measurement of Γ_1 and thus a_0 of EMC [35, 36] the value was compatible with zero ($\Delta\Sigma = 0.12 \pm 0.17$). This value was unexpectedly small. While in the naive QPM one would expect $\Delta\Sigma = 1$, applying the Ellis-Jaffe sum rule leads to $\Delta\Sigma = 0.579 \pm 0.026$ [37]. The EMC result led to the 'spin crisis in the parton model', which triggered a lot of theoretical and experimental effort (e.g. [38, 39, 40, 41] and references therein). Including the new COMPASS data shown in Fig. 2.4 together with various other experiments carried out during the last years in the determination of Γ_1 improves the accuracy for the result of $\Delta\Sigma$ to [42]

$$\Delta\Sigma(Q^2 = 4\ (\text{GeV/c})^2) = 0.237\ ^{+0.024}_{-0.029} \tag{2.65}$$

and establishes the small contribution of the quarks to the nucleon spin (result given in the $\overline{\text{MS}}$ scheme). Measurements done at SMC and recently at HERMES [40] go even further and allow to disentangle the contributions from the individual quark flavours to the nucleon spin. Fig. 2.8 shows data from HERMES on the polarised parton distribution functions $\Delta u(x)$, $\Delta d(x)$, $\Delta\bar{u}(x)$, $\Delta\bar{d}(x)$ and $\Delta s(x)$.

Bjorken Sum Rule

For the neutron the first moment of g_1 is

$$\Gamma_1^n = -\frac{1}{12}a_3 + \frac{1}{36}a_8 + \frac{1}{9}a_0. \tag{2.66}$$

In case of the QPM, where E_{NS} from Eq. (2.62) is unity, it follows with Eq. (2.61) that

$$\Gamma_1^{(p)} - \Gamma_1^{(n)} \equiv \frac{1}{6}a_3 = \frac{1}{6}\left|\frac{g_A}{g_V}\right|. \tag{2.67}$$

Eq. (2.67) is the Bjorken sum rule, which was first derived in this form by Bjorken [45, 46]. It describes a relationship between spin dependent DIS and the weak coupling constant defined in neutron β-decay. It is very fundamental because it only relies on the isospin invariance, i.e. on the $SU(2)$ symmetry between up- and down-quarks. With the corrections introduced in Eq. (2.62) follows

$$\Gamma_1^{(p)} - \Gamma_1^{(n)} = \frac{1}{6}\left|\frac{g_A}{g_V}\right| E_{NS}. \tag{2.68}$$

Beyond leading order E_{NS} depends on the number of flavours and the renormalisation scheme. Eq. (2.68) seems to be well satisfied by the data (e.g. Ref. [47]).

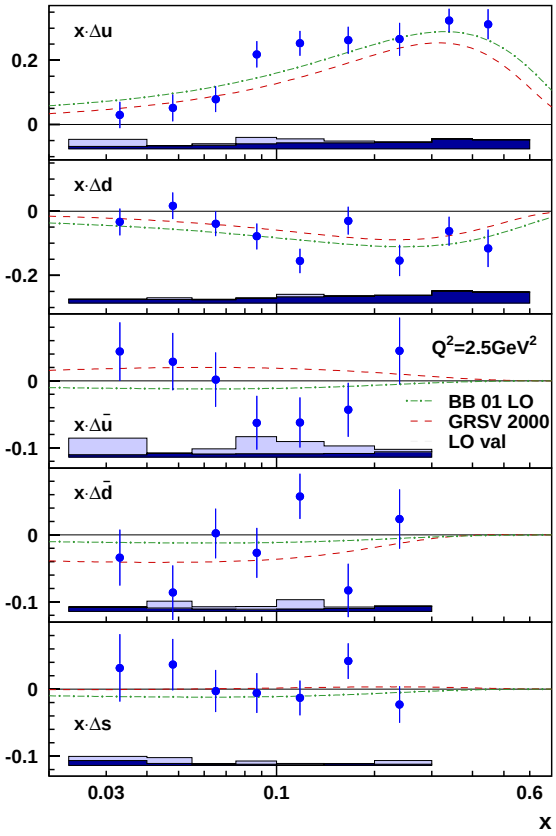

Figure 2.8: The quark helicity distributions $x\,\Delta q(x, Q^2)$ evaluated at a common value of $Q^2 = 2.5\,(\mathrm{GeV/c})^2$ as a function of x [40]. The dashed line is the GRSV2000 parametrisation (LO, valence scenario) [43] scaled with $1/(1+R)$ and the dashed–dotted line is the Blümlein–Böttcher (BB) parametrisation (LO, scenario 1) [44]. Figure taken from Ref. [40].

2.5 QCD Improved Parton Model

2.5.1 Scaling Violations

Further measurements in a wider range of Q^2 and more accurate data reveal a Q^2-dependence of F_2. Fig. 2.9 presents measurements of $F_2^{proton}(Q^2)$ for various values of x obtained by different experiments. This violation of Bjorken scaling is a signature of the gluon content inside the nucleon. Quarks can emit gluon bremsstrahlung and gluons can split in $q\bar{q}$ pairs and emit gluons themselves. If the quarks were not radiating gluons and the nucleon is probed at a certain Q^2, the pointlike partons could be seen and exact scaling should be observed. Probing an interacting quark at a higher value of Q^2, one can possibly resolve a gluon emission of this quark leading to a smaller observed momentum fraction x as illustrated in Fig. 2.10. The probability of finding a quark at lower x increases with higher Q^2

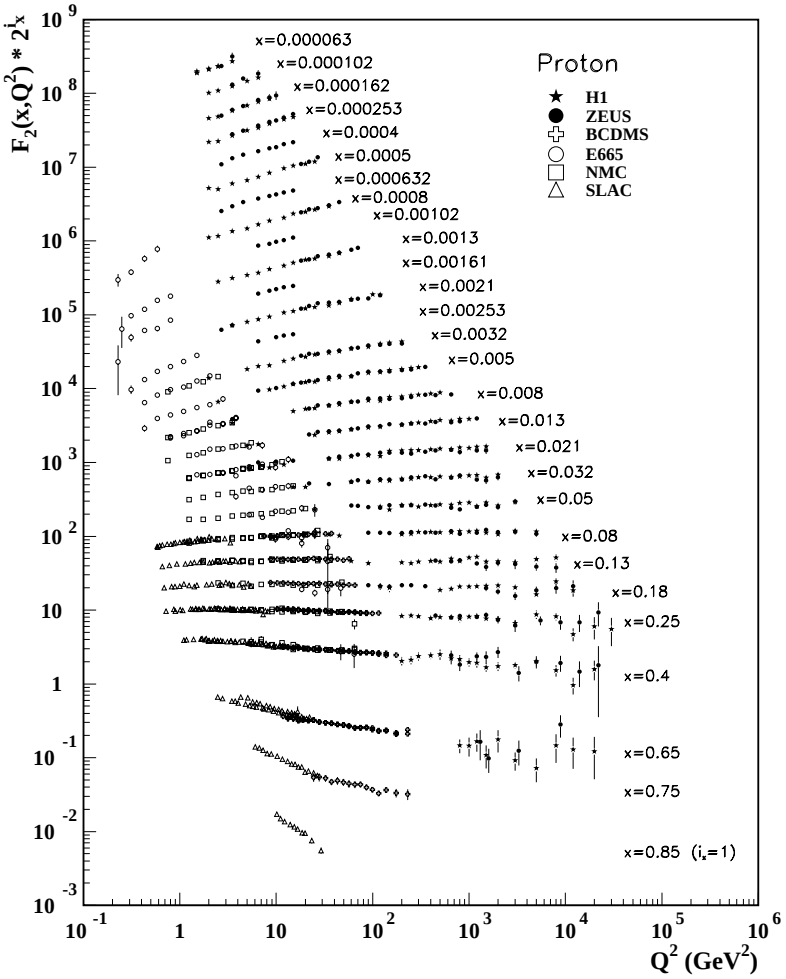

Figure 2.9: The proton structure function $F_2(x, Q^2)$ measured in electromagnetic scattering of positrons on protons at the e-p collider HERA (ZEUS and H1) and for electrons (SLAC) and muons (BCDMS, E665, NMC) on a fixed target [27].

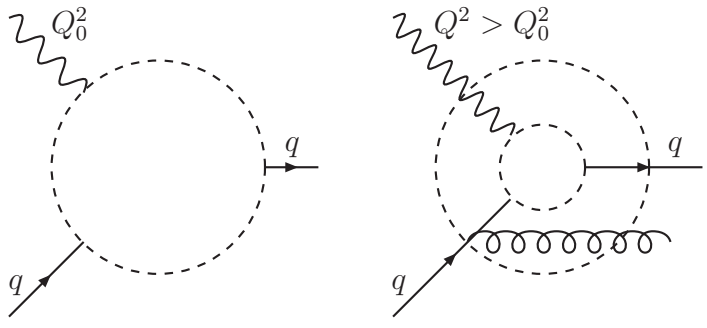

Figure 2.10: Illustration of scaling behaviour in lepton-nucleon scattering. With higher Q^2 the number of visible partons is increasing and the momentum fraction of a single parton decreases.

whereas finding one at high x decreases, because quarks carrying a high momentum fraction x loose momentum due to gluon radiation.

2.5.2 QCD Evolution Equations

A consequence of scaling violation is that the quark distribution functions are no longer functions $q(x)$ but $q(x, Q^2)$, similarly for the gluon distribution $G(x, Q^2)$. The Q^2 dependence of quark and gluon distributions at fixed x is described by a system of coupled integro-differential equations, the DGLAP equations [48, 49, 50], developed by Dokshitzer, Gribov, Lipatov, Altarelli and Parisi:

$$\begin{aligned}
\frac{dq_i(x,Q^2)}{d\ln Q^2} &= \frac{\alpha_s(Q^2)}{2\pi}\int_x^1 \frac{dy}{y}\left[q^i(y,Q^2)P_{qq}\left(\frac{x}{y}\right) + G(y,Q^2)P_{qG}\left(\frac{x}{y}\right)\right] \quad (2.69)\\
\frac{dG(x,Q^2)}{d\ln Q^2} &= \frac{\alpha_s(Q^2)}{2\pi}\int_x^1 \frac{dy}{y}\left[\sum_{i=1}^{2n_f} q^i(y,Q^2)P_{Gq}\left(\frac{x}{y}\right) + G(y,Q^2)P_{GG}\left(\frac{x}{y}\right)\right]
\end{aligned}$$

with the running QCD coupling constant

$$\alpha_s(Q^2) = \frac{4\pi}{\beta_0 \ln\frac{Q^2}{\Lambda^2}} \qquad \text{with} \qquad \beta_0 = 11 - \frac{2}{3}n_f,$$

where Λ is the QCD scale parameter and n_f the number of active flavours. The splitting functions P_{ij} are

$$\begin{aligned}
P_{qq}(z) &= \frac{4}{3}\left(\frac{1+z^2}{1-z}\right)\\
P_{qG}(z) &= \frac{1}{2}\left(z^2+(1-z)^2\right)\\
P_{Gq}(z) &= \frac{4}{3}\left(\frac{1+(1-z)^2}{z}\right)\\
P_{GG}(z) &= 6\left(\frac{1-z}{z} + \frac{z}{1-z} + z(1-z)\right), \quad (2.70)
\end{aligned}$$

the poles at $z = 1$ can be regularised by including virtual gluon diagrams, see Ref. [8]. P_{qq} represents the probability of a quark emitting a gluon and so becoming a quark with momentum fraction reduced by a fraction z (Fig. 2.11).

The DGLAP equations take into account, that a quark with momentum fraction x could have come from a parent quark with a larger momentum fraction y, which has radiated a gluon. The probability that this happens is proportional to $\alpha_s P_{qq}(x/y)$, when integrated over all possible momentum fractions y ($> x$) of the

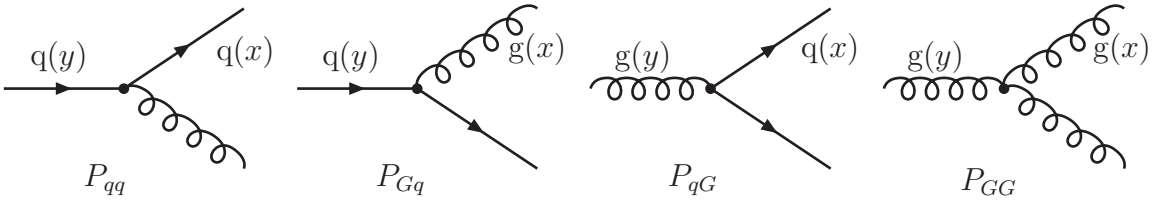

Figure 2.11: Feynman diagrams for the four splitting functions. The splitting function P_{ij} gives the probability that a parton i with momentum fraction x originates from parton j.

parent quark.

Thus QCD predicts the breakdown of scaling. The value of $q(x, Q_0^2)$ and $G(x, Q_0^2)$ for a given Q_0^2 allows for the prediction of $q(x, Q^2)$ and $G(x, Q^2)$ at any Q^2 in the frame of QCD. This so-called QCD evolution allows the determination of the gluon distribution from the measured quark distributions using the DGLAP equations. This method has been used to determine the gluon distribution presented in Fig. 2.5 in contrast to the direct measurement of $G(x)$ in Fig. 2.6. The quark distributions have to be known over a large kinematic range to achieve sufficient accuracy of the derived gluon distribution, which is the case for unpolarised data (cf. Fig. 2.9) and not for polarised.

QCD Evolution in the Polarised Case

The treatment of the evolution of the structure functions in the polarised case is completely analogue to the unpolarised case. It is convenient to split the polarised quark distributions in a flavour non-singlet (Δq^{NS}) and a flavour singlet ($\Delta\Sigma$) part [51]

$$\begin{aligned} \Delta q^{NS}(x, Q^2) &= \sum_f^{n_f} \left(\frac{e_f^2}{\langle e^2 \rangle} - 1 \right) (\Delta q_f(x, Q^2) + \Delta \bar{q}_f(x, Q^2)) \\ \Delta\Sigma(x, Q^2) &= \sum_f^{n_f} (\Delta q_f(x, Q^2) + \Delta \bar{q}_f(x, Q^2)) \end{aligned} \tag{2.71}$$

with $\langle e^2 \rangle = \frac{1}{n_f} \sum e_f^2$. The coupled DGLAP integro-differential equations for the polarised case read

$$\frac{d}{d \ln Q^2} \Delta q^{NS}(x, Q^2) = \frac{\alpha_s}{2\pi} \Delta P_{qq}^{NS} \otimes \Delta q^{NS}(x, Q^2) \tag{2.72}$$

$$\frac{d}{d \ln Q^2} \begin{pmatrix} \Delta\Sigma(x, Q^2) \\ \Delta G(x, Q^2) \end{pmatrix} = \frac{\alpha_s}{2\pi} \begin{pmatrix} \Delta P_{qq}^S & 2n_f \Delta P_{qg}^S \\ \Delta P_{gq}^S & \Delta P_{gg}^S \end{pmatrix} \otimes \begin{pmatrix} \Delta\Sigma(x, Q^2) \\ \Delta G(x, Q^2) \end{pmatrix} \tag{2.73}$$

with the convolution

$$(P \otimes q)(x, Q^2) = \int_x^1 \frac{dy}{y} P\left(\frac{x}{y}\right) q(x, Q^2).$$

One can see that gluons evolve like singlet combinations, i.e. sums of distribution functions. Valence quark distributions are non-singlet distributions and their evolution does not depend on the gluon distribution.

The structure function g_1 is then given by a convolution of the singlet and non-singlet coefficient functions, ΔC_S, ΔC_{NS}, ΔC_G with the polarised parton distribution functions

$$g_1(x, Q^2) = \frac{1}{2}\langle e^2 \rangle \{\Delta C_{NS} \otimes \Delta q^{NS}(x, Q^2) + \Delta C_S \otimes \Delta\Sigma(x, Q^2) + 2n_f \Delta C_G \otimes \Delta G(x, Q^2)\} \tag{2.74}$$

The splitting and coefficient functions depend on x and $\alpha_s(Q^2)$ and can be expanded in power series in α_s:

$$\Delta C(x, \alpha_s) = \Delta C^{(0)}(x) + \frac{\alpha_s}{2\pi} \Delta C^{(1)}(x) + O(\alpha_s^2), \tag{2.75}$$

$$\Delta P(x, \alpha_s) = \Delta P^{(0)}(x) + \frac{\alpha_s}{2\pi} \Delta P^{(1)}(x) + O(\alpha_s^2). \tag{2.76}$$

At leading order (LO),

$$\Delta C_S^{(0)}\left(\frac{x}{y}\right) = \Delta C_{NS}^{(0)}\left(\frac{x}{y}\right) = \delta\left(1 - \frac{x}{y}\right) \quad \text{and} \quad \Delta C_G^{(0)}\left(\frac{x}{y}\right) = 0,$$

g_1 decouples from δG and one obtains

$$g_1(x, Q^2) = \frac{1}{2} \sum_f e_f^2 \Delta q_f(x, Q^2), \tag{2.77}$$

where the x-dependent parton distribution functions from the quark parton model expression have been replaced by effective Q^2 dependent distributions $\Delta q(x, Q^2)$.

The splitting functions in LO, $\Delta P_{qq}^{(0)}(z) = P_{q+q+}^{(0)}(z) - P_{q-q+}^{(0)}(z)$, where $P_{q\pm q+}$ corresponds to a transition from a quark q_+ with positive helicity to a quark $q_\pm$ with positive/negative helicity, are given by

$$\Delta P_{qq}^{(0)}(z) = P_{qq}^{(0)}(z) = C_F \left(\frac{1 + z^2}{1 - z}\right), \qquad \text{with } C_F = \frac{4}{3}. \tag{2.78}$$

The polarised splitting functions are equal to the unpolarised, i.e. $P_{q-q+}^{(0)}(z) = 0$, as a consequence of helicity conservation. There is no transition between quarks

of opposite helicity allowed in massless perturbative QCD (in leading order). The spin averaged splitting functions are given by the sum

$$P_{AB}^{(0)}(z) = P_{A+B+}^{(0)}(z) + P_{A-B+}^{(0)}(z). \tag{2.79}$$

The coefficient functions C and the polarised splitting functions are known to LO [48] and next-to-leading order (NLO) [52]-[54].

In leading order, the gluons do not contribute to g_1 ($\Delta C_G^{(0)} = 0$), whereas they depend on the factorisation and renormalisation scheme in NLO. In the gauge invariant so-called Modified-Minimal-Subtraction ($\overline{\rm MS}$) scheme also the first moment of the second term in the expansion of ΔC_G (Eq. (2.75)) vanishes and so $\Delta G(x, Q^2)$ does not contribute directly to the first moment Γ_1 of g_1. In the Adler-Bardeen (AB) scheme – that conserves chirality in contrast to $\overline{\rm MS}$ – the first moment of $\Delta C_G^{(1)}$ is non-zero. Consequently Γ_1 depends on ΔG:

$$\Delta G(Q^2)_{\overline{\rm MS}} = \Delta G(Q^2)_{AB} \tag{2.80}$$

$$\Delta\Sigma(Q^2)_{\overline{\rm MS}} = a_0(Q^2) = \Delta\Sigma_{AB} - n_f \frac{\alpha_s(Q^2)}{2\pi} \Delta G(Q^2). \tag{2.81}$$

Thus the interpretation of the first moment of the structure function $g_1(x, Q^2)$ becomes scheme dependent. In the $\overline{\rm MS}$-scheme the quark distributions depend on Q^2, in the AB-scheme they do not, but the Q^2 dependence appears due to an anomalous gluon contribution explained in the next section.

An implication of this is that a small measured value of a_0 does not necessarily imply that $\Delta\Sigma$ is small, but can also be the result of the cancellation between the $\Delta\Sigma$ and the Q^2 dependent gluon helicity contribution in the AB-scheme. In the $\overline{\rm MS}$-scheme a large gluon polarisation would be absorbed in the sea quark polarisation and thus a large sea leads to a small measured a_0.

One way to determine ΔG is via the Q^2 evolution of the polarised DIS data. Several groups have performed NLO fits to polarised data. Fig. 2.12 shows the results obtained by the Asymmetry Analysis Collaboration [39] compared to results from different other groups [43]-[44], [55]-[58]. The helicity distributions for valence u and d quarks are well determined, being large and positive for u quarks and about half the size and negative for d quarks. This means that the spin carried by u-quarks is mostly parallel to the proton spin and anti-parallel for d-quarks. The sea quark helicity is small and negative with larger errors. The gluon distribution is even less well determined by the available data as it can be seen from the large errors indicated by the shaded area in Fig. 2.12.

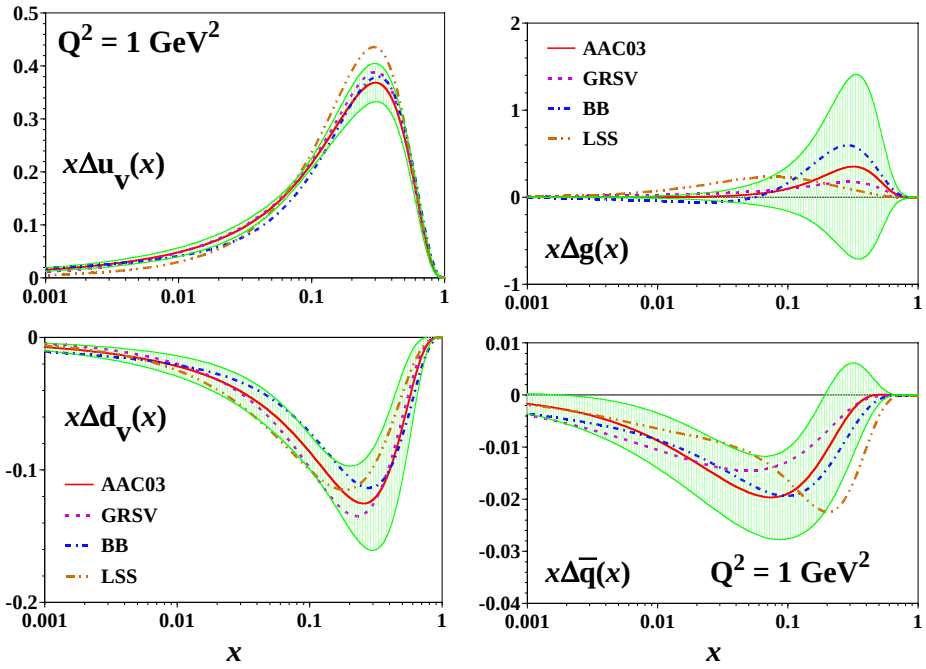

Figure 2.12: The AAC03 PDFs at $Q^2 = 1$ GeV^2 are compared with the ones for other parametrisations by GRSV2000 (standard scenario) [43, 55], BB (ISET=3) [44], and LSS ($\overline{\text{MS}}$ scheme) [56, 57, 58]. The shaded areas are the uncertainties of the AAC03 analysis. Figure taken from [39].

2.5.3 The Axial Anomaly

The result on ΔG from Section 2.5.2 can also be obtained using the operator product expansion and the already calculated proton matrix elements. Consider again the axial current (Eq. (2.54))

$$J^f_{5\mu} = \bar{\Psi}_f(x)\gamma_\mu\gamma_5\Psi_f(x)$$

made up of quark operators of definite flavour f. From the free Dirac equation of motion one finds that

$$\partial^\mu J^f_{5\mu} = 2im_f\bar{\Psi}_f(x)\gamma_5\Psi_f(x), \tag{2.82}$$

where m_f is the mass of the quark of flavour f. In the chiral limit, $m_f \to 0$, Eq. (2.82) seems to show that $J^f_{5\mu}$ is conserved, however this is not true. There is an anomalous contribution arising from the triangle diagram given in Fig. 2.13, which leads to a non vanishing derivative in Eq. (2.82). This phenomenon has first been observed in QED by Adler [59]. In the QCD case one has [60, 61]

$$\partial^\mu J^f_{5\mu} = \frac{\alpha_s}{4\pi}G^a_{\mu\nu}\tilde{G}^{\mu\nu}_a = \frac{\alpha_s}{2\pi}\mathrm{Tr}\left[G_{\mu\nu}\tilde{G}^{\mu\nu}\right] \tag{2.83}$$

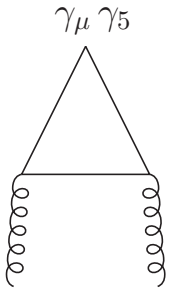

Figure 2.13: Triangle diagram giving rise to the axial anomaly. The gluons couple via the triangle to the axial current and thus contribute to the corresponding proton matrix element.

with the dual gluonic field tensor $\tilde{G}^a_{\mu\nu} = \frac{1}{2}\epsilon_{\mu\nu\rho\sigma}G_a^{\rho\sigma}$. Summing over all quark flavours (here $n_f = 3$) we obtain the gluonic contribution to a_0

$$a_0^{gluons}(Q^2) = -3\frac{\alpha_s}{2\pi}\Delta G(Q^2). \tag{2.84}$$

The anomaly introduces a pointlike interaction between the axial vector current and the gluons, because it does not depend on the momentum transfer $k_1 - k_2$ when $m_f = 0$, where k_1 and k_2 are the gluon momenta in Fig. 2.13. Therefore one gets a contribution to the matrix element of $J^0_{5\mu}$ in a hadron state from the gluonic component of the hadrons as well as from quarks [1]. Eq. (2.84) is believed to be an exact result and not to be affected by higher order corrections [62].

As a consequence of Eq. (2.84) a_0 has contributions from quarks and gluons and in the AB scheme we regain the result for a_0 given in Eq. (2.81):

$$a_0(Q^2) = \Delta\Sigma - 3\frac{\alpha_s}{2\pi}\Delta G(Q^2). \tag{2.85}$$

The gluonic term in Eq. (2.85) does not vanish at large Q^2, since the gluon spin behaves just as $[\alpha_s(Q^2)]^{-1}$ for $Q^2 \to 0$ [63, 60]. In the gauge invariant $\overline{\text{MS}}$ scheme, the term containing ΔG in Eq. (2.85) is cancelled by an additional term and there is no anomaly.

2.6 Fragmentation

Up to now, only inclusive DIS experiments, where the incoming and the scattered lepton are measured, were discussed quantitatively. However, detecting a hadron in coincidence with the scattered lepton is intimately related to the initial quarks and thus provides important information on the nucleon structure. Fig. 2.14 illustrates the process which is similar to the inclusive lepton-nucleon scattering plus one extra

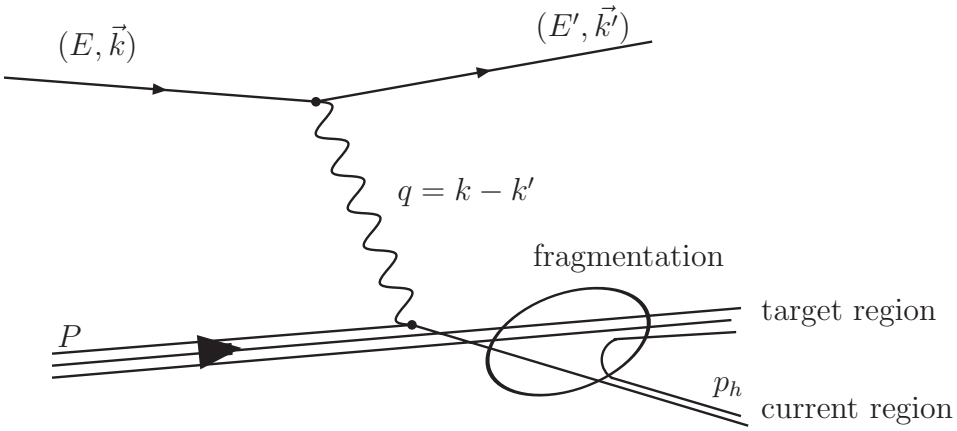

Figure 2.14: Schematic representation of hadron production in DIS.

degree of freedom associated with the momentum p_h of the additionally detected hadron. The additional variable used to describe this process is the energy fraction of the virtual photon energy carried by the hadron

$$z = \frac{E_h}{\nu}. \tag{2.86}$$

Alternatively, one can use x-Feynman

$$x_F = \frac{p_z^{c.m.}}{p_{z,max}^{c.m.}} \approx \frac{2p_z^{c.m.}}{W}, \tag{2.87}$$

the longitudinal momentum fraction p_z in the photon-nucleon c.m. system. The region of $x_F < 0$ selects preferably hadrons from the target fragmentation region, which originate from the target remnant. Hadrons which originate from the struck quark are produced in the current fragmentation region and mostly enhanced for $x_F > 0$.

The formation of hadrons out of quarks is due to confinement properties of QCD which demand that only neutral colour objects exist as free particles and thus the struck quark and the target remnant have to form colour neutral final state hadrons. This process of hadronisation cannot be described by perturbative QCD but is parametrised in the form of fragmentation functions. It is assumed, that the factorisation of the hard process and the fragmentation process holds. This means that the hard process can be calculated using perturbative QCD and the soft part, namely the fragmentation, is parametrised independently. This is in analogy to the treatment of the inclusive cross section. The hard process is

independent of the parton distributions, that are the non perturbative soft part, and the cross section is a product of both.

In the following, we concentrate on the current region, which allows to obtain information about the struck quark. The charge, the identity and the direction of the leading hadron is correlated to the flavour and the direction of the struck quark. The cross section for the production of a particular hadron h can be written, in leading order QCD, as

$$\sigma^h(x, Q^2, z) \propto \sum_f e_f^2 q_f(x, Q^2) D_f^h(z, Q^2), \tag{2.88}$$

where $D_f^h(z, Q^2)$ is the fragmentation function parametrising the fragmentation process. The fragmentation function gives the probability density that a struck quark of flavour f, probed at a scale Q^2, fragments into a hadron h of energy E_h being a fraction z of the virtual photon energy. The fragmentation functions are normalised to the particle multiplicities and conserve energy:

$$\sum_h \int_0^1 z D_f^h(z, Q^2) dz = 1. \tag{2.89}$$

Isospin symmetry and charge conjugation limits the number of independent $D_q^h(z)$, e.g. for a pion,

$$D_u^{\pi^+} = D_d^{\pi^-} = D_{\bar{d}}^{\pi^+} = D_{\bar{u}}^{\pi^-} \tag{2.90}$$

$$D_d^{\pi^+} = D_u^{\pi^-} = D_{\bar{u}}^{\pi^+} = D_{\bar{d}}^{\pi^-} \tag{2.91}$$

$$D_s^{\pi^+} = D_s^{\pi^-} = D_{\bar{s}}^{\pi^+} = D_{\bar{s}}^{\pi^-} \tag{2.92}$$

The $D_u^{\pi^+}$ etc. are the so-called favoured fragmentation functions, $D_d^{\pi^+}$ the unfavoured and $D_s^{\pi^+}$ the strange. For the favoured fragmentation the initial quark is in the pion ground state wavefunction and such processes are more probable than the unfavoured or strange cases.

Thus one can draw conclusions about the struck quark when identifying the leading hadron in an experiment. This allows e.g. flavour separated determination of the (polarised) parton distributions as shown in Fig. 2.5 and 2.8.

2.7 Determination of the Gluon Polarisation

2.7.1 Photon-Gluon Fusion

As pointed out in this Chapter, the determination of ΔG via QCD evolution at sufficient accuracy is not possible at present. The reason is the limited coverage

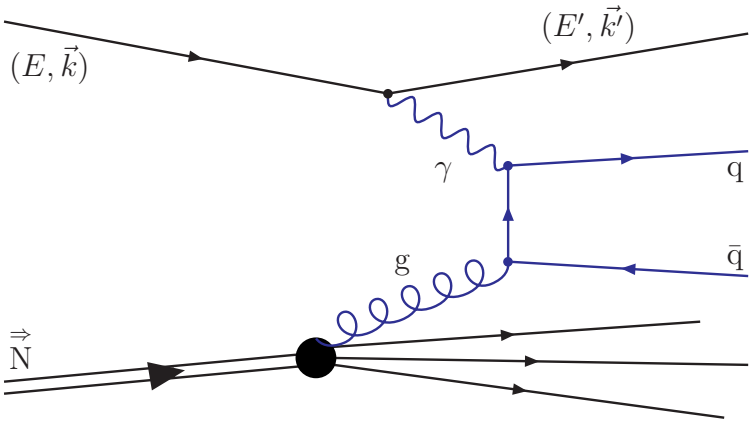

Figure 2.15: Photon-gluon fusion process.

in x and Q^2 of experiments using polarised beam and target. For an extraction of ΔG with a similar precision as for the unpolarised case, a polarised lepton-proton collider would be needed. Since this machine is neither available at present nor planned for the near future, a direct measurement of the polarised gluon distribution ΔG is necessary.

A direct measurement of ΔG is provided by the photon-gluon fusion (PGF) process in lepton-nucleon scattering. In this process the virtual photon interacts with a gluon from the nucleon via the production of a quark-antiquark pair (Fig. 2.15) and directly probes the gluons inside the nucleon. Experiments with polarised beam and polarised target are sensitive to the gluon helicity, in analogy to Fig. 2.7, and thus a measurement of the double helicity asymmetry

$$A_{PGF} = \frac{N^{\overleftarrow{\Rightarrow}}_{PGF} - N^{\overleftarrow{\Leftarrow}}_{PGF}}{N^{\overleftarrow{\Rightarrow}}_{PGF} + N^{\overleftarrow{\Leftarrow}}_{PGF}} \tag{2.93}$$

allows the extraction of the gluon polarisation $\Delta G/G$.

To tag these events experimentally, two different approaches are presented. In case of production of a $c\bar{c}$ pair, these events can be tagged using charmed mesons as explained in the following paragraph. When light quarks (u, d, s) are produced, PGF events can be enhanced by the selection of hadron pairs with high transverse momenta relative to the virtual photon as discussed afterwards.

2.7.2 Open Charm Production

The experimental asymmetry for muon production of $c\bar{c}$ pairs is

$$A^{raw} = \frac{N^{\overleftarrow{\Rightarrow}}_{c\bar{c}} - N^{\overleftarrow{\Leftarrow}}_{c\bar{c}}}{N^{\overleftarrow{\Rightarrow}}_{c\bar{c}} + N^{\overleftarrow{\Leftarrow}}_{c\bar{c}}} = P_B \cdot P_T \cdot f \cdot A^{c\bar{c}}_{\mu N} \tag{2.94}$$

with beam and target polarisation P_B, P_T respectively and the dilution factor f, which is the fraction of polarisable nucleons in the target material [64].
The asymmetry $A^{c\bar{c}}_{\mu N}(y)$ is related to the virtual photon asymmetry $A^{c\bar{c}}_{\gamma N}(y)$ by

$$A^{c\bar{c}}_{\mu N}(y) = D \cdot A^{c\bar{c}}_{\gamma N}(y), \tag{2.95}$$

where D is the dilution factor given by Eq. (2.26). The asymmetry $A^{c\bar{c}}_{\gamma N}(y)$ for longitudinal polarised beam and target (LL) is given by the ratio of the difference and sum of the helicity dependent cross sections for charm production, $\Delta\sigma^{c\bar{c}}_{\gamma N}(y)$ and $\sigma^{c\bar{c}}_{\gamma N}(y)$. They can be expressed as a convolution of the elementary photon-gluon cross sections, $\Delta\hat{\sigma}$ and $\hat{\sigma}$, with the gluon distributions ΔG and G:

$$\begin{aligned} A^{c\bar{c}}_{\gamma N}(E,y) = \frac{\Delta\sigma^{\gamma N\to c\bar{c}X}}{\sigma^{\gamma N\to c\bar{c}X}} &= \frac{\int_{4m_c^2}^{2M\nu} d\hat{s}\,\Delta\hat{\sigma}(\hat{s})\,\Delta G(x_g,\hat{s})}{\int_{4m_c^2}^{2M\nu} d\hat{s}\,\hat{\sigma}(\hat{s})\,G(x_g,\hat{s})} \\ &= \frac{\int_{4m_c^2}^{2M\nu} d\hat{s}\,\hat{a}_{LL}\,\frac{\Delta G}{G}\,\sigma(\hat{s})\,G(x_g,\hat{s})}{\int_{4m_c^2}^{2M\nu} d\hat{s}\,\sigma(\hat{s})\,G(x_g,\hat{s})} \\ &= \left\langle \hat{a}_{LL}\frac{\Delta G}{G} \right\rangle \end{aligned} \tag{2.96}$$

where $\hat{s} = (q + p_g)^2$ is the invariant mass of the photon-gluon system, q and p_g are the photon and gluon 4-momenta and $x_g = \hat{s}/(2M\nu)$ is the gluon momentum fraction. The partonic asymmetry for the photon-gluon reaction is defined as

$$\hat{a}_{LL} = \frac{\Delta\hat{\sigma}(\hat{s})}{\hat{\sigma}(\hat{s})}. \tag{2.97}$$

The $c\bar{c}$ quark pair hadronises into mesons and baryons. Per $c\bar{c}$-event 1.2 neutral D or $\bar{D}$ mesons are produced. Experimentally one selects PGF events with $c\bar{c}$ pair production via the decay of the D-meson

$$D^0 \to \pi^+K^- \quad \text{and} \quad \overline{D^0} \to \pi^-K^+$$

or

$$D^{*+} \to D^0\pi^+ \to (\pi^+K^-)\pi^+ \quad + \quad \text{charge conjugate}$$

as about 30% of the D^0-mesons come from a D^*. Since there is practically no charm inside the nucleon and charm production in hadronisation is suppressed, this channel should be relatively free of background. For more details about the PGF selection via open charm production at COMPASS see [65].

2.7.3 High-p_t Hadron Pairs

PGF events comprising the production of light quark pairs are enhanced by the selection of hadron pairs with high transverse momenta relative to the virtual photon [66]. Compared to the selection of PGF via open charm production these so-called high-p_t events are much more abundant. However, due to the light quark content in the nucleon and the fragmentation into light mesons also in other processes, there is some background which contributes and has to be dealt with. The selection of PGF events with high-p_t hadron pairs, the treatment of the background and the extraction of the gluon polarisation will be described in detail in this work. This Section gives an introduction to the method.

The background processes of importance are the leading order DIS process ($\gamma q \to q$, Fig. 2.16a), the QCD-Compton process ($\gamma q \to qg$, Fig. 2.16b) and the so-called resolved photon events, in which the hadronic contents of the photon react with a parton of the nucleon. These resolved photon events can in principle be suppressed by requiring a high photon virtuality Q^2. Looking at the PGF process (Fig. 2.15) in the photon-gluon c.m. system (Fig. 2.17), it can be seen that the two outgoing quarks are back to back. After a Lorentz boost into the laboratory system the two produced (leading) hadrons can still have large transverse momenta. This means that the transverse momentum of the outgoing hadrons is acquired in the hard parton scattering process. Another process that allows for high-p_t hadrons is the QCD-Compton process, in which the scattered quark emits a gluon in analogy to Compton scattering with emission of a photon. Beside the hard scattering, there are two other possible sources of transverse momentum, the intrinsic transverse momentum of the quarks inside the nucleon and the transverse momentum with respect to the initial quark direction obtained in the fragmentation process.

The intrinsic transverse momentum of the quarks inside the nucleon is described

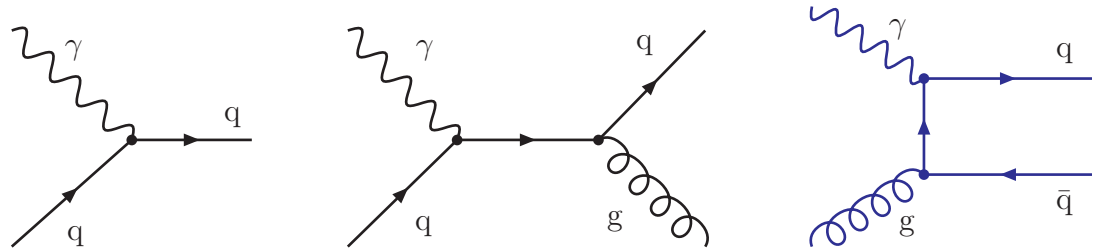

a) L.O. DIS b) QCD-Compton c) PGF

Figure 2.16: PGF and background processes.

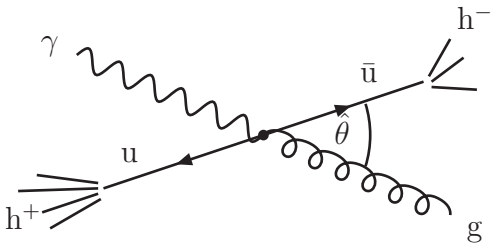

Figure 2.17: The photon-gluon fusion process in the c.m. system of gluon and photon.

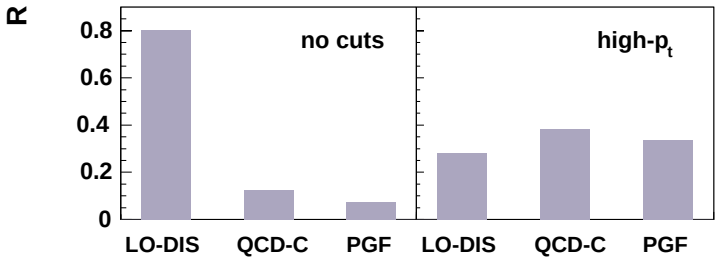

Figure 2.18: Fraction of photon-gluon fusion and background events without (left) and with (right) the application of the high-p_t cuts. Events with at least two outgoing particles in the current COMPASS acceptance are considered. They do not have to fulfil any further requirements without high-p_t cuts, but in the high-p_t case they must have a transverse momentum $p_t > 0.7\,\mathrm{GeV/c}$ and the sum of their transverse momenta squared must be $p_{t1}^2 + p_{t2}^2 > 2.5\,(\mathrm{GeV/c})^2$.

by a Gaussian distribution with a mean of about $\langle k_T \rangle \approx 440\,\mathrm{MeV}$ [67]. A hadron originating from a quark and carrying a fraction z of its momentum has a transverse momentum $\langle k_T \rangle \cdot z \; < 440\,\mathrm{MeV}$. The transverse momentum from the fragmentation process is of the same order $\langle p_{t,had} \rangle \approx 360\,\mathrm{MeV}$. Adding both quadratically leads to 570 MeV. Requiring two hadrons of larger transverse momenta effectively suppresses the L.O. contribution, for which intrinsic k_T and fragmentation are the only sources of transverse momentum. For PGF and QCD-Compton events a considerable fraction of p_t comes from the hard scattering process. The intrinsic k_T and the $p_{t,had}$ from the fragmentation only play a minor role. In Fig. 2.18 the enrichment of photon-gluon fusion events, which is obtained when applying high-p_t cuts to an event sample generated with the Monte Carlo generator LEPTO [68], is illustrated.

Since the background processes can not be separated completely by requiring two high p_t hadrons, the measured double spin asymmetry will contain contributions from all processes. The (polarised) cross section for the production of high-p_t hadron pairs can be written as (for simplicity, the explicit dependence on

the kinematic variables has been dropped in the following):

$$\begin{aligned}(\Delta)\sigma^{h_1,h_2} &= \sum_q \left[(\Delta)q \otimes (\Delta)\hat{\sigma}^{\gamma^* q\to q} \otimes D_q^{h_1,h_2}\right] \\ &+ \sum_q \left[(\Delta)q \otimes (\Delta)\hat{\sigma}^{\gamma^* q\to qG} \otimes D_{q,G}^{h_1,h_2}\right] \\ &+ \sum_q \left[(\Delta)G \otimes (\Delta)\hat{\sigma}^{\gamma^* G\to q\bar{q}} \otimes D_{q,\bar{q}}^{h_1,h_2}\right]. \end{aligned} \tag{2.98}$$

The sums $\sum_q$ run over the (anti)quark flavours. $(\Delta)\hat{\sigma}^{\gamma^* q\to q}$, $(\Delta)\hat{\sigma}^{\gamma^* q\to qG}$ and $(\Delta)\hat{\sigma}^{\gamma^* G\to q\bar{q}}$ are the (polarised) partonic hard scattering cross sections for the LO, first order α_s QCD-Compton and PGF process, respectively. The $D_i^{h_1,h_2}$ describe the fragmentation process of partons into hadrons h_1, h_2. As long as the polarisation of the final hadronic state is not studied they are assumed to be spin independent.

The double spin asymmetry A_{LL} with longitudinal polarised beam and target, expanded with $1 = q/q$ or $1 = G/G$, can be written as

$$\begin{aligned}A_{LL}^{h_1h_2} &= \frac{\Delta\sigma^{h_1,h_2}}{\sigma^{h_1,h_2}} \\ &= \frac{\sum_q \left[q\frac{\Delta q}{q} \otimes \Delta\hat{\sigma}^{\gamma^* q\to q} \otimes D_q^{h_1,h_2}\right]}{\sigma^{h_1,h_2}} + \frac{\sum_q \left[q\frac{\Delta q}{q} \otimes \Delta\hat{\sigma}^{\gamma^* q\to qG} \otimes D_{q,G}^{h_1,h_2}\right]}{\sigma^{h_1,h_2}} \\ &+ \frac{\sum_q \left[G\frac{\Delta G}{G} \otimes \Delta\hat{\sigma}^{\gamma^* G\to q\bar{q}} \otimes D_{q,\bar{q}}^{h_1,h_2}\right]}{\sigma^{h_1,h_2}}. \end{aligned} \tag{2.99}$$

Since the experimentally accessible quantity is the mean value of $\Delta G/G$ in the covered phase space region, $\Delta G/G = \Delta G/G(x_g, \hat{s})$ is replaced by the mean $\langle \Delta G/G\rangle$ and can be taken out from the convolution. The $\Delta q/q$ are treated analogously. Expanding each of the three terms with $1 = \sigma/\sigma$, the above equation reads

$$\begin{aligned}A_{LL}^{h_1h_2} &\approx \frac{\sum_q \left\langle \frac{\Delta q}{q}\right\rangle \left[q \otimes \hat{\sigma}^{\gamma^* q\to q}\left(\frac{\Delta\hat{\sigma}}{\hat{\sigma}}\right)^{\gamma^* q\to q} \otimes D_q^{h_1,h_2}\right]}{\sigma^{h_1,h_2}} \\ &+ \frac{\sum_q \left\langle \frac{\Delta q}{q}\right\rangle \left[q \otimes \hat{\sigma}^{\gamma^* q\to qG}\left(\frac{\Delta\hat{\sigma}}{\hat{\sigma}}\right)^{\gamma^* q\to qG} \otimes D_{q,G}^{h_1,h_2}\right]}{\sigma^{h_1,h_2}} \\ &+ \left\langle \frac{\Delta G}{G}\right\rangle \frac{\sum_q \left[G \otimes \hat{\sigma}^{\gamma^* G\to q\bar{q}}\left(\frac{\Delta\hat{\sigma}}{\hat{\sigma}}\right)^{\gamma^* G\to q\bar{q}} \otimes D_{q,\bar{q}}^{h_1,h_2}\right]}{\sigma^{h_1,h_2}}. \end{aligned} \tag{2.100}$$

Isolating the partonic asymmetries $\hat{a}_{LL}^i = (\Delta\hat{\sigma}/\hat{\sigma})^i$ of each term with a similar argument as above, they can be replaced by the average $\langle \hat{a}_{LL}^i\rangle$ over the accessible

kinematic region. Using

$$\sigma^{h_1,h_2} = \sigma^{PGF} + \sigma^{QCD-C} + \sigma^{L.O.}$$

and the cross section ratio for the process i to the total of all three processes

$$R_i = \frac{\sigma^i}{\sigma^{PGF} + \sigma^{QCD-C} + \sigma^{L.O.}}, \tag{2.101}$$

where $\sigma^i = q(G) \otimes \hat{\sigma}^i \otimes D_i^{h_1,h_2}$, Eq. (2.100) can then be written as

$$\begin{aligned} A_{LL}^{h_1h_2} &= A_1\langle \hat{a}_{LL}^{QCD-C}\rangle R_{QCD-C} + A_1\langle \hat{a}_{LL}^{L.O.}\rangle R_{L.O.} \\ &+ \frac{\Delta G}{G}\langle \hat{a}_{LL}^{PGF}\rangle R_{PGF}, \end{aligned} \tag{2.102}$$

where the quark asymmetries $\Delta q/q$ are approximated by the virtual photon-nucleon asymmetry A_1, Eq. (2.24). The $\langle \hat{a}_{LL}^i \rangle$, also referred to as analysing power, can be calculated in QED and QCD, respectively. A_1 has been measured in several experiments (e.g. [18]), whereas the cross section ratios R_i have to be determined using Monte Carlo simulations. Eq. (2.102) allows a determination of the gluon polarisation $\Delta G/G$.

Single High-p_t Hadrons

As an alternative to the detection of a pair of high-p_t hadrons the presence of only one hadron with a larger transverse momentum than in the case of hadron pairs can be required. Since a large p_t in the event has to be balanced, it is likely that there is another hadron, which is not necessarily detected. Requiring the p_t to be large enough, photon-gluon fusion events can be enriched compared to the background. The advantage of this method is the higher statistics as for the case of high-p_t hadron pairs. A disadvantage is the bigger role of radiative corrections, which have to be treated with more care. Several studies of this channel started at COMPASS [69, 70] as well as at HERMES [71]. Here theoretical calculation in leading and next-to-leading order on single high-p_t hadron production exist [72], which are easier to perform from the theoretical side, and can be compared to the data.

2.7.4 Determination of ΔG at Proton-Proton Colliders

Apart from DIS experiments, measurements of the gluon polarisation can be carried out in polarised proton-proton reactions. The $p-p$ collisions allow for several independent processes and therefore different ways to extract $\Delta G/G$ [73]. Fig. 2.19 shows selected lowest order Feynman diagrams for elementary processes with gluons in the initial state as they can occur in $p-p$ collisions.

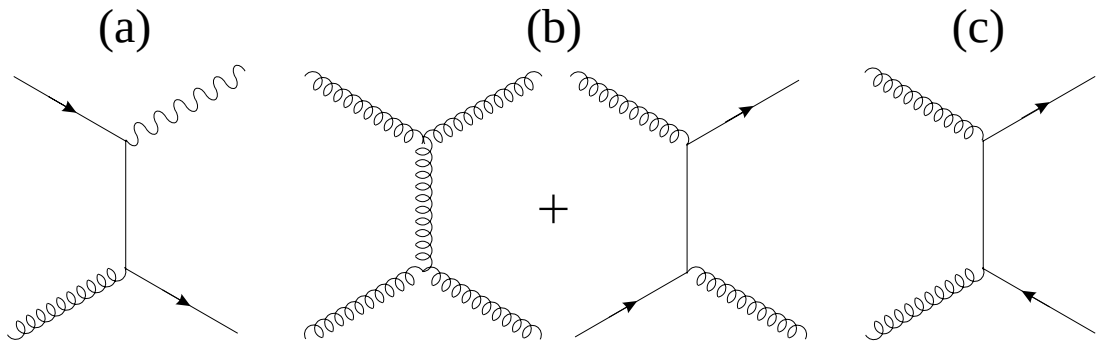

Figure 2.19: Selected lowest-order Feynman diagrams for elementary processes with gluons in the initial state in $p-p$ collisions: (a) quark-gluon Compton process with prompt photon production, (b) gluon-gluon and gluon-quark scattering for jet production, and (c) gluon-gluon fusion producing a heavy quark pair.

(a) Prompt Photon Production

At leading order, a photon in the final state is produced in reactions $gq \to \gamma q$ (Fig. 2.19 a) and $q\bar{q} \to \gamma g$. In $p-p$ colliders, as opposed to proton-antiproton reactions, the quark-gluon process is favoured since the proton quark densities are much larger than the antiquark ones. Photons produced through this partonic hard scattering show a distinct signal at colliders, namely that of an isolated photon without jets nearby. This is a very promising method to measure $\Delta G/G$ at RHIC with the experiments PHENIX [74] and STAR [75].

(b) Jet Production

If the energies at RHIC are high enough ($\sqrt{S} \approx 500\,\mathrm{GeV}$) clearly structured jets will be produced with observables showing a strong sensitivity to ΔG due to the dominance of gg and gq initiated subprocesses (Fig. 2.19 b). These studies will be performed with the STAR detector. Alternatively one can look for high-p_t leading hadrons such as π^0, $\pi^\pm$ whose production proceeds through the same partonic subprocesses. This is done at PHENIX [76], which has a limited angular coverage.

(c) Heavy Flavour Production

The production of heavy quark pairs in hadronic collisions is dominated by the gluon-gluon fusion $gg \to Q\bar{Q}$ (Fig. 2.19 c). As for prompt photon production, the channel $q\bar{q} \to Q\bar{Q}$ is suppressed because of the requirement of antiquarks in the initial state. Thus heavy quarks provide direct access to the gluons in the proton.

Chapter 3

The COMPASS Experiment

3.1 Introduction

COMPASS is a fixed target experiment at the SPS[1] at CERN. The COMPASS spectrometer is a multi-purpose detector, that will carry out measurements covering a wide range of hadron structure and spectroscopy [64]. It is located at the M2 beamline in the North Area (Prevessin) of CERN (Fig. 3.1). The M2 beamline can provide different types of beams that are produced from the SPS protons. Pions, kaons, protons and muons can be used to perform the different measurements that are foreseen with the COMPASS experiment. Depending on the beam type, muons or hadrons, different experimental programs will be realised and the spectrometer has to fulfil different requirements. Therefore the experimental setup is very flexible and within some days it can be changed from the so-called muon setup to the hadron setup, which includes e.g. the change of the target and some detectors.

The setup presented in the following has been constructed in 1998-2000 and was commissioned in 2001. 2002 was the first full year of physics data taking using a muon beam and the almost complete setup. 2003 and 2004 the setup has been upgraded with additional detectors. The program with hadron beams has started with a commissioning run in 2004. This first data taking with a hadron beam includes a measurement of the Primakoff effect, where the collected statistics already exceeds previous experiments. After a break in 2005, where the SPS is not running, the continuation of the data taking for the program with the muon beam is forseen for 2006, followed by at least two years of data taking with hadron beams.

One of the goals COMPASS has been designed for is to carry out double po-

[1] Super Proton Synchrotron

larisation measurements, among them the determination of the contributions of the different quark flavours and the gluons to the nucleon spin, with deep inelastic muon-nucleon scattering. Since the determination of the gluon polarisation, as described in Section 2.7, is the topic of this thesis, I will restrict the detector description to the muon setup. For this measurement a polarised lepton beam as well as a polarised target is needed, they are described in Section 3.2 and 3.3, respectively. The COMPASS spectrometer itself, which consists of a large number of detectors, is described in Section 3.4. The data acquisition system (DAQ), that is used to handle the large number of detector channels and the high data rates, is presented in Section 3.5.

3.2 The Muon Beam

The polarised lepton beam used in the COMPASS experiment is the M2 (anti)muon beam [77, 78]. It is a secondary beam produced by the SPS proton beam hitting a production target. Among other particles, pions and kaons are produced, that decay into muons and neutrinos. Fig. 3.1 gives an overview of the accelerator complex at CERN. The source of the SPS protons is a LINAC, then, via PS[2] booster (PSB) and PS, protons of 14 GeV are injected into the SPS. In the SPS the protons are accelerated to an energy of 400 GeV and then extracted to the North Area beamlines. The complete cycle has a duration of 16.8 sec, comprising the extraction time of 4.8 sec, the so-called spill. The intensity of the proton beam incident on the T6 production target is about 10^{13} protons per spill. The intensity of the final muon beam can be adjusted by the thickness of the T6 production target. For the nominal intensity of 2×10^8 μ^+/spill, the thickness of the beryllium target is 50 cm. The beamline following the T6 production target to the COMPASS target is sketched in Fig. 3.2.

After the target π, K or μ-beams can be selected. For a muon beam with an energy of $E_\mu = 160$ GeV at the target, pions with an energy of 177 GeV$\pm$10% are selected through the magnet system directly behind the production target. These selected hadrons are transported to a hadron decay channel of about 600 m length. The parity violating decay of the hadrons produces polarised muons ($\pi \to \mu + \nu_\mu$, $K \to \mu + \nu_\mu$). The polarisation of the muon depends on the decay angle in the hadron rest frame with respect to its direction of motion in the laboratory frame. Therefore the sign and degree of the polarisation can be chosen by selecting the corresponding muon/hadron energy ratio. The polarisation P_b of the positive

[2]Proton Synchrotron

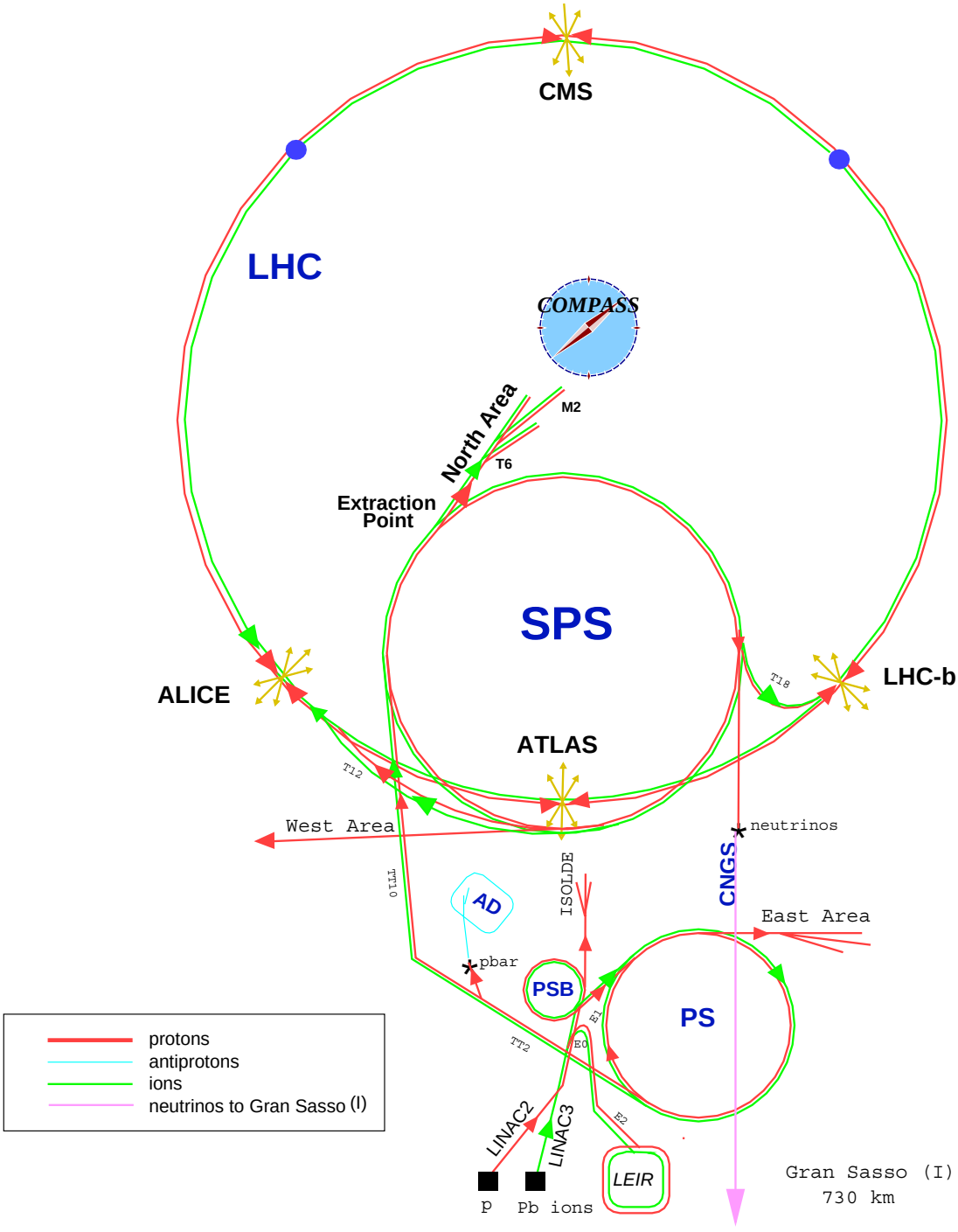

Figure 3.1: The CERN accelerator complex. The linear accelerators LINAC 2 and 3 are the injectors for protons and ions, respectively. Via PS Booster and PS they are transferred to the SPS, where they can be used to fill the Large Hadron Collider (LHC), which is planned to be operational in 2007. Alternatively they are extracted to the North Area for different experiments, like COMPASS, or sent to a target to produce a neutrino beam to investigate neutrino oscillations with a detector located at Gran Sasso in Italy (CNGS).

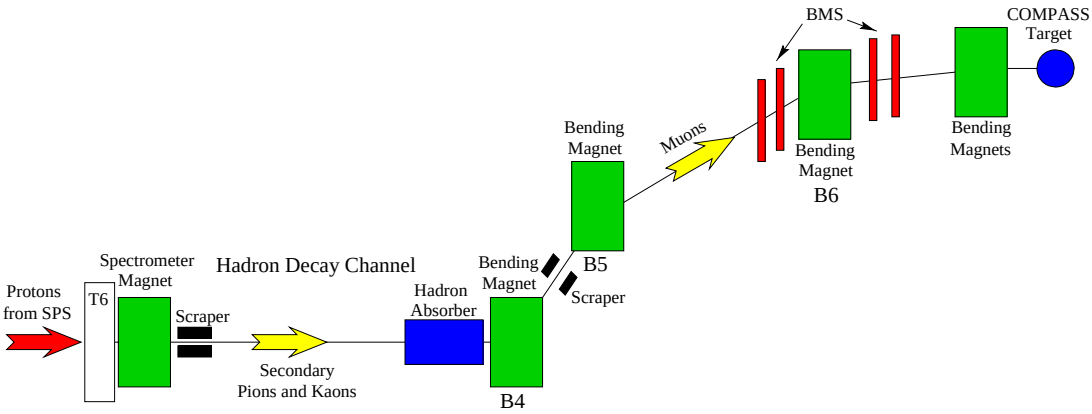

Figure 3.2: Sketch of the M2 beamline (not to scale). The particles produced at the T6 production target are selected by their momentum directly behind the target. The 600 m long decay channel is followed by muon selection with absorbers and magnets. The muon momentum is measured around the bending magnet B6 before the beam hits the target.

muons in the laboratory frame can be calculated by [47]

$$P_b = \frac{m_h^2 + (1 - 2E_h/E'_\mu)m_\mu^2}{m_h^2 - m_\mu^2}, \tag{3.1}$$

with m_μ and E'_μ being mass and energy of the muon that has been produced in the decay, and mass m_h and energy E_h of the decaying hadron. A few percent of the muons originate from kaon decay. These are highly polarised as well in these conditions and taken into account in the Monte Carlo simulation of the beam. The ratio of muon to hadron energy $E_\mu/E_\pi = 160\,\text{GeV}/177\,\text{GeV}$ has been chosen to be 0.9, leading to a polarisation of $-76\,\%$ with a relative error of $5\,\%$ [79]. In 2004 the ratio E_μ/E_π has been changed to $160\,\text{GeV}/172\,\text{GeV}$ which increased the polarisation to $-80\,\%$. In the SMC experiment, which has used the M2 beamline previous to COMPASS, the polarisation of the beam has been measured. A good agreement between the Monte Carlo simulations done in [77] and the measurements [80, 81] has been found. Therefore the polarisation is not measured in COMPASS instead simulated values are used.

Experimentally a good compromise between high polarisation and high μ intensity has to be found. With the present setup and the E_μ/E_π ratio of 0.9, about 10% of the pions decay into muons in the decay channel. After the decay channel, the remaining hadrons are absorbed by an absorber, a 9.9 m long block of beryllium. The emerging muons of 160 GeV momentum are selected by the bending magnets B4 and B5 and the scrapers in the next 330 m section. Then they are guided through the beamline to the COMPASS experimental hall. Scrapers and

magnetic shielding blocks are used to reduce unwanted halo muons at the experiment. The bending magnet B6, 100 m upstream the COMPASS target, bends the beam coming from the SPS underground to the surface level, where the experiment is located. A final section of dipoles and quadrupoles before the target provides the optics necessary for an adequate beam spot size at the target. Due to the production mechanism the muon beam has a large momentum spread (160 GeV $\pm$ 5%). It is focused to a sigma of 7 mm for the Gaussian core at the target with a divergence of about 1 mrad. Thus a measurement of momentum and position of each single incoming particle is mandatory. The momenta are measured in the beam momentum station (BMS) up- and downstream of B6 with 4 (5 in 2003, 6 in 2004) scintillating fibre hodoscopes of 5 mm granularity. The position and time of the beam at the experiment are measured with scintillating fibre detectors and silicon telescopes just upstream of the target. The association of the momentum measured in the BMS and the track position determined right in front of the target is based on time correlation and has been improved by making use of the beam optics matrix elements for the spatial correlation [82, 65].

3.3 The Polarised Target

The small cross section for muon scattering and the limited beam intensity (compared to primary beams) require the use of a large solid state polarised target. In the years 2001 to 2004 COMPASS used the former SMC polarised target system, which can be operated with proton and deuteron target material [83].

The target material is ^{6}LiD which is polarised by Dynamic Nuclear Polarisation (DNP) to about 50% [84]. It is contained in two 60 cm long target cells that are oppositely polarised. The cells are separated by 10 cm and their diameter is 3 cm. They are embedded in a superconducting solenoid magnet that provides a very homogeneous field of 2.5 Tesla. To reach the so-called frozen spin mode, where the target spins stay (anti-)aligned with the solenoid field, a temperature down to 50 mK is needed. These low temperatures, that are needed to maintain an efficient polarisation, are achieved with a ^{3}He/^{4}He dilution refrigerator. In Fig. 3.3 a side view of the polarised target system is drawn. The SMC magnet provides an acceptance of $\pm$70 mrad. The magnet designed for COMPASS will have an aperture of $\pm$180 mrad. This magnet is scheduled for the data taking in 2006. In addition to the solenoid a dipole field of 0.5 T can be applied. It is used to adiabatically reverse the nuclear spins.

Beside the target material ^{6}LiD, that is used for the measurements, ^{3}He and ^{4}He and traces of several other elements like carbon, fluor, nickel and copper are

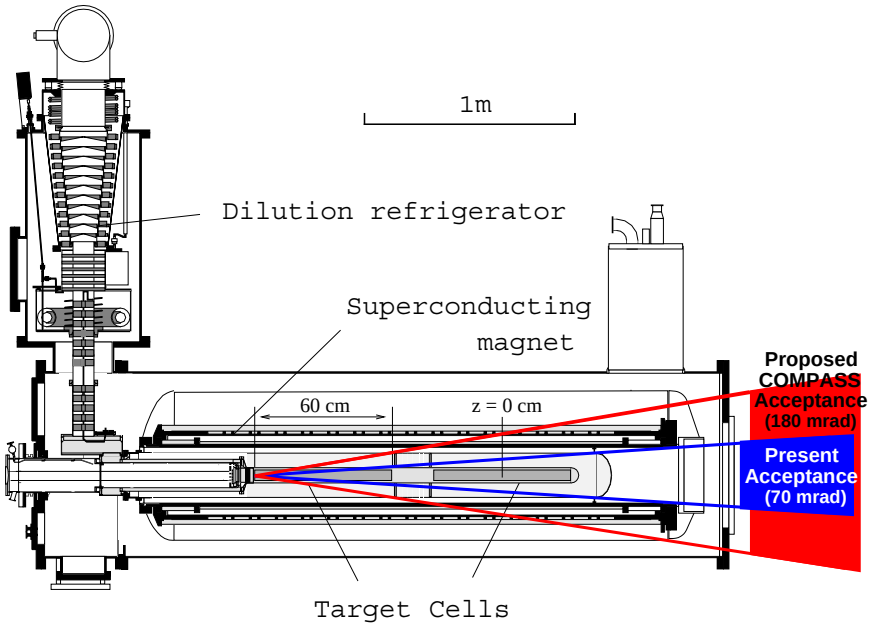

Figure 3.3: The polarised target system. The two target cells are embedded in the so-called mixing chamber, which is filled with ^{3}He/^{4}He. The beam enters from the left. The origin of the COMPASS coordinate system is located in the middle of the downstream target cell. The COMPASS acceptance of 180 mrad will be reached using a new magnet instead of the SMC magnet used at the moment.

present inside the target cells [85, 86]. Between 165 g and 180 g of ^{6}LiD occupy approximately 210 cm^3 of the 415 cm^3 target volume (the warm volume of the target is 424 cm^3). Mainly ^{3}He and ^{4}He fill almost the complete remaining volume. The NMR[3]-coils used for polarising and the polarisation measurement are made of cupronickel (CuNi) alloy with a Teflon coating containing carbon and fluor. All the materials need to be taken into account for the analysis since they dilute the polarisable material inside the target as will be described later (Chapter 5).

3.3.1 Dynamic Nuclear Polarisation

The intrinsic polarisation of nuclei in a magnetic field of 2.5 T at a temperature of 1 K is below 1%. Electrons, with their high magnetic moment, have a polarisation of 96% under these conditions. The principle of DNP is to transfer the high electron polarisation to the nuclear spins using microwaves with an appropriate frequency [87]. Therefore unpaired electrons are needed that act as the paramagnetic centres. They have been created by irradiation of the target material with an electron beam.

[3]Nuclear Magnetic Resonance

In thermal equilibrium, the population of the spin states follows a Boltzmann statistics. When the system of non-interacting spins will be placed in a magnetic field $\vec{B}_0$ pointing along the z-axis, the energy levels of the spin I are split into $2I+1$ sub-levels separated by $\hbar\omega_0 = \mu B_0/I$ with the Larmor frequency $\omega_0/2\pi$. The polarisation is given by the Brillouin function [88]

$$P(\alpha) = \frac{2I+1}{2I}\coth\left(\frac{2I+1}{2I}\alpha\right) - \frac{1}{2I}\coth\left(\frac{\alpha}{2I}\right), \tag{3.2}$$

where $\alpha = \frac{\hbar\omega_0}{k_B T} = \frac{\mu B_0}{I k_B T}$ with the Boltzmann constant k_B. When the electron and the nucleon do not interact, the Hamiltonian for such a pair is

$$H = -\vec{\mu_e}\vec{B_0} - \vec{\mu_I}\vec{B_0} = \hbar\omega_e M - \hbar\omega_I m, \tag{3.3}$$

where M and m are the magnetic quantum numbers for the electron and nucleon spin, respectively, and

$$\hbar\omega_e = |2\mu_e B_0|, \qquad \hbar\omega_I = \left|\frac{\mu_I B_0}{I}\right|.$$

Zeeman splitting produces six eigenstates $|Mm\rangle$ of the system (in the following only spin 1 nucleons are considered as done in [89]). Irradiating the system with a frequency $\omega = \omega_I(\omega_e)$ leads to transitions like $|+0\rangle \leftrightarrow |++\rangle$ with equal probability for the arrow in both directions so that no net polarisation is achieved. Transitions where both electron and nucleon spin flip simultaneously like $|+0\rangle \rightarrow |-+\rangle$ are forbidden in a non-interacting system.

But dipolar-dipolar interactions between electron and nucleus have to be taken into account and allow such simultaneous spin flippings by mixing the pure eigenstates. The spin states are illustrated in Fig. 3.4. The simultaneous flipping is still less probable than the allowed transitions but possible. In the conditions B=2.5 T and T=0.5 K electrons are highly polarised and thus the populations of $|1\rangle$, $|2\rangle$ and $|3\rangle$ are approximately zero and the states $|4\rangle$, $|5\rangle$ and $|6\rangle$ have $\frac{1}{3}$ of the total population each. By interacting with a frequency of $\hbar\omega \sim \hbar(\omega_e - \omega_I)$, one can induce the forbidden transitions $|4\rangle \rightarrow |2\rangle$ and $|5\rangle \rightarrow |3\rangle$. Because of the large magnetic moment, the electron has a fast relaxation time and the transition $|M = +\frac{1}{2}\rangle \rightarrow |M = -\frac{1}{2}\rangle$ occurs much faster than the nucleon relaxes. The spin system, that was initially in state $|4\rangle$ ($|5\rangle$) moves to state $|5\rangle$ ($|6\rangle$) via $|2\rangle$ ($|3\rangle$). The population state $|-+\rangle$ is enhanced. The state $|--\rangle$ can be enhanced analogously by choosing the frequency $\omega \sim (\omega_e + \omega_I)$.

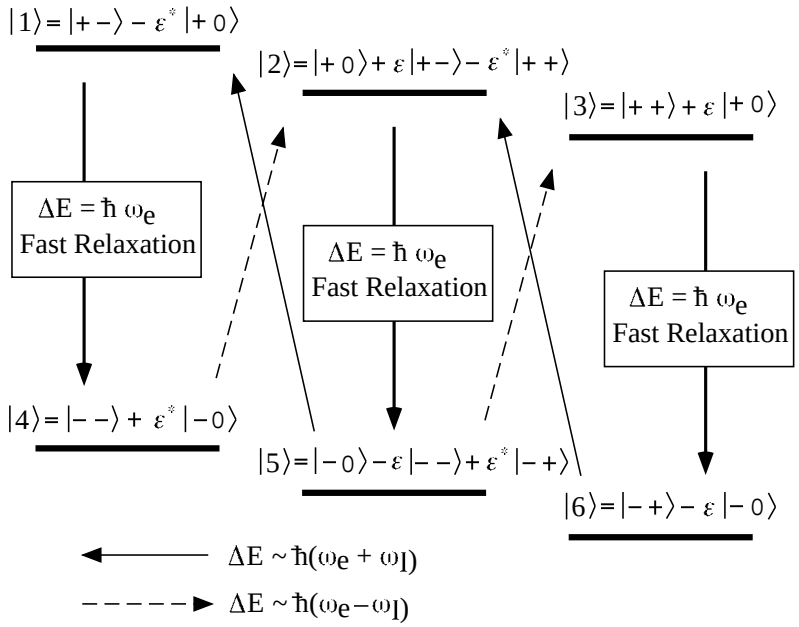

Figure 3.4: Dynamic Nuclear Polarisation mechanism using dipolar-dipolar interactions. The dipolar-dipolar interactions add small fractions (ϵ, ϵ^*) of the neighbouring states to the states of the non-interacting system. Thus originally forbidden transitions like $|4\rangle \rightarrow |2\rangle$ are allowed (drawn spin states are not normalised) [89].

Possible Spin States for the COMPASS Target

The polarisation orientation depends on the microwave setting of the DNP, i.e. if the target is irradiated with a microwave frequency $\omega_e + \omega_I$ or $\omega_e - \omega_I$, and on the magnetic field direction. Fig. 3.5 illustrates the spin configurations, that are possible with the target. From a) to b) and c) to d) the spin is reversed by the so-called field rotation where the magnetic solenoid field changes sign. The field rotation is based on the nuclear spin following the direction of an external magnetic field which is rotating slowly compared to the Larmor frequency of the nuclear spin. The field is rotated by slowly ramping up and down the dipole. The field rotation in COMPASS is performed three times per day in order to reduce systematic errors due to different acceptances of the target cells and time dependent variations of the spectrometer efficiency. Setting a)/b) and c)/d) are obtained by choosing the appropriate microwave frequencies. The spin reversal by DNP technique takes at least one day and cannot be done frequently during the beam time. It is done a least once per beam time to further suppress systematic errors due to a possible dependence of the spectrometer performance on the target magnetic field direction.

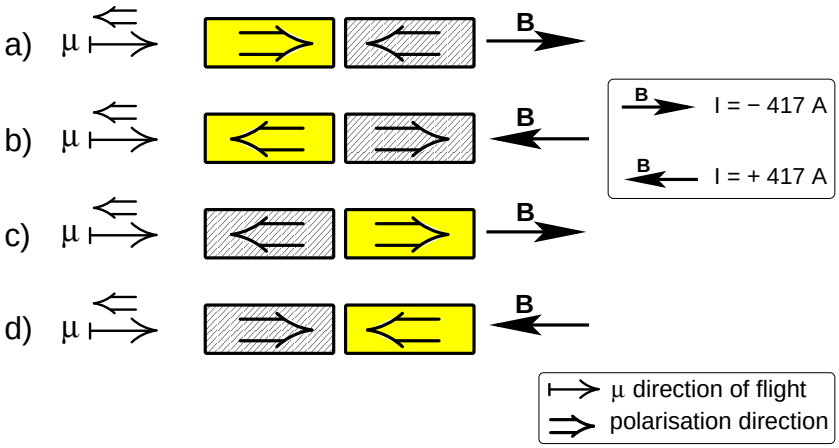

Figure 3.5: Target spin configurations as explained in the text. The magnetic field B points in the opposite direction of the incident muon for a positive solenoid current $I = +417\,\mathrm{A}$ and in the direction of flight of the incident muon for a negative solenoid current $I = -417\,\mathrm{A}$. The spins in the target cell with positive polarisation (plain yellow) are always aligned with the magnetic field lines while for the negative polarisation (striped) the spins are anti-aligned with the solenoid field lines.

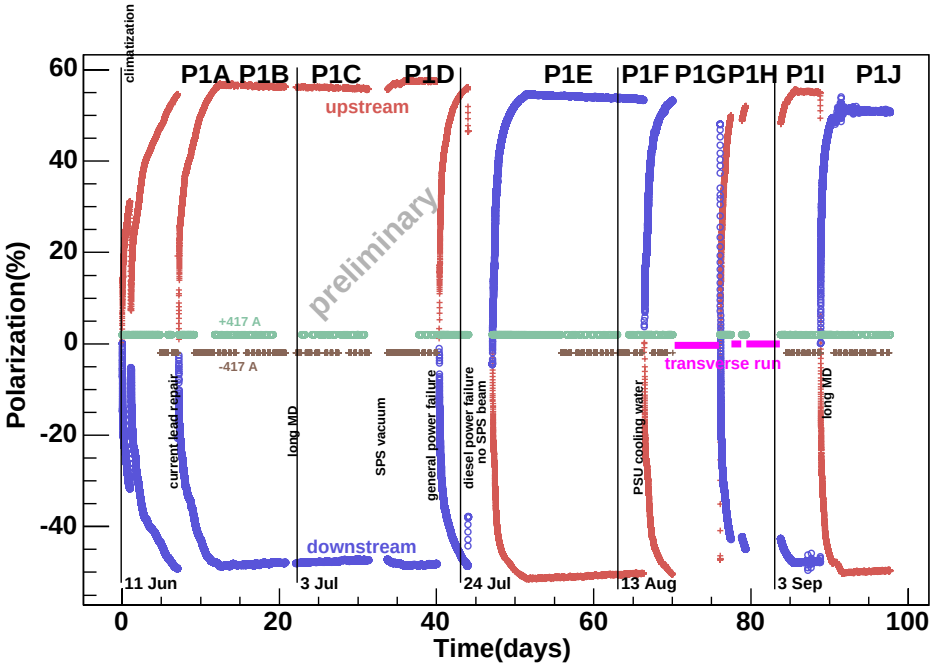

Figure 3.6: The COMPASS target polarisation in 2003. The red crosses belong to the measurement of the upstream cell polarisation, the blue open circles to the downstream cell. The actual spin direction is given by the polarisation and the sign of the current of the solenoid. Several power failures in 2003 led to a loss of polarisation since the solenoid went off. The names P1A to P1J refer to the data taking period (usually one week). In the periods P1G and P1H measurements with transverse spin orientation have been performed. It is not possible to measure the polarisation in the transverse orientation.

Fig. 3.6 shows the target polarisation of the two cells during the COMPASS beam time in 2003. The polarisation is measured by 5 NMR-coils per cell along the target [90]. Fig. 3.6 illustrates the polarisation build up, reaching a polarisation of about 50% within a few days. Then the microwave frequency is switched off and a very slow relaxation of the polarisation is visible. In the frozen spin mode the typical magnetic relaxation time is more than 1400 h at 0.42 T and more than 15000 h at 2.5 T (at T=65 mK) [91]. This allows to run the experiment for a long time without repolarising the target. Typical polarisations reached during data taking are 50 %. The maximum polarisations that have been achieved are +57 % and -52 %, respectively, depending on the polarisation direction.

3.4 The COMPASS Spectrometer

The COMPASS spectrometer [92] is a two-stage spectrometer that covers a large kinematic range ($10^{-4}\,\mathrm{GeV}^2/\mathrm{c}^2 < Q^2 < 60\,\mathrm{GeV}^2/\mathrm{c}^2$, $10^{-5} < x < 0.5$). Each stage consists of a spectrometer magnet, tracking and particle identification devices. Fig. 3.7 gives an overview of the setup.

The first spectrometer directly downstream of the target covers an acceptance of about ± 180 mrad and is referred to as large angle spectrometer (LAS). The first spectrometer magnet (SM1) has a bending power of 1 Tm. The small angle spectrometer (SAS) covers the inner 30 mrad, accordingly the second spectrometer magnet (SM2) has a higher bending power of 4.4 Tm. The tracking detectors are distributed around the magnets and can be divided into three groups, the very small area trackers (VSAT), the small area trackers (SAT) and the large area trackers (LAT). Their granularity is adapted to the particle fluxes in the different detector regions. The tracking system can detect particles with scattering angles down to $\theta \approx 0°$. Additionally, each spectrometer is equipped with tracking devices downstream of the hadron absorbers to allow muon identification. For particle identification a Ring Imaging Cherenkov Detector (RICH) is used in the LAS. Furthermore both spectrometer-stages are equipped with hadronic calorimeters.

The size of the spectrometer is about $4\times5\,\mathrm{m}^2$ and it is 50 m long. Since a major part of the μ-beam passes the target without interaction, the beam travels through the complete spectrometer. To avoid multiple interactions the amount of material in the beam region is minimised. The calorimeters and e.g. the straw detectors are constructed with physical holes. This holes are not centred, but shifted towards the Jura side of the spectrometer to follow the positively charged beam, that is bent in this direction.

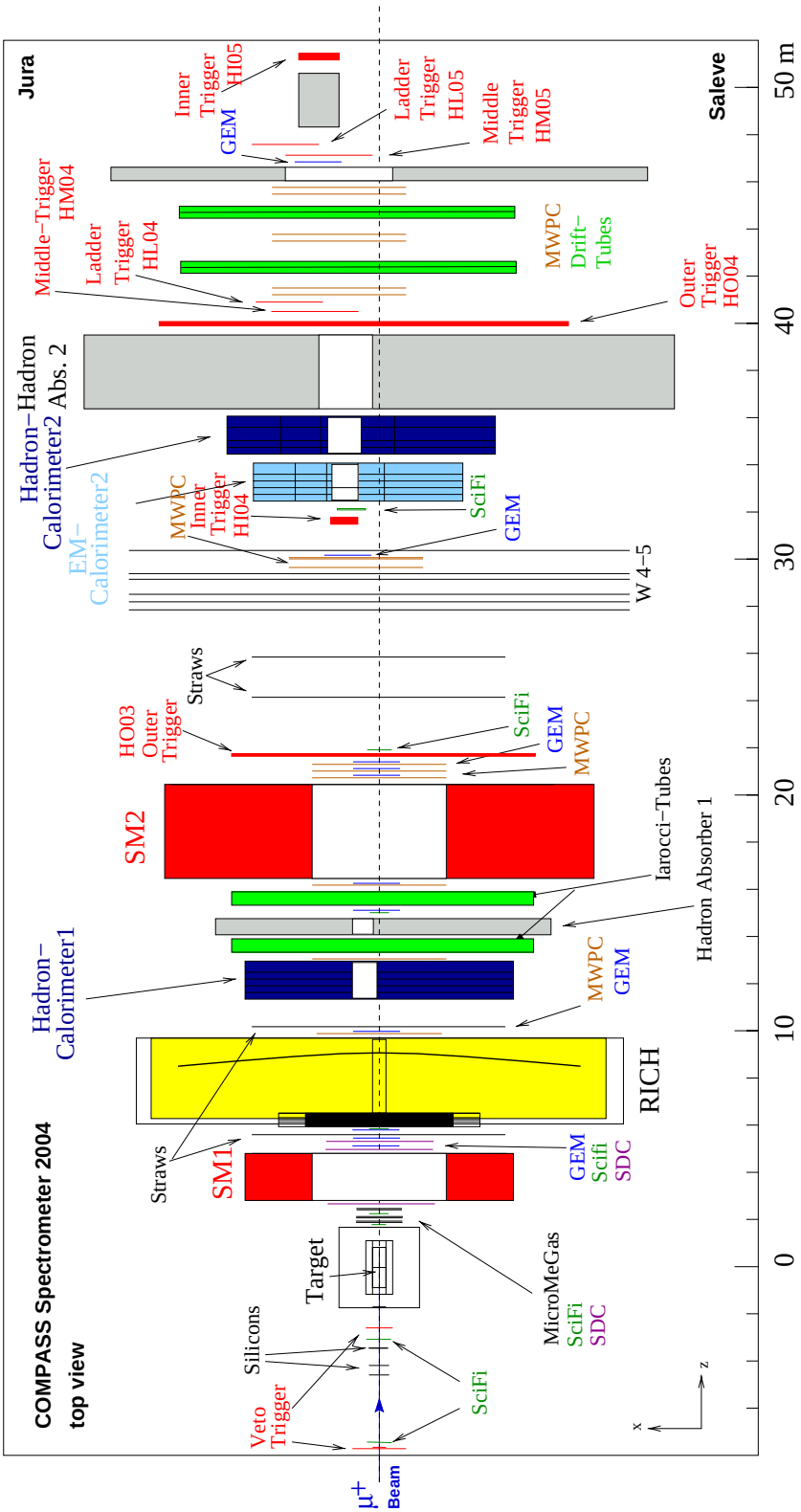

Figure 3.7: The COMPASS spectrometer as it was operational in 2004 (and, except the last GEM detector and two W 4-5 planes, also in 2003). The beam enters from the left, tracked by scintillating fibres (SciFi) and silicon detectors before it hits the target. The two spectrometer magnets SM1 and SM2 are given in red. Each spectrometer stage contains tracking devices (scintillating fibres (SciFi), Saclay Drift Chambers (SDC), MICROMEGA, GEM, MWPC, W 4-5 and Straws), hadron calorimeters and muon trackers (Iarocci tubes in the first spectrometer, drift tubes in the second). The RICH is located in the first spectrometer. The electromagnetic calorimeter in the second spectrometer is equipped successively with lead glass blocks and readout electronics. The trigger hodoscopes are behind SM2 and hadron absorber 2. The positive x-direction points towards the Jura, the negative towards the Saleve.

3.4.1 Tracking Detectors

Depending on their location, different types of detectors are used in COMPASS to provide tracking information. Table 3.1 gives an overview over these detectors.

Very Small Area Trackers (VSAT)

For the beam tracking upstream of the target as well as very small angle tracking close to the beam axis downstream, scintillation fibre detectors are used. The second type of VSAT are silicon micro-strip detectors, used for the beam tracking upstream of the target. They have an active area of $(5\text{-}10)^2\,\mathrm{cm}^2$.

Small Area Trackers (SAT)

The SAT operate in the region close to the beam, they cover a region up to 20 cm from the beam axis. In contrast to the VSAT, gaseous detectors are used here. They are based on the ionisation of a gas volume by the passing particle. The high rate capability is based on their fast collection of positive ions. To avoid damages in the very high intensity region of the beam, the high voltage in their inner regions can be switched off. This makes them insensitive to the charged particles passing this area. These dead zones are usually deactivated during normal running, but can be activated for low intensity studies and detector alignment. In COMPASS two novel types of micro-pattern gaseous detectors are used, GEM and MICROMEGA.

Large Area Trackers (LAT)

In the outer regions of the spectrometer the particle flux is reduced and the granularity of the detectors can be much larger than for the (V)SAT equipment. The large area tracking is performed by different kinds of detectors: two types of drift chambers, Saclay Drift Chambers (SDC) around SM1 and large drift chambers (W 4-5) further downstream behind SM2. Straw tubes provide tracking behind SM1 and SM2 and Multi-Wire Proportional Chambers (MWPC) act as backbone of the small angle spectrometer.

3.4.2 Particle Identification

The detectors presented up to now are used for track reconstruction. Knowing the bending power of the spectrometer magnets, the momentum of a charged particle can be determined from its track. To distinguish between different types of particles, a measurement of velocity or energy is needed or certain properties of some particle types have to be utilised. At COMPASS muon filter fulfil muon identification, hadronic calorimeters are used to discriminate hadrons from muons

and a Ring Imaging Cherenkov Detector can be used to measure the particle velocity. The RICH allows for the separation of the different types of hadrons, but this kind of particle identification is not used in this analysis.

Table 3.1: Tracking detectors in the COMPASS spectrometer as they have been used in 2003 and 2004.

detector	no of stations projections	resolution	efficiency	size deadzone
VSAT				
SciFi	8	350-500 ps	99%	$(5\text{-}10)^2\,\mathrm{cm}^2$
[92, 93, 94, 95]	21	130-250 μm		no
Silicon	3	9 - 14 μm	99%	$5\times7\,\mathrm{cm}^2$
[96, 97, 98]	12			no
SAT				
GEM	10 (2004: 11)	70 μm	97%	$31\times31\,\mathrm{cm}^2$
[99, 100, 101]	40 (2004: 44)			$\oslash$ 5 cm
MICROMEGA	3	9.4 ns	97%	$40\times40\,\mathrm{cm}^2$
[102, 103, 104]	12	90 μm		$\oslash$ 5 cm
LAT				
Drift-chamber	3	220 μm	97%	$120\times120\,\mathrm{cm}^2$
[105, 106]	12			$\oslash$ 40 cm
W 4-5	4 (2004: 6)	500 μm	90%	$2.6\times5.2\,\mathrm{m}^2$
[107, 108]	16 (2004: 24)			$\oslash$ 1 m
Straw	4	250 μm	>90%	$3.2\times2.8\,\mathrm{m}^2$
[109, 110]	15			$20\times20\,\mathrm{cm}^2$
MWPC	11	700 μm	99%	$150\times120(92)\,\mathrm{cm}^2$
[92]	34			$\oslash$ 16 cm - 22 cm

μ Identification

In both spectrometers the muon identification is performed with so-called muon filters. Large drift detectors are grouped around or behind large hadron absorbers (hadron absorber 1 (60 cm iron) and hadron absorber 2 (2.4 m concrete) in Fig. 3.7). Hadrons are stopped in the iron or concrete, if they have not already been stopped in the hadronic calorimeters in front of the absorbers. Only muons reach the detectors behind the absorber walls. In the first spectrometer Iarocci tubes [111] of $4\times2\,\mathrm{m}^2$ size are used. In the second spectrometer aluminium drift tubes of 3 cm diameter are operational. Both detectors have a relatively coarse space resolution but are sufficient to decide if a muon has passed or not.

Calorimetry

The COMPASS spectrometer is equipped with two hadronic calorimeters, and in the final layout, also two electromagnetic calorimeters are foreseen. One of the electromagnetic calorimeters (ECAL2) is already installed, however it has only been partly equipped with readout electronics. The two hadronic calorimeters, HCAL1 and HCAL2, are placed in the rear of the two spectrometer stages. In addition to the discrimination between hadrons and muons, the hadronic calorimeters are used to trigger events with hadrons in the final state (cf. Section 3.4.3).
Both hadronic calorimeters are iron-scintillator sampling calorimeters. HCAL1 consists of 40 layers of 20 mm thick iron and scintillators of 5 mm thickness [112]. The light from the scintillator is collected by a wavelength-shifting light-guide placed directly on the open sides of the scintillators that are read out by PMTs. HCAL1 consists of 480 modules ($15\times15\,\mathrm{cm}^2$, 4.8 interaction length) assembled in a $4.2\times3\,\mathrm{m}^2$ matrix with a central hole of $1.2\times0.6\,\mathrm{m}^2$. 12 modules were removed from each corner. HCAL2 is made out of 216 cells ($20\times20\,\mathrm{cm}^2$) in a matrix of 10 rows and 22 columns. The 2×2 cells hole is not centred but moved 20 cm towards Jura taking into account the beam deflection. The energy resolution of HCAL1 is

$$\frac{\sigma_{had}(E)}{E} = \left[\frac{59}{\sqrt{E}} + 8\right]\%$$

with a spatial resolution $\sigma_{x,y} = 14 \pm 2\,\mathrm{mm}$. HCAL2 reaches

$$\frac{\sigma_{had}(E)}{E} = \left[\frac{65}{\sqrt{E}} + 4\right]\%.$$

The calorimeters are shielded either with lead walls or, in case of HCAL2, with ECAL2 to avoid electromagnetic contamination.

3.4.3 The Trigger

The trigger handles the selection of event candidates in a high rate environment [113]. It has to decide within 500 ns and a minimal dead time if an interesting scattering event has occurred and then trigger the readout of the detectors. Additionally, it has to provide an event time to unambiguously associate the event with the incident muon.

The trigger is based on the detection of the scattered muon. Therefore four groups of two scintillator hodoscopes are placed in the small angle spectrometer as illustrated in Fig. 3.8. Their resolution and granularity are adapted to the rates expected in their region of operation (in analogy to the granularity of the tracking devices used in the spectrometer). The trigger has been optimised to select two classes of scattering events

- Quasi-real photon events
- DIS events

Quasi-real Photon Events

Events with small virtual 4-momentum transfer are selected to account for the rise of the open charm cross section with decreasing Q^2. To ensure a hard scale by a large invariant mass $\hat{s}$ of the partonic system, the relative energy loss of the scattered muon y has to exceed a certain value independent of the 4-momentum transfer Q^2. This led to the development of the energy loss trigger which selects events exceeding y_{min}. It uses the direction of the scattered muon track behind SM2 in the bending plane of the spectrometer. Two vertical hodoscopes with distances z_4, z_5 from the target measure the vertical positions x_4, x_5 of the deflected track (Fig. 3.8). Knowing the bending power of the magnets, the momentum of the scattered muon can be determined [114]. The energy loss trigger detects scattered muons with given minimum energy loss at scattering angles down to zero. It consists of two parts

- Inner Trigger ($0.2 < y < 0.5$)
- Ladder Trigger ($0.5 < y < 0.9$)

The Inner Trigger covers the threshold region which requires a good resolution and therefore has a fine grained structure. The Ladder Trigger covers larger angles.

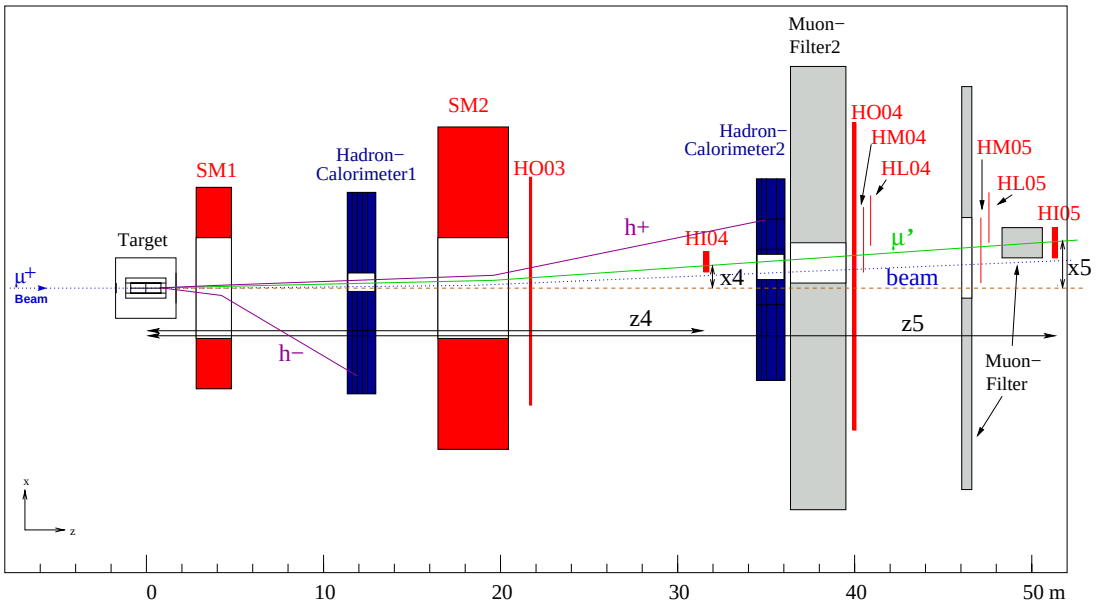

Figure 3.8: Principle of the energy loss trigger. The beam (blue, dotted) passes through the holes of the calorimeters and hadron absorbers without touching the trigger hodoscopes (outer and middle trigger have corresponding holes in their acceptance). The scattered muon (μ', continuous green line) hits the Inner Trigger hodoscopes HI04 and HI05 in the positions x4 and x5, respectively. With the knowledge of the distances z4 and z5 of the hodoscopes to the target, the momentum of the scattered muon can be determined [114]. Muons in the hodoscopes HL04 and HL05 as well as in the vertical part of the Middle Trigger (HM04 and HM05) are treated analogously. The horizontal slabs of the Middle Trigger and the Outer Trigger (HO03 and HO04) act as DIS trigger as described in the text.

The DIS Trigger

Deep inelastic scattering events with large 4-momentum transfer Q^2 are selected by larger hodoscopes. The maximum Q^2 is limited by the aperture of SM2. The DIS trigger is based on the fact that the scattered muon track points to the target. Therefore horizontal scintillator hodoscopes are used which give direct access to the scattering angle since there is no deflection caused by the spectrometer magnet in this direction. The Middle Trigger and the Outer Trigger hodoscopes are mainly used to trigger DIS events. The Middle Trigger consists of vertical as well as horizontal slabs and can thus be used for quasi-real photon and DIS triggering. The Outer Trigger consists of horizontal slabs and therefore only performs target pointing. To reject hadrons and electrons, absorbers are placed in front of the hodoscopes for all trigger types.

The Calorimeter as Part of the Trigger

In addition to the trigger hodoscope, signals of the calorimeter can be used to select events with hadrons in the final state by requiring cluster with an energy greater than the energy deposited by a muon. This makes use of the fact, that a hadron shower is laterally spread out over several calorimeter modules and deposits most of its energy in the calorimeter. On the contrary, a muon is a minimum ionising particle and leaves a small signal just along the track. The calorimeter requirement in the trigger rejects background from muon-electron scattering, radiative events as well as events from beam halo tracks since no forward hadrons are associated to these events. The calorimeter is practically demanded for all types of trigger. For the Middle Trigger in addition to the semi-inclusive trigger, an inclusive trigger without calorimeter is used as well.

To access regions of very high Q^2, where the scattered muon angle is larger than the hodoscope system can manage, a standalone Calorimeter Trigger can be used independently of the hodoscope system. Here the threshold for the energy deposited in the calorimeter is higher than it is in combination with a hodoscope trigger.

The Veto

The production mechanism of the secondary muon beam makes a halo of muons around the nominal beam with momentum deviating from the nominal beam momentum unavoidable. To reject events that might be triggered by halo muons in the hodoscopes, a veto system upstream of the target has been installed. It leaves the central region around the nominal beam uncovered and checks whether the track will pass the target. Demanding the absence of a veto signal for the trigger reduces the rate for the inclusive Middle Trigger (i.e. MT without calorimeter signal) down to 4% of the rate without veto requirement.

The Trigger Matrix

The trigger system is realised using the so-called trigger matrix that selects the combinations of hodoscope slabs of a system that fired in coincidence. Fig. 3.9 illustrates that only a muon coming from the target fulfils the matrix condition, while for a halo muon there is no coincidence between the two trigger hodoscopes. For Inner, Middle and Ladder Trigger in addition a certain amount of energy in the calorimeter is required. In Table 3.2 an overview of the trigger configurations with the combinations of hodoscopes, calorimeter and veto is given. The overall trigger efficiency is close to 100% with 99% for Inner and Ladder Trigger, 97% for Middle and 96% for the Outer Trigger.

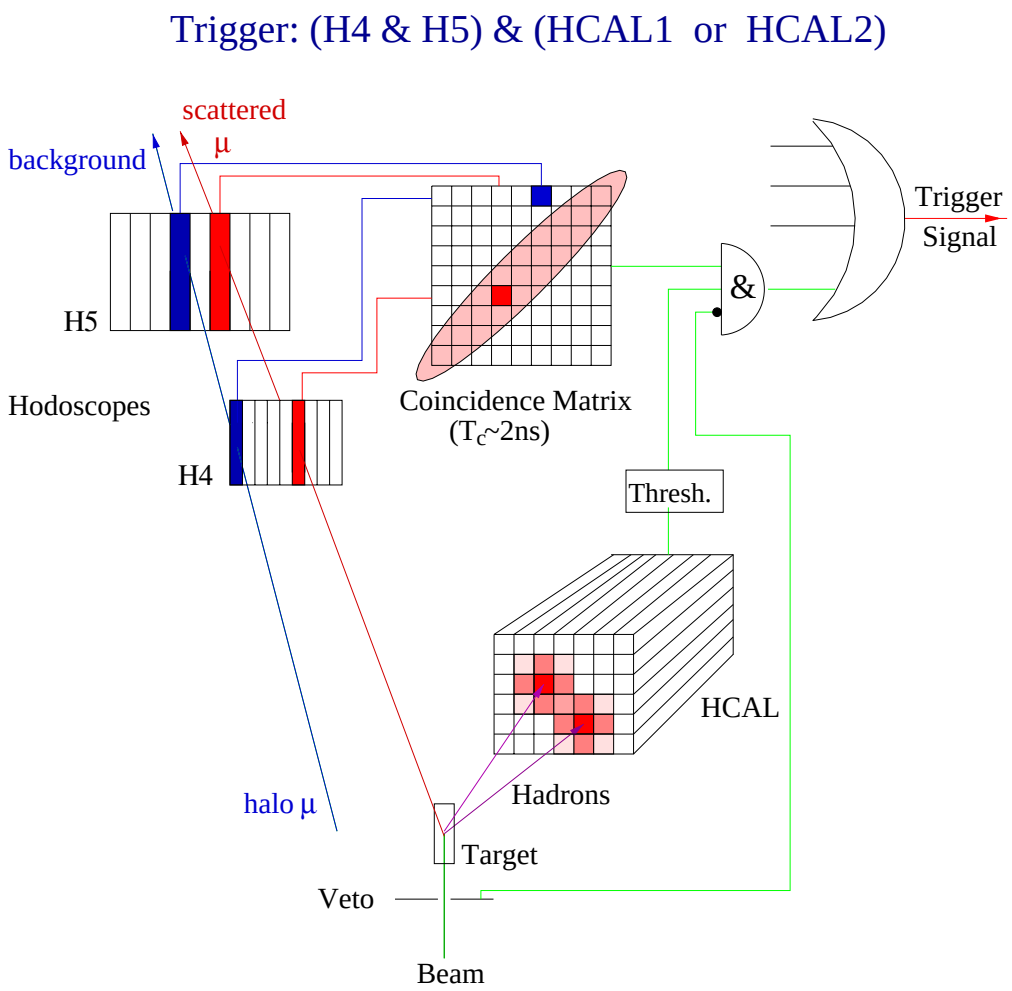

Figure 3.9: The trigger matrix. A scattered muon coming from the target hits two slabs of the hodoscopes H4 & H5. Their signals are combined in the coincidence matrix and fulfil the matrix condition (i.e. target pointing, indicated by the ellipse), whereas a halo muon does not match the matrix condition. For semi-inclusive triggers the matrix signal is given to a coincidence unit together with the calorimeter signal to create the trigger signal.

3.5 The Data Acquisition

The COMPASS spectrometer has a pipelined readout architecture to cope with the large number of channels and the high trigger rates. More than 200000 channels have to be read out, the average event size is $\sim 40\,\text{kByte}$ at a trigger rate of 5-10 kHz ($>$ 20k triggers per spill). Therefore the data acquisition has to have a negligible dead time (compared to the detector's dead time) and to be capable of recording up to several hundred MByte of data per second on tape. The data collected by the experiment add up to $\sim 300\,\text{TByte}$ per year.

To handle these data streams, the detector response is digitised already at the front-end boards on the detector itself using ADCs[4] or, in case of time measurements, the F1-TDC[5], developed in Freiburg [115]. From here the data are send through the full readout chain up to the recording by pushing the data only without handshake. From the front-end boards the data are transferred to the central readout driver via standard Ethernet cables or optical fibres. The central readout drivers for most of the detectors are the COMPASS Accumulate, Transfer and Control Hardware (CATCH), except for GEM and Silicon detectors, where

[4]Analog to Digital Converter
[5]Time to Digital Converter

Table 3.2: Trigger configurations as they are used during data taking. Different combinations of hodoscopes, calorimeters and vetos lead to the five mainly used triggers: Inner Trigger (IT), Ladder Trigger (LT), Middle Trigger (MT), Outer Trigger (OT) and Calorimeter Trigger (CT). For the standalone calorimetric trigger a higher threshold for the energy deposited in the calorimeter is applied. The veto combination of a part of V_1 and V_{bl} as applied for the Ladder Trigger, leads to a smaller reduction of the rate than V_1, V_2 and V_{bl} but also to a smaller dead time. The inclusive Middle Trigger (iMT) is similar to the Middle Trigger but does not require an energy deposition in the calorimeter.

	hodoscope	calo	V_1	V_2	V_{bl}
IT	HI04 & 05	yes	no	no	no
LT	HL04 & 05	yes	partly	no	yes
MT	HM04 & 05	yes	yes	yes	yes
OT	HO04 & 05	no	yes	yes	yes
CT	no	yes	yes	yes	yes
iMT	HM04 & 05	no	yes	yes	yes

GeSiCA (GEM Silicon Control and Acquisition) [116] are used. The CATCH module [115, 117, 118] is a VME module acting as an interface between front-end boards and the readout computers. It allows fast readout of the front-ends, performs local subeventbuilding and concentrates the data into few high bandwidth streams (160 MByte/sec/CATCH). In addition the CATCH initialises all front-ends at startup and distributes the trigger signal it receives from the Trigger Control System (TCS) [116] to the front-end boards. The data from the CATCH are guided through the readout chain while further triggers can be accepted. The data buffering at various stages minimises the dead time and avoids data losses. The modular design makes the system easily scalable and up-gradable. In 2004 138 CATCH and 10 GeSiCA were used for the readout of more than 60 detectors with about 300 detector planes.

From the CATCH the data are transferred via optical fibres using the S-Link protocol to the spill buffers (each with 512 MB RAM) [119, 120]. They are located inside the readout buffer computers (ROB), where the data of several detector planes for one event is combined, consistency checks and subeventbuilding are performed. Via Gigabit Ethernet the data are transferred to the eventbuilders. Here the data from all ROB are combined to the full events, transferred to the Central Data Recording (CDR) at the CERN main site and copied on tape for long term storage. The data receiving, processing and transferring from the CATCH to the spill buffers happens only on-spill. During the spill break the data transfer from the spill buffers via the ROB to the eventbuilders and from there to the CDR continues, to optimise the data flow. Fig. 3.10 illustrates the data flow through the readout chain. A detailed description of the DAQ and the readout of the different detectors can be found in Refs. [117, 118].

Online Monitoring

To ensure the proper functionality of the detectors, the readout electronics and the data acquisition, several monitoring tools are used.

- MURPHY TV (MTV) exemplary checks the data stream from one eventbuilder for consistency [121]. It is checked that e.g. the event numbers transferred from the CATCH match or that the event has the correct timestamp. Error words generated on the CATCH/GeSiCA will show up here. MTV allows to check if everything that has been recorded on the front-end boards contains all necessary information without any errors and has found the correct way through the readout chain.
- COOOL (COMPASS Object Oriented Online) goes one step further and uses the available mapping information, that connects the hardware address with

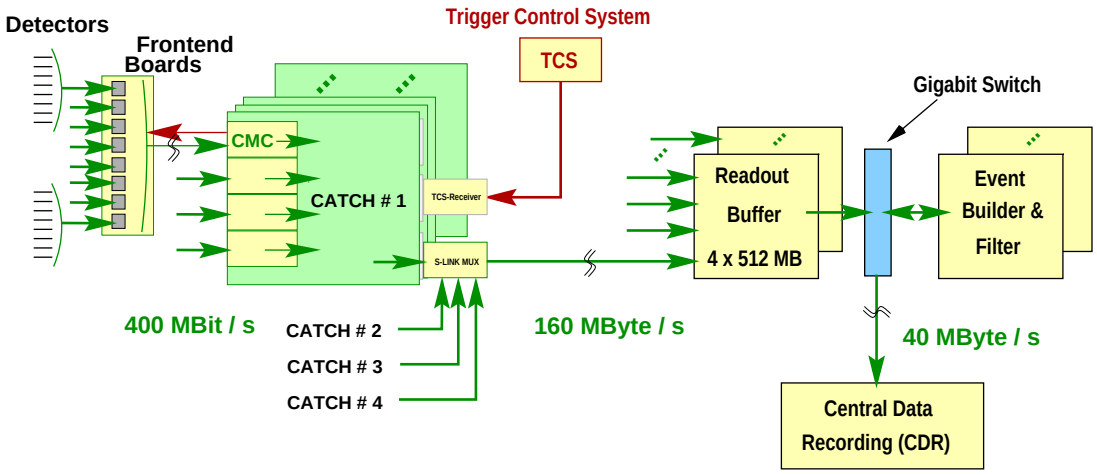

Figure 3.10: Illustration of the COMPASS readout system. The data flow is from left to right as described in the text [117].

e.g. the wire position of the corresponding detector channel, to decode the data and to histogram it [122]. The so created hit maps and time spectra of the detectors can be monitored quasi online and compared to reference files.

- The DCS (Detectors Control System) monitors everything from temperature over gas flows through the detectors to high voltages and low voltages needed for the readout electronics. The system allows for an immediate reaction to problems and an offline analysis of all monitored quantities.

The continuous use of these tools by the shift crew ensures smooth data taking. The behaviour of the DAQ and problems that appeared during data taking are documented, partly with the help of the above mentioned tools, in an electronic logbook [123].

Chapter 4

The Monte Carlo Simulation

4.1 Why a Monte Carlo Simulation?

For the determination of the gluon polarisation $\Delta G/G$ with high-p_t hadron pairs at COMPASS, it is extremely important to know the contributions from the different physics subprocesses to the measured asymmetry (cf. Section 2.7). Since it is not possible to disentangle these processes by their signatures in the data, a Monte Carlo simulation is used.

The simulation has to model the physics processes and the detector response which requires a detailed knowledge of the physics involved. On one hand the production of the particles in the primary interaction (i.e. a lepton on a fixed deuteron target) and their eventually following decay has to be understood. On the other hand all these primary and secondary particles pass through the detector, interact with matter and thus leave their marks. These are the two main parts of the simulation and they can be done independently. Section 4.2 deals with the simulation of the physics processes using Monte Carlo generators and Section 4.3 treats the detector simulation.

The complete Monte Carlo chain (Fig. 4.1) consists of a Monte Carlo generator like Pythia [124] or Lepto [68] simulating the physics processes, followed by a detector simulation, COMGeant [125], that provides an output in the similar format as for the real data, so that the reconstruction can be performed analogously.

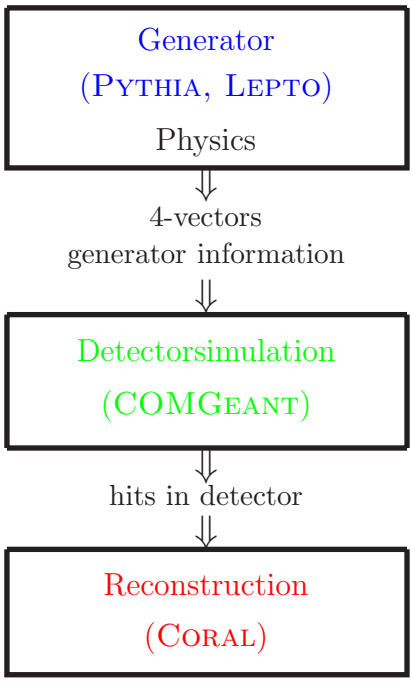

Figure 4.1: The three components of the Monte Carlo generation chain: physics and detector simulation are followed by the event reconstruction.

4.2 Simulation of Physics Processes

4.2.1 The Principle of Monte Carlo Generators

The description of a physical process like deep inelastic lepton-nucleon scattering is based on the factorisation of the different contributing subprocesses. This means that hard (short range) and soft (longer range) processes can be treated separately. Hard processes are described using perturbative QCD, the soft parts are treated with phenomenological models. Figure 4.2 illustrates the factorisation of the DIS process into the different contributions:

(A) Emission of a virtual photon by the incoming lepton which can be calculated in QED using the lepton tensor $L_{\mu\nu}$ introduced in Section 2.3.

(B) Hard scattering process of the virtual photon and a parton inside the nucleon which can be calculated in QED and QCD as well, cf. Section 4.2.2.

(C) Parton distribution functions of the nucleon. They give the probability of

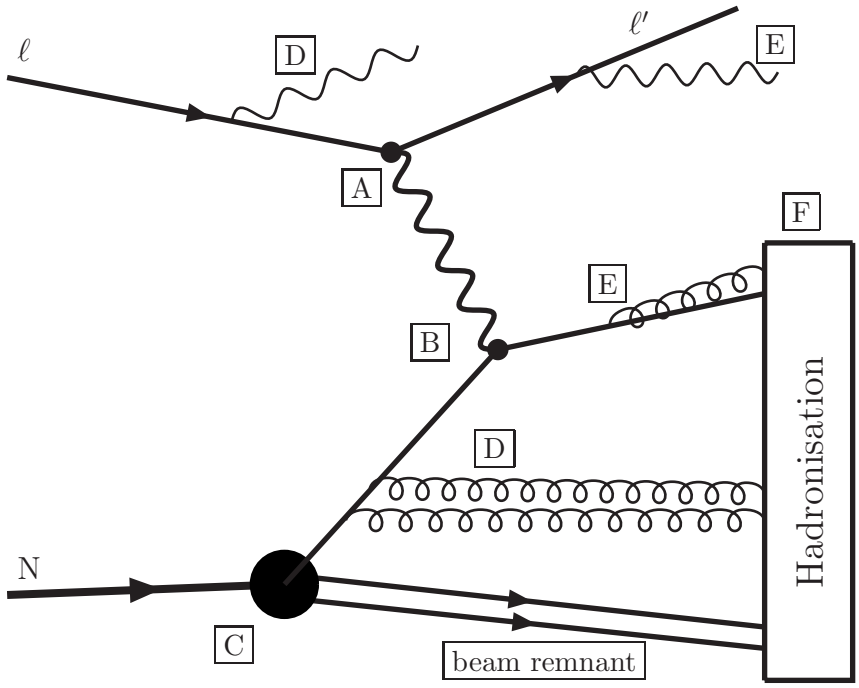

Figure 4.2: Factorisation of the DIS process in the Monte Carlo generator. The different subprocesses A - F are described in the text.

the momentum fraction of the nucleon carried by the struck quark. They cannot be calculated from first principles but must be determined from data, cf. Section 4.2.3.

(D/E) Initial and final state radiation. Initial parton showers will evolve the partons using the DGLAP equations up to the scale of the hard interaction. Similarly for outgoing partons. Electroweak radiative corrections for the lepton are treated separately (cf. Section 4.2.5).

(F) Hadronisation process, which can be divided into the fragmentation of the coloured quarks into colour neutral particles and their eventual decay into stable particles, cf. Section 4.2.4.

For all the contributions (A)-(F) the underlying physics is based on quantum mechanical processes and therefore shows some probabilistic behaviour. The Monte Carlo technique has to imitate this statistical behaviour. A parton distribution or a differential cross section can be seen as a probability distribution in several kinematic variables. Similarly for a fragmentation function $D(z)$, where the probability to have a certain value in a small interval dz around z is proportional to $D(z)dz$. A random generator is used to select phase space points and generate

events according to these distributions.

The Monte Carlo generator used for the analysis presented is LEPTO. Another widely used generator is PYTHIA. A very detailed and extensive information on Monte Carlo techniques is found in the PYTHIA manual and the references therein [124]. In this section only some of the topics relevant for this analysis will be introduced.

4.2.2 The Hard Scattering Process (B)

In deep inelastic lepton-nucleon scattering, the leading order hard scattering process is the absorption of the virtual photon by a quark ($\gamma q \rightarrow q$) inside the nucleon that is then kicked out. In first order QCD, the gluon radiation or QCD-Compton process ($\gamma q \rightarrow qg$) and the photon-gluon fusion process ($\gamma g \rightarrow q\bar{q}$) appear and can be included in the cross section, cf. Section 2.7, Figure 2.16. These three hard processes are included in the LEPTO generator which can be used in a kinematic region of $Q^2 > 1\,(\mathrm{GeV/c})^2$. PYTHIA is suitable for a much larger kinematic region, for COMPASS it is especially interesting for low Q^2 since about 90% of the data are below $Q^2 = 1\,(\mathrm{GeV/c})^2$. Covering also the transition region between DIS and real photon scattering, PYTHIA models not only the three hard scattering processes described above, but also interactions where the photon does not behave like a pointlike particle (beside many more processes not of interest for this analysis).

Nevertheless PYTHIA cannot be used alone for the analysis of $Q^2 > 1\,(\mathrm{GeV/c})^2$ data since problems in the description of the hard scattering processes occur: Comparing the cross section for PGF in LEPTO and PYTHIA for $Q^2 > 1\,(\mathrm{GeV/c})^2$ reveals that the cross section in PYTHIA falls much steeper with Q^2 than in LEPTO. The reason for this is that PGF-events are not labelled as such but as leading order events if the corresponding Q^2 of the event is larger than the p_t of the involved partons [126]. It is not possible to distinguish between real leading order events and renamed PGF-events without major changes in the generator. This does not have an influence on the total cross section in PYTHIA but on the identification of the hard scattering process of the event.

Therefore two complementary analyses are performed in COMPASS. For the analysis of the region $Q^2 < 1\,(\mathrm{GeV/c})^2$ PYTHIA is used for the Monte Carlo generation [127]-[129]. In the analysis presented in this thesis, data with $Q^2 > 1\,(\mathrm{GeV/c})^2$ are analysed. Therefore LEPTO is used for the Monte Carlo simulation.

4.2.3 Parton Distribution Functions (C)

The parton distribution function $q_f(x, Q^2)$ describes the probability to find a parton q of flavour f with a fraction x of the total momentum of the nucleon at a scale Q^2. The absolute form of parton distribution functions cannot be determined in perturbative QCD but rather has to be parametrised at some scale Q_0^2 from experimental data. The Q^2 dependence is then perturbatively calculated using the DGLAP equations (Section 2.4.1 and 2.5.2). From the evolution of the structure functions the gluon distribution can be determined. Input data are taken from lepton-nucleon fixed target experiments and electron-proton as well as proton-(anti)proton collisions at colliders.

The evaluation for the parton distribution functions is usually done in next-to-leading order. Since only Born-level matrix elements for the hard scattering processes are included in the Monte Carlo generators, it is sufficient to use the leading order calculations for the parton distribution functions, however, this approach is only good to leading order accuracy. Some of the higher order corrections are effectively included in the parton-shower treatment.

Figure 4.3 shows the distributions for up, down and strange quarks, and gluons for the GRV98 [130] and CTEQ5 [131] parametrisations in leading order as a function of the quark and gluon momentum fraction x_{Bj} and x_G, respectively.

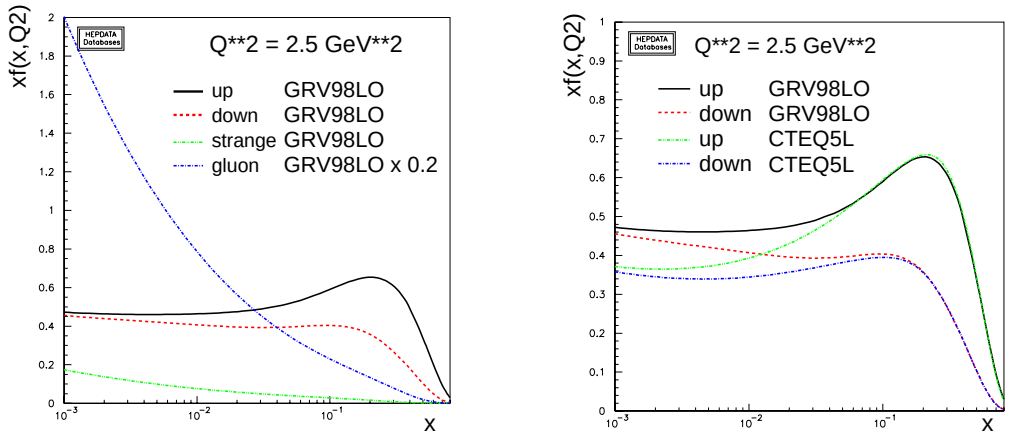

Figure 4.3: GRV98LO [130] and CTEQ5L [131] parton distribution functions. Left: up, down and strange quarks and gluons (multiplied by 0.2) obtained with the GRV98LO parametrisation at Q^2 =2.5 $\mathrm{GeV}^2/\mathrm{c}^2$. Right: Comparison between GRV98LO and CTEQ5L for up and down quark distributions.

4.2.4 Fragmentation (F)

The particles emerging from the hard scattering process are quarks and gluons (cf. Section 4.2.2). Because of colour confinement they are not observed as single quarks or gluons but as baryons and mesons and their decay products. The transition from the stage of quarks and gluons to the stage of hadrons is called fragmentation. The process of fragmentation can only be described through phenomenological models. Fragmentation functions give the probability of finding a hadron emerging from a quark or gluon, cf. Section 2.6.

For the description of the hadronisation process the widely used Lund string model [67], has been utilised for this analysis. In this model the outgoing partons, are connected by a massless relativistic string representing a one dimensional colour flux tube as sketched in Fig. 4.4. Because of the gluon self-coupling, the colour flux lines will not spread out over all space but rather be constrained to a thin tube like region. The colour flux tube contains a constant amount of field energy per unit length. The string constant κ, representing the energy per unit length of the tube, is known phenomenologically to be $\kappa \approx 1\,\mathrm{GeV/fm}$. As the q and $\bar{q}$ move apart, the potential energy stored in the string increases, the string may break and new $q\bar{q}$-pairs can be created from the available field energy within this tube. The original system breaks into smaller and smaller pieces until only ordinary hadrons remain.

Fig. 4.5 illustrates the string breaking of the colour flux between q and $\bar{q}$ with the creation of the new $q_1\bar{q}_1$-pair, such that a meson $q\bar{q}_1$ can be formed, the scaled down version of the string between $\bar{q}$ and q_1 and the further creation of new $q_i\bar{q}_i$-pairs in an interative procedure until the last two hadrons are formed. Classically the two quarks of the $q_i\bar{q}_i$-pair must be produced at a certain distance so that the field energy in between them can be used for the mass production. Quantum mechanically the quarks may be created at the same point with local flavour

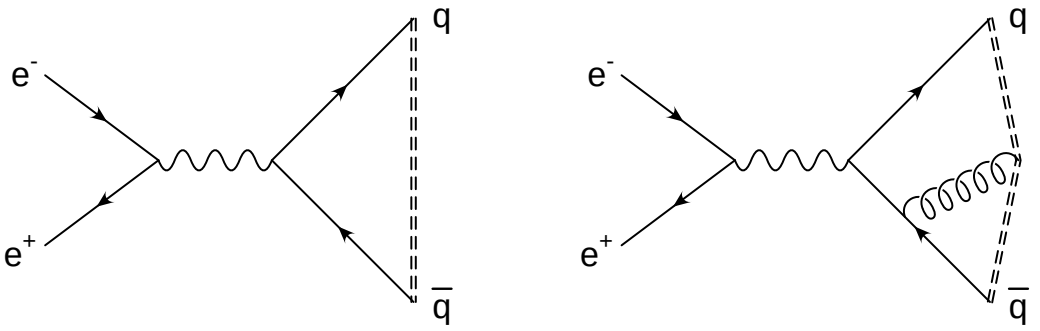

Figure 4.4: String Fragmentation in $e^+e^- \to q\bar{q}$. The string (dashed line) is stretched between a quark and an antiquark. Gluons emitted from one of the quarks appear as kinks in the string.

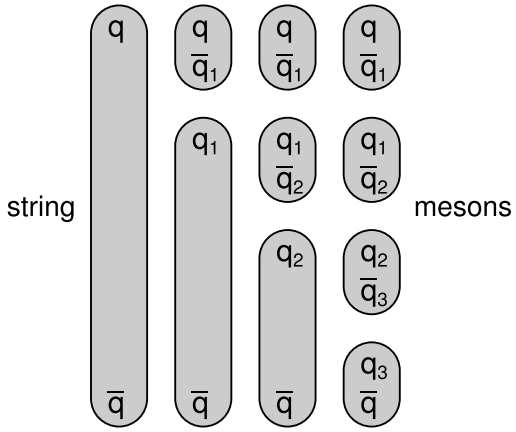

Figure 4.5: Iterative string fragmentation into hadrons. The string breaking continues as long as enough energy for the prodution of new $q\bar{q}$ pairs is available.

conservation and then tunnel out to the classically allowed region. For $q_i\bar{q}_i$-pairs generated in a tunneling process the production probability is

$$\exp\left(-\frac{\pi m_\perp^2}{\kappa}\right) = \exp\left(-\frac{\pi m^2}{\kappa}\right)\exp\left(-\frac{\pi p_\perp^2}{\kappa}\right) \tag{4.1}$$

with the mass m of the produced quark and antiquark and their transverse momenta $p_\perp$ relative to the string. Since the string is assumed to have no transverse excitations, the $p_\perp$ is locally compensated between the quark and antiquark of the pair. This leads to a flavour independent gaussian spectrum for the $k_\perp$ of the produced hadrons (i.e. the $q_i\bar{q}_j$-pairs) with a width $\sigma_{k_\perp} \approx 0.36\,\mathrm{GeV/c}$ (parameter PARJ(21) in JETSET [132, 124]). In practice there are non-gaussian tails to this shape which are modelled by a second broader gaussian that is added to the above. The width of the second gaussian is a factor PARJ(24) (=2, default value) broader than the first one and the fraction of admixture is PARJ(23) (=0.01, default value). The tunneling picture also implies a suppression of heavy quark production, $u : d : s : c \approx 1 : 1 : 0.3 : 10^{-11}$.

The two Monte Carlo generators PYTHIA and LEPTO can both use the LUND fragmentation implemented in JETSET. Equation (4.1) for the fragmentation probability is the basis for the LUND string fragmentation function for a hadron with longitudinal energy fraction z which is implemented in JETSET in the following form:

$$f(z) \propto \frac{1}{z}(1-z)^a \exp\left(-\frac{bm_\perp^2}{z}\right), \tag{4.2}$$

where the free parameters a (PARJ(41) = 0.3, default value) and b (PARJ(42) =

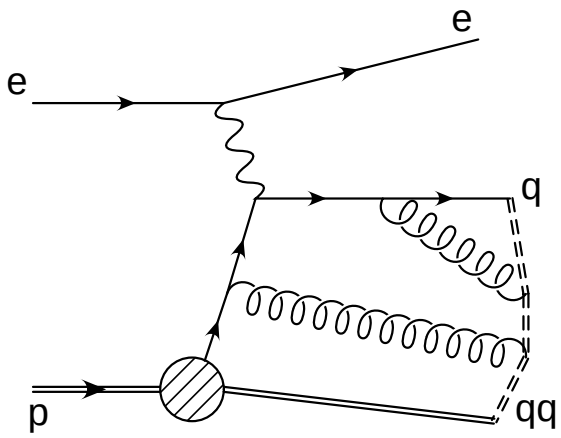

Figure 4.6: Hardronproduction in a DIS event. A quark is hit by the virtual photon and kicked out of the nucleon, then the remnant is treated as a diquark configuration and the string is stretched between the diquark and the struck quark.

$0.58\,\mathrm{GeV}^{-2}$, default value) have to be adjusted from data.

The generation of baryons can also be explained by a tunneling mechanism. In the simplest approach diquarks instead of quarks are produced in the string. A more sophisticated model is the popcorn scenario, where quarks and antiquarks are produced one after the other and baryons appear from the succesive production of several $q_i\bar{q}_i$-pairs [133].

Hadronproduction in DIS (Fig. 4.6) is analogous to the e^+e^- case since the fragmentation is universal [134]. The development depends on the struck quark only. In case a quark is hit by the virtual photon, the rest of the nucleon is treated as diquark. If a gluon is hit, a quark-diquark configuration is used.

4.2.5 Radiative Corrections (D/E)

In every process that contains coloured or charged objects in the initial or final state, gluon or photon radiation may give large corrections to the overall topology of the event. The structure is given in terms of branchings $a \to bc$, e.g. $e \to e\gamma$, $q \to qg$ or $g \to q\bar{q}$. In a DIS process there can be QED radiation on the lepton side as well as QCD corrections to the struck quark which emits partons before and after the boson-quark vertex.

The QCD radiation is treated in the parton shower approach that is implemented in Lepto and Pythia. For instance a parton close to the mass shell in

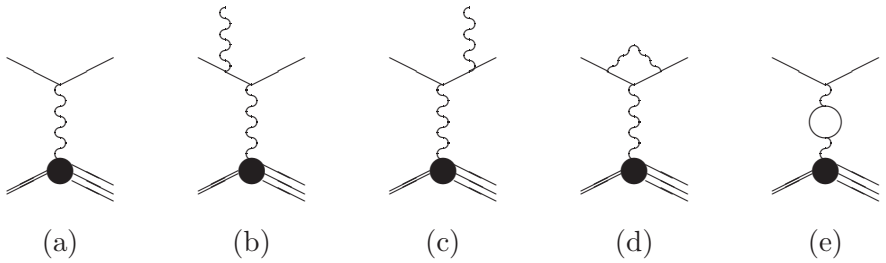

Figure 4.7: Feynman diagrams contributing to the Born and the radiative correction cross sections in lepton-nucleus scattering.

the incoming nucleon can emit parton showers and becomes a space-like quark. Then it interacts with the electroweak boson and turns into an outgoing quark. If it is not on-shell after the scattering process, it will produce final state parton showers until it is essentially on-shell. This behaviour simulates higher order effects.

Electroweak radiative corrections are not included and are added using RADGEN [135], a Monte Carlo generator for radiative events in DIS.

QED corrections using RADGEN

The QED radiative correction to the lepton-photon vertex originate from two different types of processes, namely real photon emission and loop corrections. The Feynman diagram for the Born process (one photon exchange) is presented in Fig. 4.7 (a). The radiative QED corrections at the lowest order are described by the set of Feynman diagrams shown in Fig. 4.7 (b) - (e). Diagrams (b) and (c) show the radiation of a real photon off the incoming and the outgoing lepton, respectively. The diagrams (d) and (e) come from vertex and loop corrections. They origin from the exchange of an additional virtual photon and vacuum polarisation effects.

The photon radiated in (b) and (c) could in principle be detected, whereas no additional particle is radiated in (d) and (e). Thus the last two diagrams can interfere with the Born matrix elements. The diagrams (b) and (c) may interfere with each other as well. For the Born diagram the kinematics is completely defined by the scattering angle θ and E'. If an event contains a real hard radiated photon, the kinematic variables describing the virtual photon and used to generate the final hadronic state differ from what has been presented in Section 2.2, Table 2.1, for the Born diagram (Fig. 4.7 (a)). The substitution for the exchanged momentum $q \rightarrow q - k_{RC}$, where k_{RC} is the real photon momentum, has to be made. The

invariant mass of the γ^*-nucleon system after the radiation is

$$W^2_{true} = W^2 - 2E_\gamma(\nu + M - \sqrt{\nu^2 + Q^2}\cos\theta_\gamma), \tag{4.3}$$

where θ_γ is the angle between the real (k_{RC}) and virtual (q) photon momenta. E_γ is the photon energy. The *true* Q^2 is

$$Q^2_{true} = Q^2 + 2E_\gamma(\nu - \sqrt{\nu^2 + Q^2}\cos\theta_\gamma). \tag{4.4}$$

This means that the kinematic variables which are calculated from the kinematics of the incoming and outgoing lepton, differ from the *true* kinematics. For a comparison of the data to the Monte Carlo simulation, this can be corrected either by estimating the smearing of the variables due to the radiation effects or by including these effects in the Monte Carlo, i.e. generating also events with radiative corrections, so that the simulation can be compared to the data directly.

In this analysis RADGEN is used to calculate the radiative corrections for the events that were generated with LEPTO according to their cross sections. For the analysis presented in this thesis the final high-p_t sample contains approximately 6% of events where radiative corrections were applied.

4.3 Detector Simulation & Reconstruction

The Monte Carlo generators LEPTO and PYTHIA provide as output the information of momentum, energy and identity of the produced particles as well as information about the simulated process, e.g. which hard scattering process took place and the cross section. The detector simulation has to translate these four-vectors into a detector response resulting in hits in the trackers, energy deposition in the calorimeters and RICH information. Eventual decays of short-living particles inside the detector volume and their decay products have to be taken into account as well. COMGEANT, the program used for the COMPASS detector simulation is based on Geant3 [136, 137]. Geant is a software package composed of tools which can be used to accurately simulate the passage of particles through matter. All aspects of the simulation process have been included in the toolkit, e.g. the geometry of the system and the materials involved, the tracking of particles through these materials and electromagnetic fields present in the detector. This includes physics processes of the particles interacting with the detector materials and also the response of sensitive detector components. For example multiple scattering has to be simulated correctly, the interaction of particles in the calorimeter or the movement of the particles through target and spectrometer magnets has to be described.

COMGEANT is an interface to Geant3 using all its features and providing an output equivalent to the raw data format with all the detector information. Within COMGEANT the COMPASS detector volumes, materials and magnets can be defined which then are used by Geant. It allows also for the description of the trigger by combining relevant trigger hodoscopes and eventually the calorimeter as well as the trigger matrix (cf. Section 3.4.3). The output of COMGEANT in the form of hits in detectors etc. has a similar format as the real data. It includes some additional information specific for the Monte Carlo, e.g. detector efficiencies and resolutions, that are only taken into account when reconstructing the Monte Carlo data and not already in COMGEANT. The Monte Carlo data are then reconstructed analogously to the real data using the COMPASS analysis framework CORAL [138].

Chapter 5

High-p_t Selection and Asymmetry Extraction

5.1 Outline of the Data Analysis

For an accurate determination of the gluon polarisation it is mandatory to select an event sample with a large fraction of photon-gluon fusion events. Since these kind of events directly probe the gluons inside the nucleon, they have to be enriched compared to the background by requiring hadrons pairs with large transverse momentum. The exact fraction of photon-gluon fusion events is determined with a Monte Carlo simulation.

The analysis is separated in two parts. The first part contains the analysis of the measured data and the extraction of the high-p_t photon-nucleon asymmetry. The second part consists of the Monte Carlo simulation that gives the ratio of photon-gluon fusion events and allows the determination of the gluon polarisation $\Delta G/G$. In this chapter, I will illustrate the path from the reconstructed muon-nucleon scattering data to the high-p_t asymmetry that enters into the $\Delta G/G$ extraction. The Monte Carlo simulation and the extraction of $\Delta G/G$ are dealt with in the next chapter.

The first step is the data selection based on data quality criteria. This is followed by an event selection, that on one hand chooses events containing high-p_t candidates and on the other hand ensures that only events enter which can be used for a proper asymmetry calculation (Section 5.2). Based on this primary selection the so-called high-p_t cuts are applied. This event sample contains a large fraction of photon-gluon fusion events and thus can be used for the extraction of the high-p_t asymmetry. The asymmetry extraction from this sample is presented

in Section 5.3. Due to variations in the performance of the spectrometer false asymmetries can appear. They are part of the systematic errors that are treated in Section 5.4.

5.2 Data Selection

The analysis covers the data taken with the COMPASS spectrometer in the years 2002 and 2003 with longitudinally polarised target. These were about 40 days of data taking in 2002 and about 60 days in 2003. Due to higher trigger rates and higher spectrometer efficiency, the average amount of data recorded per week in 2003 has been increased compared to 2002. The data actually used in this analysis has been selected based on data quality criteria presented in Section 5.2.1, followed by cuts on the event topology (Section 5.2.2), hadron identification and finally high-p_t selection cuts (Section 5.2.3).

5.2.1 Data Reconstruction and Data Quality

For the analysis of the raw data the COMPASS analysis framework CORAL [138] is used. It includes all steps of the event reconstruction. This starts with raw data decoding, where e.g. the positions of the hits in the drift detectors are calculated. These hits enter the tracking algorithm leading to the information about the charged tracks in the spectrometer. Clusters in the calorimeter are identified, their energy is determined and they are associated to a track. The tracks are used by the vertex algorithm to search for interaction space-points and generate the vertices. If the beam particle is included in the vertex it is referred to as the primary vertex. CORAL allows the individual user to include his or her analysis specific code in the framework in order to carry out the complete analysis with CORAL. It is disadvantageous that each time the analysis program is run, steps like hit reconstruction, tracking and vertexing are performed again. To avoid the redundant performance of this CPU-intensive steps, CORAL can be used to produce mini Data Summary Tapes (mDST). They contain the information in the form of four vectors for the reconstructed tracks and particle identification information plus further event specific information like run number, event number, event time, etc. Only events containing at least one primary or secondary vertex are written to the mDST. The mDST can be analysed with the PHysics Analysis Software Tools (PHAST) [139] which reduces the analysis time for one run from a few hours on about 100 CPU for raw data to less than one hour on one CPU. One run normally corresponds to 100 spills, which is about 30 minutes of data taking.

The mDST-production of the raw data is done at CERN. The mDST are

then distributed to the institutes involved in the analysis. The run selection and production is done by the data production team [140]. The run selection for the analysis in COMPASS is based on general criteria like minimum number of spills per run, maximum number of planes of detectors with problems or marked as *good* by the shift crew. This information is provided in the electronic logbook [123] and the runs have been selected accordingly. On this basis further quality checks are performed using criteria like numbers of primary vertices, tracks, K^0-particles per events or number of tracks per vertex [141]. This is done on the level of spills. For each data production bad spill lists are produced and those spills are discarded for the analysis. The data selection on the basis of the production of suitable runs and bad spill information is used in general for the COMPASS data analysis. For the high-p_t analysis some additional runs are discarded. These are field rotation runs since here the target dipole has been switched on which is not taken into account in the magnetic field map used in the reconstruction. This might lead to problems in the vertex reconstruction. For a few runs with detector problems it is not clear how they could affect the asymmetry calculation. As a precaution these runs have been discarded. The list of runs that were excluded can be found in Appendix A.1. In total 2498 runs have been used. Table 5.1 gives an overview of the run statistics.

5.2.2 Event Selection

The next step is to select candidates for the high-p_t sample. These events are required to have

- a primary vertex
- one scattered muon
- at least two additional outgoing particles, each with a transverse momentum relative to the virtual photon $p_t \geq 0.7\,\mathrm{GeV/c}$.

A primary vertex is defined as a vertex with a beam particle associated to it. In a few cases it is possible to have two beam track candidates and thus two primary vertices, then the PHAST function `iBestPrimaryVertex()` is used. This function selects the vertex containing more tracks or in case of equal number of tracks the one with the better χ^2. It can also happen, that an event contains more than one scattered muon candidate. These events are rejected to avoid muon contamination in the hadron sample.

Table 5.1: Number of runs used in the analysis. One run normally corresponds to 100 spills. This is about 30 minutes of data taking. Runs that have been stopped before are also used depending on their quality. For period P1I and P1J also runs with 200 spills were recorded. The period 2002P1C was discarded because of major problems during the data production. Period P2A covers two weeks of data taking with a machine development between them. Therefore it is split in two parts. P2G is split in two parts since a power failure in the middle of the period led to a loss of the target polarisation. The target was repolarised with the opposite microwave configuration so that P2G contains two different microwave configurations that have to be treated separately. P1D contains a longer break because of beamline problems and therefore is divided in two. These problems were the reason that no beam was available from 24th July to 6th of August. For P1E the last solenoid configuration is treated separately since two Micromega planes were not operational during this time.

	date	runs	no. of runs	production slot/time
2002			1072	
P2A1	18.7.-24.7.02	20413 - 20717	168	2-7 / Jul 04
P2A2	24.7.-31.7.02	20767 - 21134	216	2-7 / Jul 04
P2D	14.8.-21.8.02	22018 - 22341	163	3-7 / Mar 05
P2E	22.8.-28.8.02	22384 - 22698	213	1-5 / Apr 03
P2F	29.8.- 3.9.02	22754 - 22972	101	1-5 / Jun 03
P2Ga	3.9.- 6.9.02	23016 - 23147	73	2-7 / Jan 05
P2Gb	7.9.-11.9.02	23243 - 23449	138	2-7 / Jan 05
2003			1426	
P1A	16.6.-26.6.03	25799 - 28178	201	1-6 / May 04
P1B	26.6.-30.6.03	28235 - 28433	141	1-6 / May 04
P1C	4.7.- 9.7.03	28571 - 28834	146	1-6 / Apr 04
P1Da	9.7.-12.7.03	28881 - 29002	99	1-6 / Apr 04
P1Db	18.7.-21.7.03	29220 - 29366	81	1-6 / Apr 04
P1Ea	6.8.-12.8.03	29963 - 30350	245	1-7 / Dec 04
P1Eb	12.8.-13.8.03	30354 - 30379	19	1-7 / Dec 04
P1F	14.8.-20.8.03	30448 - 30717	175	1-6 / May 04
P1I	3.9.- 8.9.03	31581 - 31855	144	3-7 / Sep 04
P1J	9.9.-17.9.03	31930 - 32236	175	3-7 / Sep 04

Figure 5.1: COMPASS coordinate system and illustration of the target centre coordinates given in Table 5.2. The origin of the COMPASS coordinate system is in the middle of the downstream target cell. The x-axis is the horizontal axis pointing towards the Jura, the y-axis points to the ceiling and the z-axis points downstream along the beam.

Beam and Vertex Cuts

With the reconstructed beam, the scattered muon and the hadrons, the vertex position is defined. For all requirements concerning beam and vertex positions it is taken into account that the target is slightly tilted compared to its nominal position in which the x- and y-positions of the target centre are at $x, y = 0\,\text{cm}$. The actual positions of the upstream and downstream target centre deviate from this and are illustrated in Fig. 5.1 and the coordinates are given in Table 5.2. These define a target coordinate system. The following cuts concerning vertex and beam coordinates are given in the system of the tilted target. To ensure the vertex to be inside one of the target cells with a well defined polarisation, the vertex coordinates (v_x, v_y, v_z) have to be

- $-100\,\text{cm} \leq v_z \leq -40\,\text{cm}$ (upstream target cell) or
  $-30\,\text{cm} \leq v_z \leq +30\,\text{cm}$ (downstream target cell)
- $r = \sqrt{v_x^2 + v_y^2} \leq 1.4\,\text{cm}$
- $v_y \leq 1\,\text{cm}$.

The radius r is required to be 1 mm smaller than the nominal target radius of 1.5 cm to avoid inhomogeneities at the edges. The cut on the y-coordinate ($v_y \leq 1\,\text{cm}$)

Table 5.2: Target position in 2002 and 2003. x-, y- and z-coordinates of the upstream and downstream target centre in the COMPASS reference system.

	2002		2003	
	upstream	downstream	upstream	downstream
x/cm	-0.20	-0.30	$+0.04$	-0.03
y/cm	$+0.10$	-0.15	$+0.03$	-0.20
z/cm	-100	$+30$	-100	$+30$

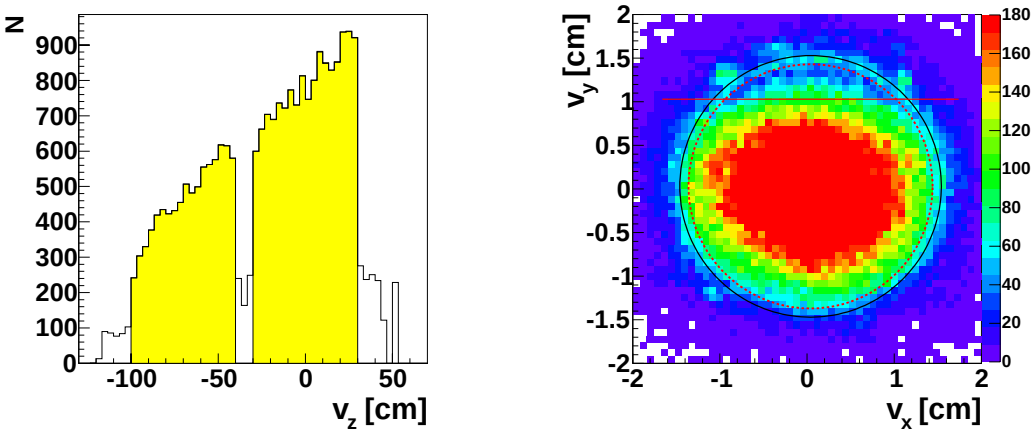

Figure 5.2: Vertex distributions for the high-p_t sample. The cuts applied to this sample are defined in the course of this section. Left: Distribution of the vertex z-coordinate. The yellow regions correspond to the two target cells. The two cells are clearly separated in the vertex reconstruction. Right: radial vertex distributions for the first 10 cm of the upstream target cell, i.e. $-100\,\text{cm} \leq v_z \leq -90\,\text{cm}$. The outer circle corresponds to the nominal target radius $r = 1.5\,\text{cm}$, the inner dashed circle to the applied cut $r \leq 1.4\,\text{cm}$. The horizontal line indicates the cut on $v_y \leq 1\,\text{cm}$. It can be seen that less target material is in the top region of the target cell.

takes into account that the target is not completely filled with target material. The cut on the vertex z-coordinate is defined by the position of the target cells. A vertex distribution for the high-p_t sample is shown in Fig. 5.2. The target cell positions are indicated by the yellow regions in the figure. The two target cells are clearly separated in the vertex distribution. Since they are embedded in liquid helium, there are also vertices, that originate from outside the target cells and cannot be used in the analysis.

Apart from having the vertex position inside the polarised target material it is important to have the same beam flux in both target cells (the setup has been developed to be independent of the beam flux). This is ensured by the requirement that the unscattered beam would cross completely both target cells within the region of the previously defined vertex cuts. Therefore the beam is extrapolated to the upstream and the downstream end of the target, where the target cell has to be hit within

- $r = \sqrt{x^2 + y^2} \leq 1.4\,\text{cm}$
- $y \leq 1\,\text{cm}$.

This requirement suppresses false asymmetries which could be produced e.g. if the beam would hit the target with a slope.

Cuts on the Scattered Muon

The scattered muon is identified using the function `iMuPrim()` from PHAST. To improve the muon identification the scattered muon track is required to have at least one cluster in or behind the last hodoscope corresponding to the event trigger type. If the event has been triggered by the pure calorimetric trigger (eTrig==16) and no scattered muon is identified in the hodoscopes, the first muon filter is used to perform the scattered muon identification. Such a track must have at least 6 hits in the 8 planes of the detector that is located behind the first hadron absorber. But this gains less than 1% of events since the pure calorimeter trigger usually fires in coincidence with one of the hodoscope triggers. This can be seen in Fig. 5.3 which displays the distribution of the trigger mask in 2002 and 2003.

Inclusive Variables

The beam and the scattered muon are required to be reconstructed to be able to select DIS events in the region

- $Q^2 > 1\,\mathrm{GeV}^2/\mathrm{c}^2$,

where the Monte Carlo generator LEPTO can be used. The cut on Q^2 drastically reduces the statistics since with our trigger setup less than 10% of the events have a negative squared four momentum transfer $Q^2 > 1\,\mathrm{GeV}^2/\mathrm{c}^2$. The fractional virtual photon energy y is required to fulfil

- $0.1 < y < 0.9$.

The lower value corresponds to the minimum y that is possible with the trigger. High y events are discarded because they are strongly affected by radiative effects. The Bjorken x_{Bj} variable is asked to be

- $x_{Bj} < 0.05$.

This cut rather belongs to the high-p_t selection to suppress background contributions to the asymmetry. The inclusive cuts on Q^2 and y define a preselection of the sample. In Table 5.3 the average values of the inclusive kinematic variables Q^2, x_{Bj}, y and of the invariant mass of the photon-nucleon system W are given for the high-p_t sample after all cuts. Fig. 5.4 (a) and Fig. 5.5 illustrate the kinematic region covered by the high-p_t analysis. Q^2 is plotted versus x_{Bj} for all triggers and versus y for the different triggers to explain the kinematic region covered by the different triggers. The kinematic cuts applied for the high-p_t analysis are indicated. Fig. 5.4 (b), (c) and (d) show the projections on the x_{Bj}, y and Q^2 axis, respectively.

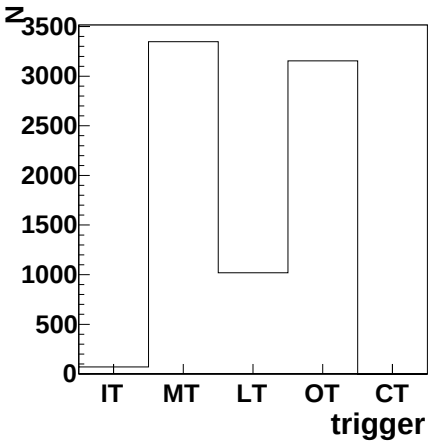

(a) 2002

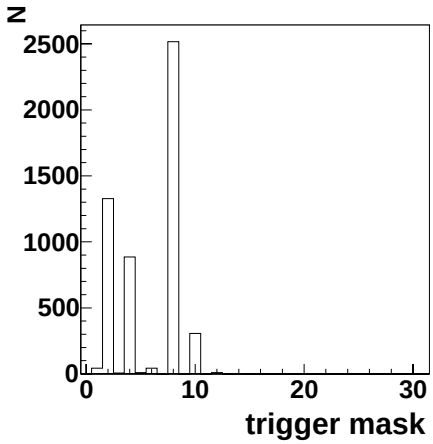

(b) 2002

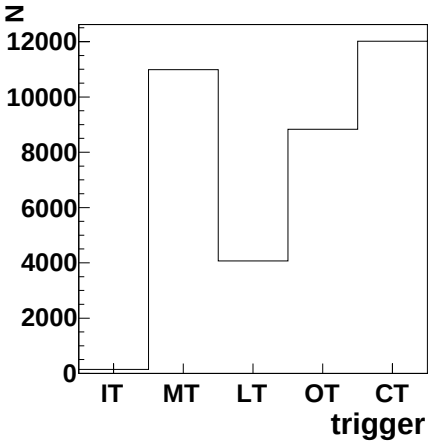

(c) 2003

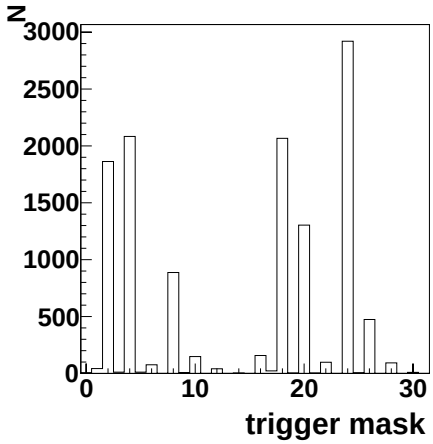

(d) 2003

Figure 5.3: Trigger Mask distribution for the high-p_t sample (the cuts applied to the high-p_t sample include $Q^2 > 1\,\mathrm{GeV}^2/\mathrm{c}^2$ and are illustrated in the course of this section). 1=IT, 2=MT, 4=LT, 8=OT, 16=CT. Usually combinations of these bits are set due to the kinematic overlap of the triggers, e.g. 12=LT+OT or 18=MT+OT etc. (a) and (c) show the distributions if at least the IT-, MT-, LT-, OT- or CT-bit has been set. (b) and (d) show the trigger mask distribution including all combinations. Events where the inclusive Middle Trigger bit is set (256=iMT) are not included in the plots due to the large overlap of MT and iMT. The pure Calorimetric Trigger (16) usually fires in coincidence with one of the hodoscope triggers, e.g. together with the Outer Trigger (24=OT+CT). The pure Calorimetric Trigger was not used for longitudinal data taking before 2003. The Inner Trigger has been designed for low Q^2-events and does not play a role in this analysis.

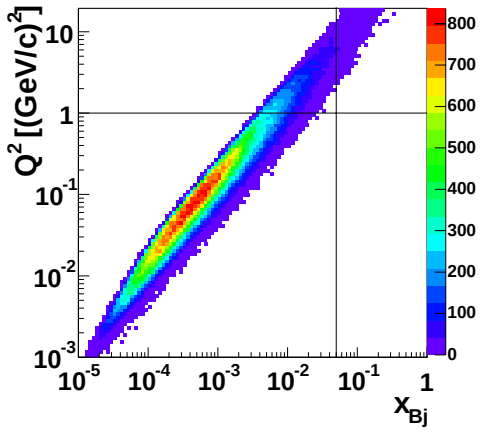

(a) Q^2 vs. x_{Bj}.

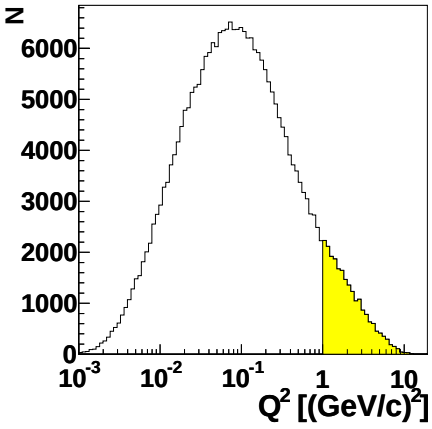

(b) Negative squared four momentum transfer Q^2.

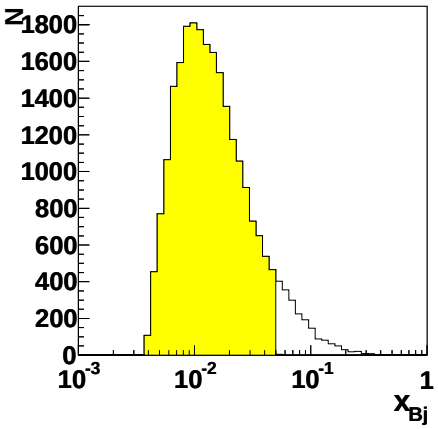

(c) Bjorken variable x_{Bj}.

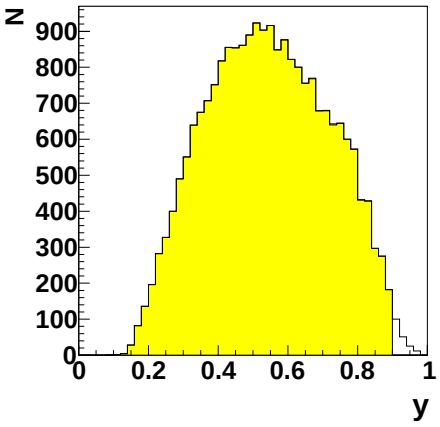

(d) Fractional virtual photon energy y.

Figure 5.4: Kinematic region covered by COMPASS in the year 2003: (a) Q^2 vs. x_{Bj} for the high-p_t sample. (b) - (d) Inclusive kinematic variables for the high-p_t sample. The cuts applied on these variables are indicated by the yellow region. All high-p_t cuts, including the cuts on the other kinematic variables, are applied for the plots, except the cuts on the variables that are plotted.

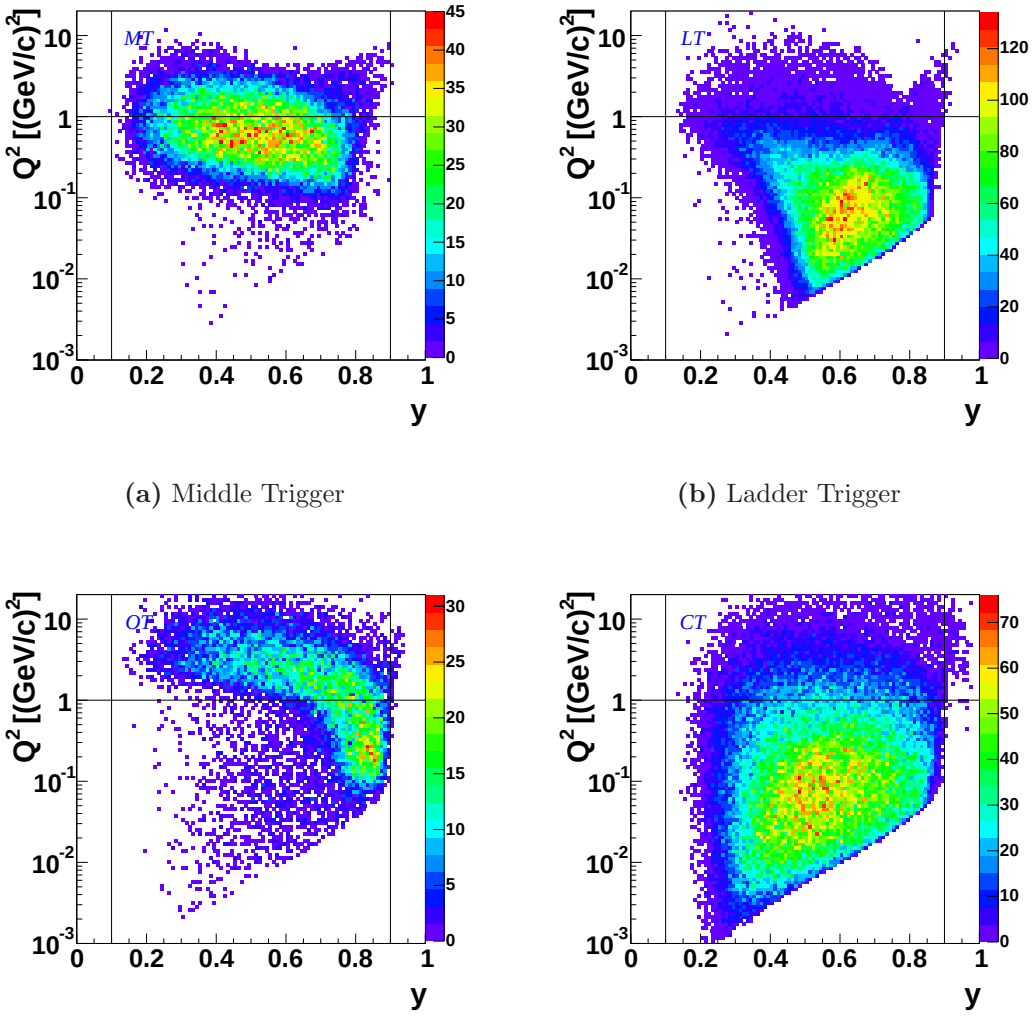

(a) Middle Trigger

(b) Ladder Trigger

(c) Outer Trigger

(d) Calorimeter Trigger

Figure 5.5: Q^2 vs. y for the different triggers if at least this trigger bit is set (2003 data only) for the high-p_t sample. The Middle Trigger (a) covers the region of intermediate to larger Q^2, the Ladder Trigger (b) selects events with lower Q^2 and large y. The Outer Trigger(c) with the large hodoscope slabs covers large angles and thus high Q^2 events. The Calorimeter Trigger (d) usually fires in coincidence with one of the hodoscope triggers and covers the whole kinematic region. All high-p_t cuts, including the cuts on the other kinematic variables are applied for the plots, except the cuts on the variables that are plotted.

5.2.3 High-p_t Hadron Selection

All outgoing tracks that are connected to the primary vertex and not identified as scattered muon are considered as hadron candidates. To ensure the reconstruction quality the hadron candidate should not be exclusively reconstructed in the fringe field of SM1. Therefore the last cluster of the track is required to be located after SM1 ($z > 3.5\,\mathrm{m}$). Furthermore a minimum track reconstruction quality is required ($\chi^2/ndf < 20$).

Hadron Identification

The hadronic calorimeters are used to identify the candidates as hadrons and discard muon contamination. The hadron candidate is rejected if $E_{cal}/p < 0.3$, where E_{cal} is the total energy measured in the hadronic calorimeter and associated to the track and p the reconstructed track momentum. In Fig. 5.6 E_{cal} is plotted versus the momentum p of the track for all hadron candidates and the ratio E_{cal}/p. The line corresponding to the cut clearly indicates the separation of hadrons from muons in the sample. The muons are visible as a line with small E_{cal} at the bottom of the plot. For about 80% of the tracks a cluster in the calorimeter is associated to the track. When no calorimeter information is available the hadron candidate is rejected if it goes through the second hadron absorber. This means that the position of the last cluster associated to the track is demanded to be before $z = 40\,\mathrm{m}$. Additionally the number of clusters of the hadron candidate in the planes of the first muon filter, that are located behind the first hadron absorber, is checked. If the number of clusters exceeds 5 the hadron candidate is rejected. This is the case for less than 1% of the high-p_t tracks.

Table 5.3: Average, minimum and maximum value for the inclusive kinematic variables $x = Q^2, x_{Bj}, y, W$.

x	$\langle x \rangle$ (2002)	$\langle x \rangle$ (2003)	x_{min}	x_{max}
Q^2 [(GeV/c)^2]	2.24	2.32	1	11
x_{Bj}	0.015	0.016	0.004	0.05
y	0.53	0.54	0.1	0.9
W [GeV/c^2]	12.5	12.5	6	17

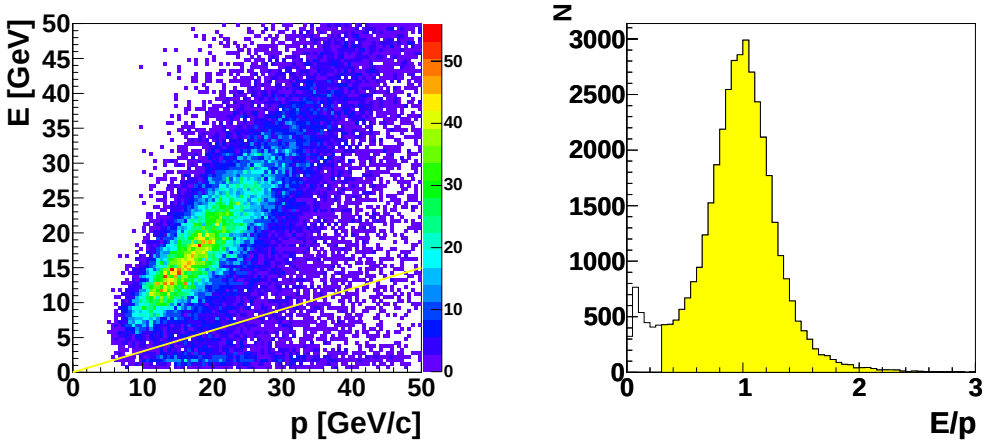

Figure 5.6: Hadron identification in the calorimeter for the high-p_t sample. Left: The energy deposited in the calorimeter E_{cal} is plotted versus the track momentum p. The yellow line indicates the cut $E_{cal}/p < 0.3$. Right: E_{cal}/p distribution. The yellow region indicates the selected events.

High-p_t Selection

The following cuts describe the actual high-p_t selection. They are applied to the leading (highest transverse momentum) and next-to-leading hadron. To ensure that the hadrons come from the current fragmentation and not from the target fragmentation the longitudinal momentum fraction in the photon-nucleon c.m. system, x_F, and the hadron energy fraction of the virtual photon, z, have to fulfil

- $x_F > 0.1$ and $z > 0.1$

for both hadrons. A cut on the sum $z_1 + z_2$

- $z_1 + z_2 < 0.95$

is performed to exclude exclusive production of mesons heavier than π-mesons. Fig. 5.7 illustrates the influence of the x_F-cut on the high-p_t sample for the first and second hadron.

By the cuts introduced up to know, pairs of hadrons from the current fragmentation and with transverse momentum $p_t > 0.7\,\mathrm{GeV/c}$ have been selected. In case an event would have been discarded because one of the first two hadrons does not fulfil the x_F or z cut, it is checked if a third hadron fulfils this criteria. When this is the case, then this event is kept for the analysis, which applies the following high-p_t cuts

- $p_t > 0.7\,\mathrm{GeV/c}$ for both hadrons

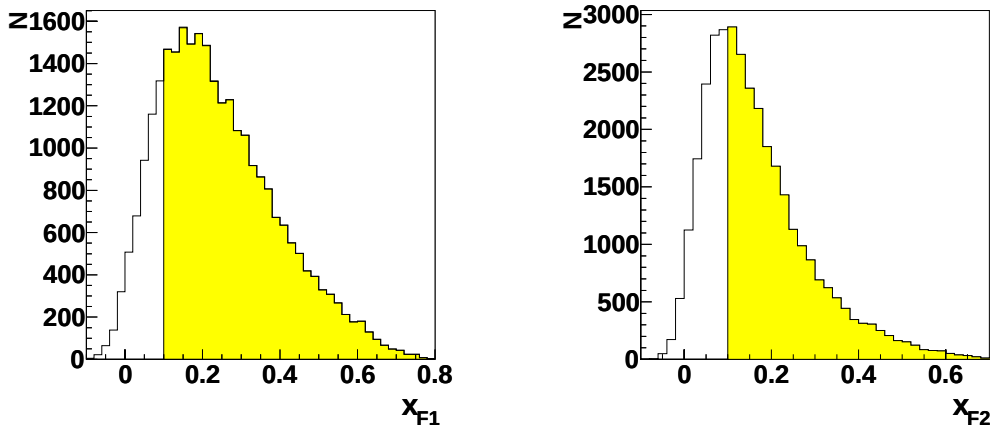

Figure 5.7: x_F distribution for both hadrons. Left: leading hadron. Right: second hadron. All high-p_t cuts are applied except the cut on x_F. The yellow region indicates the events selected with $x_F > 0.1$.

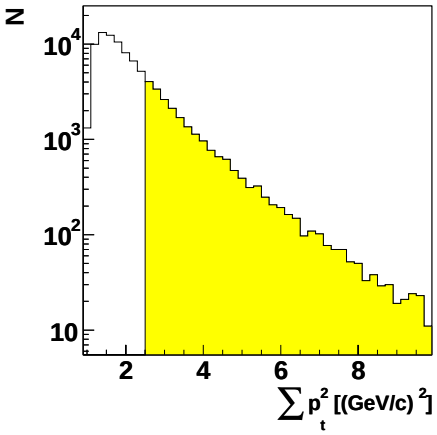

Figure 5.8: $\sum p_t^2$ distribution of the hadron pair. The yellow region indicates the selected events belonging to the high-p_t sample.

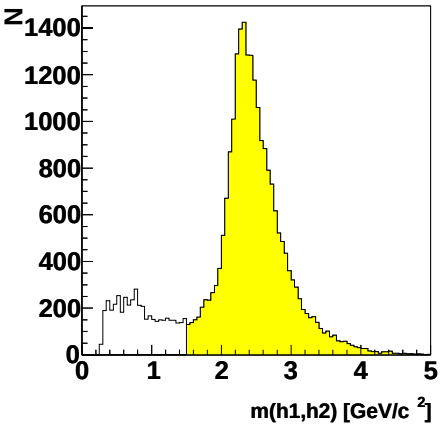

Figure 5.9: Invariant mass of the hadron pair, assuming pion masses. All high-p_t cuts are applied except the cut on the invariant mass. The yellow region indicates the events selected with $m(h_1, h_2) > 1.5\,\mathrm{GeV/c^2}$.

- $p_{t1}^2 + p_{t2}^2 > 2.5\,\mathrm{GeV^2/c^2}$ (Fig. 5.8)

and the requirement that the invariant mass of the two hadrons (assuming pion masses) is above the resonance region

- $m(h_1, h_2) > 1.5\,\mathrm{GeV/c^2}$.

In the invariant mass distribution (Fig. 5.9) a residual peak at the ρ mass ($m_\rho \approx 770\,\mathrm{MeV/c^2}$) can be seen. This peak can contain events for which the virtual photon fluctuates to a ρ-meson, which decays in $\pi^+\pi^-$ after interacting with the nucleon. The cut on the invariant mass removes these events. Table 5.4 gives an overview of the event numbers after the performed selections and cuts. The event sample that has been prepared by applying all the cuts mentioned up to now is referred to as high-p_t sample.

The cuts that are applied in this analysis to select high-p_t hadron pairs follow [66] and [142]. In [66] it is suggested to require the two hadrons opposite in azimuth to further suppress background, since the conservation of transverse momentum introduces a strong correlation. This cut is not applied explicitly in this analysis, but the cut on the invariant mass of the two hadrons suppresses pairs of

Table 5.4: Event statistics. Reduction of the event sample after the cuts explained in the text were applied. The high-p_t candidates are all events in a mDST-file that have a primary vertex with a scattered muon associated to it and two more outgoing particles with $p_t > 0.7\,\mathrm{GeV/c}$. In total 674 million (782 million including P2F and P2Ga) events are contained in the mDST-files for 2002 and 1498 million for 2003. Detailed numbers for the separate periods can be found in Table A.5.

selection	events 2002		events 2003	
	abs. #	%	abs. #	%
high-p_t candidates	2780991	100.00	6793840	100.00
beam crosses completely the target	2081874	74.86	5210555	76.70
scattered μ in trigger hodoscope	1888363	67.90	4796746	70.60
$Q^2 > 1\,\mathrm{GeV^2/c^2}$, $0.1 < y < 0.9$	100873	3.63	390052	5.74
vertex inside target	88515	3.18	344616	5.07
hadron quality (zlast$_{min}$, χ^2)	83439	3.00	320718	4.72
hadron identification (calo, zlast$_{max}$)	73165	2.63	285763	4.21
$x_F, z > 0.1$, $z_1 + z_2 < 0.95$	39340	1.41	153914	2.27
$p_{t1}^2 + p_{t2}^2 > 2.5\,\mathrm{GeV^2/c^2}$	7345	0.26	29582	0.44
$m(h_1, h_2) > 1.5\,\mathrm{GeV/c^2}$	6106	0.22	24598	0.36
$x_{Bj} < 0.05$ (high-p_t sample)	5780	0.21	22600	0.33

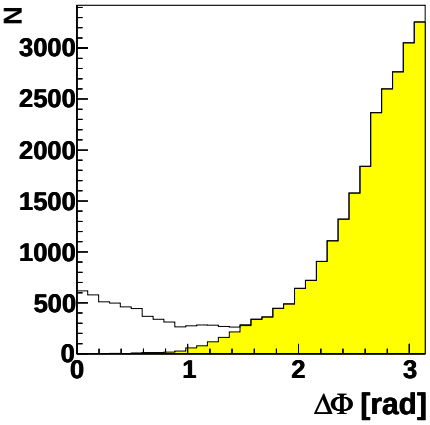

Figure 5.10: Difference in azimuth $\Delta\Phi$ for the two hadrons without and with (yellow region) the cut on the invariant mass of the two hadron $m(h_1, h_2) > 1.5\,\mathrm{GeV/c^2}$ (assuming pion masses).

hadrons with a small difference in the azimuth angle. In Fig. 5.10 the difference in the angles $\Delta\Phi$ is plotted, where Φ is the azimuthal angle between the outgoing hadron and the lepton scattering plane. Fig. 5.10 illustrates the influence of the cut on the invariant mass $m(h_1, h_2) > 1.5\,\mathrm{GeV/c^2}$ on $\Delta\Phi$ for the high-p_t sample. One can see that for events from the resonance region the hadrons are mostly in the same hemisphere.

5.3 Extraction of the Raw Asymmetries

5.3.1 Asymmetry Calculation

The first step in the extraction of $\Delta G/G$ using Eq. (2.102):

$$\begin{aligned} A_{LL}^{\gamma N\to h_1h_2X} &= \frac{\Delta G}{G}\langle\hat{a}_{LL}^{PGF}\rangle R_{PGF} \\ &+ A_1\langle\hat{a}_{LL}^{QCD-C}\rangle R_{QCD-C} + A_1\langle\hat{a}_{LL}^{L.O.}\rangle R_{L.O.} \end{aligned}$$

is the extraction of the virtual photon-deuteron asymmetry $\mathrm{A}_{LL}^{\gamma N\to h_1h_2X}$. It is related to the raw counting rate asymmetry $\frac{N^{\rightleftarrows}-N^{\leftleftarrows}}{N^{\rightleftarrows}+N^{\leftleftarrows}}$ via

$$A_{LL}^{\gamma N\to h_1h_2X} = \frac{1}{|fP_TDP_b|}\frac{1}{2}\left(\frac{N^{\rightleftarrows}-N^{\leftleftarrows}}{N^{\rightleftarrows}+N^{\leftleftarrows}} + \frac{N'^{\rightleftarrows}-N'^{\leftleftarrows}}{N'^{\rightleftarrows}+N'^{\leftleftarrows}}\right). \tag{5.1}$$

with the error of the asymmetry

$$\delta A_{LL}^{\gamma N\to h_1h_2X} = \frac{1}{|fP_TDP_b|}\frac{1}{2}\sqrt{\frac{1}{N^{\rightleftarrows}+N^{\leftleftarrows}} + \frac{1}{N'^{\rightleftarrows}+N'^{\leftleftarrows}}}. \tag{5.2}$$

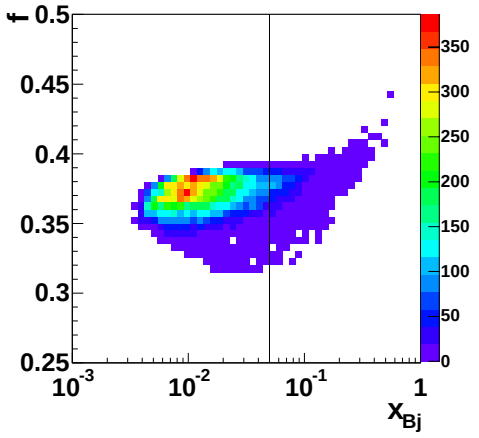

Figure 5.11: Dilution factor f as function of x_{Bj} for the high-p_t sample. The vertical line indicates the cut on $x_{Bj} < 0.05$.

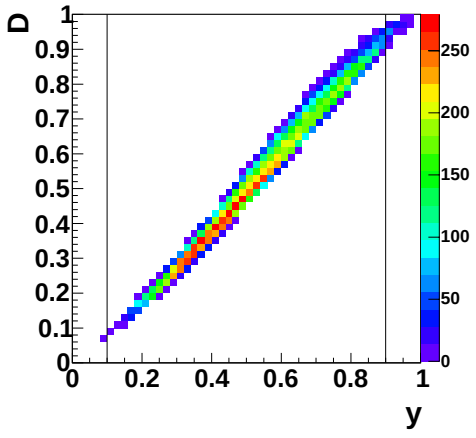

Figure 5.12: Depolarisation factor D as a function of y for the high-p_t sample. The cuts on y are indicated by the vertical lines.

f is the dilution factor, D the depolarisation factor, P_T and P_b the target and beam polarisation, respectively.
The dilution factor f takes into account the number of polarisable material inside the target. It is defined as

$$f = \frac{\text{polarisable nucleons}}{\text{all nucleons}} = \frac{n_d \sigma_d}{n_d \sigma_d + \sum_A n_A \sigma_A} \tag{5.3}$$

where n_i corresponds to the number of nuclei of type i inside the target, σ_d and σ_A are the unpolarised cross sections for the muon-deuteron and muon-nucleon scattering, respectively. Expression (5.3) can be rewritten as

$$f = \frac{n_d}{n_d + \sum_A n_A \sigma_A / \sigma_d}. \tag{5.4}$$

The ratio σ_A/σ_d is approximately proportional to the unpolarised structure function ratio F_2^A/F_2^d. The dilution factor computation for the COMPASS target uses parametrisations from NMC and EMC for the cross section ratios and measurements of the material inside the target volume [143]. The dependence of the dilution factor on the Bjorken variable x_{Bj} is shown in Fig. 5.11. The average dilution factor of the target is $\langle f \rangle = 0.37$ for the years 2002 and 2003.
The depolarisation factor D describes the polarisation transfer from the incoming muon to the virtual photon and is given by

$$D = \frac{y\left[(1+\gamma^2 y/2)(2-y) - 2y^2 m_\mu^2/Q^2\right]}{y^2(1-2m_\mu^2/Q^2)(1+\gamma^2) + 2(1+R)(1-y-\gamma^2 y^2/4)}, \tag{5.5}$$

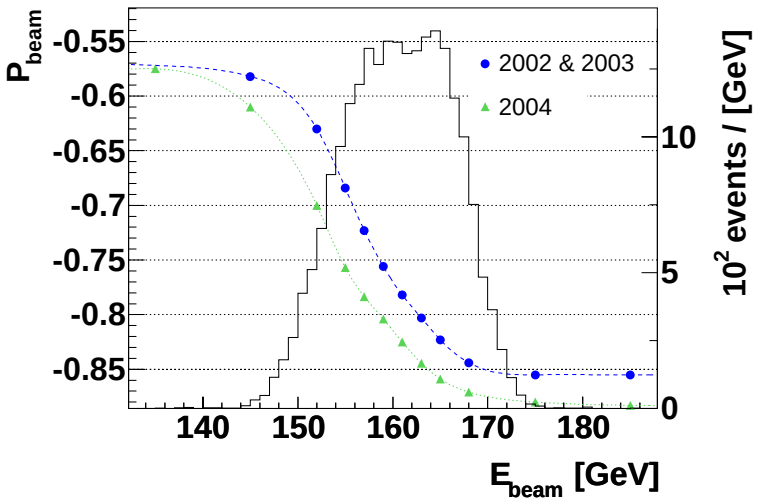

Figure 5.13: Beam polarisation and energy distribution. The spin of the beam muons is opposite to the direction of flight. Therefore the sign is negative. In the analysis only the absolute value enters. The sign is taken into account by the counting rates $N^{\rightleftarrows}$ and $N^{\leftleftarrows}$.

where $\gamma = 2Mx/\sqrt{Q^2}$ and $R = \sigma_L/\sigma_T$. Depending on x_{Bj}, R is obtained from a parametrisation of NMC data in the range $0.003 < x < 0.12$, relevant in this analysis [144]. The depolarisation factor D is in a good approximation directly proportional to y as can be seen in Fig. 5.12. The average value of the depolarisation factor was $\langle D \rangle = 0.53$ in 2002 and $\langle D \rangle = 0.54$ in 2003.
The beam polarisation P_b is obtained from the Monte Carlo simulation of the M2 beamline [77]. It provides a parametrisation of the beam polarisation as function of the beam energy that can be determined from the information of the beam momentum station (BMS). Fig. 5.13 shows the energy distribution of the beam muons and the beam polarisation as a function of the muon energy. The average beam polarisation has been $-77\,\%$ in 2002 and $-76\,\%$ in 2003. The points obtained from the parametrisation have been interpolated with a cubic spline function.
The target polarisation is averaged over the time interval in which the data for the asymmetry have been taken.
The two terms in Eq. (5.1) take into account that the solenoid field is reversed every 8 hours during normal data taking. Fig. 5.14 a) and b) illustrate the spin configurations for one microwave setting. The unprimed notation $(N^{\rightleftarrows}, N^{\leftleftarrows})$ belongs to configuration a), the primed notation $(N'^{\rightleftarrows}, N'^{\leftleftarrows})$ to configuration b) in Fig. 5.14. To cancel acceptance effects the average of the two configurations with opposite solenoid currents is used in the asymmetry calculation.

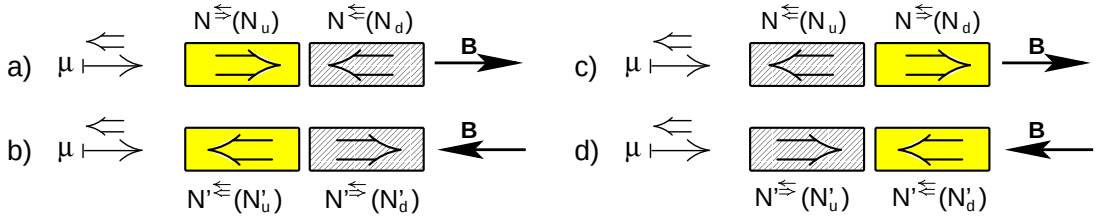

Figure 5.14: Target spin configurations for the asymmetry calculation. For the + microwave setting (a) and b)) the upstream cell is positively polarised, i.e. the spins are oriented along the magnetic field. For the − microwave setting (c) and d)) the upstream target cell is negatively polarised, i.e. the spins are anti-aligned with the field, cf. also Fig. 3.5 on page 45. In 2002 the periods P2A and P2Gb belong to the microwave configuration c) and d) and the periods P2D, P2E, P2F and P2Ga belong to a) and b). In 2003 the periods P1A, P1B, P1C, P1D and P1I have been taken with configuration a) and b) and P1E, P1F and P1J with c) and d).

To improve the statistical accuracy of the calculation, every event in the asymmetry calculation is weighted with the dilution factor, the depolarisation factor and the beam polarisation: $w = fD|P_b|$

$$A = \frac{1}{2|P_T|}\left[\frac{\sum_i^{N_u} w_i - \sum_i^{N_d} w_i}{\sum_i^{N_u} w_i^2 + \sum_i^{N_d} w_i^2} - \frac{\sum_i^{N'_u} w_i - \sum_i^{N'_d} w_i}{\sum_i^{N'_u} w_i^2 + \sum_i^{N'_d} w_i^2}\right] \tag{5.6}$$

with the error

$$\delta A = \frac{1}{2|P_T|}\sqrt{\frac{1}{\sum_i^{N_u} w_i^2 + \sum_i^{N_d} w_i^2} + \frac{1}{\sum_i^{N'_u} w_i^2 + \sum_i^{N'_d} w_i^2}}. \tag{5.7}$$

For the microwave configuration given in Fig. 5.14 a) the upstream target cell is positively polarised and the magnetic field points into the positive z-direction. For this configuration $\overleftarrow{\Rightarrow}$ events are measured in the upstream cell. To simplify the notation in the above equation, $N^{\overleftarrow{\Rightarrow}}$ is replaced by N_u and N_d corresponds to $N^{\overleftarrow{\Leftarrow}}$. For the reversed microwave configuration (Fig. 5.14 c) and d)) the sign is taken into account through the sign of the target polarisation P_T and leads to an overall minus sign in Eq. (5.6).

For the derivation of Eq. (5.1) and Eq. (5.6) some assumptions have to be made, e.g. the difference in acceptance between the two target cells is assumed to be small [145]. Since the acceptance difference for semi-inclusive and especially high-p_t events is clearly visible in the vertex distribution in Fig. 5.2 a so-called *second order method* for the asymmetry extraction is used. In combination with the weighting of the event with $w = fDP_b$ this leads to a minimal statistical error without approximations on the acceptances of the two target halves.

Second Order Weighted Method for Asymmetry Extraction

The derivation of the second order weighted method for the asymmetry follows Ref. [146]. The number of events in a given target half is

$$N = a\Phi n\sigma(1 - P_b P_T f D A). \tag{5.8}$$

Here a denotes the acceptance, Φ the muon flux, n the total number of nuclei in the target, σ the unpolarised cross-section, A the photon-nucleon asymmetry and f, D, P_b and P_T the dilution factor, depolarisation factor, beam and target polarisation, respectively. Taking into account the two solenoid field directions as shown in Fig. 5.14 leads to four equations:

$$\begin{aligned}
N_u &= a_u\Phi n_u\sigma_u(1 - P_b P_u f_u D A) = \alpha_u(1 - \beta_u A) && (5.9)\\
N_d &= a_d\Phi n_d\sigma_d(1 - P_b P_d f_d D A) = \alpha_d(1 - \beta_d A) && (5.10)\\
N'_u &= a'_u\Phi' n_u\sigma_u(1 - P_b P'_u f_u D A) = \alpha'_u(1 - \beta'_u A) && (5.11)\\
N'_d &= a'_d\Phi' n_d\sigma_d(1 - P_b P'_d f_d D A) = \alpha'_d(1 - \beta'_d A). && (5.12)
\end{aligned}$$

The asymmetry is considered only in a region of phase space, where A is approximately constant. Then all other variables are combined in

$$d\vec{x} = dQ^2 d\vec{v} dt, \tag{5.13}$$

where $\vec{v}$ and t are the vertex position and the time, respectively, and A does not depend on these variables. Eq. (5.9) - (5.12) then read

$$N_i(\vec{x}) = \alpha_i(\vec{x})(1 - \beta_i(\vec{x})A), \tag{5.14}$$

where $i = u, d, u', d'$. Integrated over all x one gets the total number of events

$$N_i = \int N_i(\vec{x}) d\vec{x}. \tag{5.15}$$

For this method, each event is weighted with w and instead of the number of events one obtains

$$\begin{aligned}
p_i &:= \int N_i(\vec{x}) w(\vec{x}) d\vec{x}\\
&\overset{(5.14)}{=} \int w(\vec{x})\alpha_i(\vec{x}) d\vec{x} - A\int w(\vec{x})\alpha_i(\vec{x})\beta_i(\vec{x}) d\vec{x}\\
&= \int \alpha_i(\vec{x}) w(\vec{x}) d\vec{x}\ (1 - A\langle\beta_i\rangle_w)\\
&= \int \Phi n_i\sigma_i d\vec{x}\ \langle a_i\rangle_w (1 - A\langle\beta_i\rangle_w), && (5.16)
\end{aligned}$$

where

$$\langle \beta_i \rangle_w = \frac{\int \alpha_i \beta_i w d\vec{x}}{\int \alpha_i w d\vec{x}} \approx \frac{\sum_i w_i \beta_i}{\sum_i w_i} \tag{5.17}$$

and

$$\langle a_i \rangle_w = \frac{\int \Phi n_i \sigma_i w a_i d\vec{x}}{\int \Phi n_i \sigma_i w d\vec{x}}. \tag{5.18}$$

δ is defined as the double ratio of the weighted integrals:

$$\begin{aligned} \delta &= \frac{p_u p'_d}{p'_u p_d} \\ &= \frac{\langle a_u \rangle_w \langle a'_d \rangle_w}{\langle a'_u \rangle_w \langle a_d \rangle_w} \cdot \frac{\int \Phi n_u \sigma_u d\vec{x} \int \Phi' n_d \sigma_d d\vec{x}}{\int \Phi' n_u \sigma_u d\vec{x} \int \Phi n_d \sigma_d d\vec{x}} \\ &\quad \cdot \frac{(1 - \langle \beta_u \rangle_w A)(1 - \langle \beta'_d \rangle_w A)}{(1 - \langle \beta'_u \rangle_w A)(1 - \langle \beta_d \rangle_w A)}. \end{aligned} \tag{5.19}$$

In a good approximation $\int \Phi n_u \sigma_u d\vec{x}$ be written as $\int \Phi d\vec{x}_1 \cdot \int n_i \sigma_i d\vec{x}_2$ with $d\vec{x}_1 = d\vec{v}dt$ and $d\vec{x}_2 =$ (all other variables), because Φ depends on the time t and the vertex position $\vec{v}$. $n_i \sigma_i$ depends only weakly on the target position if the target is homogeneously filled and does not depend on the time if the target does not move. Thus follows

$$\frac{\int \Phi n_u \sigma_u d\vec{x} \int \Phi' n_d \sigma_d d\vec{x}}{\int \Phi' n_u \sigma_u d\vec{x} \int \Phi n_d \sigma_d d\vec{x}} = \frac{\int \Phi d\vec{x}_1 \int n_u \sigma_u d\vec{x}_2 \int \Phi' d\vec{x}_1 \int n_d \sigma_d d\vec{x}_2}{\int \Phi' d\vec{x}_1 \int n_u \sigma_u d\vec{x}_2 \int \Phi d\vec{x}_1 \int n_d \sigma_d d\vec{x}_2} = 1. \tag{5.20}$$

The double ratio of the acceptances is assumed to be 1 as well

$$\kappa := \frac{\langle a_u \rangle_w \langle a'_d \rangle_w}{\langle a'_u \rangle_w \langle a_d \rangle_w} = 1 \tag{5.21}$$

Using the above two relations, (5.20) and (5.21), leads to

$$\delta = \frac{p_u p'_d}{p'_u p_d} = \frac{(1 - \langle \beta_u \rangle_w A)(1 - \langle \beta'_d \rangle_w A)}{(1 - \langle \beta'_u \rangle_w A)(1 - \langle \beta_d \rangle_w A)}. \tag{5.22}$$

This is a second order equation for the asymmetry A:

$$aA^2 - bA + c = 0, \tag{5.23}$$

where

$$\begin{aligned} a &= \delta \langle \beta'_u \rangle_w \langle \beta_d \rangle_w - \langle \beta_u \rangle_w \langle \beta'_d \rangle_w \\ b &= \delta(\langle \beta'_u \rangle_w + \langle \beta_d \rangle_w) - (\langle \beta_u \rangle_w + \langle \beta'_d \rangle_w) \\ c &= \delta - 1. \end{aligned}$$

Thus

$$A = \frac{\pm\sqrt{b^2 - 4ac} + b}{2a}, \tag{5.24}$$

where the sign depends on the sign of the target polarisation P_i. The statistical error of the asymmetry is

$$\begin{aligned}(\delta A)^2 &= \left(\frac{\partial A}{\partial \delta}\sigma_\delta\right)^2 \\ &= \frac{1}{\langle\beta\rangle_w^2}\frac{\langle w^2\rangle}{\langle w\rangle^2 N} \\ &= \frac{\langle w\rangle^2}{\langle w\beta\rangle_w^2}\frac{\langle w^2\rangle}{\langle w\rangle^2 N} \\ &= \frac{\langle w^2\rangle}{\langle w\beta\rangle_w^2}\frac{1}{N}.\end{aligned} \tag{5.25}$$

The applied weight is

$$w = fD|P_b|. \tag{5.26}$$

It is also possible to apply a correction to the first order method to take into account that the number of events in the two target cells is not balanced. Eq. (5.6) then reads [145]

$$A = \frac{1}{2|P_T|(1-\alpha^2)}\left[\frac{\sum_i^{N_u} w_i - \sum_i^{N_d} w_i}{\sum_i^{N_u} w_i^2 + \sum_i^{N_d} w_i^2} - \frac{\sum_i^{N'_u} w_i - \sum_i^{N'_d} w_i}{\sum_i^{N'_u} w_i^2 + \sum_i^{N'_d} w_i^2}\right] \tag{5.27}$$

with the error

$$\delta A = \frac{1}{2|P_T|\sqrt{1-\alpha^2}}\sqrt{\frac{1}{\sum_i^{N_u} w_i^2 + \sum_i^{N_d} w_i^2} + \frac{1}{\sum_i^{N'_u} w_i^2 + \sum_i^{N'_d} w_i^2}}, \tag{5.28}$$

where $\alpha = (r-1)/(r+1)$ and $r = N_u/N_d$ is the acceptance ratio of the two target cells. For the high-p_t sample this ratio is $r \approx 0.60$ leading to $1 - \alpha^2 \approx 0.94$.

P_T is not included in the weight since it varies with time (Fig. 3.6 on page 45) and would introduce a false asymmetry. Therefore only the average target polarisation

$$P_T = \frac{1}{4}(P_u - P_d - P'_u + P'_d) \tag{5.29}$$

is used in the calculation. The use of the two methods leads to equivalent results as will be shown in the course of the systematic studies.

5.3.2 High-p_t Asymmetries

The second order weighted method as outlined in the previous section is used to determine the asymmetry for a sample of high-p_t events. For the asymmetry calculation the data of the different solenoid configurations have to be combined. Only runs within a given data taking period (usually one week) are combined. Between two periods a machine development of the accelerator led to a break in the COMPASS data taking. During this time also maintenance works at the spectrometer were carried out. To avoid systematic effects due to the combination of data taken with different spectrometer conditions the periods were treated separately. For the analysis of the data taken within one period, there are two different ways to combine the data.

- The *global* configuration (Fig. 5.15, left). All runs belonging to $\Leftarrow\Rightarrow$ configurations, where the solenoid current has a negative or positive sign depending on the microwave configuration, and all runs belonging to $\Rightarrow\Leftarrow$ configurations with the opposite solenoid field are combined. Then the weight of all high-p_t events is used to calculate the asymmetry.

- The *consecutive* configuration (Fig. 5.15, right). The period is split into elements containing a group of runs with one solenoid current configuration and the following group of runs with opposite solenoid current. The asymmetry is calculated for each pair of solenoid current configurations. The weighted average over all pairs is performed to obtain the result for the complete period.

The advantage of the use of the consecutive configuration is that only runs that were taken close in time are combined. The asymmetry extraction is done under the assumption that the spectrometer performance stays constant over time. Since e.g. due to temperature variations, the COMPASS spectrometer is not perfectly stable, even within one week of data taking, the consecutive configurations are used to calculate the final asymmetries. The global configurations are used for consistency checks. If the spectrometer would behave perfectly stable, they should lead to the same result.

Within the data quality procedure it is also checked that the spectrometer conditions for a given configuration were similar. Depending on the spectrometer performance not only pairs of two different solenoid current configurations were combined but also groups of three, when the third configuration was taken in the same conditions as the preceeding two, but different from the following one. This avoids false asymmetries due to detector problems. Single combinations, in which the spectrometer performance changed too much compared to the neighbouring

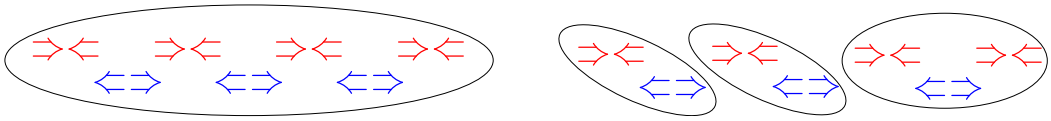

Figure 5.15: Global (left) and consecutive (right) configuration for the asymmetry calculation.

configurations are skipped. The run grouping is given in Appendix A.1. The grouping follows the data quality investigations provided in [141].

Table 5.5 and Fig. 5.16, respectively, show the results of the high-p_t asymmetries for the different periods of the data sample. The results are compatible with $\chi^2/ndf = 2.49$ for 2002 and $\chi^2/ndf = 0.66$ for 2003. In 2002 the results obtained during the periods P2F and P2Ga lead to very different asymmetries compared to the other periods. In the course of the systematic investigations illustrated in the next section it turned out that for these two periods the deviations from the expected behaviour of the false asymmetries is larger than for the other periods indicating either problems during data taking or data production. Therefore P2F and P2Ga were excluded from the analysis. Without P2F and P2Ga the χ^2/ndf for the compatibiliy of the asymmetries in 2002 reduces to $\chi^2/ndf = 0.22$.

The combination of the results obtained for the consecutive configurations for the high-p_t asymmetries for 2002 without P2F and P2Ga and 2003 leads to

$$A_{LL}^{\gamma N \to h_1 h_2 X} = \frac{A_{\parallel}}{D} = -0.019 \pm 0.076(stat.). \tag{5.30}$$

This result is the basis for the determination of the gluon polarisation $\Delta G/G$ carried out in Chapter 6. In the next section systematic uncertainties due to false asymmetries and other quantities that enter the asymmetry extraction are evaluated.

5.4 Systematic Errors

5.4.1 False Asymmetries

For the determination of the high-p_t asymmetry it is very important that the data have been taken under stable spectrometer conditions. Therefore quality and stability checks are performed and the data are grouped in configurations with similar spectrometer performance for the asymmetry calculation. For the asymmetry calculation it is assumed that the target does not move. However, it is known that with the reversal of the solenoid current the target moves about 500 μm. It is also

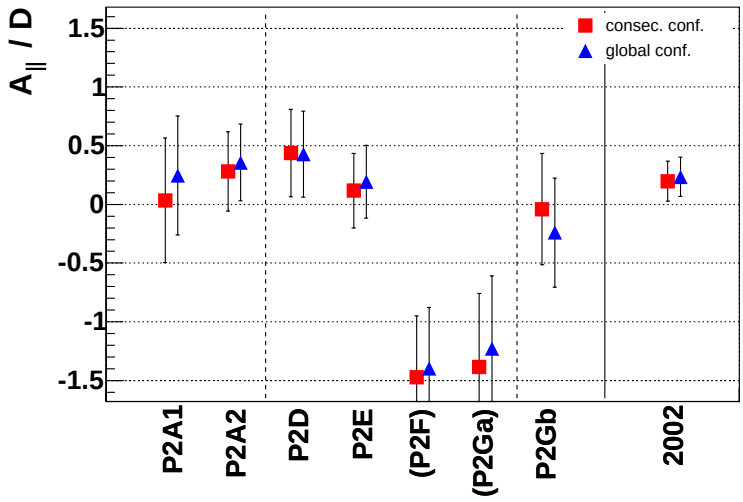

(a) High-p_t asymmetries for 2002: $\frac{A_\parallel}{D} = 0.235 \pm 0.167$. P2F and P2Ga are not included in the average for 2002.

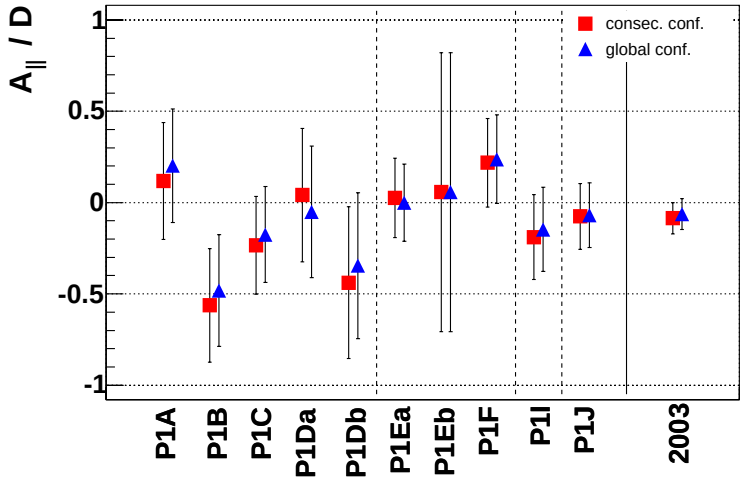

(b) High-p_t asymmetries for 2003: $\frac{A_\parallel}{D} = -0.085 \pm 0.086$.

Figure 5.16: High-p_t asymmetries for 2002(a) and 2003(b). The vertical dashed lines indicate microwave polarisation reversals. The red squares denote the asymmetries obtained with the consecutive configuration, the blue triangles the asymmetries obtained with the global configuration. The very right point is the weighted average over the periods. The exact numbers can be found in Table 5.5. Note the different scales for 2002 and 2003.

possible that the change of the solenoid current has an effect on the spectrometer itself and not only on the target. This is visible in the first Micromega detector behind the target, where the hit distribution is slightly different for the two solenoid currents.

Table 5.5: High-p_t asymmetries for 2002 and 2003 calculated for the consecutive (c.c) and the global (g.c.) configuration. The target polarisation P_T is averaged over the corresponding time interval. P2F and P2Ga are not included in the average for 2002.

	events	A (c. c.)	A (g. c.)	$\langle P_T \rangle$
P2A1	602	0.034 ± 0.531	0.246 ± 0.506	52.6
P2A2	1415	0.281 ± 0.338	0.358 ± 0.327	52.4
P2D	1196	0.438 ± 0.373	0.428 ± 0.366	50.9
P2E	1685	0.117 ± 0.317	0.194 ± 0.310	50.3
(P2F)	654	-1.472 ± 0.522	-1.397 ± 0.520	47.7
(P2Ga)	483	-1.385 ± 0.625	-1.227 ± 0.620	48.0
P2Gb	882	-0.041 ± 0.474	-0.240 ± 0.465	47.1
2002	5780	0.235 ± 0.167	0.198 ± 0.172	
P1A	1704	0.118 ± 0.320	0.202 ± 0.311	49.5
P1B	1607	-0.563 ± 0.311	-0.481 ± 0.306	51.8
P1C	2237	-0.233 ± 0.268	-0.175 ± 0.263	51.4
P1Da	1183	0.041 ± 0.365	-0.051 ± 0.360	51.2
P1Db	1004	-0.439 ± 0.416	-0.345 ± 0.400	52.4
P1Ea	3420	0.025 ± 0.217	-0.001 ± 0.211	51.9
P1Eb	252	0.057 ± 0.764	0.057 ± 0.764	51.7
P1F	2932	0.218 ± 0.243	0.238 ± 0.242	48.2
P1I	3061	-0.189 ± 0.232	-0.147 ± 0.231	50.5
P1J	5200	-0.076 ± 0.180	-0.069 ± 0.177	49.5
2003	22600	-0.085 ± 0.086	-0.063 ± 0.084	

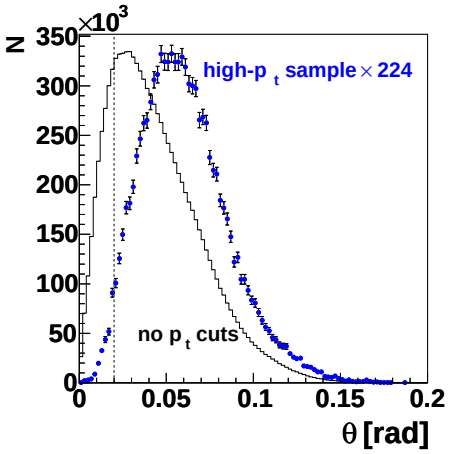

Figure 5.17: Scattering angle θ in the laboratory with (blue points) and without (black histogram) high-p_t cuts. The vertical dashed line indicates the cut on $\theta_{lab} > 0.02\,\text{rad}$ for the all-p_t sample. The histogram for the high-p_t sample is scaled by a factor of 224.

To avoid systematic effects due to target movement and changes in the spectrometer performance a microwave reversal is performed at least once per beamtime. The microwave reversal, i.e. repolarising each target cell with the opposite polarisation, leads to an opposite spin configuration with the same solenoid current (Fig. 5.14). If the same amount of data has been taken with the two different microwave settings these false asymmetries cancel out. Usually the different microwave configurations are only approximately balanced and eventual false asymmetries have to be investigated. Additionally there could be further unknown effects in the behaviour of the spectrometer that could lead to acceptance changes for different configurations and thus to false asymmetries.

Several approaches to investigate the different sources of false asymmetries are described in this section. All the following studies are not performed with the high-p_t sample due to the limited statistics, but with

- no cut on $p_t > 0.7\,\text{GeV/c}$ for both hadrons
- no cut on $p_{t1}^2 + p_{t2}^2 > 2.5\,\text{GeV}^2/\text{c}^2$
- no cut on $m(h_1, h_2) > 1.5\,\text{GeV/c}^2$.

To ensure that the same detector regions are populated a cut on the minimum scattering angle θ_{lab} in the laboratory frame is performed

- $\theta_{lab} > 0.02\,\text{rad}$.

Fig. 5.17 shows θ_{lab} for the high-p_t sample and the sample without the cuts mentioned above. The high-p_t sample populates regions of larger angles. The event sample prepared in this way will in the following be referred to as all-p_t sample in contrast to the high-p_t sample. It contains about 150 times more events than the high-p_t sample.

5.4.2 Configurations with no Physical Asymmetry expected

To verify the assumptions made for the asymmetry calculation like constant accepance ratio and stable behaviour of the spectrometer in time, it is necessary to isolate those effects due to the spectrometer from the physics asymmetries due to the polarised target. Therefore the data is divided in such a way that the physics asymmetries do not play a role in this investigations. This can be done either by looking only at one target cell or by using only data taken with one solenoid configuration.

Asymmetries for one Target Cell

For the asymmetry calculation it is assumed that the double ratio of the acceptance and also the double ratio of the luminosities and cross sections (integrated over the accessible phase space) is unity:

$$\frac{a_u a'_d}{a'_u a_d} = \frac{\Phi n_u \sigma_u \, \Phi' n_d \sigma_d}{\Phi' n_u \sigma_u \, \Phi n_d \sigma_d} = 1. \tag{5.31}$$

With the data it is not possible to check the two ratios separately since e.g. the acceptance alone is difficult to access but the product

$$\frac{a_u a'_d}{a'_u a_d} \cdot \frac{\Phi n_u \sigma_u \, \Phi' n_d \sigma_d}{\Phi' n_u \sigma_u \, \Phi n_d \sigma_d} = 1 \tag{5.32}$$

can be addressed. Therefore the ratio of the events $N = \sigma \Phi n_i a = \sigma \mathcal{L}_i a$, with the luminosity $\mathcal{L}_i = \Phi n_i$, is checked:

$$\frac{a_u \mathcal{L}_u}{a_d \mathcal{L}_d} = \frac{a'_u \mathcal{L}'_u}{a'_d \mathcal{L}'_d}. \tag{5.33}$$

The acceptance changes with the reversal of the solenoid field. As long as the relative change is the same for both target cells the acceptance cancels, the above assumptions about the ratios are justified and no false asymmetries appear. Only different changes in the acceptance for the two cells lead to $\frac{a_u a'_d}{a'_u a_d} \neq 1$ and thus to false asymmetries.

To confirm the assumption about the event ratio with the data, an asymmetry is calculated in such a way that no physical asymmetry is measured, but only false asymmetries due to acceptance effects would appear. Therefore the data from each target cell are treated separately and each cell is divided in two halves which are assumed to have opposite spins (Fig. 5.18). For each cell the asymmetry is calculated between the two halves and it is expected to be zero. The results for

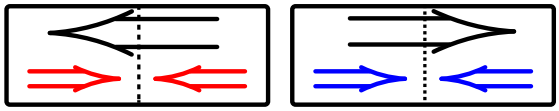

Figure 5.18: Asymmetries inside one target cell: to check the acceptances for the different solenoid currents, the asymmetry for one target cell is calculated. Therefore both cells are divided in an upstream and downstream half and treated as if they were oppositely polarised as indicated in the plot.

the asymmetries in the two halves of the upstream and downstream cell are given in Fig. 5.19. The weighted average over all periods leads to

$$\begin{aligned} A(2002,\ \text{upstream cell}) &= -0.004 \pm 0.034(stat.) \\ A(2002,\ \text{downstream cell}) &= -0.011 \pm 0.030(stat.) \end{aligned}$$

for 2002 without P2F and P2Ga and for 2003:

$$\begin{aligned} A(2003,\ \text{upstream cell}) &= 0.002 \pm 0.017(stat.) \\ A(2003,\ \text{downstream cell}) &= 0.025 \pm 0.015(stat.). \end{aligned}$$

Except the results for the downstream cell in 2003, which deviates from zero by less than 2 standard deviations, the asymmetries are compatible with zero within one standard deviation as expected. It has to be kept in mind that this method only allows to detect false asymmetries related to the variation of the ratio $\frac{a_u n_u}{a_d n_d}$ for one cell, i.e. u and d refer to the upstream and downstream halves of a given cell. A realistic false asymmetry calculated over the full target might be larger than what is estimated here.

Fake Configuration

To investigate the behaviour of the spectrometer in time, e.g. a continuous decrease of the efficiency of some detectors, a so-called *fake* configuration is used. As for the asymmetry in one target cell the data are combined in a way that no physical asymmetry is expected, however for this studies not in space but in time. Only configurations with the same solenoid current (SC) sign are combined to extract an asymmetry. Fig. 5.20 illustrates the grouping of the data. One $\Leftarrow\Rightarrow$ configuration is combined with the next $\Leftarrow\Rightarrow$ configuration that is treated as $\Rightarrow\Leftarrow$ configuration (i.e. with negative sign) so an asymmetry calculated from the two $\Leftarrow\Rightarrow$ constellations is expected to be zero. In Fig. 5.21 the results for the fake configuration are given period by period. The weighted average over the periods for 2002 without P2F and P2Ga leads to

$$\begin{aligned} A(2002,\ \text{neg. SC}) &= 0.003 \pm 0.032(stat.) \\ A(2002,\ \text{pos. SC}) &= -0.014 \pm 0.034(stat.) \end{aligned}$$

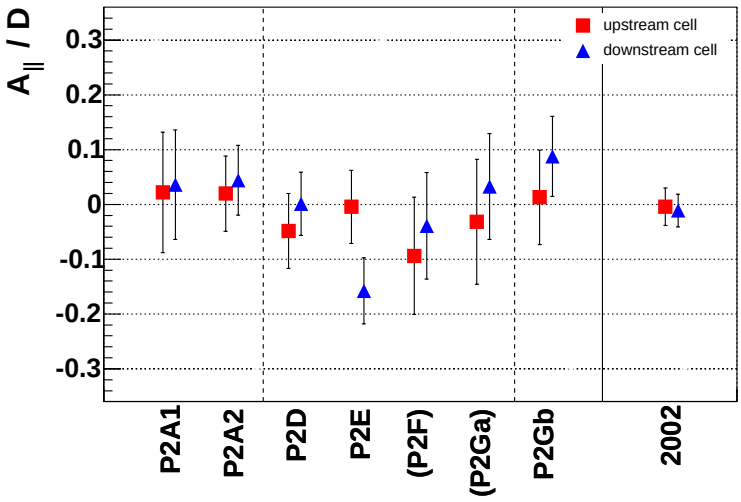

(a) False asymmetries inside one target cell for 2002. P2F and P2Ga are not included in the average for 2002.

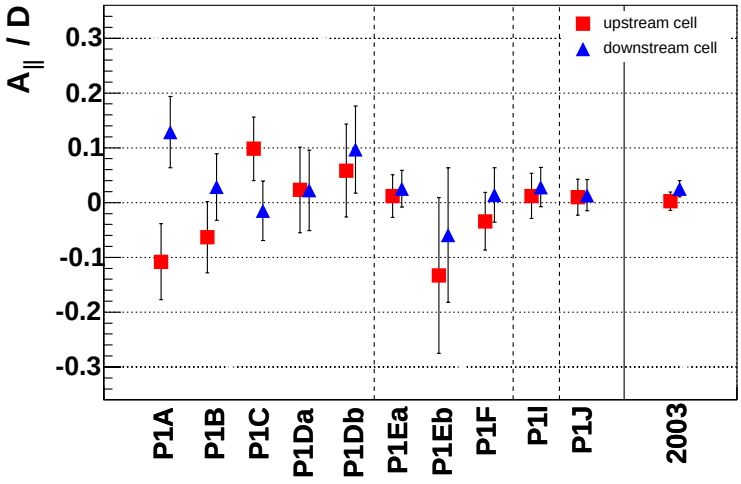

(b) False asymmetries inside one target cell for 2003

Figure 5.19: False asymmetries inside one target cell for 2002(a) and 2003(b). The vertical dashed lines indicate microwave polarisation reversals. The red squares denote the asymmetries obtained for the upstream cell, the blue triangles the asymmetries obtained for the downstream cell. The very right point is the weighted average over the periods. The exact numbers can be found in Table A.6. Note that the scale is different by a factor 5 for 2002 and a factor 3 for 2003 from the plots for the high-p_t sample shown in Fig. 5.16.

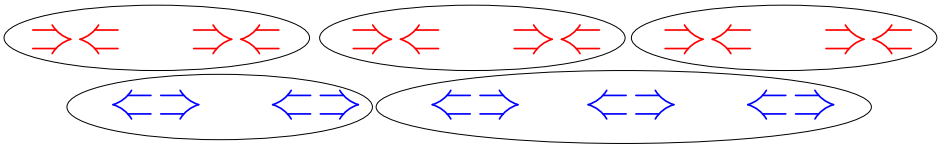

Figure 5.20: Fake Configuration used for the false asymmetry determination.

and for 2003

$$\begin{aligned} A(2003,\ \text{neg. SC}) &= -0.004 \pm 0.016(stat.) \\ A(2003,\ \text{pos. SC}) &= -0.004 \pm 0.016(stat.). \end{aligned}$$

All results are compatible with zero within their statistical errors. This indicates that the variation of the spectrometer in time does not lead to false asymmetries.

5.4.3 False Asymmetry with the Different Microwave Settings

If the properties of the apparatus depend on the orientation of the solenoid field, a false asymmetry can appear. The microwave polarisation reversal suppresses these false asymmetries since they should cancel when combining the data from the two microwave configurations.

For a given microwave configuration (a) and b) in Fig. 5.14) the asymmetry, labelled as A_+, is calculated with the acceptance corrected first order method (Eq. (5.27)):

$$A_+ = \frac{1}{2|P_T|(1-\alpha^2)} \left[\frac{\sum_i^{N_+^{\rightleftarrows}} w_i - \sum_i^{N_+^{\leftrightarrows}} w_i}{\sum_i^{N_+^{\rightleftarrows}} w_i^2 + \sum_i^{N_+^{\leftrightarrows}} w_i^2} + \frac{\sum_i^{N'^{\rightleftarrows}_+} w_i - \sum_i^{N'^{\leftrightarrows}_+} w_i}{\sum_i^{N'^{\rightleftarrows}_+} w_i^2 + \sum_i^{N'^{\leftrightarrows}_+} w_i^2} \right]. \quad (5.34)$$

Eq. 5.34 can be decomposed in the photon-nucleon asymmetry $A^{\gamma N}$ and a false asymmetry A_f.

$$\begin{aligned} A_+ &= \frac{1}{2|P_T|(1-\alpha^2)} \left[\frac{\sum_i^{N_{u+}} w_i - \sum_i^{N_{d+}} w_i}{\sum_i^{N_{u+}} w_i^2 + \sum_i^{N_{d+}} w_i^2} - \frac{\sum_i^{N'_{u+}} w_i - \sum_i^{N'_{d+}} w_i}{\sum_i^{N'_{u+}} w_i^2 + \sum_i^{N'_{d+}} w_i^2} \right] \quad (5.35) \\ &= A^{\gamma N} + A_f \end{aligned}$$

with the $\overleftrightarrows$ configuration in the upstream cell ($N_+^{\overleftrightarrows} = N_{u+}$) for one solenoid current. For the opposite solenoid current, described with the primed notation, the

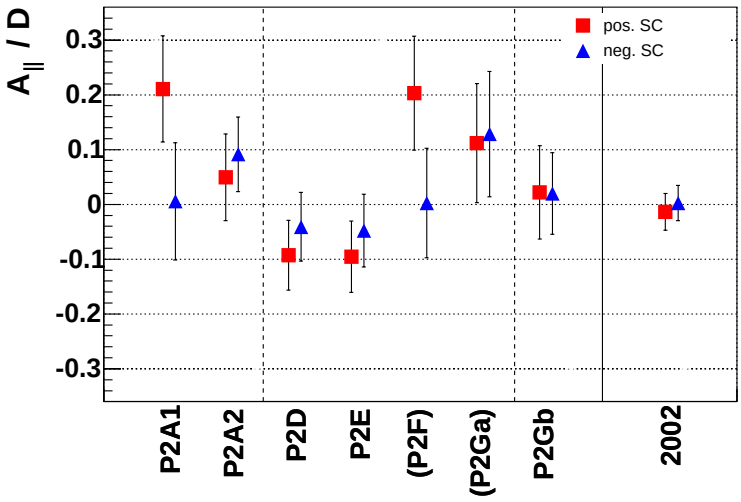

(a) Fake configuration asymmetries for 2002. P2F and P2Ga are not included in the average for 2002.

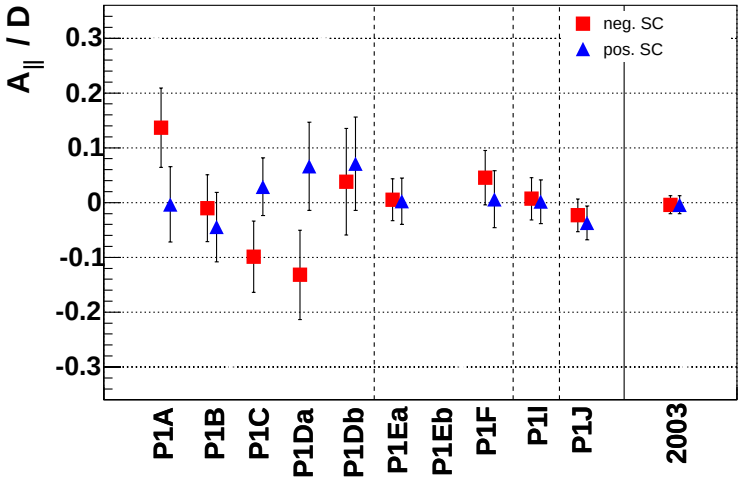

(b) Fake configuration asymmetries for 2003

Figure 5.21: Asymmetries obtained for the fake configuration for 2002(a) and 2003(b). The vertical dashed lines indicate microwave polarisation reversals. The red squares denote the asymmetries obtained for negative solenoid current, the blue triangles the asymmetries obtained for positive solenoid current. The very right point is the weighted average over the periods. The exact numbers can be found in Table A.7. Note that the scale is different by a factor 5 for 2002 and a factor 3 for 2003 from the plots for the high-p_t sample shown in Fig. 5.16. P1Eb contains only one positive and one negative solenoid configuration, therefore it is not possible to determine an asymmetry for the fake configuration for this period.

$\overleftrightarrows$ configuration is measured in the downstream cell ($N_+^{\overleftrightarrows} = N'_{d+}$), etc.

For the second microwave setting (c) and d) in Fig. 5.14) the polarisations are reversed and u and d exchange in the above equations, i.e. to obtain $A^{\gamma N}$, now labelled as A_-, with the second microwave setting, $N_{d-} - N_{u-}$ has to be calculated instead of $N_{u+} - N_{d+}$ as done in the first case:

$$\begin{aligned} A_- &= \frac{1}{2|P_T|(1-\alpha^2)} \left[\frac{\sum_i^{N_-^{\overleftrightarrows}} w_i - \sum_i^{N_-^{\leftleftarrows}} w_i}{\sum_i^{N_-^{\overleftrightarrows}} w_i^2 + \sum_i^{N_-^{\leftleftarrows}} w_i^2} + \frac{\sum_i^{N'^{\overleftrightarrows}_-} w_i - \sum_i^{N'^{\leftleftarrows}_-} w_i}{\sum_i^{N'^{\overleftrightarrows}_-} w_i^2 + \sum_i^{N'^{\leftleftarrows}_-} w_i^2} \right] \quad (5.36) \\ &= \frac{1}{2|P_T|(1-\alpha^2)} \left[\frac{\sum_i^{N_{d-}} w_i - \sum_i^{N_{u-}} w_i}{\sum_i^{N_{d-}} w_i^2 + \sum_i^{N_{u-}} w_i^2} - \frac{\sum_i^{N'_{d-}} w_i - \sum_i^{N'_{u-}} w_i}{\sum_i^{N'_{d-}} w_i^2 + \sum_i^{N'_{u-}} w_i^2} \right] \\ &= -\frac{1}{2|P_T|(1-\alpha^2)} \left[\frac{\sum_i^{N_{u-}} w_i - \sum_i^{N_{d-}} w_i}{\sum_i^{N_{u-}} w_i^2 + \sum_i^{N_{d-}} w_i^2} - \frac{\sum_i^{N'_{u-}} w_i - \sum_i^{N'_{d-}} w_i}{\sum_i^{N'_{u-}} w_i^2 + \sum_i^{N'_{d-}} w_i^2} \right] \\ &= A^{\gamma N} - A_f \end{aligned}$$

This results in a minus sign for A_f, which does not depend on the spins and therefore is not affected by the microwave polarisation reversal. It is always calculated in the same way (here $N_u - N_d$) and as a consequence of the overall minus sign in the above equation A_f changes sign.

This leads to two equations for the photon-nucleon asymmetry $A^{\gamma N}$ and the false asymmetry A_f for the two microwave settings:

$$A_+ = A^{\gamma N} + A_f \quad (5.37)$$

$$A_- = A^{\gamma N} - A_f. \quad (5.38)$$

By measuring both asymmetries A_+ and A_- one can extract $A^{\gamma N}$ and A_f

$$A^{\gamma N} = \frac{1}{2}(A_+ + A_-) \quad (5.39)$$

$$A_f = \frac{1}{2}(A_+ - A_-). \quad (5.40)$$

Determining the arithmetic mean of A_+ and A_-, A_f cancels completely and one measures $A^{\gamma N}$. Since the number of events obtained for the two microwave configurations is different, the statistical error

$$\delta A^{\gamma N} = \frac{1}{2}\sqrt{(\delta A_+)^2 + (\delta A_-)^2} \quad (5.41)$$

would be dominated by the smaller sample. Therefore $A^{\gamma N}$ is calculated using the weighted average. This means that the false asymmetry cancels only partially

and a remaining fraction has to be taken into account for the systematic error. To determine the remaining fraction the asymmetries for the all-p_t sample have been calculated. The results for the consecutive configuration for the different periods are shown in Fig. 5.22. For comparison the asymmetries obtained with the corrected first order and the second order method are given. The results for the corrected first order method are averaged for the two microwave settings in Table 5.6. Combining the values for both microwave settings leads to the following result for the false asymmetry A_f. For 2002 without P2F and P2Ga:

$$A_f(2002) = \frac{1}{2}(A_+ - A_-) = -0.018 \pm 0.023 \tag{5.42}$$

and for 2003:

$$A_f(2003) = \frac{1}{2}(A_+ - A_-) = 0.021 \pm 0.011. \tag{5.43}$$

For 2002 the result is compatible with zero within one standard deviation, whereas for 2003 it differs by about two standard deviations from zero indicating a larger false asymmetry.

Adding A_+ and A_- to obtain the final result for the asymmetry A gives

$$\begin{aligned} A &= \frac{A_+/(\delta A_+)^2 + A_-/(\delta A_-)^2}{1/(\delta A_+)^2 + 1/(\delta A_-)^2} \\ &= A^{\gamma N} + \frac{A_f(1/(\delta A_+)^2 - 1/(\delta A_-)^2)}{1/(\delta A_+)^2 + 1/(\delta A_-)^2} \\ &= A^{\gamma N} + A_F. \end{aligned} \tag{5.44}$$

Table 5.6: All-p_t asymmetries for 2002 and 2003 for the different microwave configuration. The weighted average over the periods is calculated. Detailed results can be found in Table A.8. P2F and P2Ga are not included in the average A_+ for 2002.

	periods	A
2002		
A_+	P2D, P2E	0.033 ± 0.032
A_-	P2A1, P2A2, P2Gb	0.069 ± 0.033
2003		
A_+	P1A, P1B, P1C, P1D, P1I	0.025 ± 0.017
A_-	P1E, P1F, P1J	-0.017 ± 0.015

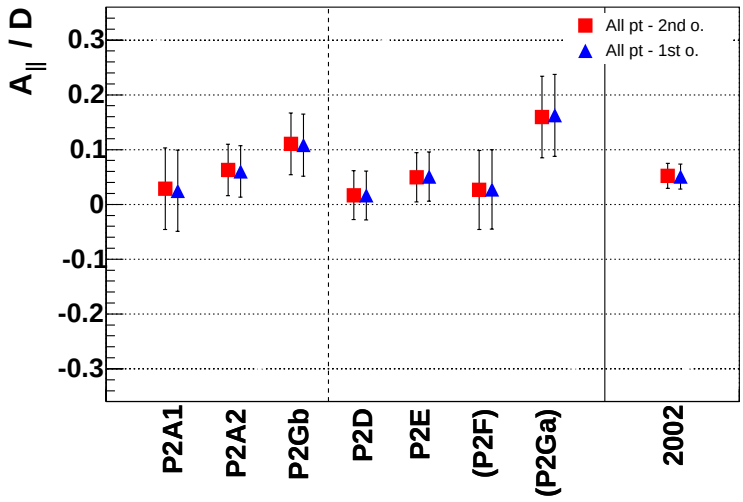

(a) All-p_t asymmetries for false asymmetry studies for 2002. P2F and P2Ga are not included in the average for 2002.

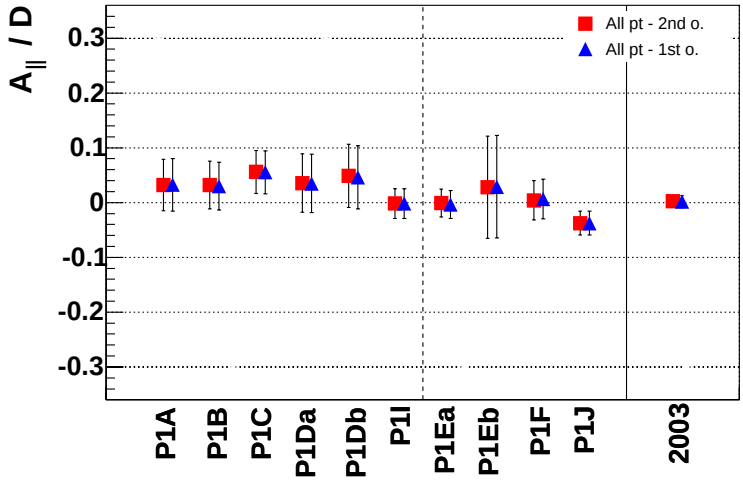

(b) All-p_t asymmetries for false asymmetry studies for 2003.

Figure 5.22: Asymmetries obtained with the all-p_t sample for 2002(a) and 2003(b). The vertical dashed lines indicate microwave polarisation reversals. The blue triangles denote the asymmetries obtained with the corrected first order method, which has been used for this study. For comparison the asymmetries obtained with the second order calculation are plotted (red squares). The very right point is the weighted average over the periods. The exact numbers can be found in Table A.8. Note that the scale is different by a factor 5 for 2002 and a factor 3 for 2003 from the plots for the high-p_t sample shown in Fig. 5.16.

Therefore the false asymmetries cancels only partially and a fraction of the false asymmetry remains. This remaining fraction depends on the balance of the two microwave configurations. The remaining false asymmetry A_F is

$$A_F = A_f \times \frac{(\delta A_-)^2 - (\delta A_+)^2}{(\delta A_-)^2 + (\delta A_+)^2} = \begin{cases} -0.001 \pm 0.001 & (2002,\ \text{no P2F, P2Ga}) \\ 0.002 \pm 0.001 & (2003). \end{cases} \tag{5.45}$$

The remaining false asymmetry A_F is of the same size but opposite sign for 2002 and 2003. In 2002 (without P2F and P2Ga) and 2003 the the amount of data taken with the different microwave settings is about to be equal. The balance of the two settings leads to a small remaining false asymmetry for both years.

5.4.4 Asymmetry Measurement in Different Parts of the Spectrometer

The COMPASS spectrometer is not left right symmetric because of the spectrometer magnets. It is also not perfectly up-down symmetric. In some cases several high voltage channels or readout modules are needed to supply one detector plane. In case of problems this could lead to different behaviour of different parts of the spectrometer. This should not result in large effects, because the tracking system provides redundant information. Additionally, runs with significant detector problems are discarded for the analysis.

However, it could be possible that, for unknown reasons, the upper part of the spectrometer produces a large negative false asymmetry and the lower part produces a large positive asymmetry that cancel in the overall asymmetry calculation and thus would not be visible in the studies described above. To investigate eventual effects of inhomogeneities of the spectrometer the data sample has been split depending on the part of the detector, in which the leading hadron is detected. In one case the sample is divided depending on the leading hadron being detected in the

- upper part
- lower part

of the spectrometer. A second study has been performed depending on the leading hadron being detected on the

- Saleve side (negative x-direction)
- Jura side (positive x-direction)

of the spectrometer (cf. Fig. 3.7 on page 47). The results are shown in Fig. 5.23 for the upper-lower-division and in Fig. 5.24 for the Saleve-Jura studies. The results for 2002 without P2F and P2Ga and 2003 are summarised in Tables 5.7 and 5.8. The difference of the values has been calculated which should be compatible with zero. Looking at Fig. 5.23 it can be seen that for the most periods in 2002, as well as in 2003, the result for the asymmetry in the upper spectrometer lies above the result obtained for the lower spectrometer. In 2002 this is balanced by the last periods and in the average for the complete year this effect cancels. For 2003 this effect last over the year and leads to a difference of the asymmetries with the leading hadron in the upper and lower part of more than two standard deviations. For the asymmetries measured with the leading hadron in the Jura and Saleve side of the spectrometer there is no clear trend for the data taken in 2003 and within the present statistical accuracy no influence on the asymmetry due to the spectrometer being not left-right symmetric can be established from the 2003 data. But in 2002 the differences for P2F and P2Ga exceed 2.5 and 3 standard deviations, respectively. Together with the result on the asymmetries this led to the decision to exclude P2F and P2Ga from the high-p_t asymmetry calculation.

Table 5.7: Asymmetries for the leading hadron detected in the upper and lower part of the spectrometer for 2002 and 2003. The difference between the asymmetries (upper-lower) is calculated. Detailed results for all periods can be found in Table A.9. P2F and P2Ga are not included in the result for 2002.

	A (2002)	A (2003)
upper spec.	0.064 ± 0.032	0.027 ± 0.016
lower spec.	0.039 ± 0.033	-0.023 ± 0.016
upper-lower	0.025 ± 0.045	0.050 ± 0.022

Table 5.8: All-p_t asymmetries with leading hadron detected in Saleve or Jura side of the spectrometer for 2002 and 2003. The difference between the asymmetries (Jura-Saleve) is calculated. Detailed results for all periods can be found in Table A.10. P2F and P2Ga are not included in the result for 2002.

	A (2002)	A (2003)
Jura	0.072 ± 0.033	0.003 ± 0.016
Saleve	0.035 ± 0.031	0.001 ± 0.015
Jura - Saleve	0.037 ± 0.045	0.002 ± 0.022

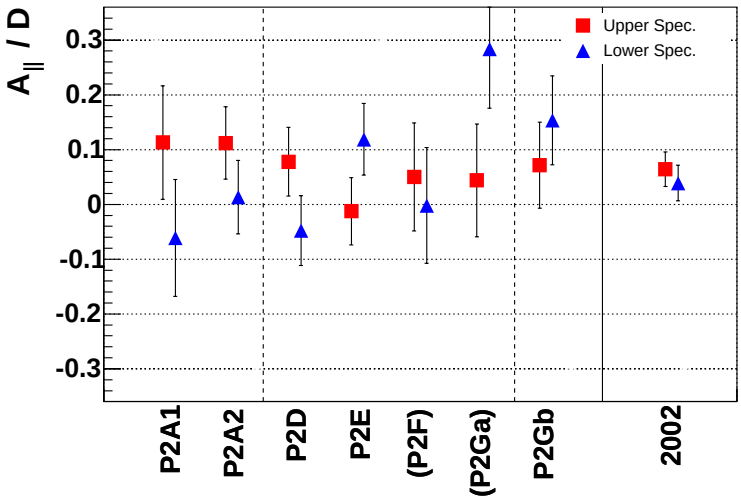

(a) Asymmetries in upper and lower detector for 2002. P2F and P2Ga are not included in the average for 2002.

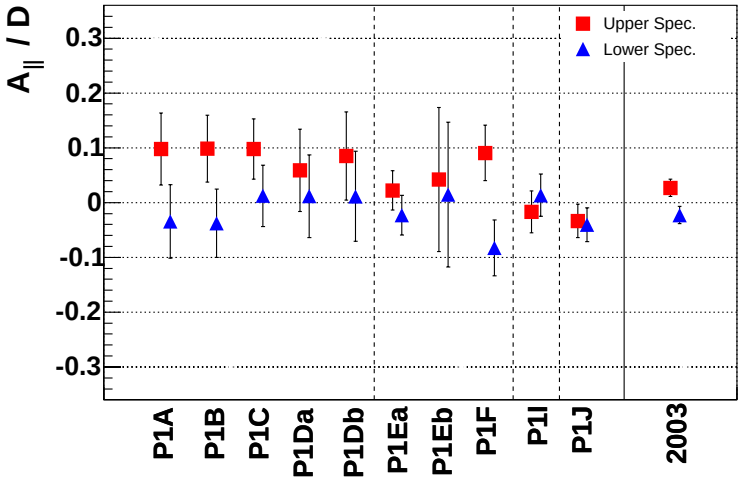

(b) Asymmetries in upper and lower detector for 2003

Figure 5.23: Asymmetries for the leading hadron detected in the upper and lower part of the spectrometer for 2002(a) and 2003(b). The vertical dashed lines indicate microwave polarisation reversals. The red squares denote the asymmetries obtained when the leading hadron is detected in the upper part of the spectrometer, the blue triangles the asymmetries obtained with the leading hadron in the lower part. The very right point is the weighted average over the periods. The exact numbers can be found in Table A.9. Note that the scale is different by a factor 5 for 2002 and a factor 3 for 2003 from the plots for the high-p_t sample shown in Fig. 5.16.

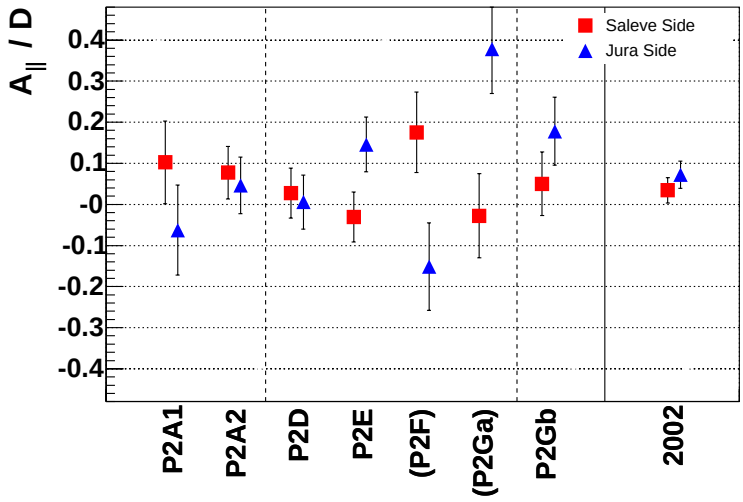

(a) Asymmetries with leading hadron detected in Saleve or Jura side for 2002. P2F and P2Ga are not included in the average for 2002.

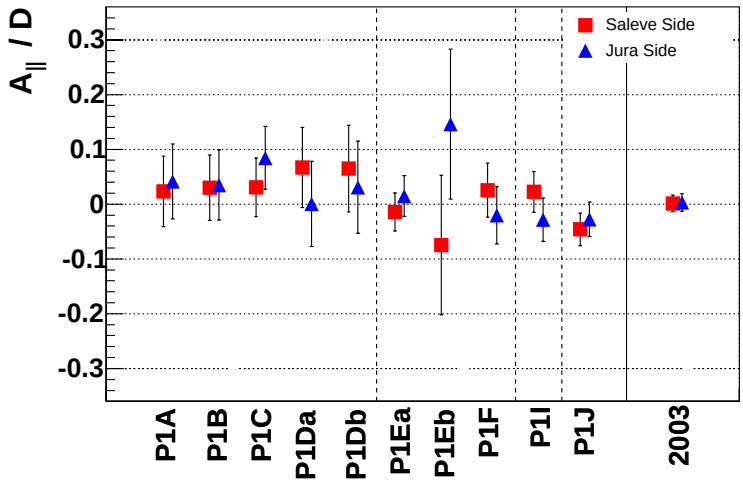

(b) Asymmetries with leading hadron detected in Saleve or Jura side for 2003

Figure 5.24: Asymmetries with leading hadron detected in Saleve or Jura side of the spectrometer for 2002(a) and 2003(b). The vertical dashed lines indicate microwave polarisation reversals. The red squares denote the asymmetries obtained when the leading hadron is detected on the Saleve side of the spectrometer, the blue triangles the asymmetries obtained with the leading hadron on the Jura side. The very right point is the weighted average over the periods. The exact numbers can be found in Table A.10. Note that the scale is different by a factor 4 for 2002 and a factor 3 for 2003 from the plots for the high-p_t sample shown in Fig. 5.16.

5.4.5 Further Sources of Systematic Errors

The weighted event numbers in a given target cell and the target polarisation enter the asymmetry calculation. The single components of the weight $w = fDP_b$ and the target polarisation P_T are obtained from parametrisations or measurements and contain errors. They are summarised in Table 5.9. The beam polarisation P_b is obtained from a parametrisation based on a Monte Carlo simulation and has a relative error of 5%. The depolarisation factor D (Eq. (5.5)) is calculated from the kinematics and contains the parametrisation of the cross section ratio R. The relative error on D is taken to be 5%. The same error is attributed to the dilution factor f, which is obtained from a parametrisation of structure function ratios and contains also a direct measurement of the target material. The target polarisation P_T itself is measured with 5 NMR-coils per cell that give slightly different values leading to a relative error of the target polarisation of 5%.

5.4.6 Combination of the Different Systematic Errors

Error on the Asymmetry due to False Asymmetries

To quantify the systematic error on the high-p_t sample due to false asymmetries or inhomogeneous spectrometer behaviour, the false asymmetry obtained in the previous sections are combined. The results are summarised in Table 5.10. Note that for the studies of the different spectrometer regions, the difference of the asymmetries obtained in the two parts is given as the false asymmetry. For that it is assumed that the false asymmetry in one part is the correct physical asymmetry without any contributions from false asymmetries and the asymmetry measured in the opposite part contains the entire false asymmetry. For 2002 without P2F and P2Ga all results are compatible with zero within one standard deviation. For 2003 this is not the case for the asymmetry measured in the downstream cell, the asymmetry obtained with the different microwave configurations and the difference between the asymmetries obtained when the leading hadron is in the upper part of the spectrometer and in the lower part. The largest systematic effect comes from the difference Saleve-Jura in 2002 and Upper-Lower in 2003.

The systematic error due to false asymmetries is then obtained from the largest

Table 5.9: Summary of further systematic errors of $x = P_b, D, f, P_T$.

x	P_b	D	f	P_T	$\sqrt{\sum \left(\frac{\delta x}{x}\right)^2}$
$\frac{\delta x}{x}$	5%	5%	5%	5%	10%

difference of the asymmetries in the different spectrometer parts. This is Saleve-Jura for 2002 and Upper-Lower for 2003. They are taken as a rectangular distribution of the quantity and are divided by $\sqrt{12}$ to obtain the systematic error. This leads to

$$\delta A(syst., \text{false asym.}) = \begin{cases} \frac{0.037}{\sqrt{12}} = 0.011 & (2002,\ \text{no P2F, P2Ga}) \\ \frac{0.050}{\sqrt{12}} = 0.014 & (2003). \end{cases}$$

Combination of False Asymmetry and the Further Systematic Errors

The other sources of systematic errors as presented in Section 5.4.5 add up to a relative error on the asymmetry of 10%. Combining the systematic errors due to false asymmetries and the other sources leads to

$$\begin{aligned} \delta A(syst.) &= \sqrt{(\delta A(syst., \text{false asym.}))^2 + (\delta A(syst., \text{others}))^2} \\ &= \begin{cases} \sqrt{0.011^2 + (0.1 * (0.235))^2} = 0.026 & (2002) \\ \sqrt{0.014^2 + (0.1 * (-0.085))^2} = 0.017 & (2003). \end{cases} \end{aligned}$$

Table 5.10: Summary of the false asymmetries obtained with the different approaches presented in the last sections. P2F and P2Ga are not included in the results for 2002.

	A (2002)	A (2003)
upstream cell	-0.004 ± 0.034	0.002 ± 0.017
downstream cell	-0.011 ± 0.030	0.025 ± 0.015
fake conf. (-SC)	0.003 ± 0.032	-0.004 ± 0.016
fake conf. (+SC)	-0.014 ± 0.034	-0.004 ± 0.016
false asym. from diff. MW conf.	-0.001 ± 0.001	0.002 ± 0.001
(upper - lower) spectr.	-0.025 ± 0.045	0.050 ± 0.022
(Saleve - Jura) spectr.	0.037 ± 0.045	0.002 ± 0.022

5.5 Final Result for the High-p_t Asymmetry

The results for the high-p_t asymmetry obtained in Section 5.3.2 and the systematic error determined in the last section lead to the following result for the high-p_t asymmetry:

$$\begin{aligned} \frac{A_\parallel}{D} &= 0.235 \pm 0.167(stat.) \pm 0.026(syst.) \quad (2002) \\ \frac{A_\parallel}{D} &= -0.085 \pm 0.086(stat.) \pm 0.017(syst.) \quad (2003) \end{aligned}$$

and the combination of the two years with the weighted average for the systematic error leads to

$$\frac{A_\parallel}{D} = -0.019 \pm 0.076(stat.) \pm 0.019(syst.) \quad (2002 + 2003).$$

Together with the Monte Carlo simulation presented in the next chapter this asymmetry is used to extract the gluon polarisation $\Delta G/G$.

Chapter 6

Extraction of the Gluon Polarisation $\frac{\Delta G}{G}$

The analysis presented in Chapter 5 has prepared a data sample with an enriched photon-gluon fusion signal, the so-called high-p_t sample. For the extraction of the gluon polarisation the exact fraction of photon-gluon fusion events in the high-p_t sample as well as the contributions from leading order and QCD-Compton background have to be determined. Therefore a Monte Carlo simulation with the LEPTO generator has been performed. To obtain a reasonable agreement between data and Monte Carlo, several Monte Carlo parameters had to be adjusted. In this chapter the Monte Carlo simulation and the extraction of the gluon polarisation is documented.

Section 6.1 covers the Monte Carlo simulation with the modified parameters, the comparison of data with Monte Carlo and the extraction of the fractions of leading order, QCD-Compton and photon-gluon fusion events. In Section 6.2 the determination of the gluon polarisation $\Delta G/G$ using the high-p_t asymmetry obtained in Chapter 5 and the results from Section 6.1 is illustrated. In Section 6.3 systematic studies covering the influence of the tuning of the Monte Carlo parameters on the ratio of photon-gluon fusion events is presented and a systematic error due to this on $\Delta G/G$ is evaluated, leading to the final result for $\Delta G/G$ given in Section 6.4. Section 6.5 and 6.6 deal with investigations about the dependence of $\Delta G/G$ on the sum of the transverse momenta of the two hadrons and the momentum fraction of the gluon x_G as well as a first look on the impact of the data taken in 2004.

6.1 The High-p_t Monte Carlo Simulation

The Monte Carlo sample used in this analysis has been generated with the Monte Carlo chain described in Chapter 4. LEPTO 6.5.1 together with JETSET was used for the event generation, COMGEANT for the detector simulation and CORAL for the reconstruction. As for the real data, mDST have been produced so that the Monte Carlo data can be analysed with PHAST in analogy to the real data. The generation of the events with LEPTO has been restricted to kinematic regions accessible with the COMPASS spectrometer and relevant for this analysis. Therefore on the generation level the following cuts have been applied:

- $Q^2 > 0.95\,\mathrm{GeV}^2/\mathrm{c}^2$
- $0.001 < x < 0.95$
- $0.06 < y < 0.94$
- $W > 3\,\mathrm{GeV}/\mathrm{c}^2$
- two outgoing particles with $p_t > 0.6\,\mathrm{GeV/c}$,
  $\theta_{lab}^{h1,h2} < 200\,\mathrm{mrad}$ and
  $x_F > -0.1$.

The Monte Carlo sample produced applying these cuts is then compared to the sample of high-p_t candidates as described in Chapter 5 and after all high-p_t cuts with the high-p_t sample. The comparison of the data with the Monte Carlo high-p_t sample is shown in Section 6.1.2. The LEPTO and JETSET parameters that have been modified, with respect to their default values, are described in the following.

6.1.1 Modified Monte Carlo Parameters

The Monte Carlo generator factorises the lepton-nucleon scattering process into different components as illustrated in Chapter 4. For this analysis modifications have been applied to the hard scattering process, the parton distribution functions and the fragmentation process, with respect to their default settings.

Cut-Offs for the Matrix Elements of the Hard Processes

The LEPTO Monte Carlo generator includes three hard scattering processes, the leading order DIS process and the QCD-corrections with the first order matrix elements for the QCD-Compton and the photon-gluon fusion process. The probability to generate a leading order DIS event P_{LO} is given by

$$P_{LO} = 1 - P_{QCD-C} - P_{PGF}$$

where P_{QCD-C} and P_{PGF} are the probabilities to generate a QCD-Compton and photon-gluon fusion event, respectively. The probabilities P_{QCD-C} and P_{PGF} are given by the integral of the relevant first order matrix elements divided by the overall differential cross section $d\sigma/(dxdQ^2)$. For the calculation of the first order matrix elements a cut-off is introduced to avoid divergences in the QCD-Compton and PGF cross sections, respectively. The cut-off scheme is the so-called $z\hat{s}$-scheme (parameter LST(20) = 5) which is the default in the LEPTO version used. The two cut-off parameters are the energy fraction of the virtual photon carried by the quark $z_{q,min}$ (PARL(8)) with $z_{q,min} < z < 1 - z_{q,min}$ and the c.m. energy $\hat{s}_{min}$ (PARL(9)) of the hard scattering system with $\hat{s} > \hat{s}_{min}$. The default values for these two parameters were optimised for higher energy interactions. This analysis follows the SMC analysis [147] where these parameters have been lowered not to miss QCD-events. The values of the parameters are summarised in Table 6.1.

Parton Distribution Functions

The default parton distribution functions coming with the LEPTO generator are obsolete (CTEQ2L [148]). Therefore the parton distribution functions GRV98LO [130], parametrisations at leading order, have been used.

The Fragmentation Process

The fragmentation of the quarks into hadrons is implemented in LEPTO via JETSET (cf. Section 4.2.4). With the default parameters a (PARJ(41)) and b (PARJ(42)) for the fragmentation function (Eq. (4.2))

$$f(z) \propto \frac{1}{z}(1-z)^a \exp\left(-\frac{bm_\perp^2}{z}\right)$$

the longitudinal variables like p, x_F or z as well as the transverse momentum p_t and the scattering angle θ of the hadron with respect to the virtual photon cannot be described properly. a and b had to be changed to improve the description of p and x_F. Fig. 6.1 illustrates the influence of these changes on the fragmentation function $f(z)$.

To improve the description of the transverse momentum, the parameters controlling the transverse momentum obtained in the fragmentation have been tuned. The Gaussian width $\sigma_{k_\perp}$ = PARJ(21) of the $k_\perp$-spectrum of the hadrons produced in the fragmentation has been reduced. In addition the fraction (PARJ(23)) of admixture and the width (PARJ(24)) of the second broader Gaussian have been enlarged. With this change a reasonable description of the p_t-spectrum of the high-p_t hadrons can be achieved. Fig. 6.2 illustrates the parameters PARJ(21, 23, 24) that have been adjusted.

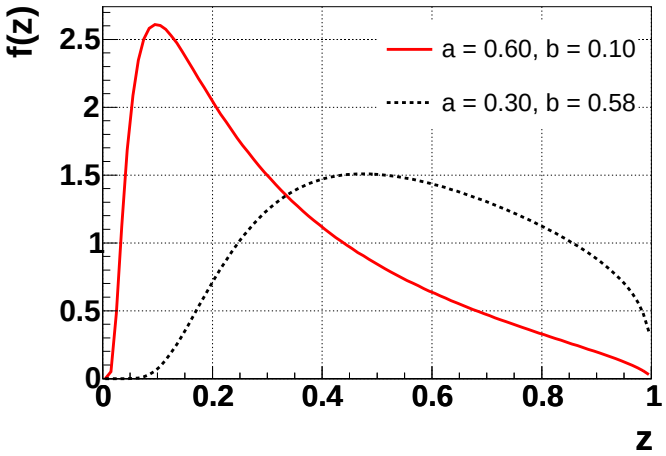

Figure 6.1: Lund fragmentation function $f(z)$. The black dotted curve gives the shape of the fragmentation function Eq. (4.2) for the default LEPTO parameters. The solid red curve is the same function plotted with the modified parameters.

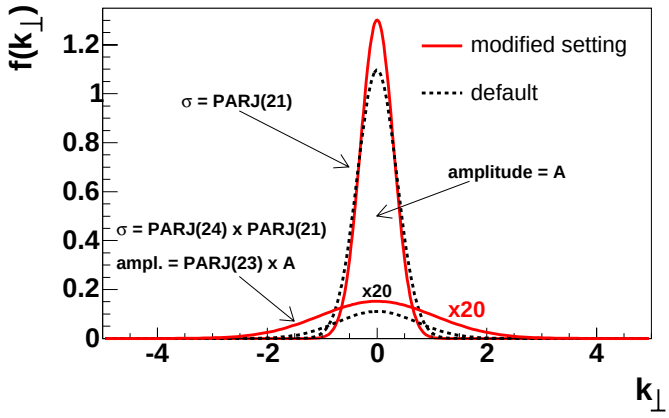

Figure 6.2: Transverse momentum in the fragmentation. The black dotted curves correspond to the default settings. The solid red curves are obtained with the modified parameters. The transverse momentum the hadrons obtain during the fragmentation process is desribed by a Gaussian of width $\sigma = \text{PARJ}(21)$. A second, factor PARJ(23) smaller Gaussian with a larger width $\sigma = \text{PARJ}(24) \times \text{PARJ}(21)$ is used to describe the non Gaussian tails. In the plot the second smaller Gaussians are enlarged by a factor 20. With the modified parameters the Gaussian distribution of the transverse momentum of the hadrons acquired in the fragmenation has a smaller width and the second Gaussian, that is added to describe the tails, is broader and has a larger amplitude than for the default setting.

Summary of the Modified Parameters

Table 6.1 lists all the LEPTO and JETSET parameters that have been modified. To obtain the final parameters that were used in the Monte Carlo simulation the tuning of PARJ(41,42) and PARJ(21, 23, 24) has been done almost separately. This was possible, because the influence of PARJ(41,42) on the transverse momentum and the scattering angle distributions is much smaller than on the momentum or x_F and the other way round for PARJ(21, 23, 24). Fig. 6.3 - 6.5 show the influence of these parameters on the distributions of x_F and p_t as an example. The upper plots compare the 2003 data (yellow histograms) with the Monte Carlo simulation (red points), the lower plots contain the ratio data over Monte Carlo (R = data/MC). It can be seen that the main improvement in the description of x_F comes from PARJ(41,42) and in p_t from PARJ(21, 23, 24). The tuning of the cut-off parameters PARL(8,9) does not have any visible influence on the distributions. Therefore all the plots in Fig. 6.3 - 6.5 contain this modification. The parton distribution functions are GRV98LO. They have been used for all Monte Carlo settings.

6.1.2 Comparison of Data and Monte Carlo

The Monte Carlo sample has been generated with the modified LEPTO as described above and tracked through the full detector simulation and reconstruction procedure. The same preselection cuts as for the real data are applied:

Table 6.1: Summary of the modified Monte Carlo parameters.

parameter		default value	modified value
PARL(8)	matrix element	0.04	0.02
PARL(9)	cut off	$4.0\,\mathrm{GeV}^2/\mathrm{c}^4$	$3.5\,\mathrm{GeV}^2/\mathrm{c}^4$
LST(15)	PDF	4046 (CTEQ2L)	5012 (GRV98LO)
PARJ(21)	transverse mom.	$0.36\,\mathrm{GeV/c}$	$0.30\,\mathrm{GeV/c}$
PARJ(23)	of hadron in the	0.01	0.02
PARJ(24)	fragmentation	2.0	3.5
PARJ(41)	LUND fragm.	0.3	0.6
PARJ(42)	function	$0.58\,\mathrm{GeV}^{-2}$	$0.1\,\mathrm{GeV}^{-2}$

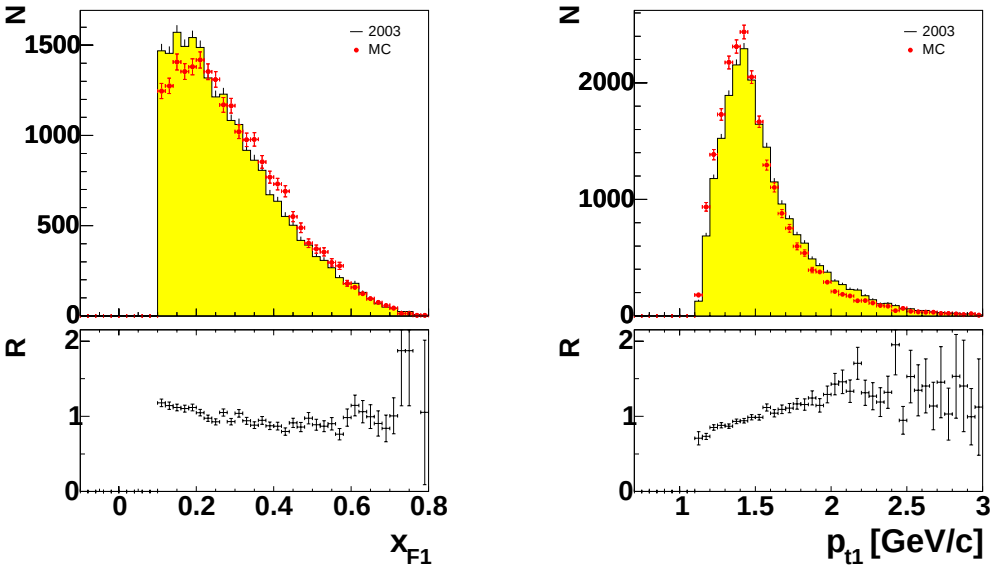

Figure 6.3: x_F and transverse momentum p_t of the leading hadron for LEPTO with default fragementation parameters, PARJ(21,23,24) = (0.36 GeV/c, 0.01, 2.0) and PARJ(41,42) = (0.3, 0.58 GeV^{-2}). R = data/MC is the ratio data over Monte Carlo.

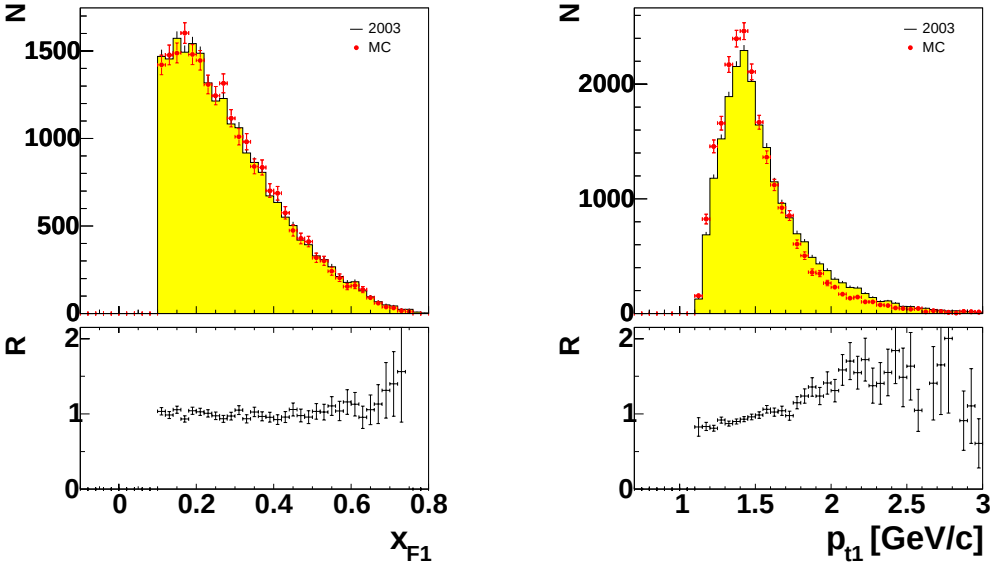

Figure 6.4: x_F and transverse momentum p_t of the leading hadron for PARJ(21,23,24) = (0.36 GeV/c,0.01,2.0) and the modified setting PARJ(41,42) = (0.6,0.1 GeV^{-2}). The agreement for x_F has clearly improved with respect to Fig. 6.3, while for p_t it hardly changed. R = data/MC is the ratio data over Monte Carlo.

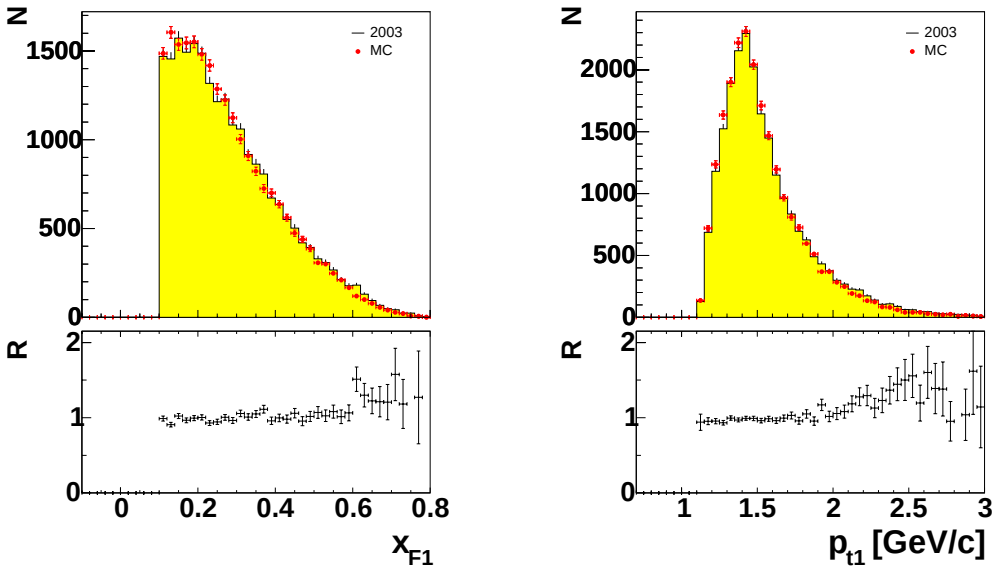

Figure 6.5: x_F and transverse momentum p_t of the leading hadron: final setting, PARJ(21,23,24) = (0.3 GeV/c,0.02,3.5) and PARJ(41,42) = (0.6,0.1 GeV^{-2}). The agreement in x_F stays almost unchanged, while the descripton of p_t improved with respect to Fig. 6.4. R = data/MC is the ratio data over Monte Carlo.

- primary vertex with associated scattered muon

- two hadrons with $p_t \geq 0.7\,\text{GeV/c}$.

The same cuts as for real data, described in Chapter 5, are applied to this sample. With 32296 events the Monte Carlo high-p_t sample contains about 1.5 times the real data statistics for 2003. Since the detector simulation for 2002 and 2003 differs, the comparision of data with Monte Carlo for the two years is separated. After the final cuts the distributions of the Monte Carlo sample are compared to the high-p_t sample of real data. In Fig. 6.6 the comparison of the inclusive variables Q^2, x, y and W for the 2003 data is given. Fig. 6.7, 6.8 and 6.9 show the hadronic variables p, x_F, p_t, $\sum p_t^2$, ϕ and θ, respectively. The upper plots compare 2003 data (yellow histograms) and Monte Carlo (red points), the lower plots contain the ratio data over Monte Carlo (R = data/MC). Because of the larger statistics the 2003 data have been used for the comparison of data with Monte Carlo and the tuning of the Monte Carlo parameters. The modifications of the parameters have been applied to the Monte Carlo for 2002 as well. In this case 22846 Monte Carlo events for 2002 are compared to the 2002 data in Appendix B.2.

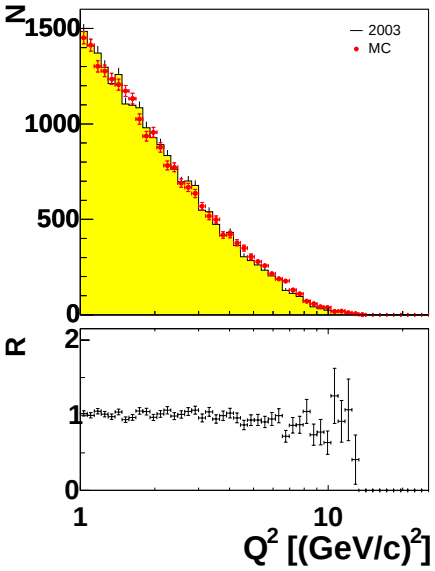

(a) Negative squared four momentum transfer Q^2.

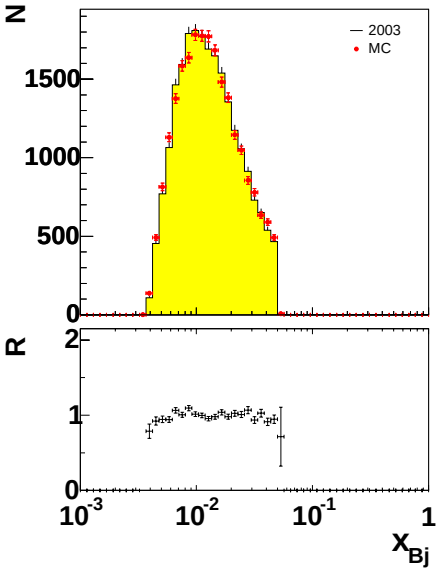

(b) Bjorken variable x.

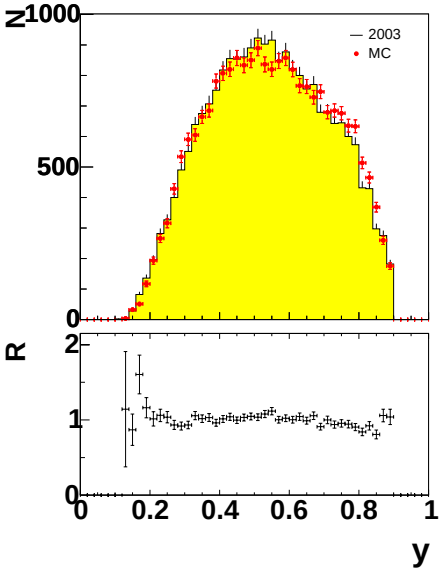

(c) Fractional virtual photon energy y.

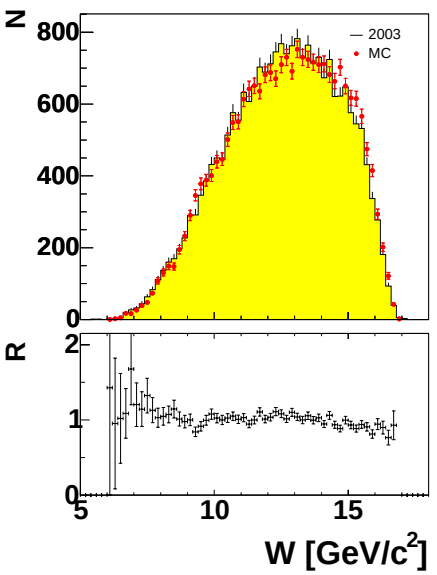

(d) Invariant mass of the photon-nucleon system W.

Figure 6.6: Comparison of 2003 data with Monte Carlo for the inclusive kinematic variables Q^2(a), x_B(b), y(c) and W(d). The histograms are normalised to the number of entries. R = data/MC is the ratio data over Monte Carlo.

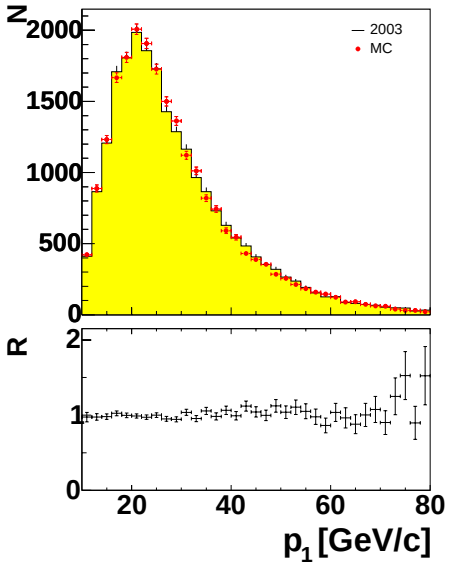

(a) Leading hadron p.

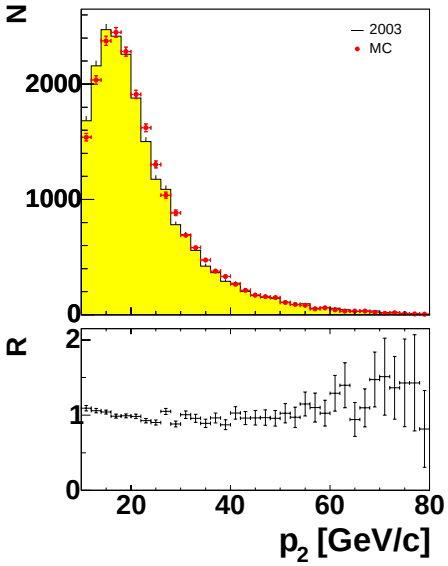

(b) Second hadron p.

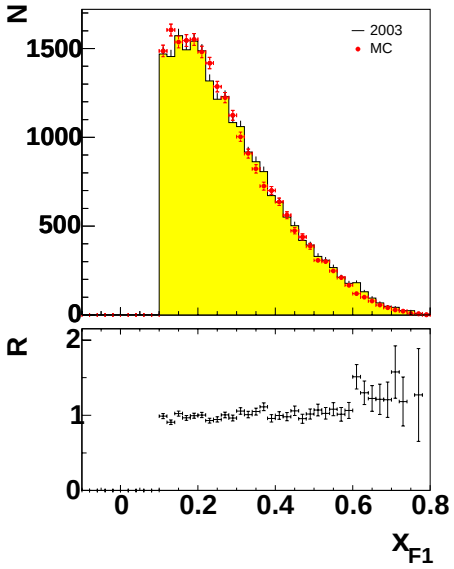

(c) Leading hadron x_F.

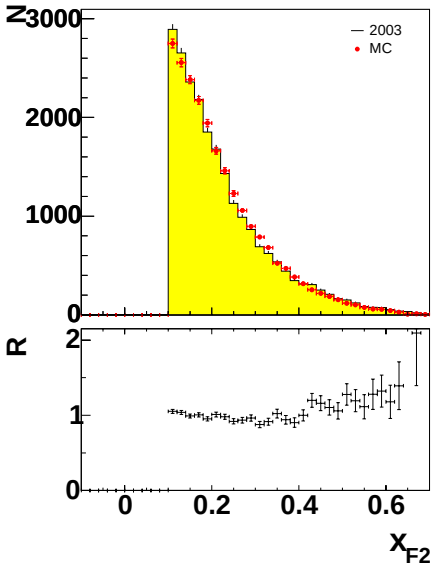

(d) Second hadron x_F.

Figure 6.7: Comparison of 2003 data with Monte Carlo for the momentum of the first (a) and second hadron (b) and x_F of the first (c) and second (d) hadron. The histograms are normalised to the number of entries. R = data/MC is the ratio data over Monte Carlo.

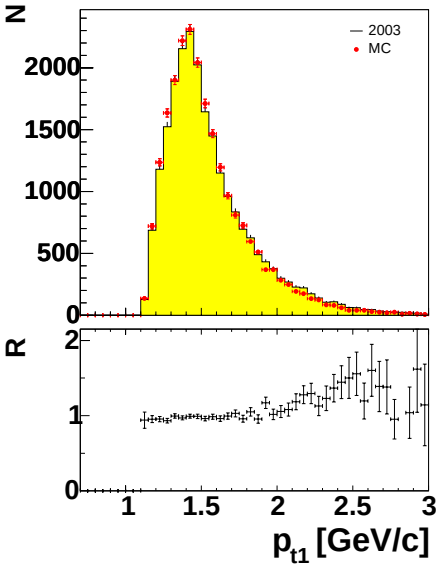

(a) Leading hadron p_t.

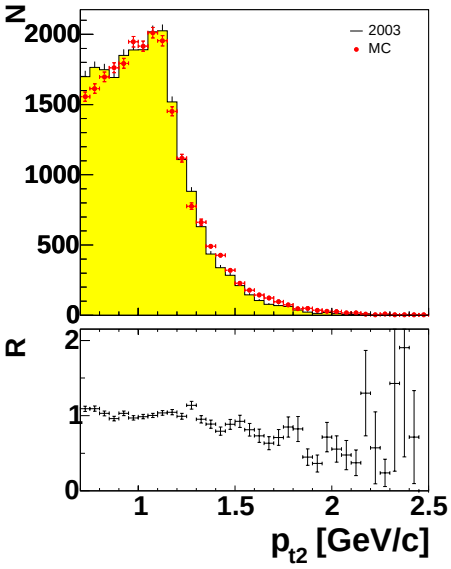

(b) Second hadron p_t.

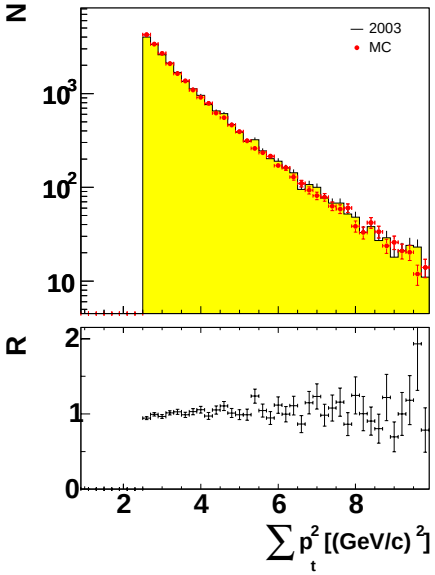

(c) Sum of the transverse momenta squared of the two high-p_t hadrons.

Figure 6.8: Comparison of 2003 data with Monte Carlo for the transverse momentum of the first (a) and second hadron (b) and $\sum p_t^2$ of the two high-p_t hadrons (c). The histograms are normalised to the number of entries. R = data/MC is the ratio data over Monte Carlo.

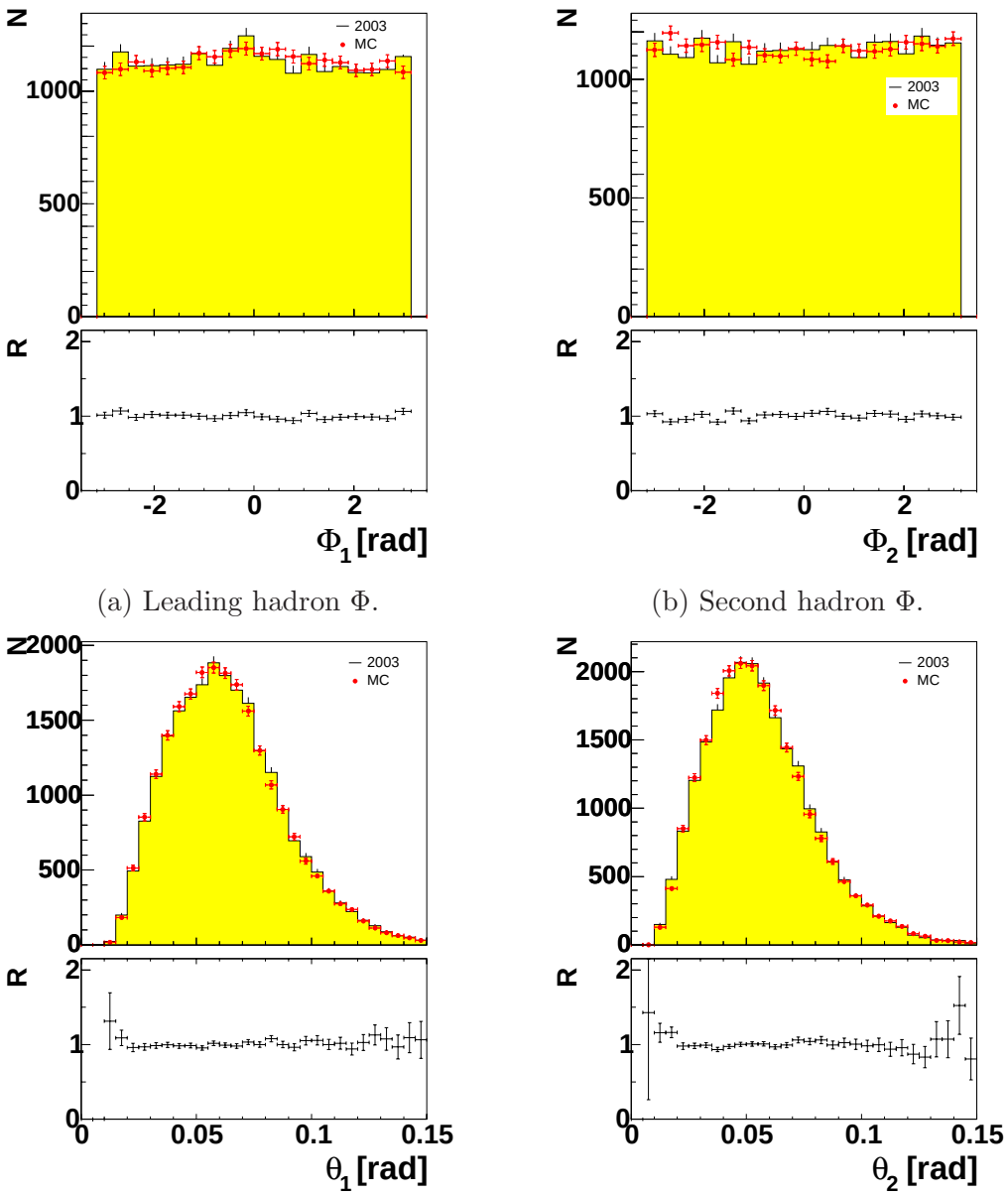

(a) Leading hadron Φ.

(b) Second hadron Φ.

(c) Leading hadron θ.

(d) Second hadron θ.

Figure 6.9: Comparison of 2003 data with Monte Carlo for the azimuthal angle between the outgoing hadron and the lepton scattering plane for the first hadron (a) and the second hadron (b) and the hadron scattering angle with respect to the virtual photon of the first (c) and second hadron (d). The histograms are normalised to the number of entries. R = data/MC is the ratio data over Monte Carlo.

6.2 Results Extracted from the Monte Carlo

To determine the gluon polarisation $\Delta G/G$ based on Equation (2.102)

$$\begin{aligned} \frac{A_{\parallel}^{\mu N}}{D} = A_{LL}^{\gamma N} &= \frac{\Delta G}{G}\langle \hat{a}_{LL}^{PGF}\rangle R_{PGF} + \\ &+ A_1\langle \hat{a}_{LL}^{L.O.}\rangle R_{L.O.} + A_1\langle \hat{a}_{LL}^{QCD-C}\rangle R_{QCD-C} \end{aligned} \tag{6.1}$$

R_{PGF}, R_{LO}, R_{QCD-C} and the analysing powers $\langle \hat{a}_{LL}^{PGF}\rangle$, $\langle \hat{a}_{LL}^{LO}\rangle$, $\langle \hat{a}_{LL}^{QCD-C}\rangle$ of the three processes have to be known. The Monte Carlo sample with the modified parameters gives a reasonable description of the presented kinematic variables and is therefore used to extract these quantities.

Extraction of R_{PGF}

The ratio of photon-gluon fusion events in the Monte Carlo high-p_t sample is

$$R_{PGF} = (36.5 \pm 0.5)\,\%.$$

QCD-Compton events contribute with $(32.5 \pm 0.5)\,\%$ and from leading order events $(31.0 \pm 0.5)\,\%$ are still left after the high-p_t selection. For 2002 the fraction of photon-gluon fusion events is $R_{PGF} = (36.6 \pm 0.6)\,\%$.

The analysing power $\hat{a}_{LL}$

The analysing power $\hat{a}_{LL} = \frac{\Delta\hat{\sigma}}{\hat{\sigma}}$ depends on the kinematics of the hard scattering process that is not known for the real data. Therefore this quantity has to be extracted from Monte Carlo. For the calculation of the $\hat{a}_{LL}$, routines from the Monte Carlo program Poldis [149] are used. They do not calculate the analysing power in the photon-gluon system, but in the muon-gluon system in leading order. Therefore they are divided by the depolarisation factor D to obtain $\hat{a}_{LL}^{\gamma g} = a_{LL}^{\mu g}/D$. The analysing power is calculated event-wise for the Monte Carlo sample depending on the hard scattering process. For leading order and QCD-Compton events not only the analysing power enters in Eq. (6.1), but $\langle \hat{a}_{LL}\rangle \times A_1$, i.e. the analysing power multiplied by the photon-nucleon asymmetry A_1. A_1 has been measured by several experiments and for this calculation it is obtained from a parametrisation based on a fit to the world data [150, 151]. The parametrisation is given in Appendix B.1. A_1 enters event-wise depending on the Bjorken x of the events and therefore $\hat{a}_{LL} \times A_1$ is calculated event by event. The products $\langle \hat{a}_{LL} \times A_1\rangle$ for the leading order and QCD-Compton contribution and the average $\langle \hat{a}_{LL}^{PGF}\rangle$ for the Monte Carlo sample are given in Table 6.2.

The Gluon Momentum Fraction x_G

In this analysis the gluon polarisation is probed at some x_G. x_G is the average momentum fraction of the nucleon that is carried by the struck gluon in the infinite momentum system. It can only be calculated with the knowledge of the kinematics of the photon-gluon fusion process:

$$x_G = \frac{\hat{s} + Q^2}{2M\nu} = x_B \left(\frac{\hat{s}}{Q^2} + 1 \right). \tag{6.2}$$

To obtain this quantity from the reconstructed data, the assumption has been made, that the two high-p_t hadrons have the same direction as the outgoing quarks. The x_G can then be reconstructed with the following approximation for the c.m. energy $\hat{s}$ of the hard scattering system [66]:

$$\hat{s} = \nu^2 \tan\theta_1^{lab} \tan\theta_2^{lab}, \tag{6.3}$$

where θ_1^{lab} and θ_2^{lab} are the scattering angles measured in the laboratory for the first and second hadron, respectively, and ν the energy of the virtual photon. The gluon momentum fraction x_G follows with Eq. (6.2). In Fig. 6.10 (a) x_G for photon-gluon fusion events calculated with the generator information on the hard scattering process for the Monte Carlo high-p_t sample and therefore with the exact knowledge of $\hat{s}$ is given. Fig. 6.10 (b) shows x_G calculated from the information on the reconstructed hadrons for photon-gluon fusion events in the Monte Carlo high-p_t sample for which approximation Eq. (6.3) is used. In Fig. 6.10 (c) the correlation between the two is presented which amounts 0.50. In Fig. 6.10 (d) the x_G calculated from the reconstructed hadron information for the high-p_t data is compared to the high-p_t Monte Carlo sample for all events. The average x_G at which the gluon distribution is probed is taken from Fig. 6.10 (a) being

$$\langle x_G \rangle = 0.12$$

with an RMS of 0.07. In 2002 $\langle x_G \rangle = 0.11$ with an RMS of 0.07.

The Scale

Another important information is the scale at which the gluon distribution is probed. For the leading order process the relevant scale is the Q^2 of the virtual photon. For the photon-gluon fusion events the transverse momentum of the outgoing partons provides the scale. Since high-p_t hadrons are required, we have a high scale and it is ensured that the factorisation of the soft part, the parton distribution functions, and the hard process holds. The average transverse momentum of the outgoing partons is

$$\langle \mu^2 \rangle = \langle k_\perp^2 \rangle = 2.4\,(\mathrm{GeV/c})^2$$

for 2002 and 2003.

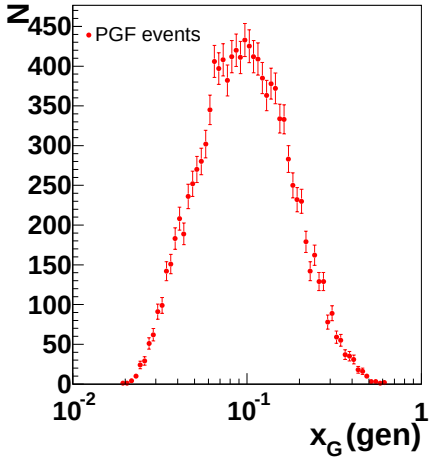

(a) x_G calculated with the generator information of the hard scattering process for the Monte Carlo sample, PGF events only.

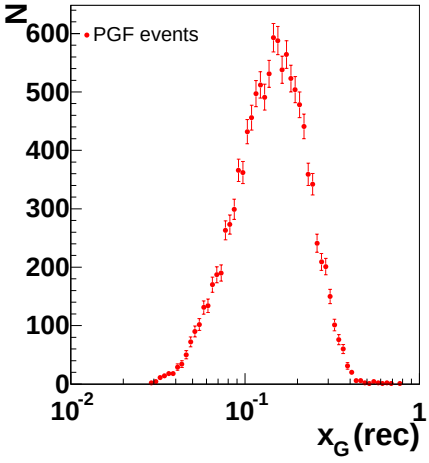

(b) x_G calculated with the information of the two reconstructed hadrons for the Monte Carlo sample, PGF events only.

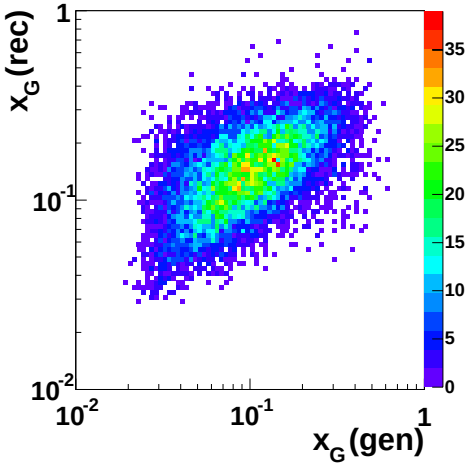

(c) Correlation of the x_G calculated with the information of the two reconstructed hadrons (b) and x_G calculated with the generator information (a), PGF events only.

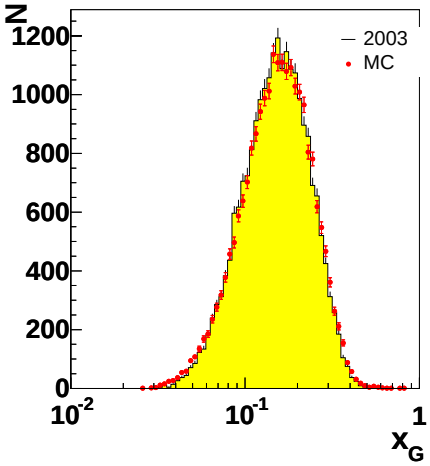

(d) x_G calculated with the information of the two reconstructed hadrons for 2003 data and the Monte Carlo sample (all events).

Figure 6.10: Gluon momentum fraction x_G for the high-p_t sample. Comparison of the gluon momentum fraction x_G obtained with the full information on the hard scattering process from the Monte Carlo generator (a) and x_G calculated from the reconstructed kinematics of the two high-p_t hadrons (b) for PGF events in the Monte Carlo sample, their correlation (c) and the comparison to data for all subprocesses (d).

6.2.1 Determination of $\Delta G/G$

Adding all ingredients obtained in this section and summarised in Table 6.2 leads to the following results for the gluon polarisation

$$\begin{aligned}\frac{\Delta G}{G}(2002) &= -0.927 \pm 0.643\,(stat.), \quad \langle x_G \rangle = 0.11, \ \langle \mu^2 \rangle = 2.4\,(\mathrm{GeV/c})^2 \\ \frac{\Delta G}{G}(2003) &= 0.311 \pm 0.334\,(stat.), \quad \langle x_G \rangle = 0.12, \ \langle \mu^2 \rangle = 2.4\,(\mathrm{GeV/c})^2\end{aligned}$$

The results are compatible within two standard deviations.

Combining the results leads to the final result for the gluon polarisation $\Delta G/G$ in the region $Q^2 > 1\,\mathrm{GeV}^2/\mathrm{c}^2$ measured with the COMPASS spectrometer in the years 2002 and 2003:

$$\begin{aligned}\frac{\Delta G}{G}(2002+2003) &= 0.049 \pm 0.296\,(stat.), \\ &\quad \langle x_G \rangle = 0.11, \ \langle \mu^2 \rangle = 2.4\,(\mathrm{GeV/c})^2.\end{aligned}$$

This result contains only the statistical error. The systematic error due to the choice of the Monte Carlo setting is evaluated in the following section.

Table 6.2: Summary of process ratios and analysing powers for the $\Delta G/G$ calculation for the year 2002 and 2003. The errors are of statistical kind only except for the products with A_1 where the error of the parametrisation is taken into account as well.

	2002	2003
R_{PGF}	$(36.6 \pm 0.6)\,\%$	$(36.5 \pm 0.5)\,\%$
$\langle \hat{a}_{LL}^{PGF} \rangle$	-0.710 ± 0.004	-0.703 ± 0.003
$R_{PGF} \times \langle \hat{a}_{LL}^{PGF} \rangle$	-0.260 ± 0.005	-0.256 ± 0.004
R_{QCD-C}	$(32.4 \pm 0.6)\,\%$	$(32.5 \pm 0.5)\,\%$
$\langle \hat{a}_{LL}^{QCD-C} \times A_1 \rangle$	-0.007 ± 0.014	-0.007 ± 0.014
$R_{QCD-C} \times \langle \hat{a}_{LL}^{QCD-C} \times A_1 \rangle$	-0.002 ± 0.005	-0.002 ± 0.005
R_{LO}	$(31.0 \pm 0.6)\,\%$	$(31.0 \pm 0.5)\,\%$
$\langle \hat{a}_{LL}^{LO} \times A_1 \rangle$	-0.011 ± 0.022	-0.011 ± 0.022
$R_{LO} \times \langle \hat{a}_{LL}^{LO} \times A_1 \rangle$	-0.003 ± 0.006	-0.003 ± 0.006

6.3 Systematic Studies

The modified parameters in the Monte Carlo generator have been chosen to get the best possible agreement between real data and Monte Carlo. A variation can lead to a better agreement for one variable, but at the same time the agreement for others can become worse. The parameters that were chosen lead to a good compromise in the description of all the distributions in the relevant kinematic regions. Since a variation of the Monte Carlo parameters also leads to a change of the quantities extracted from the Monte Carlo, like e.g. the process ratios and analysing powers, the influence of these parameters has to be studied carefully.

The largest effect on R_{PGF} comes from the tuning of the fragmentation. In a first approach the effect of PARJ(41,42) and PARJ(21,23,24) are studied separately and they are combined later. To investigate the influence of the parton distribution functions, the GRV98LO parametrisation is replaced by CTEQ5L. Furthermore the scale μ^2 at which the parton distributions are probed has been varied to $0.5\times\mu^2$ and $2\times\mu^2$. The Monte Carlo generator contains the parton distribution functions and the calculation of the matrix elements for the PGF and QCD-Compton processes in leading order. Next-to-leading order effects are simulated by the parton shower mechanism. Since the calculations of the analysing power is also done in leading order, the parton showers are the only next-to-leading order effects in the Monte Carlo simulation. To check their influence on a consistent leading order analysis, initial and final state parton showers have been switched off.

These systematic studies have been performed with the 2003 data sample only and the result is transfered to the 2002 data. Due to the limited statistics for 2002 no separate studies have been carried out. Results for $\Delta G/G$ using different parameters given in the course of the following systematic studies refer to the 2003 data only.

6.3.1 Variation of the Monte Carlo Parameters

Fragmentation Parameters PARJ(41) and PARJ(42)

The influence of the parameters PARJ(41,42) has been checked by scanning the PARJ(41)-PARJ(42) plane. Fig. 6.11 illustrates the region covered by this studies. The region with acceptable agreement of data and Monte Carlo is marked with an ellipse. The ratio R_{PGF} obtained in this region (with the modified settings for PARJ(21,23,24)) lies between

$$35.5\% \leq R_{PGF} \leq 37.2\%.$$

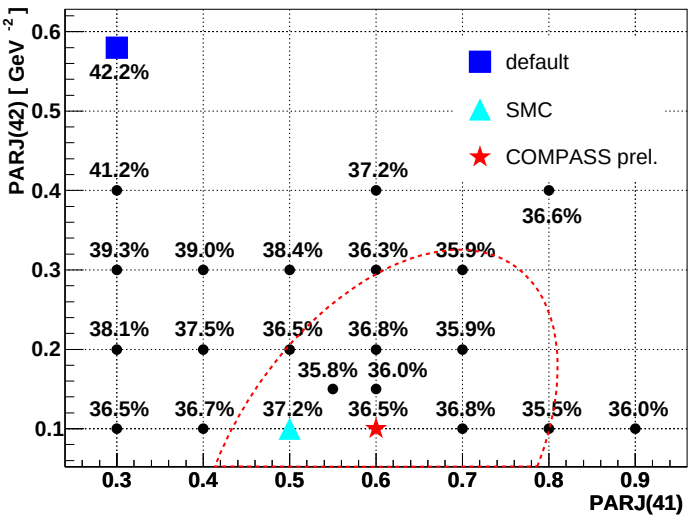

Figure 6.11: R_{PGF} for different settings in PARJ(41)-PARJ(42) plane. The blue square denotes the default values, the red star gives the parameters used in this analysis. For comparison the SMC point is given by the turquoise triangle, the black points correspond to settings that have been compared to the data. The absolute statistical error on the points lies between 0.5 % and 1 %. Not all settings have been studied with the same statistics. The regions around the default value and of larger PARJ(42) have been studied only with the default values for PARJ(21,23,24) and therefore are excluded from the plot.

This corresponds to

$$-0.250 \geq \langle \hat{a}_{LL}^{PGF} \rangle \times R_{PGF} \geq -0.262.$$

Fragmentation Parameters PARJ(21), PARJ(23) and PARJ(24)

Especially the parameter PARJ(21) has a large influence on the p_t distribution and on R_{PGF}. The smaller PARJ(21) the less transverse momentum can be obtained in the fragmentation and less leading order events survive the high-p_t cuts, i.e. R_{PGF} increases. This is partly compensated by the increase of PARJ(23) and PARJ(24) which again decreases R_{PGF}. E.g. combinations like PARJ(21,23,24) = (0.32 GeV/c, 0.025, 3.0) lead to a similar R_{PGF} and to an agreement of data and Monte Carlo that is slightly worse than for the parameters that have been used in the analysis (0.30 GeV/c, 0.02,3.5).

The variation of PARJ(21) only and PARJ(23,24) fixed has a large impact on the p_t distribution as well as on R_{PGF}. To investigate this influence the agreement between data and Monte Carlo has to be quantified. Therefore the ratio

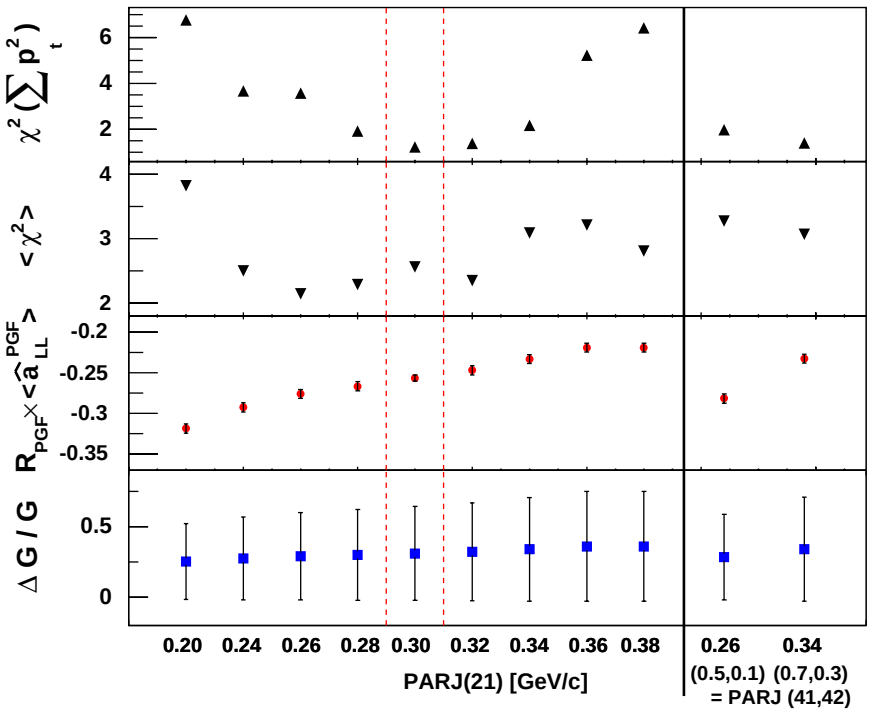

Figure 6.12: Influence of PARJ(21) on the Monte Carlo sample on $R_{PGF} \times \langle \hat{a}_{LL}^{PGF} \rangle$ with PARJ(23,24) = (0.02,3.5) and PARJ(41,42) = (0.6,0.1 GeV^{-2}). The χ^2 per degree of freedom for the compatibility of the ratio data/MC with 1 is calculated for selected variables. It is given as a function of PARJ(21). $\langle \chi^2 \rangle$ is the average for the variables Q^2, x, y, $p_{1,2}$, $p_{t1,t2}$, $x_{F1,F2}$ and $\theta_{1,2}$. The χ^2 for the $\sum p_t^2$ is given separately since the cut on this variable is considered as the main high-p_t cut. The value PARJ(21) between the dashed lines is used in the analysis. The two right points have been used for the estimation of the systematic error with PARJ(21) = 0.26 GeV/c and PARJ(21) = 0.34 GeV/c, respectively, and different parameters PARJ(41,42).

of the normalised histograms as shown in Fig. 6.6 - Fig. 6.9 were used. The χ^2 per degree of freedom for the compatibility of the ratios with 1 was calculated. Fig. 6.12 gives the average χ^2/ndf for the inclusive kinematic variables Q^2, x, y and for the hadronic variables p, p_t, x_F, θ for the first and second hadron ($\langle \chi^2 \rangle$) and for $\sum p_t^2$ ($\chi^2(\sum p_t^2)$) separately. Additionally the resulting $R_{PGF} \times \langle \hat{a}_{LL}^{PGF} \rangle$ and $\Delta G/G$ is plotted for each setting as a function of PARJ(21). While the influence on the average χ^2 is not so big, the χ^2 for $\sum p_t^2$ is more sensitive to a change in PARJ(21). It has been decided to use the values of PARJ(21), where at least one of the χ^2 is not minimal anymore to estimate the systematic error. This is at PARJ(21) = 0.26 GeV/c giving the higher bound of the absolute value of $R_{PGF} \times \langle \hat{a}_{LL}^{PGF} \rangle$ and at PARJ(21) = 0.34 GeV/c giving the lower bound of $R_{PGF} \times \langle \hat{a}_{LL}^{PGF} \rangle$.

An additional variation of PARJ(23,24) for example at PARJ(21)=0.26 GeV/c to larger values leads immediately to a worse agreement between data and Monte Carlo and therefore PARJ(21) = 0.26 GeV/c and PARJ(21) = 0.30 GeV/c are used as minimum and maximum value for the following studies. Reasonable variations of PARJ(23,24) for e.g. PARJ(21) = 0.28 GeV/c lead to results for $R_{PGF} \times \langle \hat{a}_{LL}^{PGF} \rangle$ within these minimum and maximum values.

Combination of the variation of PARJ(21,23,24) and PARJ(41,42)

To add up the effects of the boundary settings for the parameters, the extrema of the PARJ(41,42)-plane have been combined with the minimum and maximum values for PARJ(21). The combination of PARJ(21) = 0.26 GeV/c, which lead to the maximum value for $R_{PGF} \times \langle \hat{a}_{LL}^{PGF} \rangle$, with PARJ(41,42) = (0.5,0.1 GeV^{-2}), that also gives the maximum $R_{PGF} \times \langle \hat{a}_{LL}^{PGF} \rangle$ in the considered region of the PARJ(41,42)-plane, leads to

$$(R_{PGF} \times \langle \hat{a}_{LL}^{PGF} \rangle)_{max} = -0.282 \pm 0.006.$$

Analogous for the combination of parameters that lead to the minimum value:

$$(R_{PGF} \times \langle \hat{a}_{LL}^{PGF} \rangle)_{min} = -0.233 \pm 0.006$$

for PARJ(21,23,24) = (0.34 GeV/c,0.02,3.5) and PARJ(41,42) = (0.7,0.3 GeV^{-2}). The results and the χ^2 for these two combinations of the parameters are given by the two right points in Fig. 6.12. The parameter range within these two extreme settings leads to an acceptable agreement between data and Monte Carlo.

The Parametrisation for the Parton Distribution Functions

Changing the parton distribution functions from GRV98LO [130] to CTEQ5L [131] leads to a significant change in $R_{PGF} \times \langle \hat{a}_{LL}^{PGF} \rangle$

$$(R_{PGF} \times \langle \hat{a}_{LL}^{PGF} \rangle)_{\text{GRV98LO}} = -0.256 \pm 0.004$$

$$(R_{PGF} \times \langle \hat{a}_{LL}^{PGF} \rangle)_{\text{CTEQ5L}} = -0.276 \pm 0.006.$$

The influence of the parton distribution functions on the distributions of the kinematic variables is hardly visible from variables like p or x_F, the agreement in p_t is slightly worse ($\chi^2/ndf = 2.3$), but still acceptable.

The Scale of the Parton Distribution Functions

The change of the scale, at which the parton distributions are probed, to $\mu^2 \rightarrow 0.5\mu^2$ and $\mu^2 \rightarrow 2\mu^2$ causes a change in $R_{PGF} \times \langle \hat{a}_{LL}^{PGF} \rangle$ from

- -0.256 ± 0.004 to -0.248 ± 0.006 (for $0.5\mu^2$)
- -0.256 ± 0.004 to -0.252 ± 0.006 (for $2\mu^2$).

This change is hardly visible in the distributions. For the change to $0.5\mu^2$ the agreement between data and Monte Carlo becomes slightly worse, but is still acceptable.

Parton Shower

The parton showers have a larger influence on analysing power $\langle \hat{a}_{LL}^{PGF} \rangle$, R_{PGF} and the (p_t) distributions than the parameters changed in all other studies. Switching off parton showers $\langle \hat{a}_{LL}^{PGF} \rangle$ changes from 0.7 to 0.8, R_{PGF} from 36.5% to 31.7%, but the product that is relevant for the analysis merely changes from -0.256 ± 0.004 to -0.257 ± 0.005. However, this leads to a disagreement between the real data distributions and the Monte Carlo especially for $\sum p_t^2$. This can partly be cured by changing again PARJ(21) from 0.3 GeV/c to 0.36 GeV/c and PARJ(23,24) to (0.015,2.5), which leads to $R_{PGF} \times \langle \hat{a}_{LL}^{PGF} \rangle = 34.6\% \times (-0.801) = -0.277 \pm 0.007$.

Primordial $k_\perp$ of the Partons Inside the Nucleon

The variation of PARL(8) which describes the primordial $k_\perp$ of the partons inside the nucleon does not influence the distributions. Therefore the default value has been kept.

6.3.2 Combination of the Systematic Errors

Systematic Errors from the Monte Carlo

Table 6.3 summarises the results of the previous section. The largest influence on the result on $R_{PGF} \times \langle \hat{a}_{LL}^{PGF} \rangle$ arises from the change in the fragmentation and the use of different parametrisations for the parton distribution functions. Both lead to a reasonable agreement of data and Monte Carlo with different results for R_{PGF}. Switching off the parton shower mechanism leads to the same result for $R_{PGF} \times \langle \hat{a}_{LL}^{PGF} \rangle$ within the Monte Carlo statistics. But in contrast to all other systematic checks, the agreement between data and Monte Carlo gets worse in case parton showers are switchted off. Only a modification of the fragmentation parameters can improve this, but leads to a difference in $R_{PGF} \times \langle \hat{a}_{LL}^{PGF} \rangle$ of 0.021 relative to the value with parton showers on. Changes of the contributions from leading order and QCD-Compton are neglected since they enter the $\Delta G/G$ calculation in a product with A_1 which makes the term negligible compared to $A_\parallel/D$.

To estimate the total systematic error due to the tuning of the Monte Carlo parameters, the largest difference between $R_{PGF} \times \langle \hat{a}_{LL}^{PGF} \rangle$ of each study and the $R_{PGF} \times \langle \hat{a}_{LL}^{PGF} \rangle$ used for the $\Delta G/G$ extraction are added quadratically:

$$\begin{aligned} \delta\left(R_{PGF} \times \langle \hat{a}_{LL}^{PGF} \rangle\right) &= \sqrt{0.025^2 + 0.020^2 + 0.008^2 + 0.021^2} \\ &= 0.039. \end{aligned}$$

The error has been determined with the comparison of the 2003 data to Monte Carlo simulation and is assumed to be of the same size for 2002. Then it can be translated to an error of $\Delta G/G$ with the expression for $\Delta G/G$ given in Eq. (6.1):

$$\begin{aligned} \frac{\Delta G}{G} &= \frac{A_{\parallel}^{\mu N}/D - \langle A_1 \times \hat{a}_{LL}^{L.O.} \rangle R_{L.O.} - \langle A_1 \times \hat{a}_{LL}^{QCD-C} \rangle R_{QCD-C}}{\langle \hat{a}_{LL}^{PGF} \rangle \times R_{PGF}} \\ &= \frac{A}{B}. \end{aligned} \tag{6.4}$$

The error on the asymmetry includes only the error on A_1 due to the parametrisation, given in Table 6.2, thus $\delta A = \sqrt{0.005^2 + 0.006^2} = 0.008$ and $\delta B = 0.039$ as it has been determined above. The systematic error on the experimental asymmetry is taken into account separately. With the values given in Table 6.4 the systematic error due to the Monte Carlo simulation is

$$\begin{aligned} \delta\left(\frac{\Delta G}{G}\right)_{syst,\mathrm{MC}} &= \frac{\Delta G}{G}\sqrt{\left(\frac{\delta B}{B}\right)^2 + \left(\frac{\delta A}{A}\right)^2} \\ &= \begin{cases} \frac{\Delta G}{G} \times 0.15 & (2002) \\ \frac{\Delta G}{G} \times 0.18 & (2003). \end{cases} \end{aligned}$$

Table 6.3: Summary of the results of the systematic Monte Carlo studies.

	$R_{PGF} \times \langle \hat{a}_{LL}^{PGF} \rangle$		difference	
	minimum	maximum	from default	
default	-0.256			
fragmentation	-0.233	-0.282	-0.023	$+0.025$
PDFs		-0.276		$+0.020$
scale $\mu \times 0.5,\ \times 2$	-0.248	-0.252	-0.008	-0.004
parton shower off		-0.277		-0.021

Systematic Errors from the Asymmetry

The translation of the systematic error due to false asymmetries and other sources on the high-p_t asymmetry (cf. Chapter 5) to an error on $\frac{\Delta G}{G}$ is

$$\begin{aligned}\delta\left(\frac{\Delta G}{G}\right)_{syst,\text{asym.}} &= \frac{\Delta G}{G}\,\frac{\delta A}{A} \\ &= \begin{cases} \frac{\Delta G}{G} \times 0.11 & (2002) \\ \frac{\Delta G}{G} \times 0.21 & (2003). \end{cases}\end{aligned}$$

with the values given in Table 6.4 and the same notation as above.

Total Systematic Error

Combining the systematic error due to the Monte Carlo with the systematic error of the asymmetry leads to the systematic error of $\Delta G/G$:

$$\begin{aligned}\delta\left(\frac{\Delta G}{G}\right)_{syst} &= \sqrt{\left(\delta\frac{\Delta G}{G}\right)^2_{syst,\text{MC}} + \left(\delta\frac{\Delta G}{G}\right)^2_{syst,\text{asym.}}} \\ &= \begin{cases} \frac{\Delta G}{G}\sqrt{0.15^2 + 0.11^2} = \frac{\Delta G}{G} \times 0.19 & (2002) \\ \frac{\Delta G}{G}\sqrt{0.18^2 + 0.21^2} = \frac{\Delta G}{G} \times 0.28 & (2003). \end{cases}\end{aligned}$$

Table 6.4: Contributions to the error on $\Delta G/G$.

	MC contribution				asym. contr.	
	A	δA(MC)	B	δB	A	δA(exp.)
2002	0.240	0.008	0.260	0.039	0.240	0.026
2003	−0.080	0.008	0.256	0.039	−0.080	0.017

6.4 Final Result on $\Delta G/G$

In Section 6.2 the gluon polarisation with the data taken in 2002 and 2003 has been determined. Including the systematic error on the asymmetry and the systematic

error on the Monte Carlo determined in the previous section leads to the following result for $\Delta G/G$:

$$\begin{aligned}\frac{\Delta G}{G}(2002) &= -0.927 \pm 0.643(stat.) \pm 0.174(syst.) \\ &\quad \langle x_G \rangle = 0.11, \;\; \langle \mu^2 \rangle = 2.4\,(\mathrm{GeV/c})^2 \\ \frac{\Delta G}{G}(2003) &= 0.311 \pm 0.334(stat.) \pm 0.086(syst.) \\ &\quad \langle x_G \rangle = 0.12, \;\; \langle \mu^2 \rangle = 2.4\,(\mathrm{GeV/c})^2\end{aligned}$$

Combining the two years gives the final result of the gluon polarisation determined with the COMPASS experiment in the years 2002 and 2003:

$$\begin{aligned}\tfrac{\Delta G}{G}(2002+2003) &= 0.049 \pm 0.296(stat.) \pm 0.105(syst.) \\ &\quad \langle x_G \rangle = 0.11, \;\; \langle \mu^2 \rangle = 2.4\,(\mathrm{GeV/c})^2.\end{aligned}$$

6.5 Further Studies

For the determination of the cuts applied in the course of this analysis Refs. [142] and [66] have been used for orientation. Nevertheless it has to be checked if these are applicable to the COMPASS data. Therefore several checks have been made, like the dependence of $\Delta G/G$ on $\sum p_t^2$ or the question if taking into account the charge of the hadrons improves the signal to background ratio.

Furthermore the possibility of measuring $\Delta G/G$ for several values for the gluon momentum fraction has been checked and contributions from resolved photon events that are not taken into account by LEPTO have been investigated. These investigations are presented briefly in this section.

6.5.1 Dependence of $\Delta G/G$ on $\sum p_t^2$

The high-p_t cuts are applied to prepare an event sample with a large fraction of photon-gluon fusion events. The main cut for this selection is the cut on $\sum p_t^2$. To investigate the influence of this cut, the $\sum p_t^2$-range is divided in 6 bins starting from $\sum p_t^2 = 1\,(\mathrm{GeV/c})^2$, Fig. 6.13. As expected the absolute value of $R_{PGF} \times \langle \hat{a}_{LL}^{PGF} \rangle$ increases with $\sum p_t^2$. It becomes stable only for values $\sum p_t^2 > 2.5\,(\mathrm{GeV/c})^2$. But due to the decreasing statistics the error-bar of $\Delta G/G$ also increases for the high-p_t bins. From the statistical point of view it would be desirable to include the bins below $\sum p_t^2 = 2.5\,(\mathrm{GeV/c})^2$. But it would be unclear

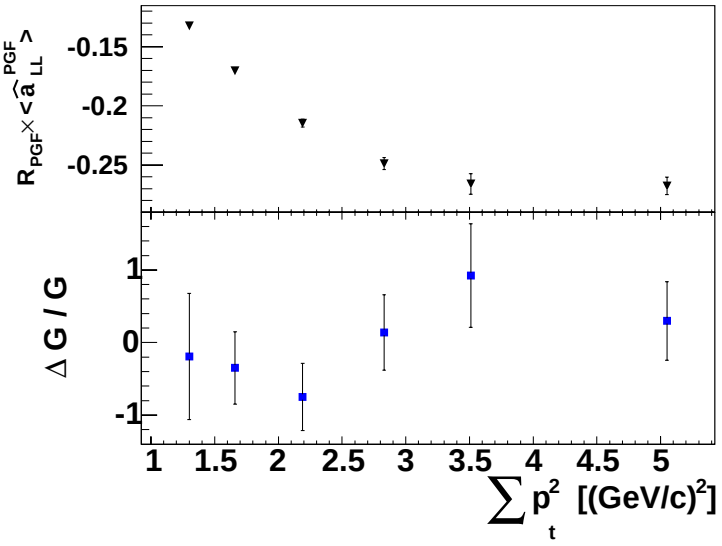

Figure 6.13: $R_{PGF} \times \langle \hat{a}_{LL}^{PGF} \rangle$ and $\Delta G/G$ as a function of $\sum p_t^2$ for the two high-p_t hadrons. The $\sum p_t^2$ range is divided in 6 bins (1-1.4-1.9-2.5-3.2-3.8-15) (GeV/c)^2. All other cuts as described in Chapter 5 are applied. Only statistical errors are given.

if there is some gluon polarisation contributing to the asymmetry at all or if everything is dominated by the photon-nucleon asymmetry A_1. Therefore it has been decided to keep the cut on $\sum p_t^2 > 2.5\,\mathrm{GeV}^2/\mathrm{c}^2$ as introduced in the SMC analysis, since in this region the variation of $\Delta G/G$ with $\sum p_t^2$ becomes smaller and thus one becomes more independent of systematic effects.

6.5.2 Dependence of $\Delta G/G$ on the Gluon Momentum Fraction x_G

To gain deeper insight into the polarisation of the gluons inside the nucleon and to better constrain QCD-fits to the data it is desirable to map the gluon polarisation for different values of x_G. The accessible x_G-range has been divided into three bins for x_G determined with the information on the reconstructed hadrons. Before the determination of $\Delta G/G$ in the individual bins, the correlation of the generated and reconstructed x_G in each bin has to be checked. Fig. 6.14 shows the corresponding distributions. For the middle bin the migration from the two neighbouring bins is very large, so that practically only the first and the last bin can be used to avoid an overlap of the bins due to the limited correlation of reconstructed and the generated x_G. Fig. 6.15 shows $\Delta G/G$ and $\langle \hat{a}_{LL}^{PGF} \rangle \times R_{PGF}$ as a function of x_G for all three bins. With the present statistics this does not provide any additional information. With more statistics it might be possible to extract a shape of $\Delta G/G$,

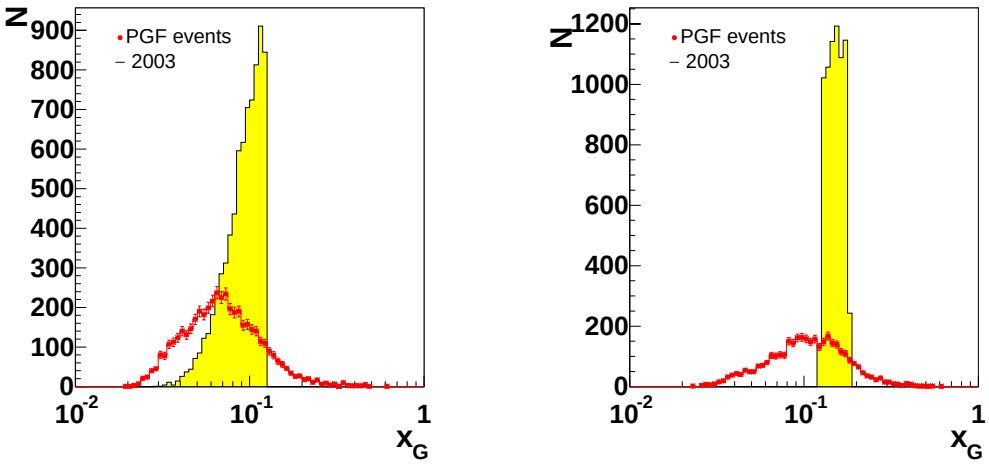

(a) $0 < x_G < 0.125$

(b) $0.125 < x_G < 0.18$.

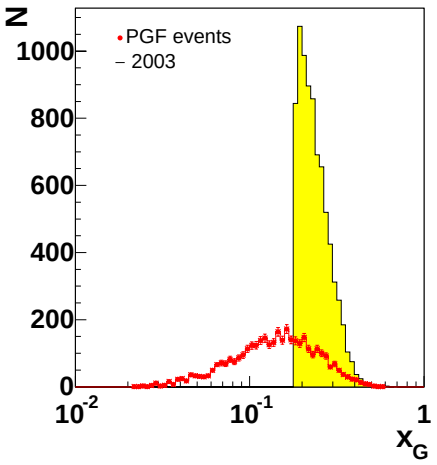

(c) $0.18 < x_G < 1$.

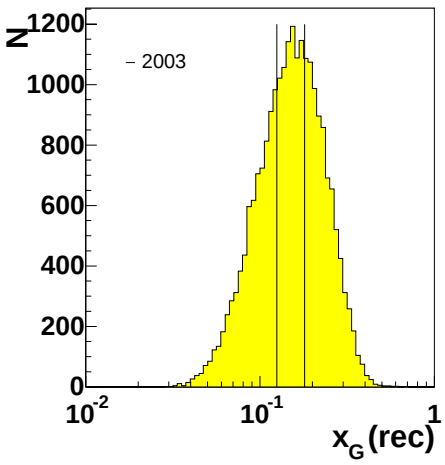

(d) Illustration of the bins in x_G.

Figure 6.14: Reconstruction of the gluon momentum fraction for different bins in x_G. The yellow histograms correspond to the x_G calculated with the information about the two reconstructed high-p_t hadrons for the 2003 data. The red points denote the x_G calculated from the Monte Carlo information about the hard scattering process for PGF events if the reconstructed x_G lies in the corresponding range.

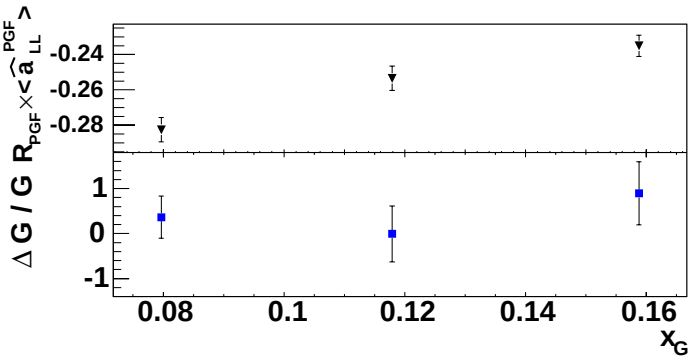

Figure 6.15: $R_{PGF} \times \langle \hat{a}_{LL}^{PGF} \rangle$ and $\Delta G/G$ as a function of the gluon momentum fraction x_G. x_G is calculated from the kinematic information of the Monte Carlo generator. The bins are given in Fig. 6.14. All other cuts as described in Chapter 5 are applied. Only statistical errors are given.

but with the limitation that the middle bin should be excluded to obtain a clear correlation between the real and the reconstructed gluon momentum fraction x_G.

6.5.3 Opposite Charged Hadron Pairs

In [66] it is suggested to require hadron pairs with opposite charge to further enrich the fraction of PGF events. This has been studied with the Monte Carlo sample produced for the $\Delta G/G$ extraction. Such further requirement does not improve the signal to background ratio but only reduces the statistics (Table 6.5). Moreover it leads to a smaller absolute value of $R_{PGF} \times \langle \hat{a}_{LL}^{PGF} \rangle$. These are the reasons why the requirement of opposite charges is not used.

6.5.4 Exclusion of Data at Large Bjorken x

Fig. 6.16 shows the ratio of the photon-gluon fusion subprocesses R_{PGF} times the analysing power $\langle \hat{a}_{LL}^{PGF} \rangle$ for the high-p_t sample with and without the cut on the Bjorken x variable. With the cut on x_B the analysing power increases and

Table 6.5: R_{PGF} with (h^+h^-) and without (h^1h^2) the requirement of opposite charged hadron pairs.

	PGF ev.	all events	$R_{PGF}/\%$	$\langle \hat{a}_{LL}^{PGF} \rangle$	$R_{PGF} \times \langle \hat{a}_{LL}^{PGF} \rangle$
h^+h^-	8198	23039	35.6 ± 0.06	-0.684 ± 0.04	-0.243 ± 0.04
h^1h^2	11783	32296	36.5 ± 0.05	-0.703 ± 0.03	-0.256 ± 0.04

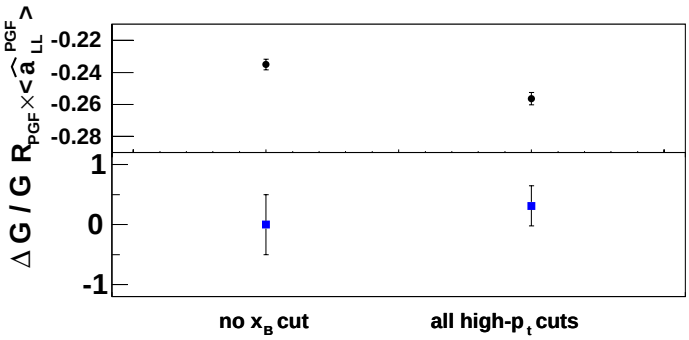

Figure 6.16: Process ratio R_{PGF} times the analysing power $\langle \hat{a}_{LL}^{PGF} \rangle$ and $\Delta G/G$ for the high-p_t sample with and without the cut on x_B.

the number of PGF events hardly decreases, meaning that at large x_B are more QCD-Compton events with a positive analysing power that are excluded with this cut.

6.5.5 Contributions from Resolved Photon Events at $Q^2 > 1\,(\mathrm{GeV/c})^2$

The analysis presented to determine the gluon polarisation $\Delta G/G$ is model dependent. It relies on the model for deep inelastic lepton-nucleon scattering implemented in LEPTO for $Q^2 > 1\,(\mathrm{GeV/c})^2$. The model implemented in PYTHIA is more extensive and therefore covers also the transition region between DIS and real photon scattering. PYTHIA models not only the three hard scattering processes as done in LEPTO but also interactions of the hadronic content of the photon. For example the fluctuation of a photon into a vector meson, predominantly a ρ^0 (Vector Meson Dominance, VMD), or into a $q\bar{q}$ pair of larger virtuality than in the VMD case. These fluctuations depend on the parton distributions of the photon. A consequence is that hard scattering takes place between a parton of the photon and a parton of the nucleon. Fig. 6.17 shows some possibilities of the resolved photon-nucleon interaction, either via qq, qg or gg. The contribution from this type of events to the total cross section decreases with higher Q^2, since the lifetime of the $q\bar{q}$ fluctuation decreases with Q^2 and thus they are not included in a generator like LEPTO [152].

Looking at the region $Q^2 > 1\,(\mathrm{GeV/c})^2$ using a Monte Carlo sample generated with PYTHIA reveals that in this model resolved photon contributions are also present for $Q^2 > 1\,(\mathrm{GeV/c})^2$. PYTHIA cannot be used for the complete analysis of $Q^2 > 1\,(\mathrm{GeV/c})^2$ data for reasons stated in Chapter 4. However, it has been

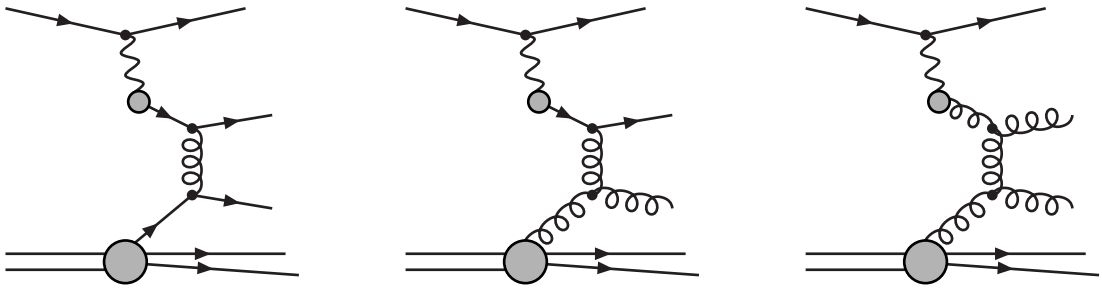

Figure 6.17: Resolved photon-nucleon interaction, via qq, qg and gg.

used to estimate the contribution of resolved photon events to the high-p_t sample for $Q^2 > 1\,(\mathrm{GeV/c})^2$. From the PYTHIA high-$p_t$ sample [153], that has been generated without a cut on Q^2 and used for the $Q^2 < 1\,(\mathrm{GeV/c})^2$ analysis, the fraction of resolved photon events for $Q^2 > 1\,(\mathrm{GeV/c})^2$ has been determined to be $(7.9 \pm 0.2)\,\%$. Fig. 6.18 shows the fraction of resolved photon events as a function of Q^2. It can be seen that above $Q^2 = 3\,(\mathrm{GeV/c})^2$ practically no resolved photon events contribute anymore.

The fact that the resolved photon contribution is not taken into account introduces an additional systematic uncertainty. For statistical reasons it is not possible to cut at larger Q^2 and thus remove this contributions. However, this information is not included into the systematic error since this would imply a mixing of the two models, LEPTO and PYTHIA. Therefore it has to be kept in mind, that the result for the gluon polarisation relies on the model implemented in the Monte Carlo generator that is used.

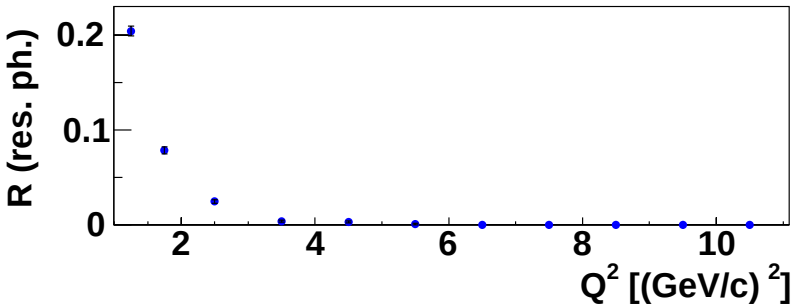

Figure 6.18: Fraction R of the resolved photon contribution for $Q^2 > 1\,(\mathrm{GeV/c})^2$. The total contribution of resolved photons to the high-p_t sample is $(7.9 \pm 0.2)\,\%$, mainly for $Q^2 < 2\,(\mathrm{GeV/c})^2$, it vanishes for $Q^2 > 5\,(\mathrm{GeV/c})^2$. The statistical error bars are partly smaller than the marker size.

6.6 Impact of the 2004-Data

For 2004 about the same amount of data as for 2002 and 2003 together is stored on tape. A first production of the data has been performed and data quality and stability information has been produced. The Monte Carlo detector simulation for 2004 is in progress. Therefore a complete analysis of the 2004 data cannot be performed yet, but a first estimate on the improvement of the error on $\Delta G/G$ is given. Using the first data quality info and data grouping available in September 2005 leads to a high-p_t asymmetry for the 2004 data of

$$\frac{A_{\parallel}}{D} = -0.026 \pm 0.062(stat.), \tag{6.5}$$

determined as described in Chapter 5. Assuming the same ratio of photon-gluon fusion events as in 2003, which is a good first approximation since the changes in the spectrometer setup between the two years are small, leads to

$$\frac{\Delta G}{G}(2004) \quad = \quad 0.080 \pm 0.243(stat.)$$

i.e. the error is smaller than the one for 2002 and 2003 together. For the combination of all years this results in

$$\begin{aligned} \frac{\Delta G}{G}(02,03,04) \quad &= \quad 0.068 \pm 0.188(stat.) \pm 0.105(syst.) \\ & \qquad \langle x_G \rangle = 0.11, \;\; \langle \mu^2 \rangle = 2.4\,(\mathrm{GeV/c})^2. \end{aligned}$$

One has to keep in mind that this is only a first estimate and especially systematic studies for the 2004 data are ongoing, so that the systematic error is based on the studies of the 2002 and 2003 data.

Chapter 7

Discussion of the Results

The gluon helicity contribution to the nucleon can be determined in two different ways, namely with measurements of the polarised structure function g_1 as input for the evolution equations or a direct measurement of $\Delta G/G$. The direct measurement provided by COMPASS using hadron pairs with high transverse momentum for $Q^2 > 1\,(\mathrm{GeV/c})^2$ data results in $\frac{\Delta G}{G}(2002 + 2003) = 0.049 \pm 0.296(stat.) \pm 0.105(syst.)$ at $\langle x_G \rangle = 0.11$ and $\langle \mu^2 \rangle = 2.4\,(\mathrm{GeV/c})^2$ which is consistent with zero within the present statistical accuracy.

Two other independent measurements of the gluon polarisation have been performed by COMPASS, one with high-p_t hadron pairs for $Q^2 < 1\,(\mathrm{GeV/c})^2$ [127]-[129] and a second one with open charm production (preliminary) [65], both covering the data taken 2002 and 2003. HERMES [154] and SMC [142] have already measured $\Delta G/G$ with high-p_t hadron pairs before, for all Q^2 and $Q^2 > 1\,(\mathrm{GeV/c})^2$, respectively. The different results are compared to several QCD-analyses for $\Delta G/G$ in Fig. 7.1. The parametrisations for ΔG of Glück, Reya, Stratmann and Vogelsang (GRSV2000) [43] and the Asymmetry Analysis Collaboration (AAC03) [39], using the parametrisation for the unpolarised gluon distribution G of Glück, Reya and Vogt (GRV98) [130], are given. For the GRSV parametrisation three options for the gluon polarisation are considered: maximal polarisation, best fit to the data and a minimal scenario with no gluon polarisation at an input scale $\mu_0^2 = 0.4\,(\mathrm{GeV/c})^2$. The parton distributions are evolved to the scale $\mu^2 = 2.4\,(\mathrm{GeV/c})^2$ with $\Delta G = 2.4$ (max.), 0.6 (best fit) and 0.2 (min. scenario), respectively. The AAC03 parametrisation is shown for the best fit to the data. All parametrisations are given in next-to-leading order. For comparison GRSV2000 is also plotted in leading order which deviates from the NLO curve only for large x. The measurement presented in this thesis is compatible with all parametrisations obtained from the best fit within the error.

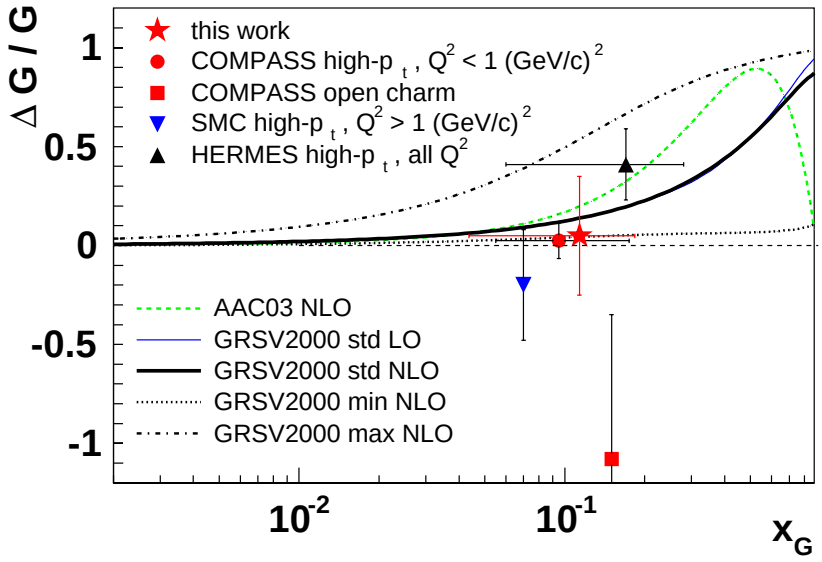

Figure 7.1: Comparison of experimental results on $\Delta G/G$ and QCD-fits. The results for the gluon polarisation obtained by COMPASS (preliminary), HERMES [154] and SMC [142] are compared to next-to-leading order QCD-fits from AAC03 [39] (green dashed line) and GRSV2000 [43] (solid black line). Beside the parametrisations for the best fit to the data by GRSV2000 the curves for the minimum (dotted black line) and maximum scenario (dotted-dashed black line) as well as the leading order parametrisation for the standard scenario (thin blue line) are given.

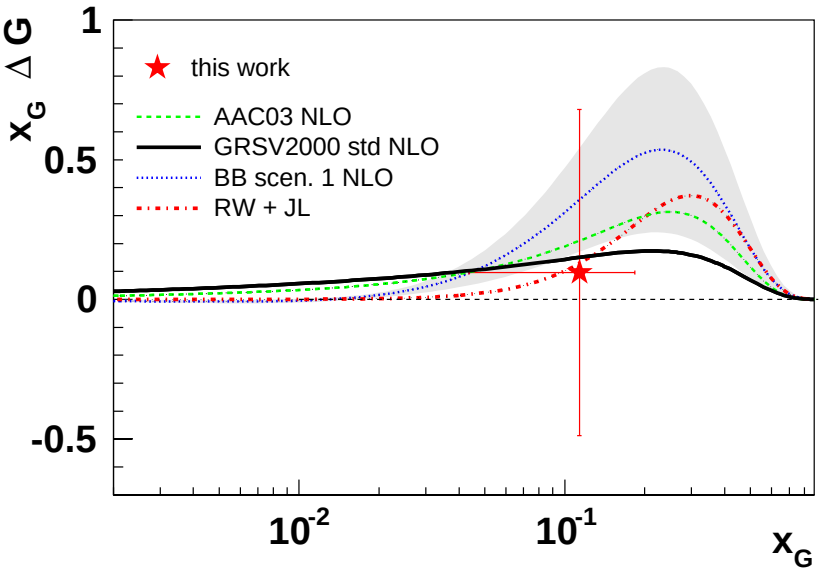

Figure 7.2: The result for ΔG presented in this work is compared to the AAC03 [39], GRSV2000 [43] and BB [44] parametrisations and to a QCD-fit done by the COMPASS collaboration [155] (RW+JL). Exemplary the uncertainty of the BB parametrisation is given by the grey band. The uncertainty of the AAC03 parametrisation can be found in Fig. 2.12.

In Fig. 7.2 the result for $\Delta G/G$ is combined with the GRV98LO parametrisation for the unpolarised gluon density, taking into account the accessible x_G distribution, which leads to

$$\Delta G(\langle x_G \rangle = 0.11,\ \langle \mu^2 \rangle = 2.4\,(\mathrm{GeV/c})^2) = 0.85 \pm 5.14(stat.) \pm 1.81(syst.).$$

Using the next-to-leading order parametrisation increases ΔG by 4%. Beside the AAC03 and the GRSV2000 best fit curves, the parametrisation of Blümlein and Böttcher (BB) [44] for ΔG is added in Fig. 7.2. A recent QCD-analysis done by the COMPASS collaboration (RW+JL) [155] including the latest data from JLAB[1]/ Hall A [156] at large x (see also Fig. 2.3) is shown as well. JLAB contributes very precise data at large x which leads to a curve for ΔG that is shifted slightly to higher x_G as compared to the others.

For a better constraint of ΔG it would be necessary to map a larger region of the gluon momentum fraction x_G, especially at larger values. Data covering a larger range in x_G are also expected from RHIC where PHENIX has already reported results about their first asymmetries in polarised $p - p$ collisions [76].

Comparing all the data presently available to the GRSV2000 parametrisations of the different scenarios for the gluon polarisation, the curves for the minimum ($\Delta G = 0.2$) and standard ($\Delta G = 0.6$) scenario seem to be favoured over the maximum ($\Delta G = 2.4$) scenario. This indicates a small gluon polarisation.

To fully clarify the composition of the nucleon spin one has to take into account that the quarks and gluons inside the nucleon also carry orbital angular momentum. Deeply virtual Compton scattering experiments will be a tool to provide further information on this topic. The measurement presented here together with the other results from COMPASS and other experiments are the first steps in the exploration of $\Delta G/G$ and the nucleon spin structure.

[1]Thomas Jefferson National Accelerator Facility

Chapter 8

Summary

The spin of the nucleon is the topic of many past and present experiments. While the quark helicity contribution to the nucleon has been well measured, the contribution from gluons and orbital angular momentum are not well constrained.

This thesis is dedicated to the determination of the gluon polarisation in the nucleon using helicity dependent cross section asymmetries in events with high-p_t hadron pairs. The analysis is based on the data taken by the COMPASS experiment at CERN during the years 2002 and 2003. From deep inelastic muon-deuteron scattering data, obtained with a polarised μ^+ beam of 160 GeV on a polarised ^{6}LiD target, events with two hadrons with large transverse momentum have been selected.

The sample of high-p_t hadron events contains an enriched fraction of photon-gluon fusion events that directly probe the gluons inside the nucleon. With the photon-deuteron asymmetry of the high-p_t sample the gluon polarisation $\Delta G/G$ has been extracted. The requirement of hadron pairs with large transverse momentum does not fully suppress leading order deep inelastic scattering and QCD-Compton events. These events contribute with the photon-deuteron asymmetry A_1 as background to the measured asymmetry, since they probe the polarised quarks inside the nucleon. A Monte Carlo simulation is used to evaluate the fractions of photon-gluon fusion, QCD-Compton and leading order events and to determine their contributions to the asymmetry.

The analysis covers the kinematic region $Q^2 > 1\,(\mathrm{GeV/c})^2$ where Lepto is used to generate Monte Carlo events. To obtain a reasonable agreement between data and Monte Carlo simulation several Lepto parameters have been adjusted. The modified Lepto provides the information needed to determine $\Delta G/G$, namely the fraction of photon-gluon fusion events in the high-p_t sample,

which is $R_{PGF} = (36.5 \pm 0.5)\%$, and the analysing power of the photon-gluon reaction of $\langle \hat{a}_{LL}^{PGF} \rangle = -0.703 \pm 0.003$.

The result for the gluon polarisation measured with the COMPASS experiment in the years 2002 and 2003 is

$$\frac{\Delta G}{G}(2002 + 2003) = 0.049 \pm 0.296(stat.) \pm 0.105(syst.)$$

at $\langle x_G \rangle = 0.11$ and $\langle \mu^2 \rangle = 2.4\,(\mathrm{GeV/c})^2$. Within the present statistical accuracy this value is consistent with zero and consistent with QCD-fits to the present data from inclusive and semi-inclusive polarised deep inelastic scattering experiments.

In combination with the high-p_t measurement for $Q^2 < 1\,(\mathrm{GeV/c})^2$, the COMPASS data taken 2004 and the data which will be taken in the coming years, a more accurate determination of the gluon polarisation $\Delta G/G$ will be possible. Results from RHIC are expected to further map the dependence of $\Delta G/G$ of the gluon momentum fraction x_G. If the gluons do not fully account for the unexplained nucleon spin, the remaining contributions probably come from the orbital angular momentum of the quarks and gluons. This will be investigated with experiments on deeply virtual Compton scattering. Together with the current developments on the theoretical side we are on the way to find the solution of the nucleon spin puzzle step by step.

Appendix A

Tables

A.1 Problematic Runs and Run Grouping

Table A.1: Runs that were not used in the analysis. Field rotation runs and runs that had been taken with problematic spectrometer conditions, e.g. problems of single detector planes or beamline problems. For details see comments in Ref. [123].

	field rotation runs
P2A	20932, 20974
P2D	22153, 22154, 22176, 22331
P2E	22584
P1C	28313, 28828, 28830
P1D	28905, 28906, 29247, 29248, 29305, 29308
P1F	30617, 30678
P1I	31636, 31638, 31669, 31690, 31691, 31733, 31756, 31774, 31775, 31788, 31789, 31820, 31829, 31830, 31839, 31840
	runs not used for other reasons
P2D	22030, 22031, 22041, 22042, 22043, 22063, 22306
P2G	23059, 23102, 23103
P1B	28232, 28233, 28320
P1C	28635, 28636, 28764, 28776, 28777, 28792, 28793, 28794, 28795, 28796, 28801, 28802, 28803
P1D	28878, 28879, 28882, 28883, 28884, 29201, 29268, 29349
P1I	31765, 31821

Table A.2: Configurations used for the asymmetry calculation 2002. A group of runs given in brackets corresponds to one configuration. The first and the last run for one solenoid current is given.

period	configurations
P2A1	(20413-20490, 20493-20511) (20515-20542, 20545-20561) (20565-20596, 20598-20619) (20622-20633, 20638-20652, 20656-20669) (20674-20692, 20715-20717)
P2A2	(20767-20792, 20797-20814) (20819-20828, 20831-20845, 20849-20864) (20869-20884, 20895-20911) (20919-20931, 20935-20947) (20951-20970, 20975-20988) (20993-21012, 21016-21025) (21029-21043, 21048-21054, 21067-21084, 21089-21104) (21108-21121, 21124-21134)
P2D	(22018-22036, 22038-22056) (22062-22075, 22078-22090) (22096-22118, 22121-22129) (22142-22152, 22155-22174) (22177-22233, 22280-22302) (22304-22312, 22314-22329, 22332-22341)
P2E	(22384-22395, 22398-22408) (22410-22424, 22428-22441) (22444-22461, 22463-22475) (22480-22491, 22493-22498) (22518-22532, 22534-22547) (22552-22565, 22569-22583, 22585-22594) (22597-22609, 22613-22629) (22632-22646, 22650-22663) (22664-22681, 22682-22698)
P2F	(22754-22771, 22773-22789) (22790-22804, 22807-22821) (22902-22916, 22919-22941) (22945-22958, 22961-22972)
P2Ga	(23016-23025, 23036-23044) (23084-23094, 23098-23110) (23114-23124, 23127-23140, 23144-23147)
P2Gb	(23243-23286, 23290-23315) (23319-23338, 23341-23351, 23360-23373) 2(3381-23395, 23398-23411) (23414-23422, 23423-23437, 23440-23449)

Table A.3: Runs belonging to a single configuration that have been discarded for the asymmetry extraction.

	single configuration runs
P2F	22824, 22825, 22827, 22884, 22885, 22886, 22887, 22890, 22891, 22892, 22894, 22896, 22897
P2G	23047, 23049, 23050, 23051, 23052, 23057, 23058, 23059, 23082

Table A.4: Configurations used for the asymmetry calculation 2003. A group of runs given in brackets corresponds to one configuration. The first and the last run for one solenoid current is given.

period	configurations
P1A	(27599-27625, 27628-27649, 27652-27666) (27796-27867, 27964-27995, 27997-28019) (28024-28043, 28047-28062) (28064-28080, 28081-28102) (28106-28121, 28126-28143, 28146-28167, 28170-28178)
P1B	(28235-28252, 28254-28272) (28283-28296, 28299-28310) (28313-28325, 28328-28341, 28344-28357) (28360-28374, 28376-28390) (28393-28409, 28412-28426, 28431-28433)
P1C	(28571-28590, 28598-28621) (28633-28650, 28656-28669, 28674-28694) (28705-28736, 28738-28754) (28759-28773, 28776-28789) (28792-28804, 28810-28827, 28831-28834)
P1D1	(28881-28905, 28906-28922) (28925-28939, 28942-28953) (28955-28970, 28973-28986, 28990-29002)
P1D2	(29220-29247, 29248-29267) (29268-29283, 29290-29304) (29310-29330, 29334-29349, 29354-29366)
P1E1	(29963-29975, 29977-30017, 30020-30027) (30032-30048, 30062-30085) (30086-30101, 30103-30114) (30119-30137, 30141-30160) (30162-30184, 30188-30205) (30211-30239, 30243-30270) (30273-30287, 30291-30311) (30314-30329, 30332-30350)
P1E2	(30354-30368, 30371-30379)
P1F	(30448-30483, 30495-30508) (30509-30522, 30525-30542) (30543-30555, 30557-30601) (30604-30616, 30618-30635) (30643-30657, 30661-30675) (30678-30695, 30698-30717)
P1I	(31581-31615, 31617-31636) (31638-31669, 31674-31689) (31691-31711, 31717-31732) (31734-31755, 31758-31773) (31776-31787, 31789-31800) (31809-31819, 31821-31828) (31832-31838, 31840-31855)
P1J	(31930-31968, 31971-31979) (31983-31992, 31993-32003) (32007-32014, 32018-32024) (32028-32036, 32041-32055) (32059-32066, 32068-32077) (32079-32091, 32095-32118) (32121-32129, 32133-32142) (32147-32152, 32155-32162) (32169-32184, 32188-32195) (32199-32216, 32220-32229, 32230-32236)

A.2 Event Statistics

Table A.5: Number of events contained in the different periods. "mDST" refers to the number of events in the mDST-files, i.e events with at least one (primary or secondary) vertex. "min. sel.": minimum selection, refers to events with at least a primary vertex and four particles associated to the vertex, which is the minimum requirement for an event to be further analysed. "hpt cd.": high-p_t candidate, one of the outgoing particles associated to the primary vertex is a scattered muon candidate, the other two particles are required to have a transverse momentum $p_t > 0.7\,\mathrm{GeV/c}$.

	mDST	min. sel.	hpt cd.		mDST	min. sel.	hpt cd.
P2A	224 M	174 047 010	975 670	P1A	156 M	68 835 909	566 962
P2D	131 M	60 420 268	607 477	P1B	130 M	61 569 554	533 033
P2E	180 M	74 690 621	745 622	P1C	141 M	70 130 856	686 437
P2F	82 M	34 257 396	307 868	P1D	172 M	84 108 130	707 474
P2G	164 M	74 374 790	682 285	P1E	213 M	97 948 326	1 048 999
				P1F	169 M	78 609 054	869 195
				P1I	203 M	92 653 796	893 939
				P1J	316 M	150 010 682	1 487 801
2002	782 M	417 790 090	3 318 922	2003	1498 M	703 866 312	6 793 840

A.3 Systematic Studies with the All-p_t Sample

Table A.6: False asymmetries inside one target cell for 2002(a) and 2003(b) as shown in Fig. 5.19, page 99. P2F and P2Ga are not included in the average for 2002.

	A (upstream)	A (downstr.)		A (upstream)	A (downstr.)
P2A1	0.022 ± 0.110	0.036 ± 0.100	P1A	-0.108 ± 0.070	0.129 ± 0.065
P2A2	0.020 ± 0.069	0.044 ± 0.064	P1B	-0.063 ± 0.065	0.029 ± 0.061
P2D	-0.049 ± 0.068	0.001 ± 0.058	P1C	0.098 ± 0.058	-0.015 ± 0.054
P2E	-0.004 ± 0.067	-0.158 ± 0.060	P1Da	0.023 ± 0.078	0.022 ± 0.074
P2F	-0.094 ± 0.107	-0.039 ± 0.097	P1Db	0.058 ± 0.085	0.097 ± 0.079
P2Ga	-0.032 ± 0.114	0.033 ± 0.097	P1Ea	0.012 ± 0.039	0.025 ± 0.033
P2Gb	0.013 ± 0.086	0.088 ± 0.073	P1Eb	-0.133 ± 0.142	-0.059 ± 0.123
			P1F	-0.034 ± 0.053	0.014 ± 0.050
			P1I	0.012 ± 0.041	0.028 ± 0.036
			P1J	0.010 ± 0.033	0.013 ± 0.029
2002	-0.004 ± 0.034	-0.011 ± 0.030	2003	0.002 ± 0.017	0.025 ± 0.015

Table A.7: Asymmetries obtained with the fake configuration for 2002(a) and 2003(b) as shown in Fig. 5.21, page 101. P1Eb contains only one positive and one negative solenoid configuration, therefore it is not possible to determine an asymmetry with the fake configuration for this period. P2F and P2Ga are not included in the average for 2002.

	A (neg. SC)	A (pos. SC)		A (neg. SC)	A (pos. SC)
P2A1	0.006 ± 0.107	0.211 ± 0.097	P1A	-0.003 ± 0.069	0.136 ± 0.072
P2A2	0.092 ± 0.068	0.050 ± 0.079	P1B	-0.044 ± 0.063	-0.010 ± 0.061
P2D	-0.041 ± 0.063	-0.093 ± 0.064	P1C	0.029 ± 0.053	-0.099 ± 0.065
P2E	-0.048 ± 0.067	-0.095 ± 0.065	P1Da	0.066 ± 0.081	-0.132 ± 0.081
P2F	0.003 ± 0.100	0.203 ± 0.104	P1Db	0.071 ± 0.085	0.038 ± 0.097
P2Ga	0.128 ± 0.115	0.112 ± 0.109	P1Ea	0.003 ± 0.042	0.005 ± 0.038
P2Gb	0.020 ± 0.074	0.022 ± 0.085	P1Eb		
			P1F	0.006 ± 0.052	0.045 ± 0.050
			P1I	0.002 ± 0.040	0.007 ± 0.039
			P1J	-0.037 ± 0.031	-0.023 ± 0.030
2002	0.003 ± 0.032	-0.014 ± 0.034	2003	-0.004 ± 0.016	-0.004 ± 0.016

Table A.8: All-p_t asymmetries for false asymmetry studies for 2002(a) and 2003(b) as shown in Fig. 5.22, page 104. P2F and P2Ga are not included in the average A_+ for 2002.

	A (1st order)	A (2nd order)		A (1st order)	A (2nd order)
P2D	0.016 ± 0.045	0.017 ± 0.045	P1A	0.033 ± 0.048	0.032 ± 0.047
P2E	0.051 ± 0.045	0.049 ± 0.045	P1B	0.030 ± 0.044	0.032 ± 0.044
P2F	0.028 ± 0.072	0.026 ± 0.072	P1C	0.055 ± 0.039	0.056 ± 0.039
P2Ga	0.163 ± 0.075	0.159 ± 0.075	P1Da	0.035 ± 0.053	0.036 ± 0.053
			P1Db	0.046 ± 0.058	0.049 ± 0.058
			P1I	-0.002 ± 0.027	-0.002 ± 0.027
A_+	0.033 ± 0.032	0.033 ± 0.032	A_+	0.025 ± 0.017	0.025 ± 0.017
P2A1	0.025 ± 0.074	0.029 ± 0.074	P1Ea	-0.003 ± 0.025	-0.001 ± 0.025
P2A2	0.060 ± 0.047	0.063 ± 0.047	P1Eb	0.029 ± 0.093	0.028 ± 0.093
P2Gb	0.108 ± 0.057	0.110 ± 0.056	P1F	0.006 ± 0.036	0.004 ± 0.036
			P1J	-0.038 ± 0.022	-0.037 ± 0.022
A_-	0.069 ± 0.033	0.072 ± 0.032	A_-	-0.017 ± 0.015	-0.016 ± 0.015

Table A.9: Asymmetries for the leading hadron detected in the upper and lower part of the spectrometer for 2002(a) and 2003(b) as shown in Fig. 5.23, page 107. P2F and P2Ga are not included in the average for 2002.

	A (lower spec.)	A (upper spec.)		A (lower spec.)	A (upper spec.)
P2A1	-0.061 ± 0.106	0.113 ± 0.104	P1A	-0.035 ± 0.067	0.098 ± 0.066
P2A2	0.013 ± 0.067	0.112 ± 0.066	P1B	-0.038 ± 0.062	0.098 ± 0.061
P2D	-0.048 ± 0.064	0.078 ± 0.063	P1C	0.012 ± 0.056	0.098 ± 0.055
P2E	0.119 ± 0.065	-0.013 ± 0.061	P1Da	0.012 ± 0.076	0.059 ± 0.075
P2F	-0.002 ± 0.106	0.050 ± 0.099	P1Db	0.012 ± 0.082	0.085 ± 0.081
P2Ga	0.284 ± 0.108	0.044 ± 0.103	P1Ea	-0.023 ± 0.036	0.022 ± 0.036
P2Gb	0.154 ± 0.081	0.071 ± 0.078	P1Eb	0.015 ± 0.132	0.042 ± 0.131
			P1F	-0.083 ± 0.051	0.091 ± 0.051
			P1I	0.013 ± 0.038	-0.017 ± 0.038
			P1J	-0.040 ± 0.031	-0.034 ± 0.030
2002	0.039 ± 0.033	0.064 ± 0.032	2003	-0.023 ± 0.016	0.027 ± 0.016

Table A.10: Asymmetries with leading hadron detected in Saleve or Jura side of the spectrometer for 2002(a) and 2003(b) as shown in Fig. 5.24, page 108. P2F and P2Ga are not included in the average for 2002.

	A (Jura)	A (Saleve)		A (Jura)	A (Saleve)
P2A1	-0.063 ± 0.110	0.102 ± 0.101	P1A	0.041 ± 0.069	0.023 ± 0.064
P2A2	0.046 ± 0.069	0.077 ± 0.064	P1B	0.035 ± 0.064	0.030 ± 0.060
P2D	0.006 ± 0.066	0.027 ± 0.061	P1C	0.085 ± 0.057	0.031 ± 0.054
P2E	0.146 ± 0.067	-0.031 ± 0.061	P1Da	0.001 ± 0.078	0.067 ± 0.073
P2F	-0.151 ± 0.107	0.175 ± 0.098	P1Db	0.031 ± 0.084	0.065 ± 0.079
P2Ga	0.378 ± 0.109	-0.028 ± 0.103	P1Ea	0.015 ± 0.037	-0.014 ± 0.035
P2Gb	0.178 ± 0.083	0.050 ± 0.077	P1Eb	0.146 ± 0.137	-0.075 ± 0.128
			P1F	-0.020 ± 0.052	0.026 ± 0.049
			P1I	-0.028 ± 0.039	0.022 ± 0.037
			P1J	-0.028 ± 0.032	-0.046 ± 0.030
2002	0.072 ± 0.033	0.035 ± 0.031	2003	0.003 ± 0.016	0.001 ± 0.015

Appendix B

Monte Carlo Parameters and Results

B.1 A_1^d Parametrisation

This parametrisation of A_1^d was obtained from the data of E143 and SMC. It is used in the estimation of the leading order and QCD-Compton contribution to the total asymmetry, section 6.2.

```
       SUBROUTINE A1DS(X,A1,SIGMA)
       implicit real*8 (A-H,O-Z)
       DIMENSION  COVAR(4,4)
c.............  E143 smc92/94/95         4/96   (WM)
       PARAMETER(AA=10.608,bb=0.35969E-01,cc=0.14615,DD=-0.18496E-03)
       DATA COVAR/  0.230E+02, 0.573E-01, 0.913E-02, 0.311E-01,
     +              0.573E-01, 0.287E-03, 0.311E-03, 0.192E-03,
     +              0.913E-02, 0.311E-03, 0.836E-03, 0.192E-03,
     +              0.311E-01, 0.192E-03, 0.192E-03, 0.162E-03/

C
C  A1 Value
C
       U=EXP(-AA*X)-1.0
       V=BB**CC -X**CC
       A1= U * V + DD
C
C  A1 error
C
       DA1DA=-X*EXP(-AA*X)*V
       DA1DB=U*CC*BB**(CC-1.0)
       DA1DC=U*(DLOG(BB)*BB**CC -DLOG(X)*X**CC)
       DA1DD=1.
```

```
      SIGMA2=COVAR(1,1)*DA1DA**2 +COVAR(2,2)*DA1DB**2
     +       +COVAR(3,3)*DA1DC**2 +covar(4,4)*DA1DD**2
     +      +2*(COVAR(1,2)*DA1DA*DA1DB
     +         +COVAR(1,3)*DA1DA*DA1DC
     +         +COVAR(1,4)*DA1DA*DA1DD
     +         +COVAR(2,3)*DA1DB*DA1DC
     +         +COVAR(2,4)*DA1DB*DA1DD
     +         +COVAR(3,4)*DA1DC*DA1DD)
c       with four parameters the 68.3% confidence level correspond to
c       chi2 --> chi2 + 4.70.
c       minuit provide the chi2 + 1 errors.
c       They have to be multiplied by sqrt(4.70)
      SIGMA=SQRT(4.70*SIGMA2)
      END
```

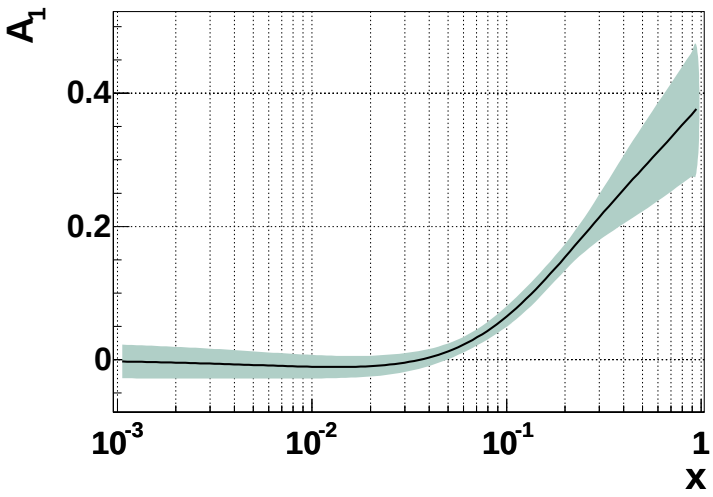

Figure B.1: Parametrisation of the photon-nucleon asymmetry A_1^d. The error is given by the grey band.

B.2 Comparison of Data and Monte Carlo for 2002

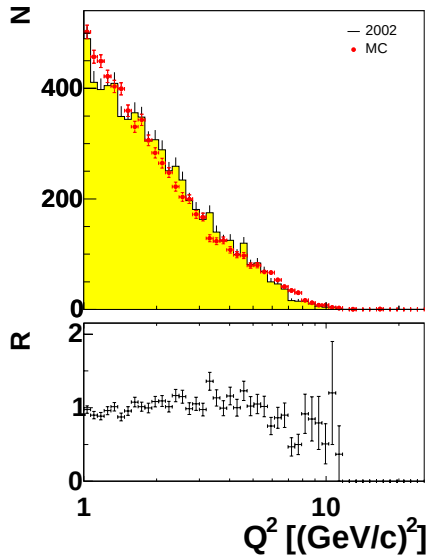

(a) Negative squared four momentum transfer Q^2.

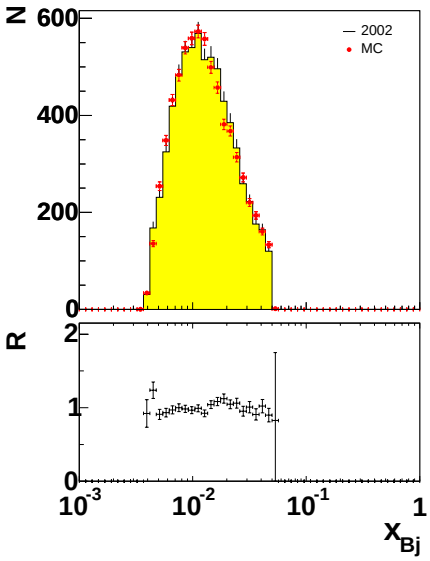

(b) Bjorken variable x_{Bj}.

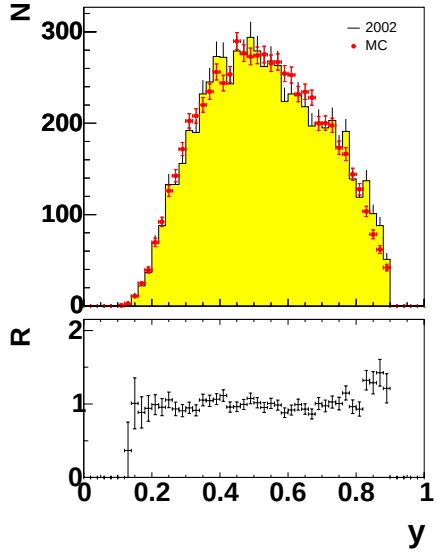

(c) Fractional virtual photon energy y.

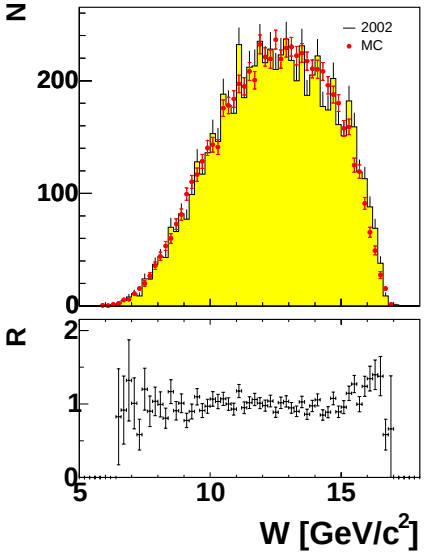

(d) Invariant mass of the photon-nucleon system W.

Figure B.2: Comparison of 2002 data and Monte Carlo for the inclusive kinematic variables Q^2(a), x_B(b), y(c) and W(d). The histograms are normalised to the number of entries. R = data/MC is the ratio data over Monte Carlo.

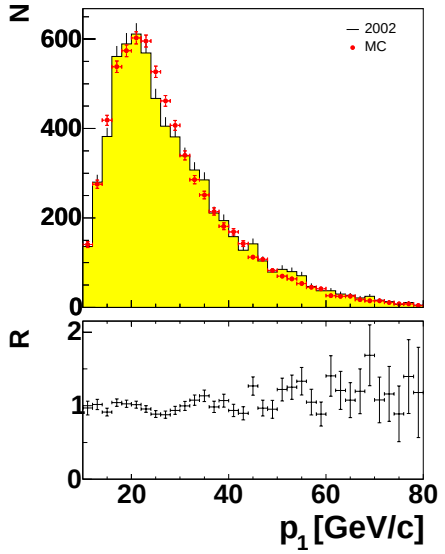

(a) Leading hadron p.

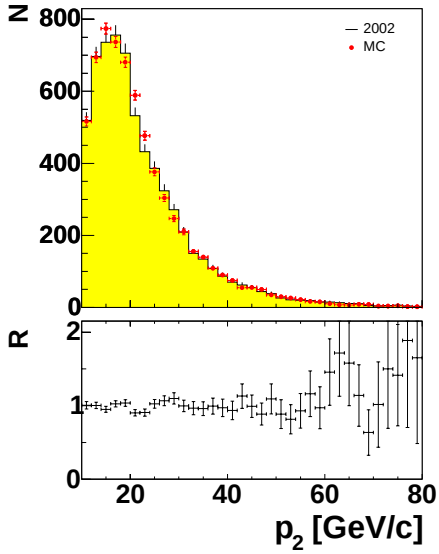

(b) Second hadron p.

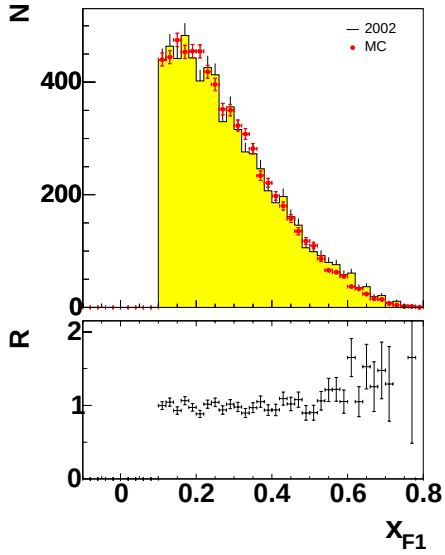

(c) Leading hadron x_F.

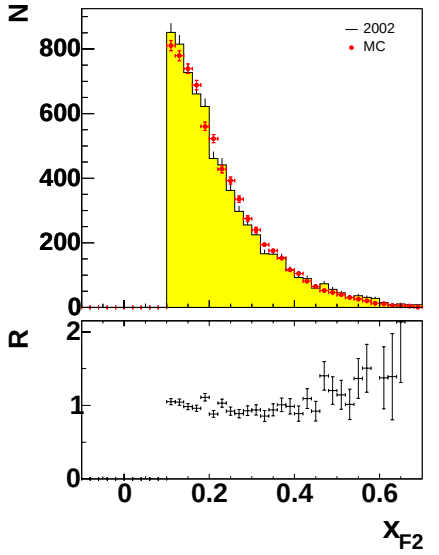

(d) Second hadron x_F.

Figure B.3: Comparison of 2002 data and Monte Carlo for the momentum of the first (a) and second hadron (b) and x_F of the first (c) and second (d) hadron. The histograms are normalised to the number of entries. R = data/MC is the ratio data over Monte Carlo.

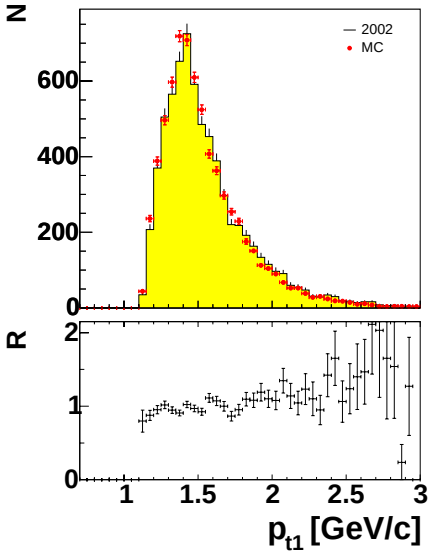

(a) Leading hadron p_t.

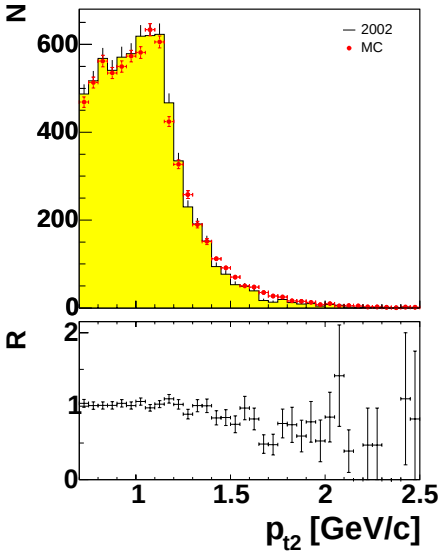

(b) Second hadron p_t.

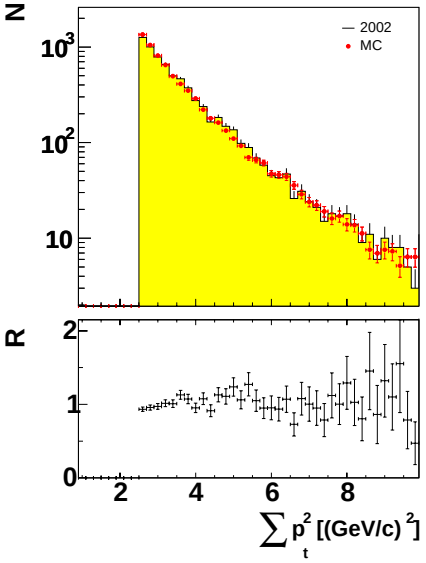

(c) Sum of the transverse momenta squared of the two high-p_t hadrons.

Figure B.4: Comparison of 2002 data and Monte Carlo for the transverse momentum of the first (a) and second hadron (b) and $\sum p_t^2$ of the two high-p_t hadrons (c). The histograms are normalised to the number of entries. R = data/MC is the ratio data over Monte Carlo.

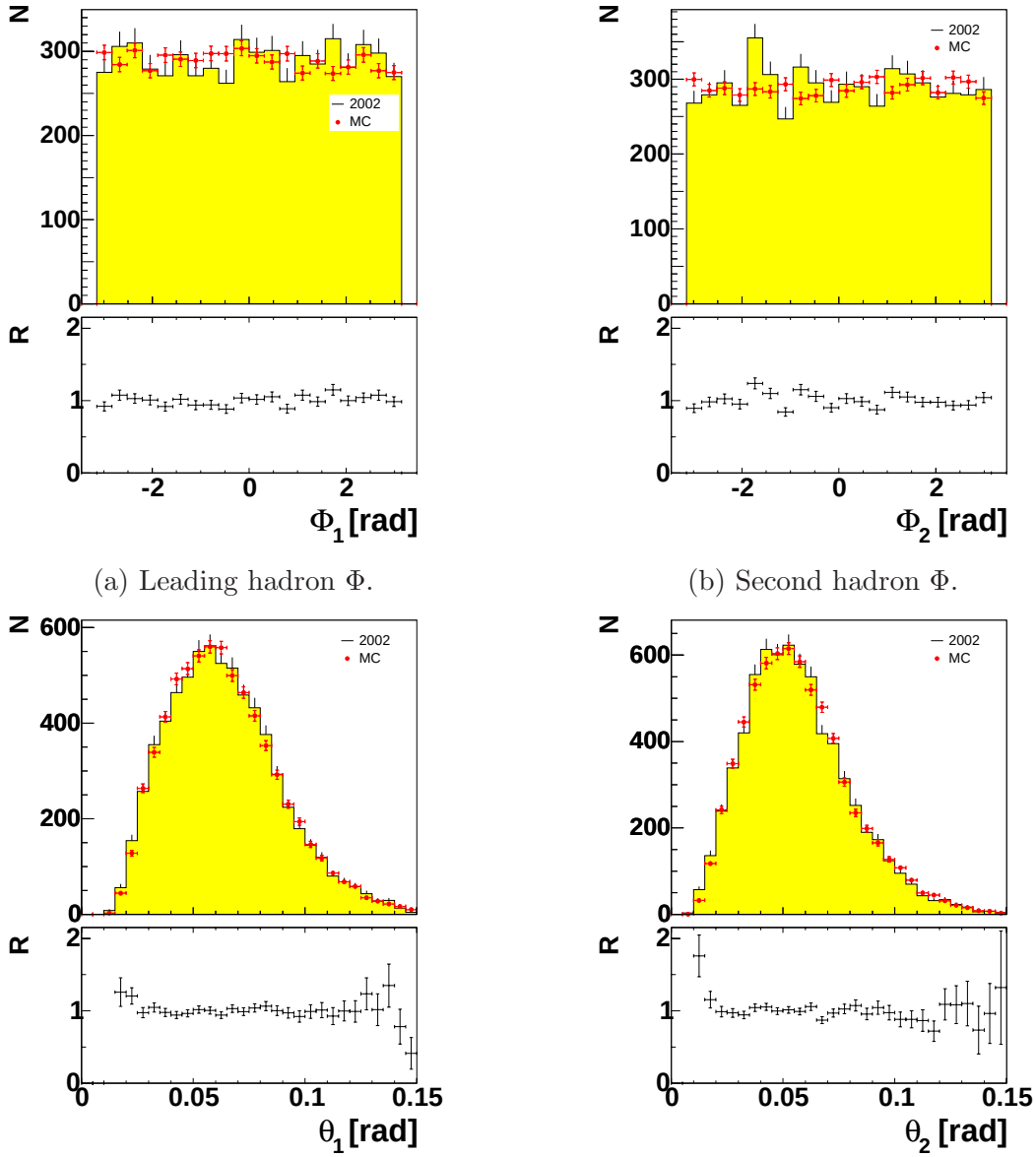

(a) Leading hadron Φ.

(b) Second hadron Φ.

(c) Leading hadron θ.

(d) Second hadron θ.

Figure B.5: Comparison of 2002 data and Monte Carlo for the azimuthal angle between the outgoing hadron and the lepton scattering plane for the first hadron (a) and the second hadron (b) and the hadron scattering angle with respect to the virtual photon of the first (c) and second hadron (d). The histograms are normalised to the number of entries. R = data/MC is the ratio data over Monte Carlo.

Bibliography

[1] M. Anselmino, A. Efremov, E. Leader, The Theory and Phenomenology of Polarized Deep Inelastic Scattering, Phys. Rep. **261** (1995) 1–124.

[2] B. Lampe, E. Reya, Spin Physics and Polarized Structure Functions, Phys. Rep. **332** (2000) 1–163.

[3] K. Rith, Spin Asymmetries in Deep Inelastic Electron-Nucleon Scattering: Selected HERMES Results, Prog. Part. Nucl. Phys. **49** (2002) 245–324.

[4] K. Rith, Quark-Gluon Structure of the Nucleon, in: F. Lenz et al. (Ed.), Lectures on QCD, Springer Verlag, 1997.

[5] E. Leader, Spin in Particle Physics, Cambridge University Press, 2001.

[6] A. V. Manohar, An Introduction to Spin Dependent Deep Inelastic Scattering, Lectures given at Lake Louise Winter Inst., Lake Louise, Canada, 1992, hep-ph/9204208 .

[7] D. J. Griffiths, Introduction to Elementary Particles, John Wiley & Sons, 1987, New York, USA.

[8] F. Halzen, A. Martin, Quarks and Leptons, John Wiley & Sons, 1984.

[9] E. D. Bloom et al., High-Energy Inelastic e-p Scattering at 6-degrees and 10-degrees, Phys. Rev. Lett. **23** (1969) 930–934.

[10] M. Breidenbach et al., Observed Behavior of Highly Inelastic Electron-Proton Scattering, Phys. Rev. Lett. **23** (1969) 935–939.

[11] R. E. Taylor, Deep Inelastic Scattering: The Early Years, Rev. Mod. Phys. **63** (1991) 573–595.

[12] H. W. Kendall, Deep Inelastic Scattering: Experiments on the Proton and the Observation of Scaling, Rev. Mod. Phys. **63** (1991) 597–614.

[13] J. I. Friedman, Deep Inelastic Scattering: Comparisons with the Quark Model, Rev. Mod. Phys. **63** (1991) 615–629.

[14] J. D. Bjorken, Asymptotic Sum Rules at Infinite Momentum, Phys. Rev. **179** (1969) 1547–1553.

[15] C. G. Callan, D. J. Gross, High-Energy Electroproduction and the Constitution of the Electric Current, Phys. Rev. Lett. **22** (1969) 156–159.

[16] L. W. Whitlow, S. Rock, A. Bodek, E. M. Riordan, S. Dasu, A Precise Extraction of $R = \sigma_L/\sigma_T$ from a Global Analysis of the SLAC Deep Inelastic e-p and e-d Scattering Cross Sections, Phys. Lett. **B250** (1990) 193–198.

[17] K. Abe et al., Measurements of $R = \sigma_L/\sigma_T$ for $0.03 < x < 0.1$ and Fit to World Data, Phys. Lett. **B452** (1999) 194–200.

[18] E. S. Ageev et al., Measurement of the Spin Structure of the Deuteron in the DIS Region, Phys. Lett. **B612** (2005) 154–164.

[19] L. D. Nardo, Polarized Inclusive Structure Functions and Fits to g_1 Data, talk given at: 11th International Workshop on Deep Inelastic Scattering (DIS 2003), St. Petersburg, Russia.

[20] M. Gell-Mann, A Schematic Model of Baryons and Mesons, Phys. Lett. **8** (1964) 214–215.

[21] G. Zweig, An SU(3) Model for Strong Interaction Symmetry and its Breaking. 2 , CERN-TH-412.

[22] R. P. Feynman, Very High-Energy Collisions of Hadrons, Phys. Rev. Lett. **23** (1969) 1415–1417.

[23] J. D. Bjorken, E. A. Paschos, Inelastic Electron-Proton and Gamma-Proton Scattering, and the Structure of the Nucleon, Phys. Rev. **185** (1969) 1975–1982.

[24] R. Devenish, A. Cooper-Sarkar, Deep Inelastic Scattering, Oxford University Press, 2004.

[25] A. D. Martin, R. G. Roberts, W. J. Stirling, R. S. Thorne, MRST2001: Partons and α_s from Precise Deep Inelastic Scattering and Tevatron Jet Data, Eur. Phys. J. **C23** (2002) 73–87.

[26] A. D. Martin, R. G. Roberts, W. J. Stirling, R. S. Thorne, Uncertainties of Predictions from Parton Distributions. I: Experimental Errors., Eur. Phys. J. **C28** (2003) 455–473.

[27] S. Eidelman et al., Review of Particle Physics, Physics Letters B **592** (2004) 1.
`http://pdg.lbl.gov`

[28] S. Aid et al., The Gluon Density of the Proton at low x from a QCD Analysis of F_2, Phys. Lett. **B354** (1995) 494–505.

[29] M. Derrick et al., Extraction of the Gluon Density of the Proton at small x, Phys. Lett. **B345** (1995) 576–588.

[30] D. Allasia et al., Inelastic J/Psi Production in Deep Inelastic Scattering from Hydrogen and Deuterium and the Gluon Distribution of Free Nucleons, Phys. Lett. **B258** (1991) 493–498.

[31] S. Aid et al., A Direct Determination of the Gluon Density in the Proton at low x, Nucl. Phys. **B449** (1995) 3–24.

[32] J. Kodaira, S. Matsuda, T. Muta, K. Sasaki, T. Uematsu, QCD Effects in Polarized Electroproduction, Phys. Rev. **D20** (1979) 627.

[33] J. Kodaira, S. Matsuda, K. Sasaki, T. Uematsu, QCD Higher Order Effects in Spin Dependent Deep Inelastic Electroproduction, Nucl. Phys. **B159** (1979) 99.

[34] J. Kodaira, QCD Higher Order Effects in Polarized Electroproduction: Flavor Singlet Coefficient Functions, Nucl. Phys. **B165** (1980) 129.

[35] J. Ashman et al., A Measurement of the Spin Asymmetry and Determination of the Structure Function g_1 in Deep Inelastic Muon-Proton Scattering, Phys. Lett. **B206** (1988) 364.

[36] J. Ashman et al., An Investigation of the Spin Structure of the Proton in Deep Inelastic Scattering of Polarized Muons on Polarized Protons, Nucl. Phys. **B328** (1989) 1.

[37] J. R. Ellis, R. L. Jaffe, A Sum Rule for Deep Inelastic Electroproduction from Polarized Protons, Phys. Rev. **D9** (1974) 1444.

[38] B. Adeva et al., A next-to-leading order QCD Analysis of the Spin Structure Function g_1, Phys. Rev. **D58** (1998) 112002.

[39] M. Hirai, S. Kumano, N. Saito, Determination of Polarized Parton Distribution Functions and their Uncertainties, Phys. Rev. **D69** (2004) 054021.

[40] A. Airapetian et al., Quark Helicity Distributions in the Nucleon for up, down, and strange Quarks from Semi-Inclusive Deep Inelastic Scattering, Phys. Rev. **D71** (2005) 012003.

[41] T. D. Averett, Nucleon Spin Structure Functions g_1 and g_2 from Polarized Inclusive Scattering, AIP Conf. Proc. **675** (2003) 88–97.

[42] J. Hannappel, Measurement of the Spin Structure of the Deuteron at COMPASS, talk given at: DIS05 - 13th International Workshop on Deep Inelastic Scattering, Madison, Wisconsin USA.

[43] M. Glück, E. Reya, M. Stratmann, W. Vogelsang, Models for the Polarized Parton Distributions of the Nucleon, Phys. Rev. **D63** (2001) 094005.

[44] J. Blümlein, H. Böttcher, QCD Analysis of Polarized Deep Inelastic Scattering Data and Parton Distributions, Nucl. Phys. **B636** (2002) 225–263.

[45] J. D. Bjorken, Inelastic Scattering of Polarized Leptons from Polarized Nucleons, Phys. Rev. **D1** (1970) 1376–1379.

[46] J. D. Bjorken, Applications of the Chiral U(6) x (6) Algebra of Current Densities, Phys. Rev. **148** (1966) 1467–1478.

[47] D. Adams et al., Spin Structure of the Proton from Polarized Inclusive Deep Inelastic Muon Proton Scattering, Phys. Rev. **D56** (1997) 5330–5358.

[48] G. Altarelli, G. Parisi, Asymptotic Freedom in Parton Language, Nucl. Phys. **B126** (1977) 298.

[49] V. N. Gribov, L. N. Lipatov, Deep Inelastic e-p Scattering in Perturbation Theory, Sov. J. Nucl. Phys. **15** (1972) 438–450.

[50] Y. L. Dokshitzer, Calculation of the Structure Functions for Deep Inelastic Scattering and e+ e- Annihilation by Perturbation Theory in Quantum Chromodynamics (in russian), Sov. Phys. JETP **46** (1977) 641–653.

[51] G. Altarelli, R. D. Ball, S. Forte, G. Ridolfi, Theoretical Analysis of Polarized Structure Functions, Acta Phys. Polon. **B29** (1998) 1145–1173.

[52] W. Vogelsang, A Rederivation of the Spin-Dependent Next-to-leading Order Splitting Functions, Phys. Rev. **D54** (1996) 2023–2029.

[53] W. Vogelsang, The Spin-Dependent Two-Loop Splitting Functions, Nucl. Phys. **B475** (1996) 47–72.

[54] R. Mertig, W. L. van Neerven, The Calculation of the Two-Loop Spin Splitting Functions P(ij)(1)(x), Z. Phys. **C70** (1996) 637–654.

[55] M. Glück, E. Reya, M. Stratmann, W. Vogelsang, Next-to-leading Order Radiative Parton Model Analysis of Polarized Deep Inelastic Lepton-Nucleon Scattering, Phys. Rev. **D53** (1996) 4775–4786.

[56] E. Leader, A. V. Sidorov, D. B. Stamenov, A New Evaluation of Polarized Parton Densities in the Nucleon, Eur. Phys. J. **C23** (2002) 479–485.

[57] E. Leader, A. V. Sidorov, D. B. Stamenov, Polarized Parton Densities in the Nucleon, Phys. Rev. **D58** (1998) 114028.

[58] E. Leader, A. V. Sidorov, D. B. Stamenov, A New Study of the Polarized Parton Densities in the Nucleon, Phys. Lett. **B462** (1999) 189–194.

[59] S. L. Adler, Axial Vector Vertex in Spinor Electrodynamics, Phys. Rev. **177** (1969) 2426–2438.

[60] R. D. Carlitz, J. C. Collins, A. H. Mueller, The Role of the Axial Anomaly in Measuring Spin Dependent Parton Distributions, Phys. Lett. **B214** (1988) 229.

[61] G. Altarelli, G. G. Ross, The Anomalous Gluon Contribution to Polarized Leptoproduction, Phys. Lett. **B212** (1988) 391.

[62] S. L. Adler, W. A. Bardeen, Absence of Higher Order Corrections in the Anomalous Axial Vector Divergence Equation, Phys. Rev. **182** (1969) 1517–1536.

[63] C. S. Lam, B.-A. Li, Total Gluon Helicity and Polarized Deep Inelastic Scattering, Phys. Rev. **D25** (1982) 683–694.

[64] G. Baum et al., COMPASS: A Proposal for a Common Muon and Proton Apparatus for Structure and Spectroscopy, CERN-SPSLC-96-14 .

[65] M. v. Hodenberg, Ph.D. Thesis, Universität Freiburg (in preparation).

[66] A. Bravar, D. von Harrach, A. Kotzinian, Large Gluon Polarization from Correlated High-p_T Hadron Pairs in Polarized Electro-Production, Phys. Lett. **B421** (1998) 349–359.

[67] B. Andersson, G. Gustafson, G. Ingelman, T. Sjostrand, Parton Fragmentation and String Dynamics, Phys. Rep. **97** (1983) 31.

[68] G. Ingelman, A. Edin, J. Rathsman, LEPTO 6.5 - A Monte Carlo Generator for Deep Inelastic Lepton-Nucleon Scattering, Comput. Phys. Commun. **101** (1997) 108–134.

[69] R. Kuhn, Ph.D. Thesis, TU München (in preparation).

[70] D. Matthiä, Measurement of Cross Sections and Asymmetries in Semi-Inclusive Deep Inelastic Scattering, Diploma Thesis, Universität Freiburg (2005).

[71] P. Liebing, Can the Gluon Polarization in the Nucleon be extracted from HERMES Data on Single High-p_t Hadrons?, Ph.D. Thesis, Universität Hamburg (2004).

[72] B. Jäger, Studies of the Hadronic Spin Structure in Hard Scattering Processes at the Next-to-Leading Order of QCD, Ph.D. Thesis, Universität Regensburg (2004).

[73] G. Bunce, N. Saito, J. Soffer, W. Vogelsang, Prospects for Spin Physics at RHIC, Ann. Rev. Nucl. Part. Sci. **50** (2000) 525–575.

[74] PHENIX/Spin Collaboration, Proposal on Spin Physics using the RHIC Polarized Collider, BNL-PROPOSAL-R5 .

[75] M. E. Beddo et al., STAR: Conceptual Design Report for the Solenoidal Tracker at RHIC, BNL-PUB-5347 .

[76] S. S. Adler et al., Double Helicity Asymmetry in Inclusive Mid-rapidity π^0 Production for Polarized p + p Collisions at $\sqrt{s}$ = 200 GeV, Phys. Rev. Lett. **93** (2004) 202002.

[77] N. Doble, L. Gatignon, G. von Holtey, F. Novoskoltsev, The Upgraded Muon Beam at the SPS, Nucl. Instrum. Meth. **A343** (1994) 351–362.

[78] L. Gatignon, M2 Beamline, User Manual.
`http://gatignon.home.cern.ch/gatignon/M2manual.html`

[79] L. Gatignon, Private Communication.

[80] B. Adeva et al., Measurement of the Spin-Dependent Structure Function $g_1(x)$ of the Deuteron, Phys. Lett. **B302** (1993) 533–539.

[81] B. Adeva et al., Measurement of the Polarization of a High-Energy Muon Beam, Nucl. Instrum. Meth. **A343** (1994) 363–373.

[82] M. v. Hodenberg, A First Reconstruction of COMPASS Data, Diploma Thesis, Universität Freiburg (2002).

[83] D. Adams et al., The Polarized Double Cell Target of the SMC, Nucl. Instrum. Meth. **A437** (1999) 23–67.

[84] J. Ball et al., First Results of the Large COMPASS ^{6}LiD Polarized Target, Nucl. Instrum. Meth. **A498** (2003) 101–111.

[85] N. Doshita, J. Koivuniemi, K. Kondo, S. Neliba, Target Material Data of 2002 Run, COMPASS Note 2003-5.

[86] N. Doshita, F. Gautheron, Y. Kisselev, J. Koivuniemi, K. Kondo, Target Material Data of Run 2003, COMPASS Note 2003-8.

[87] A. Abragam, M. Goldman, Principles of Dynamic Nuclear Polarisation, Rept. Prog. Phys. **41** (1978) 395.

[88] A. Abragam, M. Borghini, Dynamic Polarization of Nuclear Targets, in: Progress in Low-Temperature Physics Vol 4, Ed. C. J. Gorter (North Holland Publ. Co.), 1964, p. 384.

[89] N. Takabayashi, Polarized Target for the Measurement of the Gluon Contribution to the Nucleon Spin in the COMPASS Experiment, Ph.D. Thesis, Nagoya University (2002).

[90] K. Kondo et al., Polarization Measurement in the COMPASS Polarized Target, Nucl. Instrum. Meth. **A526** (2004) 70–75.

[91] N. Doshita et al., Performance of the COMPASS Polarized Target Dilution Refrigerator, Nucl. Instrum. Meth. **A526** (2004) 138–143.

[92] G. K. Mallot, The COMPASS Spectrometer at CERN, Nucl. Instrum. Meth. **A518** (2004) 121–124.

[93] I. Daito et al., Time Resolution of Multi-Cladding Scintillating Fiber Hodoscope, Nucl. Instrum. Meth. **A433** (1999) 587–591.

[94] J. Bisplinghoff et al., A Scintillating Fibre Hodoscope for High Rate Applications, Nucl. Instrum. Meth. **A490** (2002) 101–111.

[95] A. Teufel, Entwicklung und Bau von Hodoskopen aus szintillierenden Fasern für das COMPASS Experiment, Ph.D. Thesis, Universität Erlangen (2003).

[96] H. Angerer et al., Present Status of Silicon Detectors in COMPASS, Nucl. Instrum. Meth. **A512** (2003) 229–238.

[97] M. Wiesmann, A Silicon Microstrip Detector for COMPASS and A First Measurement of the Transverse Polarisation of Λ^0-Hyperons from Quasi-Real Photo-Production, Ph.D. Thesis, TU München (2004).

[98] A.-M. Dinkelbach, Private Communication (August 2005).

[99] F. Sauli, GEM: A New Concept for Electron Amplification in Gas Detectors, Nucl. Instrum. Meth. **A386** (1997) 531–534.

[100] M. C. Altunbas et al., Construction, Test and Commissioning of the Triple-GEM Tracking Detector for COMPASS, Nucl. Instrum. Meth. **A490** (2002) 177–203.

[101] Q. Weitzel, Performance of the GEM Detectors, COMPASS Collaboration Meeting, Paris (March 2004).

[102] Y. Giomataris, P. Rebourgeard, J. P. Robert, G. Charpak, MICROMEGAS: A High-Granularity Position-Sensitive Gaseous Detector for High Particle-Flux Environments, Nucl. Instrum. Meth. **A376** (1996) 29–35.

[103] D. Thers et al., Micromegas as a Large Microstrip Detector for the COMPASS Experiment, Nucl. Instrum. Meth. **A469** (2001) 133–146.

[104] C. Bernet et al., The 40-cm x 40-cm Gaseous Microstrip Detector Micromegas for the High-Luminosity COMPASS Experiment at CERN, Nucl. Instrum. Meth. **A536** (2005) 61–69.

[105] H. P. da Costa, Développement de Chambres à Dérive pour les Hauts Flux dans l'Expérience COMPASS, Ph.D. Thesis, Université de Paris-Sud (2001).

[106] S. Panebianco, Performances of Drift Chambers and MicroMegas in 2003, COMPASS Collaboration Meeting, Lissabon (October 2003).

[107] M. Leberig, Status and Performance of W45, COMPASS Collaboration Meeting, Lissabon (October 2003).

[108] M. Leberig, W45 Calibration and Resolution, COMPASS Analysis Meeting, CERN, Geneva (May 2004).

[109] V. N. Bychkov et al., Construction and Manufacture of Large Size Straw-Chambers of the COMPASS Spectrometer Tracking System, Part. Nucl. Lett. **111** (2002) 64–73.

[110] A. Zvyagin, Performance of the STRAW Detectors in COMPASS, COMPASS Collaboration Meeting, CERN, Geneva (Dezember 2003).

[111] E. Iarocci, Plastic Streamer Tubes and their Applications in High-Energy Physics, Nucl. Instrum. Meth. **217** (1983) 30–42.

[112] O. Gavrishchuk et al., Calorimeter for Hadron Detection in the Energy-Range 10 - 100 GeV, Tech. Rep. JINR D13-2004-186, Dubna (2004).

[113] J. Hannapel et al., The COMPASS Trigger System for Muon Scattering, Nucl. Instrum. Meth. **A550** (2005) 217–240.

[114] M. Leberig, Das COMPASS Triggersystem zur Messung von ΔG, Ph.D. Thesis, Universität Mainz (2002).

[115] H. Fischer et al., The COMPASS Data Acquisition System, IEEE Trans. Nucl. Sci. **49** (2002) 443–447.

[116] B. Grube, The Trigger Control System and the Common GEM and Silicon Readout for the COMPASS Experiment, Diploma Thesis, TU München (2001).

[117] T. Schmidt, A Common Readout Driver for the COMPASS Experiment, Ph.D. Thesis, Universität Freiburg (2002).

[118] A. Grünemaier, Eine universelle Ausleseschnittstelle für das COMPASS-Experiment, Ph.D. Thesis, Universität Freiburg (2002).

[119] R. McLaren et al., The S-Link Project.
`http://hsi.web.cern.ch/HSI/s-link/`

[120] E. van der Bij, R. A. McLaren, O. Boyle, G. Rubin, S-Link, a Data Link Interface Specification for the LHC Era, IEEE Trans. Nucl. Sci. **44** (1997) 398–402.

[121] W. Kastaun, Erste Untersuchungen zur Hadron-Produktion am COMPASS-Experiment, Diploma Thesis, Universität Freiburg (2002).

[122] C. Bernet, Caractérisation des Micromégas et Mesure de la Polarisation des Gluons sur COMPASS, Ph.D. Thesis, Université Paris 7 (2004).

[123] COMPASS, Electronic Log Book.
`http://wwwcompass2.cern.ch/runLogbook/dirphp/`

[124] T. Sjostrand, L. Lonnblad, S. Mrenna, P. Skands, PYTHIA 6.3: Physics and Manual, hep-ph/0308153 .

[125] V. Alexakhin, COMGEANT web page.
`http://valexakh.home.cern.ch/valexakh/wwwcomg/`

[126] R. Windmolders, Comparison of MC Generators for high-p_T Hadronic Events, COMPASS Analysis Meeting (March 2004).

[127] C. Bernet, S. Hedicke, J.-M. L. Goff, S. Procureur, Measurement of Delta G/G in the Production of High-p_T Hadrons Pairs at low Q2 (2002 data), COMPASS Note 2005-8.

[128] C. Bernet, S. Hedicke, J.-M. L. Goff, S. Procureur, Measurement of Delta G/G in the Production of High-p_T Hadrons Pairs at low Q2 (2003 data), COMPASS Note 2005-9.

[129] E. S. Ageev et al., Gluon Polarization in the Nucleon from Quasi-Real Photoproduction of High-p_T Hadron Pairs, submitted to Phys. Lett. B.

[130] M. Glück, E. Reya, A. Vogt, Dynamical Parton Distributions Revisited, Eur. Phys. J. **C5** (1998) 461–470.

[131] H. L. Lai et al., Global QCD Analysis of Parton Structure of the Nucleon: CTEQ5 Parton Distributions, Eur. Phys. J. **C12** (2000) 375–392.

[132] T. Sjostrand, PYTHIA 5.7 and JETSET 7.4: Physics and manual, hep-ph/9508391 .

[133] B. Andersson, G. Gustafson, T. Sjostrand, Baryon Production in Jet Fragmentation and Upsilon Decay, Phys. Scripta **32** (1985) 574.

[134] B. A. Kniehl, G. Kramer, B. Potter, Testing the Universality of Fragmentation Functions, Nucl. Phys. **B597** (2001) 337–369.

[135] I. Akushevich, H. Böttcher, D. Ryckbosch, RADGEN 1.0: Monte Carlo Generator for Radiative Events in DIS on Polarized and Unpolarized Targets, hep-ph/9906408 .

[136] GEANT - Detector Description and Simulation Tool, CERN Program Library Long Writeup W5013, CERN, Geneva.

[137] S. Agostinelli et al., GEANT4: A Simulation Toolkit, Nucl. Instrum. Meth. **A506** (2003) 250–303.

[138] B. Gobbo et al., CORAL web page.
`http://coral.web.cern.ch/coral/`

[139] S. Gerassimov, PHAST web page.
`http://ges.home.cern.ch/ges/phast/index.html`

[140] J. Zhao, A. Pretz et al., Production web page.
`http://na58dst1.home.cern.ch/na58dst1/dstprod.html`

[141] S. Koblitz, A. Korzenev, Data Quality web page.
`http://wwwcompass.cern.ch/compass/software/offline/input/stab/index.html`

[142] B. Adeva et al., Spin Asymmetries for Events with High-p_T Hadrons in DIS and an Evaluation of the Gluon Polarization, Phys. Rev. **D70** (2004) 012002.

[143] K. Gustafsson, Computation of the Dilution Factor for the Year 2002 COMPASS Data, COMPASS Note 2003-3.

[144] B. Badelek, Spin Independent Structure Functions, $F_2(x, Q^2)$ and $R(x, Q^2)$, in the COMPASS Kinematic Region, COMPASS Note 2004-6.

[145] J.-M. L. Goff, Asymmetry Extraction, COMPASS Note 2004-3.

[146] J. Pretz, A New Method for Asymmetry Extraction, COMPASS Note 2004-11.

[147] K. Kowalik, Selection of the Photon Gluon Fusion Process by Requiring High-p_T Hadrons in Muon-Nucleon Scattering, Ph.D. Thesis, Soltan Institute for Nuclear Studies, Warszawa (2004).

[148] J. Botts et al., CTEQ Parton Distributions and Flavor Dependence of Sea Quarks, Phys. Lett. **B304** (1993) 159–166.

[149] A. Bravar, K. Kurek, R. Windmolders, POLDIS: A Monte Carlo for Polarized (Semi-Inclusive) Deep inelastic Scattering, Comput. Phys. Commun. **105** (1997) 42–61.

[150] K. Abe et al., Measurements of the Proton and Deuteron Spin Structure Functions g_1 and g_2, Phys. Rev. **D58** (1998) 112003.

[151] B. Adeva et al., Spin Asymmetries A_1 and Structure Functions g_1 of the Proton and the Deuteron from Polarized High-Energy Muon Scattering, Phys. Rev. **D58** (1998) 112001.

[152] K. Ackerstaff et al., Observation of a Coherence Length Effect in Exclusive ρ^0 Electroproduction, Phys. Rev. Lett. **82** (1999) 3025–3029.

[153] S. Procureur, Private Communication (August 2005).

[154] A. Airapetian et al., Measurement of the Spin Asymmetry in the Photoproduction of Pairs of High-p_T Hadrons at HERMES, Phys. Rev. Lett. **84** (2000) 2584–2588.

[155] A. Korzenev, J. Lichtenstadt, R. Windmolders, Update of the COMPASS QCD Analysis, COMPASS Note 2005-18.

[156] X. Zheng et al., Precision Measurement of the Neutron Spin Asymmetry A_1^n and Spin-Flavor Decomposition in the Valence Quark Region, Phys. Rev. Lett. **92** (2004) 012004.

List of Figures

List of Tables

Acknowledgements

I would like to thank Prof. Kay Königsmann for giving me the opportunity to perform my PhD thesis in his group at the University of Freiburg and at CERN in Geneva. He always helped in organisatorial things and gave me the possibility to spend much time at CERN to learn a lot about COMPASS and many other things.

Thanks to Horst Fischer and Fritz-Herbert Heinsius for helping to become familiar with the COMPASS experimental setup, keeping computers running and for proofreading my thesis. I am thankful to Jürgen Franz, Frank Nerling and Christian Schill for critical reading and many helpful comments.

Thanks to my PhD colleagues Martin von Hodenberg, Donghee Kang and Anselm Vossen for sharing their knowledge in the smaller and larger problems of daily life doing data analysis and helpful discussions. I'm thankful to Anna Danasino, Inga Ludwig, Jürgen Reymann, Daniel Matthiä and Andreas Mutter for being a good company in our office as well as to Donghwa Kang, Dominik Setter, Sebastian Trippel, Julia Vogel and Eric Weise for many barbecues and events at CERN and Oliver Kilias for asking many questions about things I thought I have forgotten. Thanks to Rainer Fastner for organising all the little things making office and laboratory life more comfortable.

I am indebted to Thomas Schmidt and Andreas Grünemaier for patient explanations about the COMPASS DAQ and their help getting started.

I am grateful to the COMPASS high-p_t group where I learned a lot about the physics we want to explore and how approach it, especially to Jean-Marc Le Goff, Jörg Pretz and Roland Windmolders. Thanks to Colin Bernet who helped a lot getting started with the Monte Carlo and to Sébastien Procureur for being a patient cross-checker.

I am indebted to all the people in the COMPASS collaboration who put a lot of effort in building and running the experiment, designed the tools for the data analysis and simulation and helped to learn about all this during many shifts and even more meetings. They all made this work possible.

I am especially thankful to my parents for their support and understanding throughout the years and to Frank for his support and patience.